THÈSE

Pour obtenir le grade de

DOCTEUR DE L'UNIVERSITÉ GRENOBLE ALPES

École doctorale : STEP - Sciences de la Terre de l'Environnement et des Planètes
Spécialité : Sciences de la Terre et de l'Environnement
Unité de recherche : Institut des Géosciences de l'Environnement (IGE)

Interpolation des précipitations journalières pour l'estimation des événements intenses en zones de montagne

Interpolation of daily précipitation data focusing on high values in mountain areas

Présentée par :

Valentin DURA

Direction de thèse :

Anne-Catherine FAVRE PROFESSEURE DES UNIVERSITES, GRENOBLE INP - UGA	Directrice de thèse
Guillaume EVIN CHARGE DE RECHERCHE, INRAE - IGE	Co-directeur de thèse
David PENOT EDF DTG	Co-encadrant de thèse

Rapporteurs :

Vincent FORTIN
SENIOR SCIENTIST, Environment and Climate Change Canada
Denis ALLARD
DIRECTEUR DE RECHERCHE, INRAE centre Provence-Alpes-Côte d'Azur

Thèse soutenue publiquement le **15 décembre 2025**, devant le jury composé de :

Jean-Philippe VIDAL, DIRECTEUR DE RECHERCHE, INRAE Lyon-Grenoble Auvergne-Rhône-Alpes	Président
Anne-Catherine FAVRE, PROFESSEURE DES UNIVERSITES, Grenoble INP - UGA	Directrice de thèse
Guillaume EVIN, CHARGE DE RECHERCHE HDR, INRAE Lyon-Grenoble Auvergne-Rhône-Alpes	Co-directeur de thèse
Vincent FORTIN, SENIOR SCIENTIST, Environment and Climate Change Canada	Rapporteur
Denis ALLARD, DIRECTEUR DE RECHERCHE, INRAE centre Provence-Alpes-Côte d'Azur	Rapporteur
Clotilde AUGROS, CHARGEE DE RECHERCHE, Météo France	Examinatrice

Invités :

David PENOT
INGENIEUR DOCTEUR, EDF-DTG

Remerciements

La réalisation de cette thèse n'aurait pas été possible sans le soutien précieux de nombreuses personnes.

Je souhaite commencer par remercier ma formidable équipe de direction/encadrement de thèse : Guillaume Evin, Anne-Catherine Favre et David Penot. J'ai beaucoup bénéficié de votre complémentarité et je mesure la chance d'avoir pu faire cette thèse avec vous.

Guillaume, merci de m'avoir accordé ta confiance dès mon stage de 2A à l'ENSAI, sans quoi je n'aurais sans doute pas eu la chance d'effectuer cette thèse. Au cours de ces trois années, j'ai été impressionné par ta carrière de chercheur, menée avec brio. Tu as su garder une expertise technique en statistiques, l'appliquer à l'hydrologie avec talent, tout en restant très disponible pour tes stagiaires et thésards : c'est inspirant ! Merci pour le cadrage du sujet, tes remarques constructives et toujours pertinentes, qui ont grandement enrichi la qualité scientifique de ce travail. J'ai aussi beaucoup apprécié nos discussions plus générales sur les rouages de la recherche académique.

Anne-Catherine, j'ai été impressionné par ta disponibilité malgré tes responsabilités à la présidence de l'UGA. Merci pour tes nombreuses relectures d'articles, qui ont contribué à en améliorer la qualité. Merci aussi d'avoir participé si régulièrement à nos réunions hebdomadaires, toujours avec bonne humeur, ce qui m'a beaucoup encouragé et motivé. J'ai particulièrement apprécié ton soutien dans les moments charnières, comme la constitution du jury.

David, merci tout d'abord pour ta passion pour l'hydrologie et ta créativité scientifique, qui ont grandement contribué à la réussite de ce travail. J'ai aussi beaucoup apprécié ta réactivité et ta capacité à t'adapter aux travaux que je te présentais. Il ne fallait pas jouer au bingo avec « David, t'as deux secondes ? », secondes qui se transformaient allègrement en minutes de discussions passionnantes ! Merci également d'avoir géré toutes les démarches administratives à EDF, qui ont rendu cette thèse possible ; j'imagine le temps que cela t'a demandé.

Je remercie également les membres de mon CSI, Samuel Morin et Martin Ménégoz, pour leur suivi attentif et leurs conseils lors des évaluations annuelles. Vos recommandations, qu'il s'agisse d'analyses supplémentaires ou de la présentation des objectifs de la thèse, ont été précieuses.

Merci à l'ensemble de mon jury de thèse, constitué dans l'urgence mais avec efficacité. Merci aux rapporteurs, Vincent Fortin et Denis Allard, pour leurs remarques pertinentes qui ont contribué à améliorer ce travail. Merci à Clotilde Augros pour sa participation aux discussions scientifiques lors de la soutenance, et à Jean-Philippe Vidal pour avoir accepté de présider ce moment important.

Je tiens également à remercier l'ensemble du service Études du département Eau Environnement. Un merci particulier à Manu, Joël et Matthieu, qui ont supervisé ce travail de plus loin, et partagé leurs connaissances et passion communicative pour l'hydrologie. Merci à Florent pour tes discussions toujours stimulantes, ton humour, tes conseils scientifiques... et de vie ! Je te salue depuis mon four à pain en lisant R for Data Science ! Merci à Alexandre pour nos discussions sur les chemins de vie que la recherche ouvre (ou ferme) et les choix qu'elle implique. Merci à tout le service, et plus particulièrement à Claire pour m'avoir préparé aux entretiens. Merci à vous tous de m'avoir si bien accueilli : j'ai hâte de collaborer avec vous sur de nouveaux sujets !

Un grand merci aussi à toute l'équipe HMCIS de l'IGE, mon laboratoire d'accueil. Merci à mes co-bureaux Alice, Nelson et Victoire, qui ont rendu mes rares visites au labo particulièrement agréables.

Je voudrais exprimer toute ma gratitude à ma famille pour avoir été à mes côtés durant cette aventure et avoir rendu ce parcours professionnel possible. Merci à mes grands-parents de m'avoir transmis leur sens du travail, et surtout beaucoup d'amour. J'ai aimé partager avec vous quelques bribes de mon sujet de thèse, ou évoquer des souvenirs communs. Merci à mes parents et à mon frère pour tous ces moments passés ensemble qui réchauffent le cœur, votre esprit rassembleur et vos précieux conseils de vie.

Merci également à mes amis pour ces moments de joie partagés, qui ont contribué au bon déroulement de ces trois années. Merci à mes amis d'enfance, pour les souvenirs dorés du basket, et pour les grands moments partagés aussi bien en montagne qu'à la pétanque. Merci à mes amis de prépa, je ne vous citerai pas tous, vous êtes beaucoup trop nombreux, et en plus vous coûtez cher ! Un merci spécial à Alexandre et PA : que nos escapades en montagne et nos discussions près d'un feu ou en bivouac perdurent longtemps ! Comment oublier mes amis de l'ENSAI pour tous ces moments partagés, à Grenoble, à Paris ou en vacances, qui m'ont permis de déconnecter de la thèse.

Enfin, je ne saurais trop remercier Inès, celle qui m'accompagne depuis six ans. Tu as été un soutien infaillible dans les rares moments de doute avec ton écoute bienveillante, et une source de grande joie avec nos discussions profondes. Merci pour ton amour.

Abstract

Accurate quantification of precipitation is a key element for hydrological studies in mountain regions, where available data are limited and phenomena are strongly influenced by topography. However, existing spatial interpolation products have limitations : they tend to underestimate totals at higher elevations and smooth out spatial variability, which reduces their relevance for water balance analyses and extreme events such as floods.

This thesis introduces a new interpolation method, called ISARD (Interpolation of Station precipitation for Alpine Region at Daily resolution), designed to overcome the limitations of an existing approach. The approach combines rain-gauge observations with simulations from convection-permitting regional climate models (CP-RCM). Station totals are corrected for wind-induced undercatch, while climatological fields, built from a fusion of stations and CP-RCM outputs, explicitly account for orographic effects. Daily anomalies are then interpolated using conditional simulation, relying on anisotropic variograms derived from CP-RCM daily fields, which enables a more accurate representation of directional precipitation structures. For each day, an ensemble of 100 realizations is generated, providing an ensemble-based estimate of precipitation fields and thus a quantification of interpolation uncertainty.

Results show that integrating CP-RCM climatologies improves the representation of elevation gradients, and that using anisotropic variograms, hard to estimate from stations alone, better captures the spatial variability of intense events. Evaluations conducted with independent measurements (high-altitude watershed water balances, snow water equivalent, winter glacier mass balances) indicate that the ISARD method produces less biased estimates than SPAZM. In hydrological modeling, it also improves flood reproduction by explicitly accounting for interpolation-related uncertainty.

This thesis demonstrates that the combined use of rain-gauge data and CP-RCM simulations can generate an ensemble product of daily precipitation that accurately represents both high-elevation totals and the spatial variability of intense precipitation. The potential applications are numerous, ranging from distributed hydrological modeling to probabilistic estimation of extreme precipitation in sparsely instrumented catchments.

Keywords : Altitudinal gradients, Conditional simulation, Covariance, Climatological fields, Hydrological modeling, Regional Climate Model with Resolved Deep Convection, Precipitation, Spatial interpolation

Résumé

La quantification précise des précipitations est un élément central pour les études hydrologiques en montagne, où les données disponibles sont limitées et les phénomènes fortement influencés par la topographie. Les produits existants d'interpolation spatiale présentent toutefois des limites : ils tendent à sous-estimer les cumuls en altitude et à lisser la variabilité spatiale, ce qui réduit leur pertinence pour l'analyse des bilans hydriques et des événements extrêmes comme les crues.

Cette thèse propose une nouvelle méthode d'interpolation, baptisée ISARD (Interpolation of Station precipitation for Alpine Region at Daily resolution), pour pallier les limites d'une approche existante. L'approche combine observations pluviométriques et simulations issues de modèles régionaux de climat à convection profonde résolue (CP-RCM). Les cumuls aux stations sont corrigés pour la sous-captation liée au vent, tandis que les champs climatologiques, construits à partir d'une fusion entre stations et CP-RCM, intègrent explicitement les effets orographiques. Les anomalies journalières sont ensuite interpolées par simulation conditionnelle de champs Trans-Gaussiens, en s'appuyant sur des variogrammes anisotropiques dérivés des champs journaliers du CP-RCM, permettant ainsi de mieux représenter les structures directionnelles des précipitations. Chaque jour, un ensemble de 100 réalisations est généré, ce qui offre une estimation ensembliste des champs de précipitations et ainsi une quantification de l'incertitude d'interpolation.

Les résultats montrent que l'intégration des climatologies CP-RCM améliore la représentation des gradients altitudinaux et que l'usage de variogrammes anisotropiques, difficilement estimables avec les seules stations, permet de mieux reproduire la variabilité spatiale des événements intenses. Les évaluations menées à l'aide de mesures indépendantes (bilans hydriques de bassins versants de haute altitude, équivalent en eau de la neige, bilans de masse hivernaux de glaciers) indiquent que la méthode ISARD fournit des estimations moins biaisées que SPAZM. En modélisation hydrologique, elle améliore également la représentation des crues, grâce à la prise en compte explicite de l'incertitude liée à l'interpolation.

Cette thèse démontre que l'utilisation conjointe de données pluviométriques et de simulations CP-RCM permet de générer un produit ensembliste de précipitations quotidiennes, capable de représenter à la fois les cumuls en altitude et la variabilité spatiale des précipitations intenses. Les perspectives d'application sont nombreuses, allant de la modélisation hydrologique spatialisée à l'estimation probabiliste des précipitations extrêmes dans des bassins peu instrumentés.

Mots clés : Champs climatologiques , Covariance, Gradients altitudinaux, Interpolation

spatiale, Modélisation hydrologique,Modèle Régional de Climat à Convection Profonde Résolue, Precipitation, Simulation conditionelle

Table des matières

1 Introduction **1**

1.1 Mise en contexte . . . 1
1.2 Etat de l'art . . . 5
1.2.1 Les sources de données disponibles . . . 5
1.2.2 Les modèles d'interpolation spatiale . . . 9
1.2.3 Covariables pour l'amélioration de l'interpolation spatiale . . . 13
1.3 Positionnement de la thèse . . . 14
1.4 Questions scientifiques . . . 16

2 Variabilité spatiale des gradients de précipitations altitudinaux dans les régions à topographie complexe - application en France **19**

2.1 Introduction . . . 20
2.2 Domain and data under study . . . 22
2.2.1 A complex mountainous region . . . 22
2.2.2 A dense network of stations . . . 23
2.2.3 Gridded precipitation products . . . 24
2.3 Methods . . . 27
2.3.1 Description of the relationship between precipitation and altitude . . . 27
2.3.2 Regression at nested spatial scales . . . 28
2.3.3 Linearity of the regressions . . . 29
2.4 Results . . . 30
2.4.1 Ability of gridded precipitation products to reproduce the variability of the relationship between annual/seasonal precipitations and elevation . 30
2.4.2 Spatial and seasonal variability of Precipitation Lapse Rates . . . 34
2.4.3 Linearity of the relationship between annual precipitation and altitude 37
2.5 Discussion . . . 38
2.5.1 Ability of gridded precipitation products to capture the relationship between annual/seasonal precipitations and altitude . . . 38
2.5.2 Values and spatial variability of Precipitation Lapse Rates . . . 39
2.5.3 Dependence of the Precipitation Lapse Rates to the spatial scale . . . 41
2.5.4 Uncertainty in the study and outlooks . . . 42
2.6 Conclusion . . . 42

3 Interpolation spatiale des précipitations saisonnières à l'aide de données pluviométriques et de simulations de modèles climatiques régionaux à convection résolue dans une région à la topographie complexe 45
3.1 Introduction . . . 46
3.2 Domain and data under study . . . 47
3.3 Methods . . . 49
3.3.1 Kriging . . . 49
3.3.2 Geographically Weighted Regressions . . . 50
3.3.3 Random Forest . . . 51
3.3.4 Evaluation of spatial interpolation methods . . . 52
3.4 Results . . . 52
3.4.1 Interpolation ability and robustness of the models . . . 52
3.4.2 Altitude extrapolation performances . . . 55
3.4.3 Seasonal precipitation maps . . . 56
3.5 Discussion . . . 57
3.5.1 Statistical model abilities . . . 57
3.5.2 Physical interpretation of seasonal precipitation climatology . . . 62
3.5.3 Uncertainty and outlooks . . . 62
3.6 Conclusion . . . 63
3.A Hyper-parameters tested in the training process . . . 65
3.A.1 Ordinary Kriging (OK) . . . 65
3.A.2 Kriging with altitude drift (KED_z) . . . 65
3.A.3 Kriging with altitude drift (KED_{arome}) . . . 65
3.A.4 Geographically Weighted Regression (GWR) . . . 65
3.A.5 Random Forest (RF) . . . 65
3.A.6 Random Forest ratio (RF_{ratio}) . . . 65

4 Amélioration de l'interpolation des précipitations à l'aide de variogrammes anisotropiques dérivés de simulations de modèles climatiques régionaux à convection résolue 67
4.1 Introduction . . . 68
4.2 Domain and data under study . . . 69
4.2.1 Study domain . . . 69
4.2.2 Meteorological data . . . 70
4.3 Methods . . . 71
4.3.1 Spatial Interpolation . . . 71
4.3.2 Evaluation . . . 73
4.4 Results . . . 75
4.4.1 Evaluation of ensemble means . . . 75
4.4.2 Spatial evaluation using radar-analysis . . . 75
4.4.3 Probabilistic performances and Uncertainty Quantification . . . 77
4.4.4 Case studies . . . 78
4.5 Discussion . . . 80
4.5.1 Ensemble from conditional simulations versus local regression approach 80
4.5.2 Covariance estimation . . . 81
4.5.3 Quantification of interpolation uncertainty . . . 82
4.6 Conclusion . . . 83

5 Un cadre géostatistique reproductible pour les ensembles de précipitations quotidiennes en terrain montagneux : évaluation multi-échelle et applications hydrologiques **85**
5.1 Introduction . . . 86
5.2 Study domain and hydrometeorological data . . . 87
5.2.1 Study domain . . . 87
5.2.2 Gridded precipitation products . . . 88
5.2.3 Hydrological models . . . 90
5.3 Methods . . . 90
5.3.1 Interpolation framework . . . 90
5.3.2 Evaluation . . . 92
5.4 Results . . . 94
5.4.1 Accumulated precipitation amounts in mountain catchments . . . 94
5.4.2 Accumulated precipitation amounts at high-elevation sites . . . 95
5.4.3 Hydrological modeling of floods . . . 96
5.5 Discussion . . . 98
5.5.1 Seasonal accumulation in mountains . . . 98
5.5.2 Reproduction of floods using hydrological models . . . 100
5.5.3 Scope and reproducibility of the framework . . . 101
5.6 Conclusion . . . 102
5.A Solid fraction of precipitation . . . 103
5.B Random Forest hyperparameters . . . 103
5.C Transformation into Gaussian distribution and back-transformation . . . 103
5.D Anisotropic distance . . . 103

6 Conclusions and perspectives **105**
6.1 Contributions . . . 105
6.1.1 Contributions à l'estimation des cumuls saisonniers de précipitations en montagne . . . 105
6.1.2 Contributions à la représentation des précipitations journalières intenses 107
6.2 Perspectives . . . 108
6.2.1 Renforcer la qualité et la quantité de données . . . 108
6.2.2 Affiner la méthodologie . . . 109
6.2.3 Étendre le champs d'action d'ISARD . . . 110
6.2.4 Valoriser l'utilisation opérationnelle à EDF-DTG . . . 111

Bibliographie **114**

Table des figures

1.1 Précipitations du 21 et 22 août 2005 dans le massif de Belledonne. Le fond de carte représente le relief. La taille des points est proportionnelle au cumul de précipitations. . . . 2

1.2 Les précipitations orographiques. OpenAI (2025), ChatGPT 4, Récupéré 10 juillet 2025 de https ://chat.openai.com/ . . . 2

1.3 Illustration du processus d'interpolation spatiale : passage de précipitations journalières observées aux pluviomètres à un produit grillé. Le modèle statistique utilisé pour cette illustration est le Krigeage Ordinaire, voir sous-section 1.2.2.2 pour son explication. . . . 4

1.4 Illustration du lissage des cellules de précipitations : REF correspond à un champ radar, N100 et N1000 sont des champs reconstruits par Krigeage Ordinaire avec 100 et 1000 pluviomètres virtuels (extrait du champ radar). . . . 5

1.5 Un pluviomètre *PG2000* utilisé à EDF-DTG. . . . 6

1.6 réseau radar ARAMIS (Météo-France, 2019). La couverture des radars est représentée par des cercles. La couleur des cercles correspond aux différents types de radars : bande C (bleu), bande S (rouge) et bande X (vert). Source : https://commons.wikimedia.org/wiki/File:ARAMIS_2019.png?uselang=fr, licence CC BY-SA 4.0. . . . 7

1.7 Les différentes sources de mesure des précipitations. OpenAI. (2025). ChatGPT 4. Récupéré 10 juillet 2025 de https ://chat.openai.com/ . . . 9

1.8 Découpage de la thèse. . . . 18

2.1 **(a)** Topography of France and boundaries of eight sub-regions of interest. The extent of the study domain is located in France and is bordered by Spain, Italy, and Switzerland. **(b)** Location of stations, blue points refer to rain gauges (RG) and red points to NPT (see subsection 2.2.2). **(c)** Catchments and the corresponding number of stations. Boundaries of massifs located in the Alps are also indicated in black. **(d)** Histogram of the altitude of stations (rain gauges (RG), and NPT) and of the covered surface area (in green). . . . 24

2.2 Mean annual precipitation for the gridded precipitation products (AROME, CERRA-Land, COMEPHORE, ERA5-Land, PDIR, SERVAL, SPAZM), on the period 2007–2017. . . . 27

2.3 Comparison between the altitude dependence of precipitation from AROME, CERRA-Land, COMEPHORE, ERA5-Land, PDIR, SERVAL, SPAZM, stations (rain gauges and NPT) in seven regions. The lines show the median precipitation amount in each altitude zone and the bars denote the number of rain gauges in each area. Comparisons are done at **(a)** the station locations at the annual scale and **(b)** both station locations and on all pixels from the gridded products at the seasonal scale. At the seasonal scale, only AROME, CERRA-Land, COMEPHORE, and SPAZM are analyzed for the sake of visualization. The season *DJF* refers to the winter (December, January, February) and the season *JJA* corresponds to the summer (June, July, August). 32

2.4 Comparison of precipitation relative difference (%/100 m) computed with stations and gridded rainfall products. PRDs are derived for all couples of neighboring stations. Scatter plot between observed and gridded PRD at station locations. The dotted lines indicate the 1 :1 lines. 33

2.5 Transects in the Cévennes **(a)** and the Northern Alps **(b)**. Winter *DJF* and summer *JJA* precipitations extracted across the transects are colored according to gridded products **(c), (d)**. Elevation is represented in brown as an altitude profile. 34

2.6 Spatial distribution of R^2 **(a), (c)** and precipitation lapse rates (precipitation change per 100 m altitude difference divided by area-average precipitation) **(b), (d)** extracted from the precipitation-altitude regressions for all grids within each area. Categorical results are displayed in the French Alps at regional and catchment scales for both winter *DJF* and summer *JJA* precipitations. The area indicated as "NA" and filled in white represents regions with insufficient altitudinal variability to compute precipitation gradient. The indexes of the massifs are also printed and refer to Table 2.3. 36

2.7 Spatial distribution of winter *DJF* and summer *JJA* precipitation lapse rates (precipitation change per 100 m altitude difference divided by area-averaged precipitation) extracted from the precipitation-altitude regressions for all grids within each area. Categorical results are displayed in the study domain at the catchment scale. The area indicated as "NA" and filled in white represents catchments with insufficient altitudinal variability (standard deviation of the altitude lower than 50 m) or R^2 inferior to 0.5. 37

2.8 **(a)** Scatter plots of AROME annual precipitation (mm) as a function of the altitude for some catchments taken as illustrative examples of the different categories of BIC ratio. Linear (red lines) and piecewise linear (blue curves) regressions are superimposed. **(b)** Spatial representation of the logarithm of the BIC ratios between linear and piecewise linear regression (annual precipitation $\sim$ altitude) models. The numbers expressed in % correspond to the percentage of catchments within the classes of the BIC ratio. **(c)** Distribution of the surface area of the catchments according to the categories of BIC ratio. 38

2.9 **(a)** Catchments located in the Vercors massif and colored according to their geographic locations. Three groups of catchments are distinguished : the Vercors plateaus, the Western Vercors, and the Southern Vercors. ID numbers are printed for each catchment. **(b)** Scatter plot of AROME annual precipitation and altitude for the pixels in the Vercors (gray dots). The colors of dots correspond to the colors used in panel a). 41

3.1 **(a)** Topography of France. The study domain is located in France, bordered by Spain, Italy, and Switzerland, and is indicated by the dotted red rectangle. The names of the main mountainous regions are displayed in black. Green points refer to rain gauges. **(b)** Histogram of the rain gauges and pixels elevations. . 48

3.2 Mean AROME seasonal precipitation over the 1982–2018 period. Winter (*DJF*), spring (*MAM*), summer (*JJA*), and autumn (*SON*) precipitations are displayed. 49

3.3 Model performances under different station densities. Scores (KGE, R, β, and γ) are computed for each combination of the season (winter (*DJF*), spring (*MAM*), summer (*JJA*), and autumn (*SON*)), models (OK, KED_z, KED_{arome}, GWR, RF, and RF_{ratio}), and proportion of stations in the training dataset (0.10, 0.25, 0.50, 0.75, 0.90). The highest possible scores are equal to 1. 53

3.4 Scatter plot between winter (*DJF*) observed and predicted precipitations at evaluation stations. 10% of the stations were used in the training process. The scatter plots are illustrated for each model (OK, KED_z, KED_{arome}, GWR, RF, RF_{ratio}) and for AROME. The dotted lines indicate the 1 :1 lines. R, Beta, Gamma, and KGE scores are printed. 54

3.5 Scatter plot between seasonal observed and predicted precipitations at rain gauges used to evaluate the extrapolation skills at higher altitudes. The scatter plots are illustrated for each model (OK, KED_z, KED_{arome}, GWR, RF, RF_{ratio}), and AROME, for two seasons (winter (*DJF*), autumn (*SON*)). The dotted lines indicate the 1 :1 lines. R, Beta, Gamma, and KGE scores are printed. . . 55

3.6 **(a)** Annual precipitations extracted across the transect are colored according to the following models : OK, KED_z, KED_{arome}, GWR, RF, RF_{ratio}. AROME annual precipitation is added in black. The elevation is represented in brown as an altitude profile in **(b)**. 56

3.7 **(a)** Precipitation maps obtained from KED_{arome} and RF_{ratio} , using all the rain gauges, for all seasons (winter (*DJF*), spring (*MAM*), summer (*JJA*), and autumn (*SON*)). **(b)** Precipitation maps differences (KED_{arome} - RF_{ratio}) for all seasons (winter (*DJF*), spring (*MAM*), summer (*JJA*), and autumn (*SON*)). 57

3.8 Spatial distribution of the ratios obtained with the model RF_{ratio}. Winter (*DJF*), spring (*MAM*), summer (*JJA*), and autumn (*SON*) ratios are displayed. 61

4.1 Study domain (1.7—5.5°E, 42.8–45.6°N), colored by the elevation (height above sea level in meters), borders of the Cevennes region (black lines), borders and ID of four catchments (red lines, used in sections 3–5), and location of rain gauge stations (dots, around 800 stations available per day). The colors of the stations (dots) are explained in Section 3. Table 1 gathers information about the catchments. 70

4.2 Cross-validation mean error (ME, **(a)**) and mean absolute error (MAE, **(b)**) for rain gauge stations in the Cevennes region, considering days with more than 50 mm. Results are shown for deterministic models (SPAZM) and stochastic models (rgISO, rgANISO, arISO, arANISO). For stochastic models, the cross-validation is conducted on the mean of 100 ensemble members from conditional simulations. Black contours indicate the Cevennes region. 76

4.3 Distribution of TWS scores for deterministic models (SPAZM) and stochastic models (rgISO, rgANISO, arISO, arANISO). Low values of TWS scores indicate better image gradients, using COMEPHORE fields as references. The distributions of TWS scores are plotted for low estimated anisotropy ratio ($0.75 \leq \eta \leq 1$, left), medium estimated anisotropy ratio ($0.5 \leq \eta \leq 0.75$, center), and strong estimated anisotropy ratio ($0 \leq \eta \leq 0.55$, right). The number of events is displayed per event class. For the stochastic models, the evaluation is conducted over the mean of 100 ensemble members of conditional simulations. 76

4.4 Distribution of cross-validation CRPS scores for stochastic models (rgISO, rgANISO, arISO, arANISO). 1 mean value of CRPS is obtained for each station within the Cevennes region for the days with more than 50 mm. Lower CRPS values indicate better spatial interpolation. The distributions of CRPS scores are plotted for low estimated anisotropy ratio ($0.75 \leq \eta \leq 1$, left), medium estimated anisotropy ratio ($0.5 \leq \eta \leq 0.75$, center), and strong estimated anisotropy ratio ($0 \leq \eta \leq 0.5$, right). 77

4.5 Scatter plot between mean catchment COMEPHORE (x-axis) and simulated (y-axis) precipitations in two rain gauge density scenario : using all rain gauge available (*Gauged*, left panels), removing the rain gauge of the main catchment (*Ungauged*, right panels). The 20 days with the highest COMEPHORE precipitation are considered for each catchment represented in the vertical panels. The simulations are derived from conditional simulations with anisotropic covariance (arANISO). The vertical lines in red (grey) illustrate the 25-75 (0-100) % range of simulations. Black points indicate the ensemble means. The dashed line represents the diagonal. 78

4.6 Daily precipitation field illustrations, with a focus on the four catchments for the 2008-05-26 **(a)** and 2014-09-18 **(b)** days. Daily precipitation fields are obtained with deterministic models (COMEPHORE, SPAZM) and stochastic models (rgISO, rgANISO, arISO, arANISO). For the stochastic models, the fields correspond to the mean of 100 ensemble members derived from conditional simulations. Precipitation is expressed in mm. Figure 4.1 shows the locations of the catchments. 79

4.7 Anisotropic (arANISO) illustration of conditional simulations of daily precipitation fields, with a focus on the four catchments for the 2008-05-26 **(a)** and 2014-09-18 **(b)** days. Five members are randomly sampled from a 100 ensemble. Precipitation is expressed in mm. Figure 4.1 shows the locations of the catchments. 80

4.8 Examples of two AROME daily precipitation fields used to derive anisotropic variograms for the 2008-05-26 **(a)** and 2014-09-18 **(c)** days. Precipitation is expressed in mm. Black contours represent the Cevennes region. In the 2D variograms **(b)**, **(d)**, low (high) gamma values indicate strong (weak) spatial autocorrelation between observations, spaced from dx (dy) in horizontal (vertical) km scale. 81

5.1 Study domain with elevation (meters). Grey dots indicate rain gauges, light blue dots mark glacier sites, and red triangles show Cosmic Ray Snow Sensors (NRC). Names of major mountain regions and associated catchments are labeled in bold and black, while catchments used for hydrological modeling are highlighted in red. To assess the hydrological mass balance constraints (see sub-section 5.3.2), 11 (AlpesSud), 46 (Cévennes), 42 (MassifCentral), and 20 (Pyrénées) catchments are colored in grey. 88

5.2 Workflow for generating an ensemble of 100 daily precipitation fields. The process integrates rain gauge undercatch correction, topographical variables, and convection-permitting climate model simulations. These inputs are used in a random forest spatial interpolation to produce climatological fields by weather patterns. Simultaneously, climate model outputs inform 2D daily anisotropic variograms, which are used to generate 100 conditional simulations of daily anomalies. The final ensemble is obtained by multiplying climatological fields with daily anomalies. 91
5.3 Turc–Pike model results showing the runoff coefficient (y-axis) as a function of the humidity index (x-axis). Black points represent individual catchments. Vertical facets correspond to different regions, and horizontal facets to different gridded precipitation products. Within each facet, the dotted line indicates the fitted Turc–Pike curve, with the fitted parameter n and the sum of squared errors (SSE) reported. 95
5.4 (a) Interannual variability of winter snow water equivalent (SWE) accumulation and accumulated precipitation from 1 December to 28 February, for CERRA-Land, ERA5-Land, SPAZM, and ISARD. Black points denote *in-situ* measurements. (b) Same as (a), but for glacier winter mass balance measurements. 97
5.5 Interpolation workflow illustrated for 11 January 1996. **(a)** Climatological background field (shown three times for visualization), **(b)** three randomly selected daily anomaly fields from conditional simulations, and **(c)** daily precipitation estimates from ERA5-Land, CERRA-Land, SPAZM, and three ensemble members of ISARD corresponding to the simulated anomalies. Catchment outlines are indicated ; simulated runoff for the blue and red catchments is presented in Fig. 5.6. 98
5.6 Simulated catchment precipitation and runoff for the 1995 hydrological year (1 September to 31 August), colored by gridded precipitation product, for **(a)** the Issole at Mourefrey catchment and **(b)** the Var at Entrevaux catchment. Black curves indicate observed runoff. 98
5.7 **(a)** Continuous Ranked Probability Skill Score (CRPSS, % relative to SPAZM) for flood modeling across catchments (y-axis) and months (x-axis), stratified by gridded precipitation products (horizontal facets) and hydrological models (vertical facets). Catchments are ordered by increasing surface area. Box colors correspond to CRPSS values, with red (blue) indicating performance degradation (improvement) relative to SPAZM. Boxes marked with a star indicate more than 10 flood events for the given catchment and month, while empty boxes correspond to fewer than 2 events. **(b)** Distribution of quantile relative errors (y-axis) for the two hydrological models (x-axis), filled by gridded precipitation products and stratified by quantiles (horizontal facets). 99

Liste des tableaux

1.1 Comparaison des principales méthodes d'interpolation spatiale des précipitations 12
1.1 Comparaison des principales méthodes d'interpolation spatiale des précipitations 13

2.1 Summary of the characteristics of the gridded precipitation products used in this study, namely available period, domain, horizontal resolution, frequency, type of observations, provider, and reference. 27
2.2 Interpretation of the chosen categories of B_r. M_0 refers to the linear model and M_1 to the piecewise linear model. 29
2.3 Values of precipitation lapse rates (precipitation change per 100 m altitude difference divided by area-averaged precipitation) and R^2 at the sub-regional scale for the 23 French massifs for both winter *DJF* and summer *JJA*. The Massif Number is indicated in Fig. 2.6. 35
2.4 Summary of the studies on precipitation lapse rates (PLRs), namely study domain, data, spatial scale, period, findings, and reference. 40

3.1 Mean, minimum, maximum, and standard deviation in mm of seasonal observed precipitations. 48
3.2 Number of rain gauges in the training dataset for different proportions, sampling strategy and the mean surface area covered by one rain gauge. For 10% of rain gauges in the training dataset, there is 1 station per 476 km^2 on average. 53
3.3 Major weaknesses and strengths of the six statistical models : OK, KED$_z$, KED$_{arome}$, GWR, RF, RF$_{ratio}$. 59

4.1 ID, name, surface area in km^2, mean and maximum altitude in m of the four catchments. Figure 4.1 shows the locations of the catchments. 70
4.2 Metrics computed for evaluation. 74
4.3 Anisotropy parameters estimated with daily AROME precipitation fields, namely the angle (θ) of dominant spatial autocorrelation and the anisotropy ratio (η) with the corresponding orthogonal direction. Deciles summarize the parameter values. 80

1 Introduction

1.1 Mise en contexte

Le 21 août 2005, un épisode de précipitation intense s'abat sur le massif de Belledonne. En 48 heures, 278 mm de pluie tombent au refuge de la Pra, contre seulement 32 mm au Versoud, à quelques kilomètres en contrebas (voir Figure 1.1). Ce contraste illustre la complexité de la pluie en montagne : localisée, intense et difficile à mesurer. Comment représenter un tel événement à l'échelle d'un bassin versant ?

Les précipitations journalières résultent de conditions atmosphériques variées, et peuvent être classées en deux grandes catégories :

— Les précipitations stratiformes, associées à des systèmes de grande échelle (synoptiques, côtiers ou orographiques), qui apportent des cumuls distribués uniformément sur une large zone, avec une faible intensité, et souvent sur une longue période.
— Les précipitations convectives, souvent localisées, liées à des orages isolés ou organisés, et caractérisées par une forte intensité sur de courtes durées.

Des cellules convectives peuvent coexister au sein de cellules stratiformes, générant par endroits des cumuls de précipitations plus importants. Les précipitations orographiques, une forme particulière de précipitations stratiformes, se produisent lorsque des masses d'air, entraînées par le vent, rencontrent un relief. Cette interaction provoque une accumulation plus importante de précipitations en altitude sur les versants exposés au vent, tandis que les versants situés sous le vent reçoivent des quantités moindres, voir Figure 1.2.

Cette diversité de processus engendre une forte variabilité spatiale et altitudinale des précipitations, difficile à appréhender avec les seuls réseaux de mesure conventionnels (Suri and Azad, 2024). En effet, les densités des réseaux pluviométriques varient spatialement et peuvent être insuffisantes pour capter la variabilité spatiale des précipitations. En cas d'orages très localisés, les cellules convectives de précipitations peuvent facilement tomber entre les mailles du réseau pluviométrique. De plus, le réseau pluviométrique est historiquement plus dense en plaine qu'en montagne, car plus difficile à maintenir dans ces endroits où la neige est courante. Les précipitations orographiques peuvent donc être également manquées ou mal représentées si les pluviomètres ne sont installés que dans les vallées ou en relative faible altitude.

Pour pallier ce manque de représentativité spatiale des pluviomètres, les radars météorologiques qui offrent une mesure indirecte mais spatiale des précipitations sont largement utilisés. Les données radars ne seront toutefois pas exploitées dans cette thèse, qui vise à produire des estimations de précipitations journalières remontant jusqu'à 1960. En effet, le déploiement

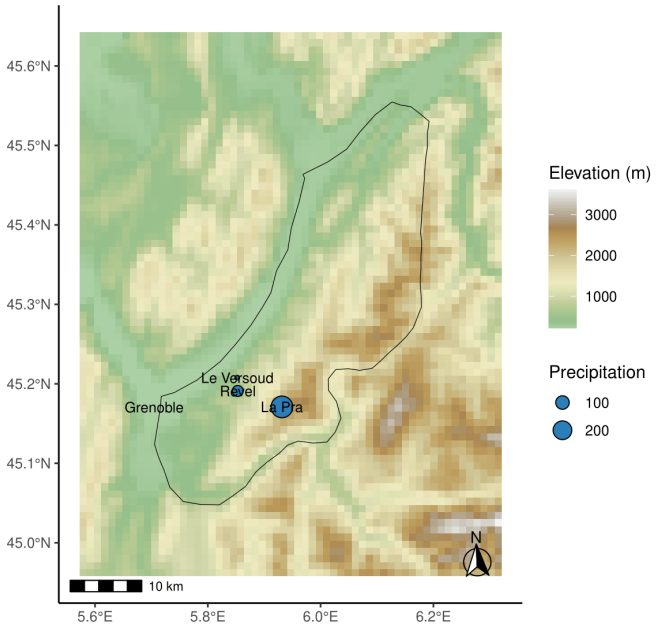

Figure 1.1 – Précipitations du 21 et 22 août 2005 dans le massif de Belledonne. Le fond de carte représente le relief. La taille des points est proportionnelle au cumul de précipitations.

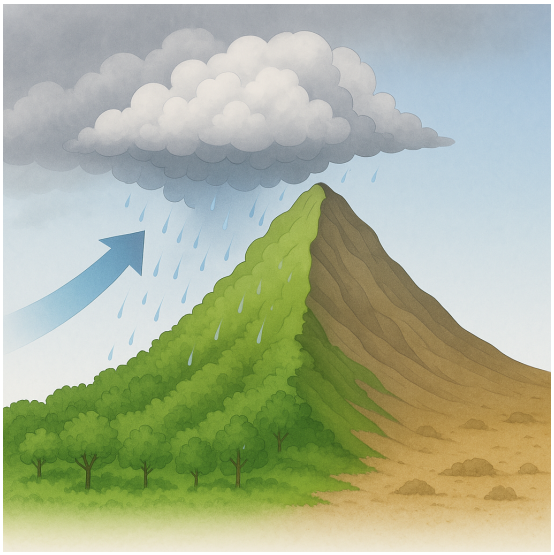

Figure 1.2 – Les précipitations orographiques.
OpenAI (2025), ChatGPT 4, Récupéré 10 juillet 2025 de https ://chat.openai.com/

massif des radars météorologiques en France n'a débuté qu'à partir de 1997. Le nombre de radars installés a graduellement augmenté au cours des années, ce qui rend hétérogènes temporellement les produits radars. De plus, leur fiabilité reste limitée en zones montagneuses en raison de problèmes de mesure. Par conséquent, seules les données de pluviomètres, qui font office de référence de mesure de cumul de précipitations, seront exploitées.

Cependant, de nombreuses applications nécessitent l'obtention de précipitations journalières sur de larges domaines avec une grande profondeur temporelle, souvent sous forme de produits grillés à fine résolution spatiale. En météorologie, ces produits grillés de précipitations servent de référence pour l'évaluation rétrospective d'événements intenses. En climatologie, ces données sont essentielles pour suivre l'évolution du changement climatique, mais aussi pour évaluer des modèles de climat. En hydrologie, ils fournissent des précipitations moyennées sur un bassin versant sur une longue période pour alimenter des modèles pluie-débit dont l'usage est multiple :

— **Gestion et aménagement du territoire :** aide à la planification des usages de l'eau (agricoles, énergétiques, touristiques), calcul d'indicateurs de sécheresse hydrologique ou agricole, suivi des réserves en eau de surface et souterraine.
— **Gestion des risques :** alimentation des modèles de prévision de crues (en temps réel ou mode réanalyse), études de fréquence des extrêmes hydrologiques (pluies intenses, sécheresses, crues) pour le dimensionnement d'ouvrages hydroélectriques, cartographie d'événements extrêmes.

Pour obtenir des produits grillés de précipitations journalières sur une longue période temporelle, deux familles de méthodes sont principalement utilisées :

1. Les **réanalyses météorologiques**, qui combinent des observations et des données de simulation de modèle météorologique, encore appelées ébauches pour rejouer le passé et obtenir des données homogènes temporellement. Le modèle météorologique le plus récent donne une première estimation du champ journalier, qui est ensuite corrigé par les observations du jour à l'aide de méthodes d'assimilation de données.
2. Les **interpolateurs** qui spatialisent des observations à l'aide de modèles statistiques. Le modèle statistique permet de passer d'observations ponctuelles irrégulièrement distribuées spatialement à une estimation de précipitation dans des zones non instrumentées sous forme de produit grillé (voir Figure 1.3).

Dans le cadre de cette thèse appliquée à l'hydrologie de montagne, nous privilégierions l'utilisation d'interpolateurs statistiques. Les réanalyses sont en effet basées sur des modèles météorologiques qui peuvent induire des biais en montagne en raison d'une sous-estimation ou sur-estimation des phénomènes orographiques, avoir une résolution spatiale trop grossière et mal représenter les événements convectifs intenses. En hydrologie, le processus d'interpolation spatiale soulève deux défis majeurs :

1. L'estimation des cumuls de précipitations en montagne, souvent sous-estimés en raison de biais liés à la mesure et à la modélisation. La sous-estimation des précipitations en montagne résulte à la fois des limitations instrumentales et des approximations des modèles statistiques. En conditions venteuses, les pluviomètres sous-captent significativement la neige en raison de la formation de tourbillons d'air autour de l'instrument, perturbant la collecte (Pollock et al., 2018; Kochendorfer et al., 2020). Ce biais augmente avec l'altitude, où les précipitations neigeuses sont plus fréquentes et les vitesses de vent plus élevées. Par ailleurs, les modèles d'interpolation peuvent mal représenter les gradients altitudinaux des précipitations, c'est-à-dire le taux d'augmentation des

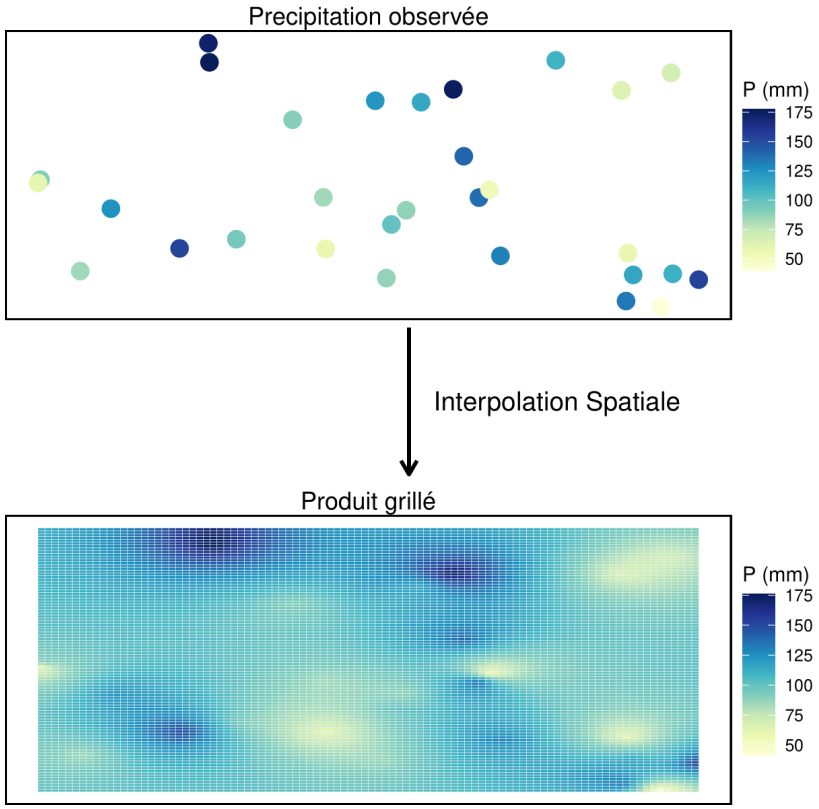

Figure 1.3 – Illustration du processus d'interpolation spatiale : passage de précipitations journalières observées aux pluviomètres à un produit grillé. Le modèle statistique utilisé pour cette illustration est le Krigeage Ordinaire, voir sous-section 1.2.2.2 pour son explication.

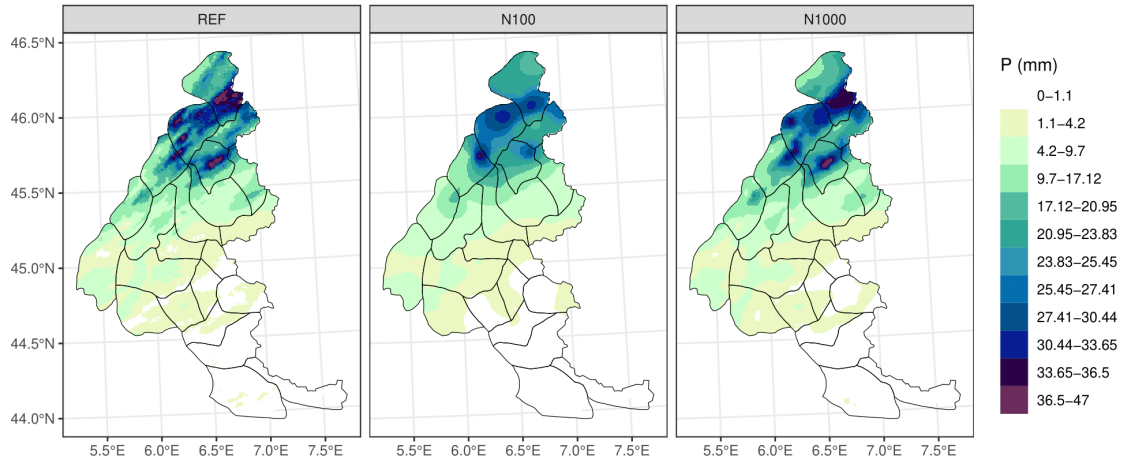

Figure 1.4 – Illustration du lissage des cellules de précipitations : REF correspond à un champ radar, N100 et N1000 sont des champs reconstruits par Krigeage Ordinaire avec 100 et 1000 pluviomètres virtuels (extrait du champ radar).

précipitations avec l'altitude, en les sous-estimant ou en les exagérant, ce qui affecte la précision des cumuls estimés en zone de montagne.

2. La représentation des précipitations intenses, dont la variabilité spatiale est souvent atténuée par les méthodes d'interpolation, conduit à des champs trop lissés (Olea and Pawlowsky, 1996; Beguería et al., 2016). Cette limitation est en grande partie liée au cadre théorique des modèles utilisés, souvent fondés sur le paradigme du *Best Linear Unbiased Estimator* (BLUE). Ce cadre, bien qu'optimal en termes de biais et de variance globale, tend à lisser les événements intenses et à réduire artificiellement la variabilité spatiale (Gervais et al., 2014). Il en résulte une sous-estimation de l'intensité maximale des cellules de précipitations et une sur-estimation de l'occurrence des précipitations. Ce phénomène est amplifié dans les régions peu instrumentées. En conséquence, les événements localisés à forte intensité, tels que les orages convectifs, sont mal représentés dans les produits interpolés, ce qui peut compromettre leur utilisation en hydrologie pour la modélisation des crues (Vischel et al., 2009). Figure 1.4 illustre ce phénomène : le lissage est évident avec l'utilisation de 100 pluviomètres virtuels (*N100*), est atténué mais persiste avec un réseau virtuellement dense (*N1000*).

1.2 Etat de l'art

Les produits grillés de précipitations existants diffèrent selon les données digérées et les modèles statistiques d'interpolation spatiale employés. Chaque source de données présente des avantages et des limites, et le choix du modèle d'interpolation optimal dépend de la zone d'étude et de l'objectif d'utilisation.

1.2.1 Les sources de données disponibles

1.2.1.1 Les mesures de précipitations

1. Les **pluviomètres** représentent la méthode d'observation des précipitations la plus directe. Ils fournissent des mesures ponctuelles généralement fiables, disponibles pour



Figure 1.5 – Un pluviomètre *PG2000* utilisé à EDF-DTG.

certaines stations depuis les années 1950. Selon le type d'appareil, la résolution temporelle des données varie d'environ 6 minutes à un pas journalier. Les longues séries de mesures peuvent présenter des inhomogénéités temporelles, dues notamment à des changements de localisation ou de matériel. En France, les pluviomètres à augets basculants chauffants sont les plus courants. Figure 1.5 illustre un pluviomètre *PG2000* d'EDF-DTG, disposant d'une surface de captage de 2000 cm^2.Ils se composent d'un entonnoir qui recueille l'eau de pluie et la dirige vers un dispositif à deux augets. Chaque auget recueille un volume d'eau défini ; lorsqu'il est plein, il bascule, se vide, et l'autre auget prend le relais. Chaque basculement est enregistré électroniquement, permettant ainsi de déterminer la quantité totale de précipitations. Ce système est largement utilisé pour sa précision, sa fiabilité et son fonctionnement automatique. Les pluviomètres demeurent ainsi une référence pour de nombreux domaines, allant de l'hydrologie à la glaciologie. Toutefois, la représentativité spatiale des pluviomètres est limitée, en particulier dans les zones de relief marqué. La densité souvent insuffisante des réseaux pluviométriques empêche de capter la forte variabilité spatiale et altitudinale des précipitations. De plus, leur capacité à détecter des événements localisés, comme les orages d'été, est réduite, ce qui peut conduire à une sous-estimation des cumuls moyens à l'échelle du bassin versant.

2. Les **radars météorologiques** estiment les précipitations en mesurant la réflectivité des hydrométéores dans l'atmosphère. Le principe repose sur l'émission d'ondes électromagnétiques, qui sont renvoyées vers l'antenne radar lorsqu'elles rencontrent des précipitations. L'intensité du signal réfléchi, exprimée en décibels de réflectivité (dBZ), est ensuite convertie en intensité de précipitation (mm/h) à l'aide de relations empiriques (relation Z-R). Contrairement aux pluviomètres, qui ne mesurent qu'en un point donné, les radars produisent des champs grillés de précipitations, permettant de représenter la structure spatiale des événements pluvieux, leur évolution dans le temps, ainsi que leur intensité sur de vastes territoires. Cependant, l'utilisation des radars en milieu montagneux présente plusieurs limitations. Le blocage du faisceau radar par le relief entraîne

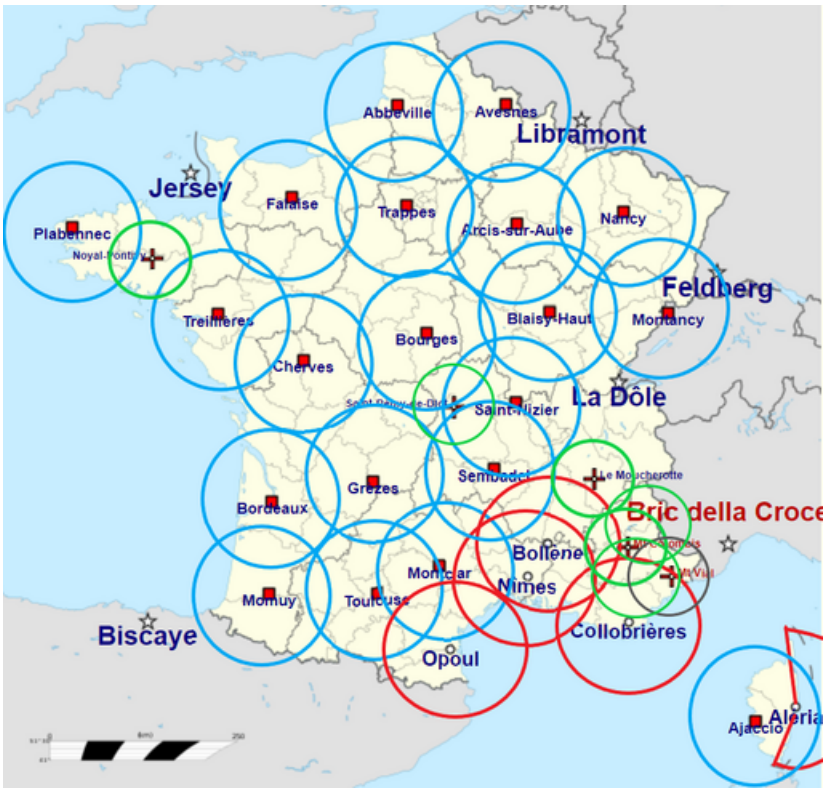

Figure 1.6 – réseau radar ARAMIS (Météo-France, 2019). La couverture des radars est représentée par des cercles. La couleur des cercles correspond aux différents types de radars : bande C (bleu), bande S (rouge) et bande X (vert).
Source : https://commons.wikimedia.org/wiki/File:ARAMIS_2019.png?uselang=fr, licence CC BY-SA 4.0.

une sous-estimation des précipitations. De plus, le phénomène de la bande brillante, qui se manifeste dans la zone de fusion des flocons de neige en pluie, provoque une surestimation locale de la réflectivité, biaisant ainsi l'estimation de l'intensité des précipitations. Ces effets réduisent la fiabilité des mesures radar dans les zones de haute altitude ou à topographie complexe. En France, le réseau ARAMIS (Application Radar à la Météorologie Infra-Synoptique), exploité par Météo-France, regroupe une trentaine de radars répartis sur l'ensemble du territoire. Leur emplacement est indiqué sur la Figure 1.6. Une mosaïque radar est calculée grâce à la fusion des données des radars individuels.

3. Les **satellites météorologiques** permettent d'estimer les précipitations à partir de mesures radiométriques effectuées depuis l'espace. Ces mesures sont obtenues soit par des capteurs passifs, qui enregistrent le rayonnement naturel émis ou réfléchi par les nuages et la surface terrestre (notamment en infrarouge ou en micro-ondes), soit par des capteurs actifs, comme les radars embarqués, qui émettent un signal et analysent son retour après interaction avec les hydrométéores. Ces observations ne mesurent pas directement la pluie, mais permettent d'en inférer l'intensité et la distribution à l'aide de modèles physiques et statistiques. Les satellites couvrent l'ensemble du globe à une fine résolution temporelle, y compris les régions peu ou pas instrumentées, comme les océans ou les zones montagneuses. Toutefois, la résolution spatiale reste limitée, ce qui empêche la fine représentation de la variabilité des précipitations, en particulier en terrain complexe. De plus, les estimations sont indirectes et peuvent être entachées d'erreurs, notamment en présence de nuages sans précipitation ou de précipitations faibles sous les nuages. Parmi les produits les plus utilisés mondialement, PDIR-NOW est un produit récent

basé sur l'infrarouge et l'intelligence artificielle, offrant une haute fréquence d'observation (15 minutes). IMERG, développé dans le cadre du programme GPM de la NASA, combine des données issues de capteurs micro-ondes, radar et infrarouge. Il offre une bonne précision, notamment dans sa version finale. CMORPH, produit par la NOAA, repose sur le suivi des systèmes convectifs à partir d'images micro-ondes et infrarouge. Il est particulièrement adapté aux régions tropicales.

4. Les **modèles climatiques régionaux (RCM)** (Tobin et al., 2011; Ban et al., 2021; Caillaud et al., 2021) sont des outils numériques qui permettent de simuler le climat à l'échelle régionale avec une résolution plus fine que celle des modèles globaux (GCM). Lorsqu'ils sont forcés par des réanalyses atmosphériques à grande échelle, les RCM peuvent reconstituer le climat passé en reproduisant les structures spatiales des variables météorologiques, notamment les précipitations. Leur résolution typique, de l'ordre de 10 à 25 km, permet une meilleure prise en compte des effets du relief et des contrastes côtiers. Toutefois, à ces échelles, les processus convectifs doivent être paramétrés, ce qui introduit des biais dans la localisation, l'intensité et la fréquence des précipitations, en particulier pour les événements intenses. À l'échelle journalière ou horaire, ces simulations restent entachées de biais spatio-temporels (Caillaud et al., 2021), mais une agrégation à des pas de temps climatologiques (mensuel, saisonnier) permet souvent d'obtenir une représentation réaliste de l'effet de la topographie sur les précipitations. Pour surmonter les limites liées à la paramétrisation de la convection, des modèles à convection explicite (CP-RCM) ont été développés. Ces modèles, dont la résolution est généralement inférieure à 4 km, permettent de simuler directement les processus convectifs, sans recours à des schémas paramétrés. Cela améliore significativement la représentation des précipitations intenses, des orages et des phénomènes locaux liés au relief. Les CP-RCM offrent ainsi une avancée majeure pour les études d'impact hydrologique, la gestion des risques liés aux précipitations extrêmes et la compréhension fine des processus atmosphériques. Lundquist et al. (2019) affirme que dans les régions de montagne, les simulations de modèle météorologique donnent souvent des estimations plus fiables que certaines réanalyses disponibles. Néanmoins, leur coût computationnel est élevé, ce qui limite leur usage à des périodes courtes ou à des domaines géographiques restreints. Dans le cadre de l'initiative EURO-CORDEX, plusieurs modèles régionaux sont utilisés pour produire des simulations climatiques sur l'Europe. Parmi les plus courants figurent ALADIN, développé par Météo-France, adapté aux simulations à résolution intermédiaire ; AROME, également développé par Météo-France, utilisé pour les simulations à convection explicite ; COSMO, modèle conçu par un consortium européen, largement utilisé en Allemagne, Suisse et Italie ; et WRF (Weather Research and Forecasting model), modèle très répandu dans la communauté scientifique internationale. Ces modèles sont utilisés pour produire des ensembles de simulations RCM à 12 km de résolution, ainsi que des expériences CP-RCM à 2.2 km. Ces produits constituent aujourd'hui une base essentielle pour l'analyse du climat passé, la validation de modèles hydrologiques et l'amélioration des projections climatiques à haute résolution.

1.2.1.2 Des mesures alternatives

D'autres données peuvent permettre d'inférer des cumuls de précipitations, soit ponctuels, soit spatiaux.

1. Les mesures de **neige**, en particulier celles issues des Nivomètres à Rayonnement Cosmique (NRC) (Gottardi, 2009) déployés par EDF sur les principaux massifs français (Alpes, Pyrénées, Massif Central), offrent une estimation indirecte des précipitations accumulées. Ces capteurs mesurent l'équivalent en eau du manteau neigeux à une fré-

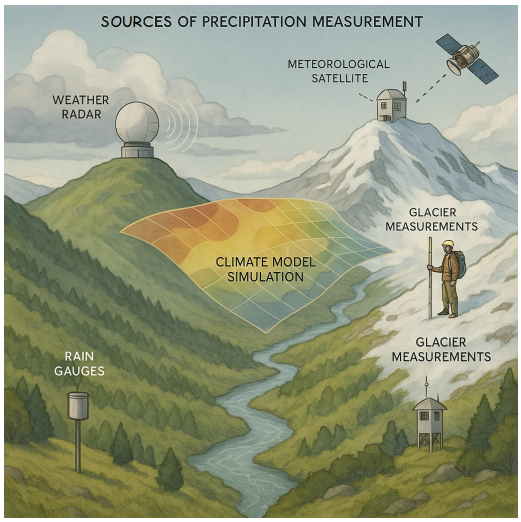

Figure 1.7 – Les différentes sources de mesure des précipitations. OpenAI. (2025). ChatGPT 4. Récupéré 10 juillet 2025 de https ://chat.openai.com/

quence journalière. Bien que précises, ces mesures restent ponctuelles et leur représentativité spatiale est donc limitée.

2. Les **bilans de masse glaciaires** réalisés par les glaciologues fournissent des estimations saisonnières des précipitations à haute altitude. En supposant une fonte négligeable en hiver, l'accumulation de neige mesurée en fin de saison peut être assimilée à la précipitation totale. Ces données, bien que rares, sont précieuses pour évaluer les estimations dans les zones les plus élevées.
3. Les données de **débits** peuvent être exploitées, de manière indirecte, dans des bilans hydriques ou des modèles hydrologiques afin d'estimer, via des approches de modélisation inverse, les précipitations spatiales moyennées sur un bassin. En convertissant le débit annuel moyen en écoulement et en l'associant à une estimation empirique de l'évapotranspiration (Oudin et al., 2006), il est ainsi possible d'évaluer la précipitation annuelle moyenne d'un bassin versant à partir du bilan hydrique (Turc, 1955; Pike, 1964). Cette approche demeure toutefois soumise à plusieurs sources d'incertitude : les mesures de débit présentent une erreur d'environ 12,5 % pour les forts débits (Salamon and Feyen, 2010), bien que cette erreur soit souvent supposée être de moyenne nulle. De plus, les estimations d'évapotranspiration restent par nature imparfaites. Enfin, avec l'appui de modèles hydrologiques, l'estimation des précipitations de bassin peut être affinée à des échelles temporelles plus fines (horaire ou journalière) (Grundmann et al., 2019), mais elle reste contrainte par les limites inhérentes aux données de débit et aux modèles hydrologiques disponibles.

1.2.2 Les modèles d'interpolation spatiale

Dans cette thèse, nous nous focaliserons sur des modèles d'interpolation spatiale plutôt que sur l'assimilation de données, utilisée dans la construction de réanalyse. L'interpolation spatiale des précipitations consiste à estimer les valeurs en des lieux non instrumentés à partir d'observations ponctuelles. Selon la complexité des méthodes, différentes hypothèses sont supposées sur la structure spatiale du phénomène, l'influence des variables explicatives et la capacité des méthodes à modéliser l'incertitude d'interpolation. Nous présentons ici les principales approches statistiques, organisées du plus simple au plus élaboré, en distinguant cinq grandes familles : méthodes empiriques, géostatistiques, régressions spatiales, Machine Lear-

ning et approche probabiliste. Notre découpage est intentionnellement inexact car certaines approches probabilistes se retrouvent dans d'autres catégories. Néanmoins, nous avons choisi d'isoler ces méthodes qui permettent une quantification explicite de l'incertitude.

1.2.2.1 Les méthodes empiriques

Les méthodes **empiriques** reposent uniquement sur la distance géographique entre les pluviomètres et le point cible à prédire. Elles ne tiennent pas compte de la structure de la variabilité spatiale ni d'éventuelles covariables.

La méthode *Nearest Neighbor (NN)* (Thiessen, 1911) attribue la valeur du pluviomètre le plus proche. Cette méthode a pour intérêt son extrême simplicité, mais introduit des discontinuités spatiales irréalistes.

L'Inverse Distance Weighting (IDW) (Willmott et al., 1985) pondère les observations aux pluviomètres selon leur distance au point cible. Cela permet d'améliorer la continuité spatiale, mais sans réellement prendre en compte la dépendance réelle entre les mesures. Cette pondération est erronée lorsque les deux pluviomètres les plus proches du point cible sont séparés par une chaîne de montagnes, par exemple.

Ces méthodes sont adaptées à des réseaux denses et à des terrains relativement homogènes spatialement, mais elles montrent leurs limites dès que la topographie se complexifie ou que la densité de pluviomètres diminue.

1.2.2.2 Les modèles géostatistiques

Pour dépasser les limites des méthodes empiriques, les approches **géostatistiques** (Cressie, 1993; Goovaerts, 2000) introduisent une modélisation explicite de la corrélation spatiale des observations, à travers un modèle de covariance (ou variogramme). Généralement, les approches géostatistiques supposent un modèle de covariance stationnaire au second ordre et isotrope par manque de données ou par souci de simplicité de modélisation. Ce type de covariance suppose que la corrélation spatiale des observations ne dépend que de la distance entre elles, et non de leurs localisations, et n'est pas fonction de la direction. Certains auteurs utilisent une covariance anisotropique (Velasco-Forero et al., 2009; Schiemann et al., 2011; Gyasi-Agyei, 2016), et d'autres implémentent une covariance non-stationnaire (Paciorek and Schervish, 2006; Ingebrigtsen et al., 2014; Risser and Calder, 2017).

Le *Krigage ordinaire (OK)* estime une valeur comme une combinaison linéaire optimale des observations voisines, en minimisant la variance d'erreur sous contrainte d'un biais nul. Cette méthode est adaptée lorsque l'autocorrélation spatiale des observations explique une part significative de la variance. Cependant, des variables explicatives comme l'altitude, la pente, ou encore la distance à la mer peuvent expliquer une part importante de la variabilité spatiale des précipitations. Ne pas prendre en compte ces variables peut entraîner de larges biais spatiaux comme des sous-estimations en montagne et des sur-estimations dans les vallées.

Le *Krigeage à Dérive Externe (KED)* intègre des covariables pour expliquer une partie de la variabilité spatiale. Cette méthode est donc adaptée à des terrains complexes, mais est seulement capable de prendre en compte des effets linéaires. Ainsi, les méthodes de krigeage conviennent bien à des phénomènes autocorrélés spatialement, mais présentent des limites dès lors que la topographie explique une part importante de la variabilité spatiale de façon non linéaire.

1.2.2.3 Les méthodes de régressions spatiales

Lorsque les précipitations sont influencées de manière significative par des caractéristiques topographiques, les modèles de **régressions spatiales** (Daly et al., 1994; Gottardi, 2009;

Thornton et al., 2021) permettent de mieux intégrer cette variabilité. Contrairement aux modèles géostatistiques, ils s'appuient sur des relations explicites entre la variable cible et des covariables. Le modèle *Geographically Weighted Regression (GWR)* estime des relations linéaires localement dans un voisinage défini spatialement. Les coefficients de la régression varient donc spatialement. La taille du voisinage peut dépendre du nombre d'observations voisines considérées, de la distance (euclidienne ou non) maximale entre le point cible et les observations. Le choix du voisinage reflète un compromis biais-variance. Un voisinage très resserré autour du point cible induit un faible biais mais une forte variance, ce qui implique un manque de robustesse d'estimation. À l'inverse, un large voisinage donne des modèles sous-ajustés, avec un fort biais, mais une faible variance.

Les *Generalized Additive Models* (GAM) (Haylock et al., 2008) modélisent des relations non-linéaires via une combinaison de splines. Cette méthode s'avère très flexible, mais tout comme les modèles de régression linéaire, le choix du nombre de degrés de liberté des splines constitue un compromis biais-variance. En pratique, la taille du voisinage ou le nombre de degrés de liberté des splines est souvent déterminé par validation croisée. La densité des réseaux pluviométriques peut différer significativement, spatialement. Dans ce cas, les modèles GAM expliquent moins finement la variabilité spatiale dans les régions les moins instrumentées.

Ces approches permettent d'intégrer les effets topographiques, en particulier dans des régions montagneuses ou côtières. Néanmoins, elles restent limitées dès lors que les interactions entre covariables et précipitation deviennent trop difficiles à modéliser explicitement.

1.2.2.4 Les méthodes de Machine Learning

L'émergence des approches de **Machine Learning** offre une alternative puissante aux méthodes paramétriques classiques. Ces modèles apprennent directement les relations complexes entre les données d'entrée et la variable cible, sans hypothèse forte sur la forme de ces relations.

Les *Réseaux de neurones* artificiels (ANN) et convolutifs (CNN) permettent d'apprendre des relations complexes entre précipitations et un vaste ensemble de co-variables. Ces méthodes sont très énergivores en données mais sont particulièrement intéressantes pour l'interpolation de variables fortement influencées par des interactions non-linéaires avec des covariables, comme les précipitations. Cependant, ces méthodes n'améliorent pas la prédiction des précipitations intenses par rapport à des modèles plus traditionnels (Fan et al., 2021).

Parmi les modèles de Machine Learning , les modèles *Random Forest (RF)* sont souvent les plus performants (Zandi et al., 2022; Bonsoms and Ninyerola, 2024). Les RFs utilisent une combinaison d'arbres de décision pour modéliser des relations complexes. Cette méthode est robuste, mais sans modélisation de l'autocorrélation spatiale explicite. Des auteurs ont étendu cette méthode pour prendre en compte le caractère spatial des données, en intégrant des covariables illustrant l'autocorrélation spatiale (Hengl et al., 2018; Sekulić et al., 2020).

Les méthodes de Machine Learning posent aussi la question du choix de la fonction de perte, notamment lorsque l'on souhaite modéliser correctement les précipitations intenses (Rudy and Sapsis, 2023). Pendant la phase d'entraînement du modèle, on cherche à minimiser la fonction de perte, qui quantifie les écarts entre les prédictions du modèle et les observations utilisées pendant la phase d'entraînement. La fonction de perte peut pénaliser les erreurs sur les fortes valeurs (erreurs au carré) ou au contraire les erreurs sur les faibles valeurs (racine carrée des erreurs). De plus, Bonsoms and Ninyerola (2024) illustre la sous-estimation des gradients altitudinaux de précipitations et de températures, dont la représentation est critique dans cette thèse.

1.2.2.5 Les modèles probabilistes

Enfin, certaines méthodes avancées visent à fournir non seulement une estimation ponctuelle, mais également une distribution de probabilité sur les valeurs interpolées. La dimension **ensembliste** s'est largement démocratisée dans le cas de la prévision probabiliste (Scheuerer, 2014; Schlosser et al., 2019; Xu et al., 2022), mais reste peu utilisée pour l'interpolation spatiale opérationnelle (Cornes et al., 2018; Frei and Isotta, 2019). Elles sont particulièrement utiles pour quantifier l'incertitude, notamment dans des contextes de modélisation des précipitations intenses.

Les *simulations gaussiennes conditionnelles* permettent de générer des champs normaux équiprobables conditionnés aux observations, illustrant l'incertitude d'interpolation. Il est également possible de combiner l'incertitude d'interpolation avec d'autres incertitudes (paramètres de covariance, effet des covariables) avec une *inférence bayésienne* (Frei and Isotta, 2019). Cette méthode permet une meilleure quantification de l'incertitude, et donc une meilleure représentation des événements intenses, mais peut être techniquement exigeante et coûteuse en temps de calcul. Pour pallier ces problèmes techniques, Rue et al. (2009); Lindgren et al. (2011) ont mis à disposition la méthode INLA, qui, par des approximations de Laplace, permet une interpolation spatiale bayésienne plus efficace en temps de calcul.

Table 1.1 – Comparaison des principales méthodes d'interpolation spatiale des précipitations

Méthode	**Type de modèle**	**Avantages**	**Limites**
Nearest Neighbor (NN)	Empirique	Très simple, rapide	Discontinuités spatiales, pas de prise en compte de la topographie
Inverse Distance Weighting (IDW)	Empirique	Lissage spatial, facile à implémenter	Ne modélise pas la dépendance réelle, sensible à la densité du réseau
Ordinary kriging (OK)	Géostatistique	Meilleure estimation linéaire non-biaisée, modélise l'autocorrélation spatiale	Hypothèse de stationnarité, pas de covariables explicites
Kriging with External Drift (KED)	Géostatistique	Intègre des effets topographiques simples et l'autocorrélation spatiale	Limité aux relations linéaires, relations avec les covariables appliquées globalement
Geographically Weighted Regression (GWR)	Régression	Coefficients de régression variables spatialement, adapté aux terrains complexes	Sensible au choix du voisinage, compromis entre biais et variance
Generalized Additive Models (GAM)	Régression	Modélisation de relations non linéaires de covariables	Sensible au nombre de degrés de liberté des splines, compromis entre biais et variance

Suite page suivante...

Méthode	Type de modèle	Avantages	Limites
Neural networks (ANN, CNN)	*Machine Learning*	Très puissants pour données complexes	Nécessitent beaucoup de données, sous-estimation des précipitations intenses
Random Forest (RF)	*Machine Learning*	Modélisation non linéaire, peu sensible aux hyperparamètres	Pas bon en dehors du domaine d'apprentissage donc sous-estimation en montagne pour les précipitations intenses
Simulation gaussienne conditionnelle	Probabiliste	Fournit des champs équiprobables, quantifie l'incertitude	Coûteux en calcul, nécessite un bon modèle de covariance
Inférence bayésienne	Probabiliste	Estimation complète de l'incertitude, efficace avec INLA	Complexité technique, choix des distributions *a priori*

Table 1.1 – Comparaison des principales méthodes d'interpolation spatiale des précipitations

Le choix d'une méthode d'interpolation dépend de nombreux facteurs : densité du réseau de mesures, complexité du relief, nature des précipitations (stratiformes ou convectives), qualité des données auxiliaires, ou encore nécessité d'estimer l'incertitude. Les méthodes les plus simples (NN, IDW) peuvent suffire dans des régions fortement instrumentées relativement à la complexité des processus atmosphériques, tandis que des approches plus avancées (GAM, RF, bayésiennes) s'imposent dès que l'on souhaite modéliser des relations complexes ou quantifier la variabilité spatiale de manière robuste.

1.2.3 Covariables pour l'amélioration de l'interpolation spatiale

1.2.3.1 Les champs climatologiques

Dans des régions à la topographie complexe, les variables topographiques sont souvent utilisées pour modéliser une partie de la variabilité spatiale des précipitations journalières. Cependant, l'estimation des liens entre précipitations et variables topographiques peut être compliquée à l'échelle journalière, et donc conduire à des modèles de régression qui n'expliquent qu'une faible partie de la variance des observations. Pour pallier ce problème, la notion de champs climatologiques de référence est largement utilisée dans la littérature (Haylock et al., 2008; Masson and Frei, 2014). L'idée est de modéliser le lien entre précipitations et variables topographiques à une échelle de temps plus agrégée. Il est par exemple plus facile de modéliser le lien entre précipitations et altitude sur de longues périodes climatologiques de plus de 30 ans. Ces champs climatologiques de référence peuvent alors être utilisés soit directement comme variables explicatives, soit comme une première estimation d'un champ de précipitations, que l'on cherchera à ajuster avec les observations du jour. Plus la densité de pluviomètre est faible comme en montagne, plus ces champs climatologiques auront un poids important dans le processus d'interpolation journalière. Les champs climatologiques de référence sont couramment utilisés dans les produits de précipitations journalières spatialisés à des fins opérationnelles. La majorité des approches existantes, telles que celles développées dans les produits SPAtialisation en Zone de Montagne (SPAZM)(Gottardi, 2009), Alpine Precipitation Grid Dataset (APGD) (Isotta et al., 2014), SeNorge2 (Lussana et al., 2018) reposent sur

des modèles de régression spatiale inspirés de PRISM (Daly et al., 1994). Le modèle PRISM est fondé sur l'estimation de coefficients locaux de régression entre les précipitations climatologiques et l'altitude, en tenant compte de facteurs topographiques tels que l'orientation des versants. Toutefois, ces modèles peuvent présenter un manque de robustesse dans l'estimation des coefficients de régression, comme discuté précédemment. D'autres auteurs (Crespi et al., 2018; Hiebl and Frei, 2018; Jiang et al., 2023) ont exploré des alternatives statistiques pour la construction de ces climatologies. Jiang et al. (2023) se distingue notamment en intégrant des sources de données additionnelles aux seuls pluviomètres pour l'interpolation spatiale.

1.2.3.2 Les données radars

Pour pallier le manque de pluviomètres, la fusion de données pluviométriques et radars est fréquente. L'idée est de valoriser les forces de ces deux mesures : la précision des pluviomètres et la variabilité spatiale du champ de précipitation radars. Le radar est ainsi souvent employé en variable explicative dans des modèles de krigeage (Velasco-Forero et al., 2009; Schiemann et al., 2011), ou utilisé dans des modèles de copule (Vogl et al., 2012; Wasko et al., 2013). Cependant, la mesure radar peut être de mauvaise qualité en montagne (blocage du faisceau radar, phénomène de la bande brillante), avec de fréquentes et fortes sous-estimations de cumul en montagne, limitant son utilisation dans des zones à la topographie complexe. Certains auteurs (Vernay et al., 2025) essaient de corriger les mesures radars pour fournir des cumuls appropriés en zone de montagne.

1.3 Positionnement de la thèse

Au vu de sa future utilisation hydrologique, le produit de précipitation créé devra disposer d'une résolution spatio-temporelle assez fine pour représenter la forte variabilité des précipitations, d'une profondeur historique suffisante et être disponible sur les principaux massifs montagneux français. Certains produits disposent déjà de ces caractéristiques. Toutefois, selon les modèles et les données utilisés pour l'interpolation, les produits grillés de précipitations existants répondent généralement à l'un des deux besoins fondamentaux de l'hydrologie de montagne, mais rarement aux deux simultanément :

i) Fournir des cumuls saisonniers fiables en altitude, essentiels pour estimer la quantité de neige et donc la ressource en eau disponible au printemps et en été,
ii) Représenter la variabilité spatiale des événements intenses, qui conditionne les débits de crue sur les petits bassins versants.

En France, plusieurs produits opérationnels existent. Ils répondent chacun à des besoins spécifiques, mais ils présentent tous des limites spécifiques pour l'hydrologie de montagne :

— COmbinaison en vue de la Meilleure Estimation de la PréCIPitation HOraiRE (COMEPHORE) (Champeaux et al., 2009) est un interpolateur de précipitations de référence développé par Météo-France. Ce produit repose sur une combinaison de données radar et pluviométriques, interpolées via un krigeage avec dérive externe, et fournit des champs de précipitation à haute résolution spatiale (1 km^2) et temporelle (1 h) depuis 1997 sur la France métropolitaine. Son intérêt réside notamment dans sa capacité à représenter avec finesse la variabilité spatio-temporelle des précipitations, en particulier lors d'événements intenses. Les performances de COMEPHORE ont connu une amélioration significative au fil du temps, notamment grâce à l'introduction du module ANTILOPE (Champeaux et al., 2009) après 2006, qui a permis une meilleure intégration des données radar, en particulier pour les pluies convectives. ANTILOPE est aussi le nom de la méthode et de l'analyse réalisée en temps réel, disponible à un pas de temps de 15

min depuis 2017, qui fusionne observations pluviométriques et la mosaïque radar nommée *Système d'élaboration des produits radar et de visualisation centralisé* (SERVAL, précédemment PANTHERE, Champeaux et al., 2009). COMEPHORE se distingue par sa réactivité face aux événements de forte intensité, en estimant des valeurs intenses plus élevées que les méthodes classiques de krigeage, notamment dans les régions méditerranéennes et montagneuses. Cependant, malgré ces atouts, COMEPHORE présente certaines limites structurelles. L'une des principales faiblesses concerne l'absence de prise en compte explicite de l'altitude dans le processus d'interpolation. Cette lacune se traduit par une sous-estimation systématique des précipitations en altitude (Evin et al., 2024) notamment dans les Alpes et les Pyrénées et une surestimation en fond de vallée. D'autres limites sont liées à l'utilisation des données radar, notamment l'atténuation du signal par les précipitations, le masquage par le relief (*beam blockage*), ou encore la représentativité limitée d'une mesure en altitude pour une estimation au sol. L'emplacement des radars est souvent le compromis entre une bonne visibilité du faisceau et une limitation de l'extrapolation verticale de la mesure (Boudevillain, 2018). En outre, le lissage inhérent au krigeage peut conduire à une représentation atténuée des orages localisés, voire à des surestimations ponctuelles lorsque des stations voisines enregistrent de fortes précipitations, mais que la station cible reste sèche. COMEPHORE constitue un outil précieux pour la reconstitution des précipitations horaires, particulièrement dans les zones dépourvues de stations et pour l'étude des épisodes intenses. Cependant, les limites des mesures radar en terrain montagneux réduisent sa pertinence dans ces secteurs. Ces constats soulignent l'intérêt de développer des approches d'interpolation intégrant explicitement les effets orographiques, afin d'améliorer la représentation des précipitations intenses en terrain complexe.

— SAFRAN (Vidal et al., 2010) est une réanalyse météorologique développée par Météo-France, conçue pour fournir des champs de variables atmosphériques à haute résolution spatiale, notamment en montagne. Elle repose sur une partition du territoire en zones supposées homogènes, à l'intérieur desquelles les variables sont interpolées en fonction de l'altitude. Cette approche permet une bonne représentation des gradients verticaux, mais présente certaines limites en contexte de forte variabilité spatiale. L'une des principales faiblesses de SAFRAN réside dans son hypothèse d'homogénéité intra-zone. Dans les régions à fort gradient horizontal de précipitations, comme la vallée du Rhône ou le versant méditerranéen du Massif Central, cette hypothèse conduit à des biais localisés importants. Des stations très proches peuvent présenter des erreurs de signe opposées (Quintana-Seguí et al., 2008), révélant l'incapacité du système à représenter la variabilité fine à l'intérieur des zones. Par ailleurs, SAFRAN tend à surestimer la fréquence des faibles précipitations (0–5 mm/j) et à sous-estimer les jours sans pluie ainsi que les événements intenses (Quintana-Seguí et al., 2008). De plus, dans le cadre du modèle, les différences de précipitation entre les points d'une même zone ne dépendent que de l'altitude, ce qui limite la représentation des effets locaux non-orographiques. Ainsi, si SAFRAN constitue un outil robuste pour la modélisation climatique et hydrologique à l'échelle régionale, son application est limitée dans des contextes de forte hétérogénéité spatiale, notamment en zone méditerranéenne ou convective.

— EDF a développé le produit SPAZM (Gottardi, 2009) avec pour volonté d'améliorer l'estimation des cumuls de précipitations en montagne pour la gestion du parc hydroélectrique. SPAZM est un modèle d'interpolation de précipitations journalières développé pour les zones montagneuses, intégrant les effets orographiques à travers une approche par type de temps. Il fournit des champs de précipitation à haute résolution spatiale (1

km²) et a démontré une bonne capacité à reproduire les cumuls annuels observés, tant à l'échelle du pixel qu'à celle de grands bassins versants (Gottardi, 2009). SPAZM présente certaines limites, notamment une tendance au lissage des cellules intenses, conduisant à une sous-estimation moyenne d'environ 10 % des quantiles de pluie pour des temps de retour supérieurs à 10 ans (Penot, 2014). Cette sous-estimation est liée à une mauvaise représentation de la variabilité des intensités journalières et des maxima annuels, en particulier sur de petits bassins versants. Le modèle reproduit bien la moyenne des précipitations, mais sous-estime leur écart-type, ce qui affecte la queue de la distribution et peut limiter son usage pour des applications hydrologiques sensibles aux précipitations intenses.

L'objectif scientifique de cette thèse vise à fournir un produit journalier de précipitations capable de représenter les événements intenses tout en fournissant des cumuls annuels adéquats en montagne. L'objectif opérationnel consiste à améliorer l'interpolateur SPAZM utilisé par EDF-DTG, en renforçant sa capacité à représenter les événements intenses, tout en conservant sa force principale : l'estimation fiable des cumuls annuels en montagne.

1.4 Questions scientifiques

L'objectif scientifique énoncé ci-dessus peut se décliner en trois axes principaux, dont l'enchaînement est décrit par la Figure 1.8.

1. **Documenter et modéliser la variabilité spatiale du lien précipitation-altitude à l'échelle climatologique.** Une meilleure compréhension des gradients altitudinaux permet d'estimer les précipitations dans les zones d'altitudes non instrumentées. Peu d'études ont quantifié l'ordre de grandeur et la variabilité spatiale de ces gradients. Cette thèse explorera les données et les modèles statistiques les plus pertinents pour représenter cette relation. Elle permettra de répondre aux interrogations suivantes :

   (a) **Quelle source de données utiliser pour représenter les gradients de précipitations altitudinaux ?**
   (b) **Quelle est la variabilité spatiale des gradients de précipitations altitudinaux ?**
   (c) **Quel modèle d'interpolation spatiale utiliser pour construire des champs climatologiques de référence, incluant l'effet de la topographie sur les précipitations ?**

   Le chapitre 2 constitue une première étape dans le développement de cet axe en s'intéressant à l'estimation des gradients altitudinaux de précipitations. Il compare plusieurs produits de données disponibles et analyse la variabilité spatiale de ces gradients, fournissant ainsi des éléments clés pour la compréhension des structures orographiques des précipitations. Sur cette base, le chapitre 3 explore différentes sources de données et modèles statistiques afin de construire des champs climatologiques saisonniers de référence. Ces champs servent de support spatiaux à l'interpolation des précipitations journalières, en assurant la représentation d'effets orographiques.

2. **Développer un produit journalier de précipitations capable de représenter la variabilité spatiale des événements intenses.** Le socle méthodologique repose sur la géostatistique, en se focalisant sur le modèle de covariance spatiale utilisé. Cet axe permettra de répondre aux questions suivantes :

(a) **Peut-on exploiter les simulations de CP-RCM pour estimer la covariance spatiale des précipitations journalières ?**
(b) **La prise en compte d'une covariance anisotropique améliore-t-elle l'interpolation spatiale des précipitations journalières ?**
(c) **Quelle est l'incertitude d'interpolation ?**

Pour y répondre, l'objectif consiste à identifier un modèle statistique capable de reproduire à la fois les intensités maximales et la variance spatiale des champs journaliers de précipitation, tout en fournissant une incertitude d'interpolation. Bien que les approches bayésiennes et les méthodes issues du *Machine Learning* soient prometteuses, leur mise en œuvre dans un cadre opérationnel demeure complexe. Nous privilégierons donc la simulation conditionnelle de champs gaussiens, qui permet de surmonter certaines limites des méthodes déterministes, telles que le lissage excessif des champs de précipitation ou la sous-estimation des événements intenses. Dans cette approche, l'estimation précise de la structure de covariance spatiale est cruciale pour représenter la variabilité des précipitations. Par souci de simplicité, et en raison de la disponibilité limitée des données, cette covariance est souvent supposée isotrope (Vischel et al., 2009; Renard et al., 2011; Cornes et al., 2018; Frei and Isotta, 2019). À l'instar de Gyasi-Agyei and Pegram (2014), nous explorerons l'utilisation de sources de données alternatives pour estimer une anisotropie potentielle de la structure spatiale. Le chapitre 4 s'appuie sur ces éléments pour mettre en œuvre un modèle géostatistique d'interpolation journalière et confronter plusieurs hypothèses sur la structure de la covariance spatiale, dans la recherche de la meilleure reproduction de la variabilité spatiale des champs de précipitation

3. **Évaluer exhaustivement le produit développé avec des données alternatives et complémentaires**, au vu de son utilisation opérationnelle pour l'hydrologie de montagne. L'évaluation des réanalyses ou des interpolateurs est souvent limitée. Les validations croisées, bien que courantes, ne permettent pas d'évaluer la variabilité spatiale des précipitations en montagne, car la majorité des pluviomètres se situent dans les vallées (Daly, 2006). De plus, les validations croisées ne peuvent pas évaluer des précipitations aggrégées spatialement, quantité d'intérêt pour l'hydrologie. Le produit devra permettre à la fois la reproduction des crues intenses et des cumuls saisonniers en montagne, y compris dans les zones peu instrumentées. Ce travail vise à traiter les questions ci-dessous.

   (a) **Le produit journalier de précipitations permet-il de représenter les cumuls annuels/hivernaux en zone de montagne ?**
   (b) **Le produit journalier de précipitations permet-il de modéliser les crues intenses ?**
   (c) **Comment l'incertitude sur les précipitations journalières se traduit-elle sur l'estimation des crues intenses ?**

   Pour répondre à ces questions, nous utiliserons des données alternatives pour évaluer le produit journalier de précipitation créé dans le chapitre 5. L'accent est mis à la fois sur sa capacité à reproduire les cumuls annuels en zone de montagne et à modéliser les crues intenses, critères essentiels pour les usages en gestion des ressources en eau et en prévention des risques dans le contexte opérationnel d'EDF-DTG. Les données de débits permettent d'évaluer à la fois les cumuls en montagne via le respect des bilans hydrologiques et les précipitations intenses via la modélisation des crues (Evin et al., 2024). De plus, les données de neige (Pulka et al., 2024; Vernay et al., 2025) et de glaciers (Immerzeel et al., 2015) constituent des indicateurs révélateurs des cumuls de

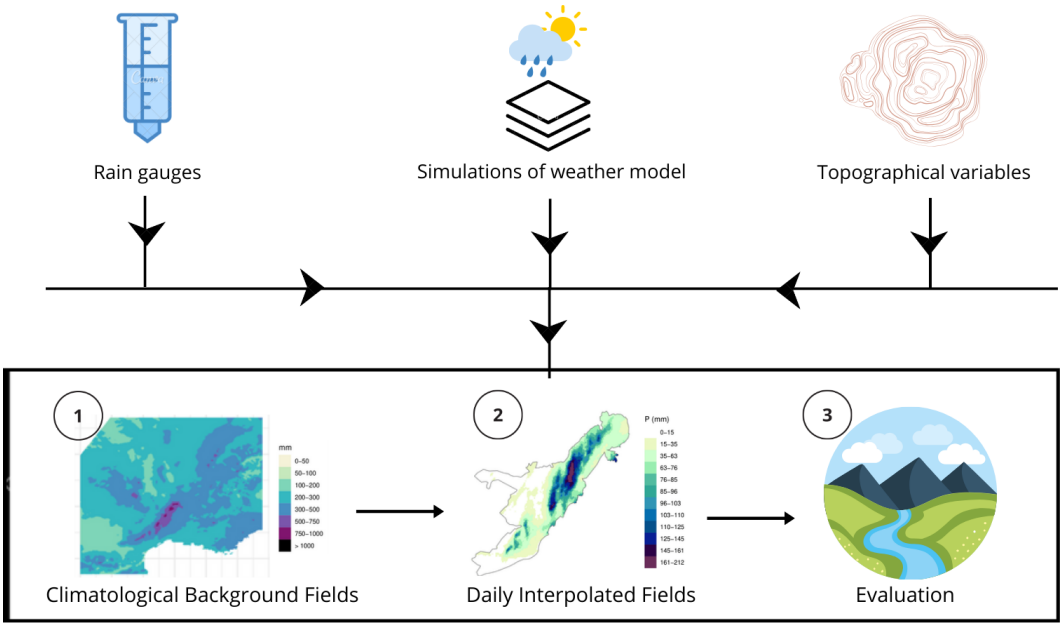

Figure 1.8 – Découpage de la thèse.

précipitations en zone de montagne.

Ce travail de thèse adopte le format d'un manuscrit structuré autour de quatre publications scientifiques. Chaque chapitre est associé à un article : les deux premiers ont été publiés, le troisième est actuellement en cours d'évaluation, et le quatrième est en cours de finalisation. Nous souhaitons soumettre ce quatrième article au journal Geoscientific Model Development (GMD).

Liste de publications :

- Dura, V., Evin, G., Favre, A. C., and Penot, D. (2024). Spatial variability in the seasonal precipitation lapse rates in complex topographical regions–application in France. Hydrology and Earth System Sciences, 28(12), 2579-2601.
- Dura, V., Evin, G., Favre, A. C., and Penot, D. (2024). Spatial Interpolation of Seasonal Precipitations Using Rain Gauge Data and Convection-Permitting Regional Climate Model Simulations in a Complex Topographical Region. International Journal of Climatology, 44(16), 5745-5760.
- Dura, V., Evin, G., Favre, A. C., and Penot, D. (2025). Improving Precipitation Interpolation Using Anisotropic Variograms Derived from Convection-Permitting Regional Climate Model Simulations. EGUsphere, 2025, 1-25.

2

Variabilité spatiale des gradients de précipitations altitudinaux dans les régions à topographie complexe - application en France

Abstract Seasonal precipitation estimation in ungauged mountainous areas is essential for understanding and modeling a physical variable of interest in many environmental applications (hydrology, ecology, cryospheric studies). Precipitation Lapse Rates (PLRs), defined as the increasing or decreasing rate of precipitation amounts with the elevation, play a decisive role in high-altitude precipitation estimation. However, the documentation of PLR in mountainous regions remains weak even though their utilization in environmental applications is frequent. This article intends to assess the spatial variability and the spatial-scale dependence of seasonal PLRs in a varied and complex topography region. At the regional scale (10,000 km^2), seven different precipitation products are compared in their ability to reproduce the altitude dependence of the annual/seasonal precipitations of 1,836 stations located in France. The Convection-Permitting Regional Climate Model (CP-RCM) AROME is the best in this regard, despite severe precipitation overestimation in high altitudes. The fine resolution of AROME allows for a precise assessment of the influence of altitude on winter and summer precipitations on 23 massifs at the sub-regional scale ($\sim$ 1,000 km^2) and 2,748 small catchments ($\sim$ 100 km^2) through linear regressions. With AROME, PLRs are often higher in winter at the catchment scale. The variability of PLR is higher in high-altitude regions such as the French Alps, with higher PLRs at the border than inside the massifs. This study emphasizes the interest of conducting PLR investigation at a fine scale to reduce spatial heterogeneity in the seasonal precipitations–altitude relationships.

2.1 Introduction

Precipitation Lapse Rates (PLRs) refer to the increasing or decreasing rate of precipitation amounts with elevation. The rise of moist air above an orographic barrier such as hills or mountains generates precipitations that affect the ice cover and the precipitation amount contained in snowpacks (Bales et al., 2006; Viviroli et al., 2007; Mott et al., 2014; Dozier et al., 2016; Wrzesien et al., 2019). Therefore PLR is the main factor that controls the water budget of high-altitude catchments (Jiang, 2003) and partly explains the freshwater supply in the summer season. On shorter time scales like hourly or daily scales, PLRs help understand the physical mechanisms of orographic precipitations responsible for natural hazards such as avalanches, landslides, and floods (Caracena et al., 1979; Caine, 1980; Conway and Raymond, 1993; Buzzi et al., 1998; Panziera et al., 2015). PRLs can also be of importance for hydrological modeling, for which precipitation inputs are often spatialized with geostatistics models (Daly et al., 1994; Gottardi, 2009; Frei and Isotta, 2019) or can be distributed by altitudinal bands using assumed PLR values (Bergström, 1992; Ragettli and Pellicciotti, 2012; Markstrom et al., 2015; Garavaglia et al., 2017; Ruelland, 2020; Kumar et al., 2022) to complete the hydrological balance (Oudin et al., 2006) in high-altitude catchments. The investigation of PLR is a topical and crucial issue in multiple domains such as energy production, agriculture, tourism, condition of ecosystems, risk management (Pimentel et al., 1997; Gössling et al., 2012).

The relationship between altitude and precipitation accumulation is not straightforward on small-time scales and depends on precipitation type (stratiform *vs* convective), wind, and flow directions (Sevruk and Mieglitz, 2002; Schäppi, 2013). PLR at the hourly scale may even exhibit a negative trend during extreme events (Formetta, 2021) due to the drying of the air mass. When aggregated over extended periods, the relationship between precipitation and elevation becomes simpler to model, with generally a precipitation increase as elevation increases (Barrows, 1933; Spreen, 1947; Schermerhorn, 1967; Smith, 1979). However, PLR values can differ among seasons and regions due to different weather processes (Napoli et al., 2019; Ménégoz et al., 2020). In the Alps, large-scale processes mainly generate winter precipitation. Convective processes are more frequent in summer.

In a hydrology framework, PLRs refers to the slope of the linear regression between precipitation and elevation on spatial areas (e.g. Sevruk, 1997; Gottardi, 2009; Ogrin and Kozamernik, 2020; Avanzi et al., 2021; Bell et al., 2022) rather than on vertical atmospheric columns. In some cases, the relationship in high-altitude regions appears to be non-linear with a threshold impact (Schäppi, 2013; Napoli et al., 2019) due to the drying of the air masses, and the use of quadratic regression is then recommended (Mahmood et al., 2021).

PLRs are often estimated from ground measurements from rain gauges, observations of Snow Water Equivalent (SWE) (Avanzi et al., 2021) derived from manual coring or radiation, and snow/rain gauges totalizator (Gottardi, 2009) measures. Using only ground stations to estimate PLRs requires a sufficient coverage of high-elevation areas, which is rarely met in practice (Hofstra et al., 2010). High-elevation stations are prone to precipitation under-catch (Groisman and Legates, 1994; Pollock et al., 2018) and snow-redistribution. Strong winds coupled with a significant amount of solid precipitation might even induce an annual underestimation of up to 25% (Sevruk, 1997). Moreover, the robustness of the regressions and the local influences of altitude on precipitation must be balanced because of the irregular spatial sampling of punctual observations (Gottardi, 2009). In practice, in sparse rain gauge regions, PLR can only be computed on vast areas and fails to reflect the local relationship between altitude and precipitation.

As an alternative, gridded precipitation products can help analyze the spatial variability of PLR at a fine spatial scale. Radar products that indirectly measure precipitation from reflectivity have been extensively used in hydrology (e.g. Ochoa-Rodriguez et al., 2019). However, radar data are inherently biased in mountainous regions due to ground echoes and beam blockage (e.g. Berne and Krajewski, 2013), which results in an underestimation of PLR (Faure et al., 2019). Satellite precipitation products, despite certain limitations, are another easily accessible source of data. The biases in mountain regions and the relatively low resolution of the data present challenges in calculating PLR from satellite data (Li et al., 2017). Composite products merging radar or satellite to rain gauge data (Champeaux et al., 2009; Nie et al., 2015; Nguyen et al., 2020) can also be an option for the assessment of PLRs. However, the latter products are sensible on the density of the rain gauge network and suffer where no rain gauge are available (Silverman et al., 2013; Shen et al., 2018; Frei and Isotta, 2019). Regional Climate models (RCM) have been used in numerous studies to evaluate the variability of PLR at regional scales (e.g. Kotlarski et al., 2012; Cuo and Zhang, 2017; Ménégoz et al., 2020). All results show that PLRs obtained with RCM data are larger and more spatially varying than those using rain gauges. Convection-Permitting Regional Climate Models (CP-RCMs) have recently emerged as an appealing tool for producing fine-resolution ($1-4$ km^2) climate simulations (Rockel et al., 2008; Brousseau et al., 2016; Keuler et al., 2016; Belušić et al., 2020). CP-RCMs are a refined extension of RCM where deep convection parametrization, a dominant source of precipitation error (Hohenegger et al., 2008; Foley, 2010; Kendon et al., 2012), is turned off. To produce a long series of CP-RCM simulations, including precipitation, a Numerical Weather Prediction (NWP) model is often driven by a RCM or a satellite-based reanalysis. CP-RCMs produce better precipitation intensities and frequencies than RCMs during heavy events (Ban et al., 2021; Caillaud et al., 2021). CP-RCMs represent more accurately orographic precipitation than RCMs because they explicitly resolve deep convective processes and include a finer representation of the topography (Lucas-Picher et al., 2021). These improvements occur especially in summer when convective events play a major role (Ban et al., 2021). Today, CP-RCMs are considered more reliable than reanalysis (Lundquist et al., 2019) in ungauged mountainous areas, despite current precipitation overestimation (Gerber et al., 2018; Dallan et al., 2023).

This paper explores the spatial variability of winter and summer PLR across a complex topographical region, with a dense network of 1,836 stations used as ground truth. The first

objective is to compare seven types of gridded products (interpolator, reanalysis, satellite, radar, CP-RCM) in their ability to capture the relationship between observed annual/seasonal precipitations and altitude. The second goal is the investigation of the spatial variability of winter and summer PLR values at the sub-regional ($\approx 1,000$ km^2) and catchment (≈ 100 km^2) scales using a gridded precipitation product without ground station assimilation. Nesting of catchments in sub-regions allows the study of the spatial-scale dependence of PLR to provide guidelines for future precipitation interpolation studies. To our knowledge, only Jiang et al. (2022) explores these questions in the Third Pole. In a sparse rain gauge region, the authors found an accurate PLR reproduction with downscaled ERA5 precipitation product (Jiang et al., 2021). They highlighted the spatial variability of PLR at the catchment scale and emphasized the importance of conducting PLR studies at the finest possible spatial scale.

This paper is organized as follows. Section 2.2.3.6 describes the study domain and the available precipitation products. Section 2.4.1 presents the method used to derive PLR. Section 2.4 shows the results of the reproduction and spatial variability of PLR by the different products considered. Section 2.5.3 compares the findings to the literature and discusses some perspectives. Section 2.6 gives the conclusions.

2.2 Domain and data under study

2.2.1 A complex mountainous region

Figure 2.1**(a)** shows the study domain, which corresponds to the intersection of the spatial extents of the seven gridded precipitation products. The topography of the region is complex and varied, including three major mountain chains : the Alps, the Pyrénées, and the Massif Central. The Massif Central is a mid-mountain range reaching 1,885 m in the center of the Southern half of France and covers 85,000 km^2, which makes it the largest mountainous region of the country (15 % of the total surface area of France). The Massif Central is bordered by the Rhone Valley in its Western part and the Mediterranean coastal plain in its Southern part. This region is mainly composed of large plateaus ranging in altitude from 600 m to 900 m and enclosed by mountains with circular summits corresponding to extinct volcanoes. The altitude presents an asymmetrical profile with summits in the South and the East (Cévennes) and less elevated areas in the northwest. The landscapes are varied and contain limestone plateaus cut by deep canyons, mountain peaks, and deep river valleys. The Massif Central is exposed to the Western wind and captures the precipitation coming from the Atlantic Ocean.

The Alps are the highest mountain range in Europe, reaching 4,808 m at the Mont-Blanc. The chain has a 40,000 km^2 surface area and is 1,200 km long, crossing seven countries : France, Switzerland, Italy, Germany, Liechtenstein, Austria, and Slovenia. The French Alps are separated from the Massif Central by hills and are divided into the Northern and the Southern parts. The Northern Alps are higher and have large valleys. In the Southern Alps, valleys are narrower. The climate of the French Alps has three main influences. The moist air can come from the West Atlantic. The warm air comes from the Mediterranean and blows Northward. In winter, easterly weather fronts coming from the Italian Alps can bring large amounts of precipitation in the east of the French Alps (Garavaglia et al., 2010). Generally, these meteorological events do not reach the foothills of the French Alps. The Northern Alps are more rainy than the Southern Alps, which have almost 300 days per year of sunshine. The French Alps is a territory of high altitude and complex topography. The significant variations in mountain elevation and exposure result in the coexistence of multiple climates at small spatial scales. Mountains create micro-climatic conditions and influence daily weather. The Jura is a sub-alpine mountain range located in the North of the French Alps. It covers a surface area of 5,000 km^2 and reaches 1,700 m. It is a mid-mountain range composed of plateaus with a mean altitude of 600 m.

The Pyrénées form a natural border between France and Spain by joining the Atlantic Ocean to the Mediterranean Sea over 430 km long. It covers 19,000 km^2 and reaches 3,200 m on the French side, making it the second-highest mountain range in France. Most valleys are running South-North. The Spanish part is more arid and rocky than the French part, which catches the precipitation from the Atlantic. The French Pyrénées splits into the Atlantic, Central, and Eastern parts. The relief rises steeply from sea level to hills in the Atlantic and Eastern parts. The Central Pyrénées host sharp peaks but are more rounded than the Alps because of erosion. The Atlantic part gets more precipitation because of rainy Northwest winds. The wind from the Southwest brings warmer air in summer. The topography is diverse, with snow-capped mountains, deep green valleys, and coastal hills. The remaining of France consists of plains and are not included in this study.

In this study, we consider three spatial scales : the regional scale (10,000 km^2), the sub-regional scale (1,000 km^2), and the catchment scale (100 km^2). The sub-regional scale consists of areas named "massif", which form a set of continuous reliefs, often separated by rivers and valleys. An ensemble of massifs constitutes a mountain range (Alps, Pyrenees). In the French Alps, 23 massifs have been identified through climatological homogeneity of precipitation in Pahaut (1991). PLR computation will be conducted at the massif (climatological homogeneity) and catchment (hydrologic interpretation) scales. The surface areas of the massifs range from 450 to 1,600 km^2, with a median value of 870 km^2. The 2,748 catchments collected from Sandre (2020) have a mean surface area ranging from 0.009 to 1,000 km^2, with a median value of 100 km^2. Figure 2.1**(c)** illustrates the massifs and the catchments analyzed in this study. The altitude is represented with a digital terrain model of 1 km resolution. The study domain is divided into squares of 1 km^2 that are referred to as "pixels".

2.2.2 A dense network of stations

Figure 2.1**(b)** presents the dense rain gauge network of 1,836 stations used in this study, with an average density of one rain gauge per 160 km^2. Electricité de France (EDF, the main electricity provider in France) and Meteo-France provide 673 and 1,163 stations, respectively. We aggregate available daily precipitation data to obtain seasonal and annual precipitation. Figure 2.1**(d)** shows the number of rain gauges per altitudinal band. A small number of rain gauges is available above 2,000 m, causing an under-representation of high-altitude regions. To overcome this limitation, EDF has implemented a snow rain gauges totalizator (Nivo Pluviomètre Totalisateur, NPT in French) device (Gottardi, 2009). NPTs collect annual precipitation in a small orifice protected from the wind by a large collar. Snow falling in the orifice feeds a reservoir containing a saline solution able to melt solid precipitation. The operating period ranges from 1945 to 1977 and differs among NPTs. We restricted the period to 1957–1973, where the spatial density of NPT is at its maximum. An exploratory analysis of the annual precipitation from NPTs removes outliers and missing values. Following this analysis, we keep 130 NPTs among 216 for the study. NPTs are primarily found in the Mont-Blanc region and are more uncommon, for instance, in the center of the Pyrénées. Figure 2.1**(c)** illustrates the irregular number of weather stations per catchment. Mountainous regions like the Alps and the Cévennes are more covered than plains, where weather processes are less subject to spatial variability. Nevertheless, the Southern Alps, the Massif Central, and the Pyrénées have a complex topography and few stations. The sparse stations in some mountainous regions and their location in valleys largely constrain the ability to compute PLR using only precipitation aggregated from rain gauges.

In France, precipitation patterns differ among seasons. Thus in this study, four seasons are considered : winter (December, January, February (DJF)), spring (March, April, May (MAM)), summer (June, July, August (JJA)), and autumn (September, October, November (SON)).

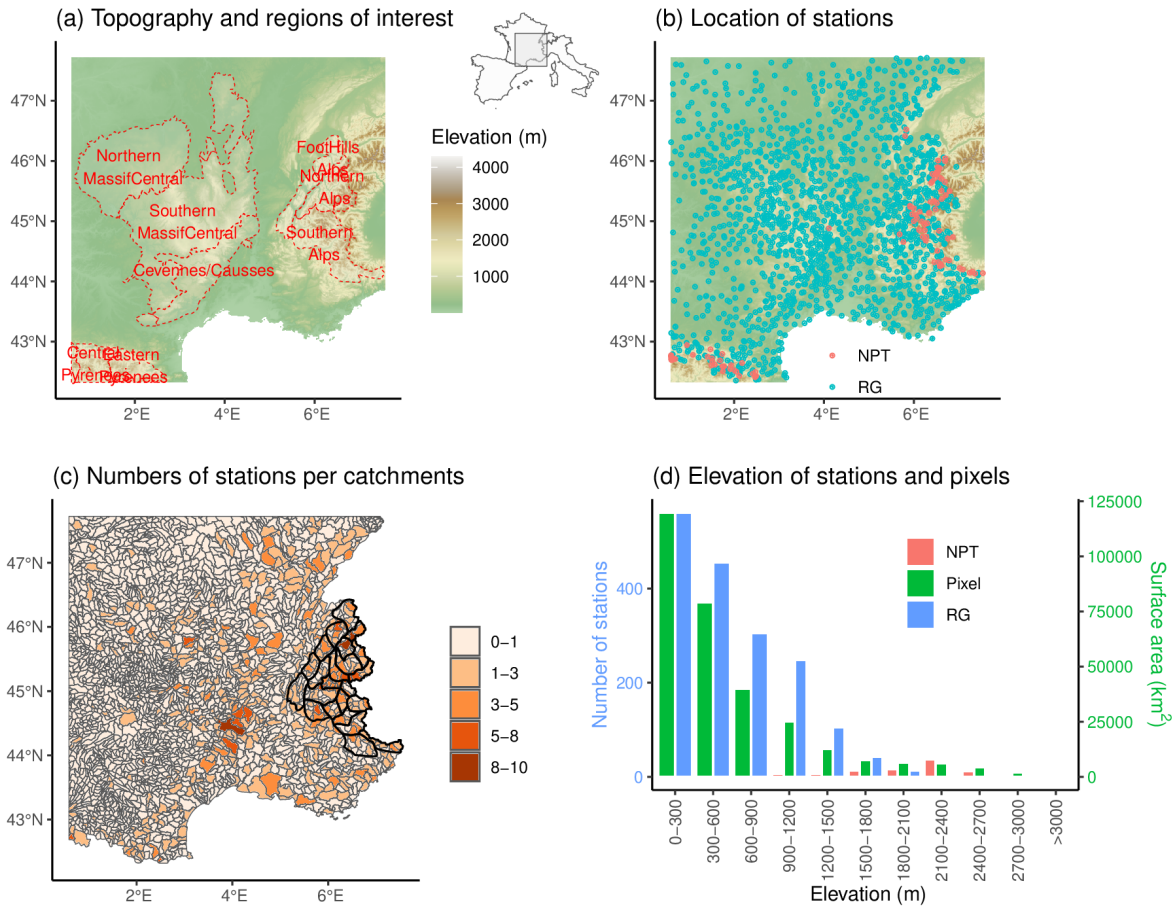

Figure 2.1 – **(a)** Topography of France and boundaries of eight sub-regions of interest. The extent of the study domain is located in France and is bordered by Spain, Italy, and Switzerland. **(b)** Location of stations, blue points refer to rain gauges (RG) and red points to NPT (see subsection 2.2.2). **(c)** Catchments and the corresponding number of stations. Boundaries of massifs located in the Alps are also indicated in black. **(d)** Histogram of the altitude of stations (rain gauges (RG), and NPT) and of the covered surface area (in green).

2.2.3 Gridded precipitation products

This study explores the ability of multiple gridded precipitation products to assess the relationship between annual precipitation and altitude. Precipitations from gridded products are available at daily, hourly, or sub-hourly timescales and aggregated to obtain seasonal precipitations. These products are briefly described hereafter and are summarized in Table 2.1.

2.2.3.1 ERA5-Land

ERA5-Land (Muñoz-Sabater et al., 2021) is a global reanalysis that operates by simulating atmospheric and surface variables, including hourly precipitation. It uses the ERA5 atmospherical fields downscaled with linear interpolation at the resolution of 9 km. ERA5-Land assimilates satellite data and does not rely on rain gauges. The quality of ERA5-Land precipitation is dependent on the density of satellite and radar networks used in the assimilation process (Hassler and Lauer, 2021). As a result, the quality is better in Central Europe and the U.S. than in tropical oceans. The improved horizontal resolution of 9 km compared to 31 km (ERA5) or 80 km (ERA-Interim) is a benefit of ERA5-Land (Muñoz-Sabater et al., 2021).

This results in a better representation of spatial precipitation patterns (Gomis-Cebolla et al., 2023).

2.2.3.2 CERRA-Land

Copernicus European Regional ReAnalysis Land (CERRA-Land) (Le Moigne, 2021) is the most up-to-date reanalysis available in Europe since September 1984 at a horizontal resolution of 5.5 km. It uses ERA5 as lateral boundary conditions to run the atmospherical model HIRLAM ALADIN Regional/Mesoscale Operational NWP In Europe (HARMONIE) every 3 hours at a native resolution of 5.5 km. The analysis is given to the MESCAN system (Soci et al., 2016) to produce daily precipitation fields by merging it with nearly 8,000 daily rain gauge measurements through optimal interpolation. Le Moigne (2021) found that CERRA-Land leads to a better representation of the seasonality of snow depth in the Alps compared to ERA5-Land.

2.2.3.3 PDIR-NOW

PERSIANN Dynamic Infrared-Rain Rate (PDIR-NOW, Nguyen et al., 2020) is a satellite-based product using high-frequency (15 min) sampled infrared imagery, at a 4 km spatial resolution. PDIR-NOW estimates precipitation based on empirical cloud-top temperature–precipitation rate relationships. Errors resulting from this method are corrected by calibrating the empirical relationships regionally based on monthly precipitation climatology. PDIR-NOW has better diurnal cycle representation, rain/no rain days estimation, and regional precipitation patterns compared to the other PERSIANN family products (Nguyen et al., 2020). The inter-annual, annual, and seasonal precipitations are less biased with PDIR-NOW (Huang et al., 2021; Uysal, 2022). In the following, PDIR-NOW will be referred to as PDIR.

2.2.3.4 SERVAL

The *Système d'élaboration des produits radar et de visualisation centralisé* (SERVAL, previously PANTHERE, Champeaux et al., 2009) product provides precipitation amounts at a frequency of 5 minutes and a spatial resolution of 1 km by merging individual radar fields. Before any radars are combined, each one is individually calibrated using data from hourly rain gauges, with a mean hourly correction ratio applied uniformly across the whole radar coverage. If a pixel falls under the coverage of multiple individual radars, the selected precipitation corresponds to the maximum of precipitation seen by the considered radars. As already mentioned, radars are affected by many sources of potential errors, such as beam blocking and ground echoes. Ground echoes are removed using pixel precipitation probabilities, which are derived from a cloud classification filter. Bright band and signal attenuation phenomena are also corrected.

2.2.3.5 COMEPHORE

The *COmbinaison en vue de la Meilleure Estimation de la Précipitation HOraiRE* (COMEPHORE, Champeaux et al., 2009) is a precipitation reanalysis based on the combination of the previous SERVAL product with a dense rain gauges data set of more than 4,000 observations. Kriging of the rain gauge values is applied to obtain the stratiform part, while the convective part involves the radar precipitation re-calibration with the rain gauge amounts. The main idea underlying this product is to combine the coherent spatial structure of the radars with the accuracy of rain gauge measurements to provide an hourly precipitation field at 1 km resolution. COMEPHORE underestimates mountains annual precipitation (Rouzeau, 2013; Roger, 2017) since the altitude is not considered at any modeling stages.

2.2.3.6 SPAZM

The *SPAtialisation en Zones de Montagne* (SPAZM, Gottardi, 2009) is a precipitation interpolator that integrates rain gauge values with a meteorological guess conditioned by topography, and the weather type of the day. Eight weather situations are identified based on geopotential fields (Garavaglia et al., 2010) and eight corresponding mean daily precipitation fields are created through local linear regression between mean daily observed precipitation at stations and altitude, at the daily timescale and 1 km resolution. For a given day, the corresponding mean daily precipitation field is modified using the precipitation of the current day. SPAZM incorporates 2,201 various stations from EDF (rain gauges and NPT), Meteo-France, MeteoSwiss, Arpa Piemonte, and Instituto Nacional de Meteorología (INM) networks. SPAZM used fewer but higher stations than COMEPHORE. Its ability to provide accurate estimates of yearly precipitation makes it a valuable tool for hydrological applications (Gottardi, 2009; Ménégoz et al., 2020; Ruelland, 2020).

2.2.3.7 CNRM-AROME

The CNRM-AROME model is a CP-RCM based on the nonhydrostatic, convective-scale, limited-area model called *Applications de la Recherche à l'Opérationnel à Méso-Echelle* (AROME) used for the national weather prediction by Meteo-France since 2008 (Seity et al., 2011; Brousseau et al., 2016). 37 years of CNRM-AROME simulations are available at a horizontal resolution of 2.5 km, at the hourly timescale (Caillaud et al., 2021), for an Alpine domain defined in the Flagship Pilot Study of the Coordinated Regional Climate Downscaling Experiment (CORDEX-FPS, Coppola et al., 2020). The Atlantic Pyrénées are not contained in the domain. The version of AROME applied to obtain this long simulation is related to cycle 41t1 (Termonia et al., 2018) and corresponds to the version in operational use at Meteo-France, between December 2015 and December 2017. In the remainder of the paper, CNRM-AROME CP-RCM will be referred to as AROME. The initial atmospheric conditions of AROME are provided every hour by a CNRM-ALADIN RCM simulation, itself driven by the ERA-Interim reanalysis. The fine resolution of the model enables a good representation of the deep convection scheme despite the absence of data assimilation. Precipitation from this version has been evaluated recently in multiple studies (Ban et al., 2021; Caillaud et al., 2021; Monteiro et al., 2022). Heavy precipitations are better represented than in the RCM CNRM-ALADIN but suspicious snow accumulation is pointed out in high altitudes. A first pre-processing stage is required to address large errors in precipitation seasonal amounts at the pixel scale. An iterative technique is applied to deal with the problematic pixels, whereby the abnormal values are replaced with the weighted (according to the altitude) average of the precipitation amount of the nearby pixels. A pixel is qualified as problematic if a difference of more than 500 mm in seasonal precipitations is noticed compared to a neighboring pixel.

Some gridded precipitation products present non-homogeneous data because of their large temporal depths. Most radars have been integrated since 2006, and others have been gradually incorporated since 2015 in mountainous regions (Beck and Bousquet, 2013). The use of SERVAL and COMEPHORE is therefore tainted with temporal non-homogeneity. Station density also affects the temporal homogeneity of COMEPHORE, CERRA-Land, and SPAZM. Changes in instrumentation have been corrected in COMEPHORE and SPAZM with homogenization of rain gauge precipitation (Gottardi, 2009; Mestre et al., 2013).

Figure 2.2 displays the mean annual precipitation for all gridded precipitation products. Fig. S1 in the Supplements provides the same information on a seasonal basis. We first notice the effect of the resolution. Annual precipitations from ERA5-Land and PDIR are very smooth on the considered domain compared to the other gridded products available at a finer resolution. The precipitation difference between plains and mountains is not very prominent

Table 2.1 – Summary of the characteristics of the gridded precipitation products used in this study, namely available period, domain, horizontal resolution, frequency, type of observations, provider, and reference.

	Available period	Domain	Horizontal resolution	Frequency	Type of observations	Provider	Reference
ERA5-Land	1950–2023	World	9 km	Hourly	Reanalysis ECMWF replay	ECMWF	Muñoz-Sabater et al. (2021)
CERRA-Land	1984–2023	Europe	5.5 km	Daily	Reanalysis	C3S	Le Moigne (2021)
PDIR	2000–2023	60°N to 60°S	4 km	Hourly	Reanalysis Satellite	CHRS	Nguyen et al. (2020)
SERVAL	2006–2020	France	1 km	5min	Radar	Météo-France	Champeaux et al. (2009)
COMEPHORE	2007–2020	France	1 km	Hourly	Reanalysis Rain gauges + radar	Météo-France	Champeaux et al. (2009)
SPAZM	1950–2020	France	1 km	Daily	Reanalysis Rain gauges	EDF	Gottardi (2009)
AROME	1982–2018	Pan-Alps	2.5 km	Hourly	CP-RCM	Météo-France	Caillaud et al. (2021)

in the radar products SERVAL and COMEPHORE. Comparatively, the Pyrénées, the Massif Central, and the Alps receive more annual precipitation with AROME, CERRA-Land, and SPAZM. SPAZM leads to marked patterns in the alpine valleys and produces a higher correlation to altitude. AROME gives a large amount of precipitation in mountains, especially in the Massif Central. The seven gridded precipitation products show different precipitation amounts, especially in mountainous regions, due to more or less fine horizontal resolutions, different types of assimilated data, and differences in the treatment of the altitude effect.

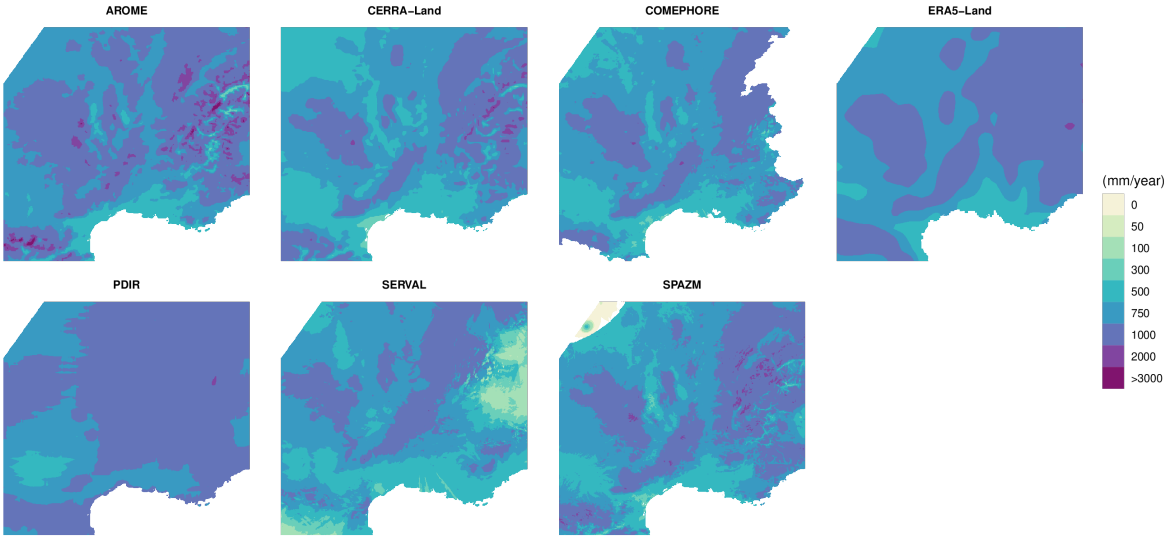

Figure 2.2 – Mean annual precipitation for the gridded precipitation products (AROME, CERRA-Land, COMEPHORE, ERA5-Land, PDIR, SERVAL, SPAZM), on the period 2007–2017.

2.3 Methods

Let *Pobs* and *Pgrid* denote respectively the observed (by rain gauges and NPT) and gridded precipitation (annual or seasonal) expressed in mm. Let Z indicate the altitude in m. The indices i and j refer to stations while the index p indicates the pixels.

2.3.1 Description of the relationship between precipitation and altitude

Annual and seasonal precipitations from the gridded products are extracted at station locations to evaluate the reproduction of the altitudinal variability of precipitation. The precipitations from the NPT are only available at the annual scale. The stations are grouped by regions defined in Fig.2.1**(a)** and by 300-meter elevation bands b_{alt} ranging from 0–300 m to 3000–3300 m. For each elevation band and region, the median of observed ($Pobs_{b_{alt}}$) and

gridded ($Pgrid_{b_{alt}}$) precipitation (annual and seasonal) is computed using all the locations of the stations belonging to this region and elevation band :

$$Pobs_{b_{alt}} = \hat{Pobs}_{i_{50\%}}, i \in b_{alt}, \tag{2.1}$$

$$Pgrid_{b_{alt}} = \hat{Pgrid}_{i_{50\%}}, i \in b_{alt}. \tag{2.2}$$

The median values should represent the considered region and elevation band and be unaffected by anomalous values resulting from a specific station location. A compromise between a high number of rain gauges per band and a sufficient number of bands led to a 300 m bandwidth selection. The bands with fewer than five rain gauges are not displayed in Fig.2.3**(a)** to prevent any misunderstandings or misrepresentations. To study the behavior of gridded precipitation products in high altitudes where no rain gauges are available, we compare the median of seasonal precipitations $\hat{Pgrid}_{p_{50\%}}, p \in b_{alt}$ extracted from pixels within the altitudinal bands.

To test a gridded precipitation product in reproducing the spatial variability of the relationship between seasonal precipitations and altitude at a finer scale, we also compute Precipitation Relative Difference (PRD) for several couples of close neighboring stations with sufficient elevation difference. The two stations should have a separation distance lower than 20 km and have an elevation difference superior to 100 m. PRD should not be assimilated to Precipitation Lapse Rates (PLR) calculated at the catchment scale, see subsection 2.3.2. For the neighboring stations i and j, we compute PRD at station locations for observed ($PRD_{Pobs_{ij}}$) and gridded ($PRD_{Pgrid_{ij}}$) precipitation :

$$PRD_{Pobs_{ij}} = 100 \times 100 \times \frac{Pobs_i - Pobs_j}{Z_i - Z_j} \Big/ \frac{Pobs_i + Pobs_j}{2}, \tag{2.3}$$

$$PRD_{Pgrid_{ij}} = 100 \times 100 \times \frac{Pgrid_i - Pgrid_j}{Z_i - Z_j} \Big/ \frac{Pgrid_i + Pgrid_j}{2}. \tag{2.4}$$

The gradient of seasonal precipitations relative to the altitude is divided by the mean precipitation of the two stations and multiplied one time by 100 to get the result in percentage relative to the mean precipitation. This result is again multiplied by 100 to express PRD in percentages per hundred meters (%/100 m).

2.3.2 Regression at nested spatial scales

The primary focus of this study is the investigation of the spatial variability of seasonal PLRs at the sub-regional and catchment scales. It is possible to use stations at the regional scale, but the PLRs would be too dependent on their spatial sampling at the sub-regional and catchment scales. Indeed, some catchments contain zero or only one station (Fig.2.1**(c)**). As an alternative, we propose to use AROME to study the spatial variability of PLR at the sub-regional and catchment scales. The choice of AROME will be motivated in subsection 2.4.1. We assume linear relationships between seasonal precipitations and altitude. This strong hypothesis will be discussed later in subsection 2.4.3. The PLRs are calculated with linear regression between seasonal precipitations and altitude, expressed as follows :

$$Parome_p = \alpha + \beta \times Z_p + \epsilon_p, \text{with } \epsilon_p \sim \mathcal{N}(0, \sigma^2). \tag{2.5}$$

$Parome_p$ is the seasonal precipitations in mm for the pixel p, α is the y-intercept in mm, β is the slope expressed in mm/m, and Z_p is the altitude in m of the pixel p. The regression fit is

performed using the maximum likelihood method implemented in the R function *lm*. PLRs are derived from β using the following formula :

$$PLR = 100 \times 100 \times \frac{\beta}{\bar{P}}. \tag{2.6}$$

where $\bar{P}$ is the average seasonal precipitation from AROME over the area where the linear regression is performed. The slope of the regression β is multiplied by 100 twice, first to obtain the result as a percentage and once more to express PLR in percentage per hundred meters (%/100 m), relative to the average seasonal precipitation from AROME. The expression of PLR in %/100 m overcomes the biased nature of gridded precipitation products and allows a spatial comparison despite significant spatial and seasonal variation in precipitation amounts across France (Fig.2.2). To investigate the dependence of PLR on a given spatial scale, regressions will be conducted on 23 massifs of the Alps and catchments. On the catchments, a regression will only be performed if there is sufficient variability in elevation, *i.e.* if the standard deviation of altitude is higher than 50 m.

2.3.3 Linearity of the regressions

In our formulation (Eq. 2.6), PLRs are defined as the slopes of the linear regressions. The linearity of the relationship between annual precipitation and altitude at the catchment scale is a questionable hypothesis. For example, Avanzi et al. (2021) found non-linearity in two catchments located in the Italian Alps. Smoothing splines provide more flexibility than linear regressions to model annual precipitation through altitude. However, smoothing splines are not interpretable in terms of PLRs. For this reason, we use piecewise linear regressions implemented in the R package *segmented* (Muggeo, 2008). We perform piecewise linear regressions (unknown break-point between the first and third quartile of altitude) between annual precipitation and altitude on all catchments with sufficient variability (standard deviation of the altitude higher than 50 m) in altitude. To compare the linear (M_0 model) and the piecewise (M_1 model) linear models, taking inspiration from the Bayes factor defined in the Bayesian paradigm (Kass and Raftery, 1995), we compute the logarithm of the BIC ratio (B_r) as :

$$B_r = \frac{BIC_{M_0} - BIC_{M_1}}{2} \tag{2.7}$$

If the logarithm of B_r equals zero, the two models fit the data with the same quality. Negative values indicate better fits and positive values refer to worse fits than the linear regression.

B_r category (log scale)	Interpretation
<0	Anecdotal evidence for M_0
0 to 4.5	Anecdotal evidence for M_1
4.5 to 9	Moderate evidence for M_1
9 to 13.5	Strong evidence for M_1
>13.5	Decisive evidence for M_1

Table 2.2 – Interpretation of the chosen categories of B_r. M_0 refers to the linear model and M_1 to the piecewise linear model.

2.4 Results

2.4.1 Ability of gridded precipitation products to reproduce the variability of the relationship between annual/seasonal precipitations and elevation

The altitude dependencies of the gridded precipitation products are compared to those from rain gauge data in the regions presented in Fig. 2.1**(a)**. Figure 2.3**(a)** displays the median annual precipitation by 300 m altitudinal bands, for the seven gridded precipitation products, extracted at the location of the stations. In all regions of interest, annual precipitation observed at stations (*i.e.* the black curves showing the annual precipitations obtained with the rain gauges and NPT) increases as a function of the altitude. In the mid-range mountains such as the Northern Massif Central, the Southern Massif Central, and the foothills of the Alps, the annual precipitation always increases from one altitudinal band to another. The maximum increase of observed annual precipitation occurs in the foothills of the Alps with a gain of 500 mm in 1500 m altitude. In more complex topographical regions such as the Northern Alps, the Southern Alps, and the Pyrénées, the enhancement of annual precipitation with the altitude is unclear, and only visible on a reduced range of altitude. For instance, the observed annual precipitation does not seem to increase in the Pyrénées below 1800 m. In mountain regions, even the mid-range ones like the foothills of the Alps, ERA5-Land, PDIR, and SERVAL often lead to more moderate increases in annual precipitation with the altitude compared to the stations. In the Cévennes/Causses region, annual precipitation from ERA5-Land slowly changes with altitude. In the Northern Massif Central, all gridded precipitation products, except for PDIR, are in agreement with the observed enhancement of precipitation with altitude. In the foothills of the Alps, the underestimation of SERVAL increases through the altitudinal bands, reaching 1000 mm at 1500 m altitude. AROME overestimates annual precipitation in all regions of interest, and the bias generally increases at high altitudes. For example, at 2400–2700 m in the Southern Alps, AROME captures more than 1500 mm of median annual precipitation, while the stations record only 1000 mm. Nevertheless, median annual precipitation from AROME and observations are strongly correlated. Without data assimilation, AROME reproduces abrupt rises in precipitation at high altitudes. In the Northern Alps, AROME and the observed precipitations increase by the same amount of 500 mm from 1800–2100 m to 2100–2400 m. In some regions of interest such as the Pyrénées and the Northern Massif Central, the bias of AROME is constant through the altitudinal bands. It reflects that, in those regions, the altitude impacts AROME and the station precipitations in the same way. The reanalysis CERRA-Land, based on rain gauges, is biased in some regions (Cévennes/Causses, Northern Alps, Pyrénées, Southern Massif Central). The bias is not constant and can be positive at low altitudes and negative at high altitudes such as in the Pyrénées region. The bias of CERRA-Land is relatively small in comparison to the bias of ERA5-Land, PDIR, SERVAL, and AROME as it reaches a maximum of 375 mm in the Northern Alps at 1800–2100 m. The reanalysis COMEPHORE and the interpolator SPAZM accurately reproduce precipitation data from stations in all regions of interest, as both products assimilate rain gauge values. However, COMEPHORE underestimates precipitation above 2100 m, which is only visible in high-altitude regions, such as the Northern Alps and the Southern Alps. In the Northern Alps, the median annual precipitation from COMEPHORE is smaller than 1000 mm at 2400–2700 m, compared to more than 1300 mm measured with stations for the same altitudinal band. Figure 2.3**(a)** shows that COMEPHORE, CERRA-Land, and SPAZM reproduce well the relationship between altitude and observed annual precipitation in the regions of interest. AROME, without rain gauge assimilation, exhibits the same precipitation/altitude trends that the stations, although it usually overestimates annual precipitation, especially at high altitudes. It can be added that the relationship between annual precipitation and altitude

derived from the location of stations is dependent on the spatial sampling, which explains the variability of the curves in Fig.2.3**(a)**. Nevertheless, the poor relationships between the annual precipitation obtained with ERA5-Land, PDIR, and SERVAL and the altitude disqualify them for further analysis of the PRLs.

Figure 2.3**(b)** shows the median precipitations by altitudinal bands on a seasonal basis, at station locations (solid curves), and by considering all the pixels belonging to a region (dotted curves). The study of seasonal precipitations is extended above the altitude of the stations. The results are only displayed for the four highest altitude regions (Foothills of the Alps, Northern Alps, Pyrénées, Southern Alps). Only precipitation from AROME, CERRA-Land, COMEPHORE, and SPAZM are investigated seasonally because of the highly biased nature of annual precipitation from ERA5-Land, PDIR, and SERVAL. Figure S2 in the Supplement presents the results for all seasons, products, and regions. At station locations (solid curves), the seasonal precipitations from AROME, CERRA-Land, COMEPHORE, and SPAZM are close to the observed ones. Only AROME overestimates seasonal precipitations, but the bias is not altitude-related. The relationship between seasonal precipitations and altitude is different at station locations (solid curves) and with all pixels (dotted curves) in the Northern and Southern Alps. The dotted curves are more regular and above the solid ones, illustrating that the stations are not representative of the altitudinal bands of the regions. When all pixels belonging to a region (dotted curves) are taken into account, differences grow among seasonal precipitations from AROME, CERRA-Land, COMEPHORE, and SPAZM. COMEPHORE experiences both lower winter and summer precipitation than AROME, CERRA-Land, and SPAZM. COMEPHORE precipitation remains unchanged or even decreases with altitude. As a result, the differences in precipitation amounts between COMEPHORE and the other products become larger in high altitudes. For example, in the Northern Alps, the winter precipitations from AROME, CERRA-Land, and SPAZM increase by 250 mm between 3000–3300 m to 3300–3600 m whereas COMEPHORE declines between these two altitudinal bands, leading to a 350 mm gap. CERRA-Land and SPAZM show common seasonal precipitation patterns with altitude in the Northern Alps and the Pyrénées. In the Northern Alps, CERRA-Land and SPAZM agree on slow changes in seasonal precipitations below 3000 m and more rapid increases above this threshold. In the Southern Alps, the increase of seasonal precipitations with altitude is larger with SPAZM than CERRA-Land. AROME produces a larger amount of seasonal precipitations in comparison to COMEPHORE, CERRA-Land, and SPAZM, especially in winter. In summer, AROME shows a suspicious precipitation amount of 1500 mm at high altitudes in the Northern Alps. In winter, the difference between AROME and the other gridded products is larger at high altitudes. For instance, in the foothills of the Alps, AROME matches SPAZM producing 250 mm at 0–300 m but is 300 mm higher at 2400–2700 m.

To investigate the ability of AROME, CERRA-Land, COMEPHORE, and SPAZM to reproduce the observed precipitation change with altitude at a fine spatial scale, Fig. 2.4 shows scatter plots of observed versus gridded precipitation relative difference (PRD). PRDs are defined for two neighboring (closest) stations as the difference in precipitation relative to the difference in altitude, see Sect. 2.3.2. PRDs are computed on all pairs of closest stations within the region of interest. Fig. S3 in the Supplement presents the PRDs scatter plots for all seasons. The same results observed in Fig. 2.3**(b)** appear. PRDs from COMEPHORE and SPAZM are unbiased, the points being close to the 1 :1 lines. The variance of PRD errors is higher with AROME and CERRA-Land. PRDs from CERRA-Land seem unbiased on average, and those from AROME are a little too high in winter. Fig. 2.4 also reveals more difficulties for AROME, CERRA-Land, COMEPHORE, and SPAZM to reproduce observed summer than winter PRDs. PRDs with AROME are unbiased on average. This is possible to use AROME to model the altitude effect on seasonal precipitations at a fine spatial scale.

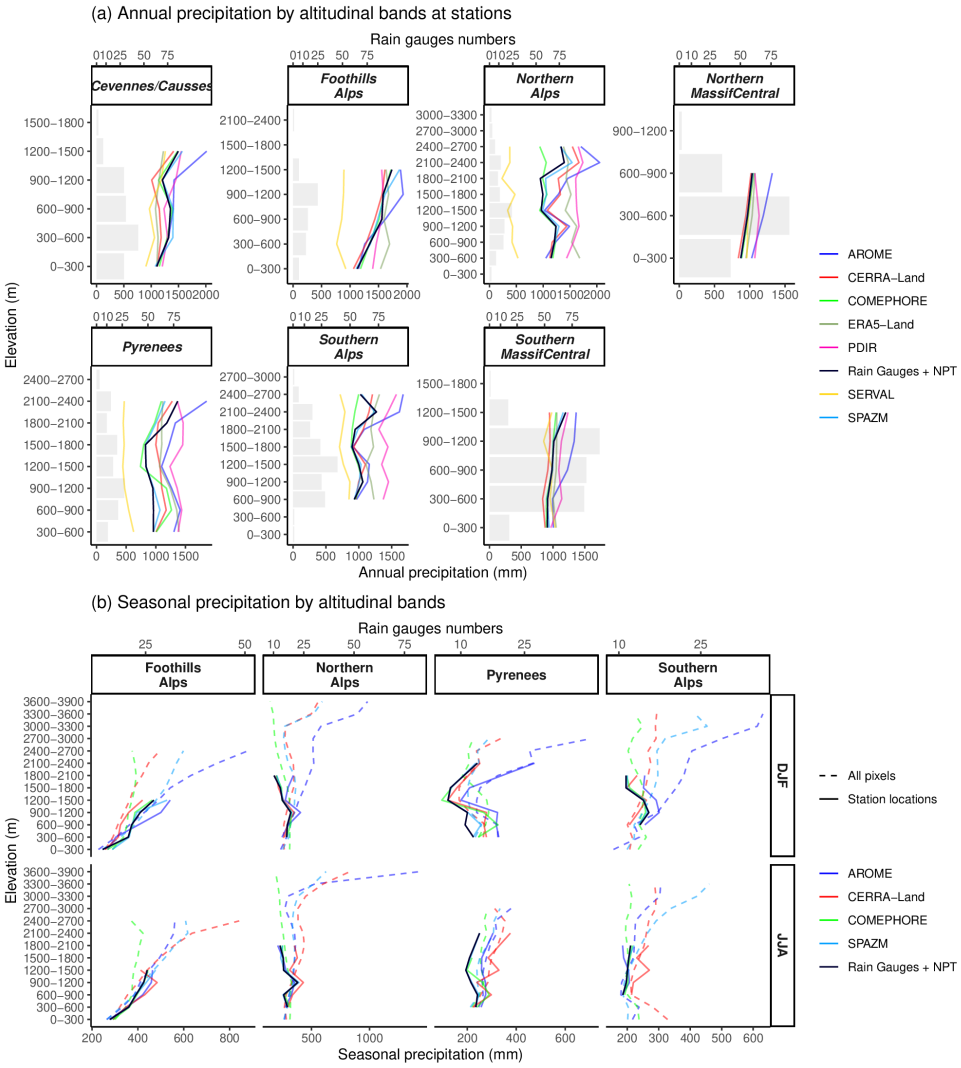

Figure 2.3 – Comparison between the altitude dependence of precipitation from AROME, CERRA-Land, COMEPHORE, ERA5-Land, PDIR, SERVAL, SPAZM, stations (rain gauges and NPT) in seven regions. The lines show the median precipitation amount in each altitude zone and the bars denote the number of rain gauges in each area. Comparisons are done at **(a)** the station locations at the annual scale and **(b)** both station locations and on all pixels from the gridded products at the seasonal scale. At the seasonal scale, only AROME, CERRA-Land, COMEPHORE, and SPAZM are analyzed for the sake of visualization. The season *DJF* refers to the winter (December, January, February) and the season *JJA* corresponds to the summer (June, July, August).

Figure 2.5 illustrates the relationship between seasonal precipitations and elevation through two transects in the Cévennes and the Northern Alps. A transect indicates a virtual line crossing the topography. Figure S4 in the Supplements shows the transects for all seasons. Seasonal precipitations from SPAZM are, by construction, fully correlated to the altitude, reacting to slight variations of terrain. COMEPHORE and CERRA-Land are both less correlated to the altitude than SPAZM. CERRA-Land gives the same winter precipitation as SPAZM but different summer precipitation patterns. COMEPHORE produces similar amounts of precipitation as SPAZM in the Cévennes transect but lower ones in the Northern Alps transect. AROME has a strong relationship with the altitude. It is the gridded product with usually the highest seasonal amounts in high altitudes. For example, winter precipita-

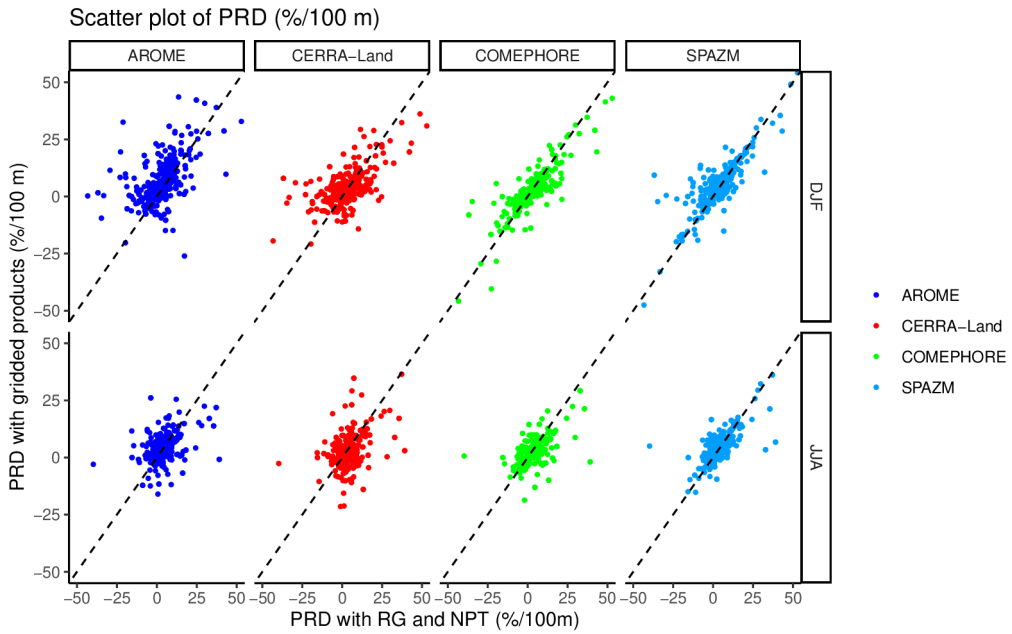

Figure 2.4 – Comparison of precipitation relative difference (%/100 m) computed with stations and gridded rainfall products. PRDs are derived for all couples of neighboring stations. Scatter plot between observed and gridded PRD at station locations. The dotted lines indicate the 1 :1 lines.

tions reach 600 mm in the Cévennes with AROME, almost 500 mm with SPAZM, and 400 mm with COMEPHORE and CERRA-Land.

COMEPHORE and CERRA-Land sometimes exhibit a negative correlation to the altitude. The behavior of COMEPHORE is surprising in the Northern Alps between 8 and 15 km after the beginning of the transect. COMEPHORE summer precipitation amount is the lowest for the highest pixel on the transect. CERRA-Land is different from the other gridded products in summer on the Cévennes with a negative association with the altitude for the first 80 km of the transect. SPAZM exhibits a higher correlation than AROME to the local topography. As a result, SPAZM precipitation maximums coincide with the summits while those of AROME are reached before the summits in the Northern Alps, for example. Another major difference between AROME and SPAZM is the seasonality of precipitation. In the first 20 km of the Northern Alps transect, while SPAZM shows similar seasonal precipitation patterns, AROME seasonality is more marked with two peaks in precipitation in winter at 5 and 15 km and only one in summer. Moreover, in the Northern Alps transect, SPAZM produces higher summer precipitation than winter precipitation (400 mm against 300 mm), unlike AROME.

Overall, AROME and SPAZM demonstrate the ability to replicate the altitude-dependent variations of annual and seasonal precipitations in the regions of interest. In comparison to commonly used gridded precipitation products such as satellite and radar data, AROME and SPAZM exhibit stronger correlations with observed precipitation. The evolution of AROME seasonal precipitations with altitude is consistent with that of stations, despite suspicious summer precipitation in very high altitudes in the Northern Alps and a too rapid rise of winter precipitation. In regions with sparse networks of stations, products based on stations such as SPAZM may be unable to capture the impact of local topography on precipitation. Since our objective is to investigate the spatial variability of PLR at the catchment scale, SPAZM will be inadequate for this purpose. AROME should be preferred to SPAZM in ungauged areas. PLRs are therefore computed with AROME simulations from 1982 to 2018. The long temporal period of more than 30 years allows for the investigation of PLR at the

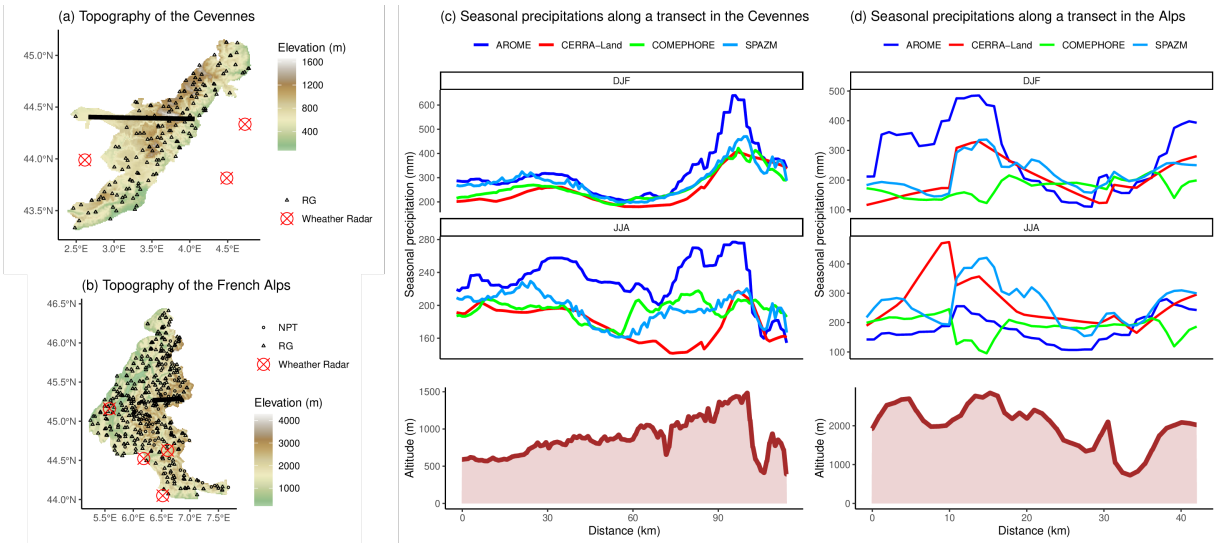

Figure 2.5 – Transects in the Cévennes **(a)** and the Northern Alps **(b)**. Winter *DJF* and summer *JJA* precipitations extracted across the transects are colored according to gridded products **(c), (d)**. Elevation is represented in brown as an altitude profile.

climatological scale.

2.4.2 Spatial and seasonal variability of Precipitation Lapse Rates

Initially, seasonal PLRs are computed at the sub-regional scale on the 23 massifs in the French Alps. Secondly, seasonal PLRs are computed on catchments that form a subdivision of the massifs. Figure 2.6**(a)** displays the R^2 at the sub-regional (massif) scale of the regressions between AROME seasonal precipitations and the altitude. Values of PLRs and R^2 at the sub-regional scale are provided in Table 2.4. In winter, values of R^2 are close to 0.5 in the foothills of the Alps (Chartreuse, Bauges, Aravis, Chablais), in the Northern Alps (Beaufortin, Belledonne, Mont-Blanc), and in the Southern Alps (Queyras, Thabor, Oisans, Devoluy, Champseur, Pelvoux, Ubaye, Haut-Var-Haut-Verdon). Regression quality in the Central Alps (Grandes-Rousses, Maurienne, Vanoise, Haute-Tarentaise) is not high enough to conclude on PLR values. Winter precipitation from AROME is for instance not correlated to the altitude in the Haute-Tarentaise massif (R^2 equals 0.12). In summer, the same spatial pattern is observed with lower values of R^2, indicating that the altitude is better correlated with winter precipitations than summer precipitations in the French Alps.

The fine resolution of AROME provides the possibility to investigate the spatial variability of the relationship between seasonal precipitations and altitude at the catchment scale. Figure 2.6**(c)** shows the R^2 values at the catchment scale. R^2 obtained from regressions are higher at the catchment scale than at the sub-regional scale for both winter and summer seasons. Similarly to the sub-regional scale, R^2s are generally higher in winter than in summer. In winter, regression quality does not show a clear spatial pattern except for lower R^2 in the Eastern Alps (Haute-Tarentaise, Haute-Maurienne, Thabor, Queyras). The R^2s show a large spatial variability. In the foothills of the Alps (Vercors, Chartreuse, Bauges, Aravis), strong R^2 (0.75–1) can be found at the borders of the massifs next to small R^2 (0–0.5) inside the massifs. In summer, the regressions are of poor quality in the Northern and Central Alps. The massifs in the Southern Alps and some in the foothills of the Alps (Chartreuse, Bauges, Chablais) do not show a clear deterioration of R^2 compared to the winter. In some massifs like the Maurienne, in winter, the R^2 are superior to 0.5 at the catchment scale and close to 0 at the sub-regional scale. In the same way, the massifs, where the regression fits are correct at the

sub-regional scale (Thabor, Haute-Maurienne), do not necessarily contain the best fit at the catchment scale. It indicates that the previous regressions (Fig.2.6**(a)**) are likely conducted over excessively broad areas.

Figures 2.6**(b),(d)** respectively display the PLRs of AROME seasonal precipitations at the sub-regional and catchment scales. We remark higher PLRs at the catchment scale (a mean of 5.43 %/100 m in winter and 3.31 %/100 m in summer) than at the sub-regional scale (a mean of 4.73 %/100 m in winter and 2.79 %/100 m in summer). We consider that a R^2 inferior to 0.5 is too small to interpret the slope of the regressions. The spatial variability of seasonal PLRs can therefore not be investigated at the sub-regional scale. We will only describe PLR values at the catchment scale because of better regressions. Figure 2.6**(d)** reveals higher PLRs in winter with very high values (8-15 %/100 m) and high values (5-8 %/100 m) mainly located at the border of the Alps (Devoluy, Thabor, Chablais). Moderate (3-5 %/100 m) PLRs are present in almost all massifs and do not show a clear spatial pattern, such as a North-South separation. Small (0-3 %/100 m) PLRs are mainly found inside the massifs of the foothills of the Alps (Vercors, Chartreuse, Aravis) and in the Far-Southern Alps (Mercantour, Haut-Var-Haut-Verdon). In summer, the majority of PLRs are small (0-3 %/100 m), but some catchments at the border of the Alps (Bauges, Devoluy, Haut-Var-Haut-Verdon) have moderate (3-5 %/100 m) or high PLRs (5-8 %/100 m). Figure 2.6 shows that the quality and slope of the regression can vary widely across the French Alps, with higher values at the borders. A sub-region like the Vercors massif covers around 1,350 km^2 and presents a considerable geographic heterogeneity in PLR values. Figures S5, S6, S7, and S8 in the Supplements illustrate the results of the regressions for all seasons.

Massif Number	**Massif Name**	**DJF PLR (% /100m)**	**DJF PLR (% /100m)**	**JJA R^2**	**JJA R^2**
1	Chablais	5.9	2.7	0.57	0.45
2	Aravis	4.3	2.3	0.45	0.43
3	Mont-Blanc	4.1	4.3	0.66	0.45
4	Bauges	4	3.6	0.5	0.52
5	Beaufortin	4.1	1.9	0.45	0.21
6	Haute-Tarentaise	2.2	0	0.11	0
7	Chartreuse	5.4	3.9	0.57	0.58
8	Belledonne	6.6	4.1	0.8	0.66
9	Maurienne	2.1	0.3	0.11	0
10	Vanoise	3.5	0.6	0.31	0.01
11	Haute-Maurienne	5.2	3.5	0.51	0.39
12	Grandes-Rousses	3.6	1.3	0.28	0.09
13	Thabor	9.1	5.2	0.52	0.34
14	Vercors	4.5	1.7	0.31	0.14
15	Oisans	4	1.4	0.55	0.21
16	Pelvoux	6.3	4.3	0.49	0.52
17	Queyras	5.5	4.2	0.51	0.49
18	Devoluy	6.8	3.5	0.56	0.3
19	Champsaur	4.7	3	0.67	0.58
20	Parpaillon	2.8	3.2	0.17	0.5
21	Ubaye	4.3	2.2	0.48	0.46
22	Haut-Var-Haut-Verdon	3.2	2.3	0.49	0.36
23	Mercantour	2.6	2.9	0.28	0.33

Table 2.3 – Values of precipitation lapse rates (precipitation change per 100 m altitude difference divided by area-averaged precipitation) and R^2 at the sub-regional scale for the 23 French massifs for both winter *DJF* and summer *JJA*. The Massif Number is indicated in Fig. 2.6.

Figure 2.7 shows the winter and summer PLRs at the catchment scale in the study domain. Results for the other seasons are available in Fig. S9 and S10 in the Supplements. The catchments located in the Morvan, the Massif Central, the Jura, the Eastern Pyrénées, and

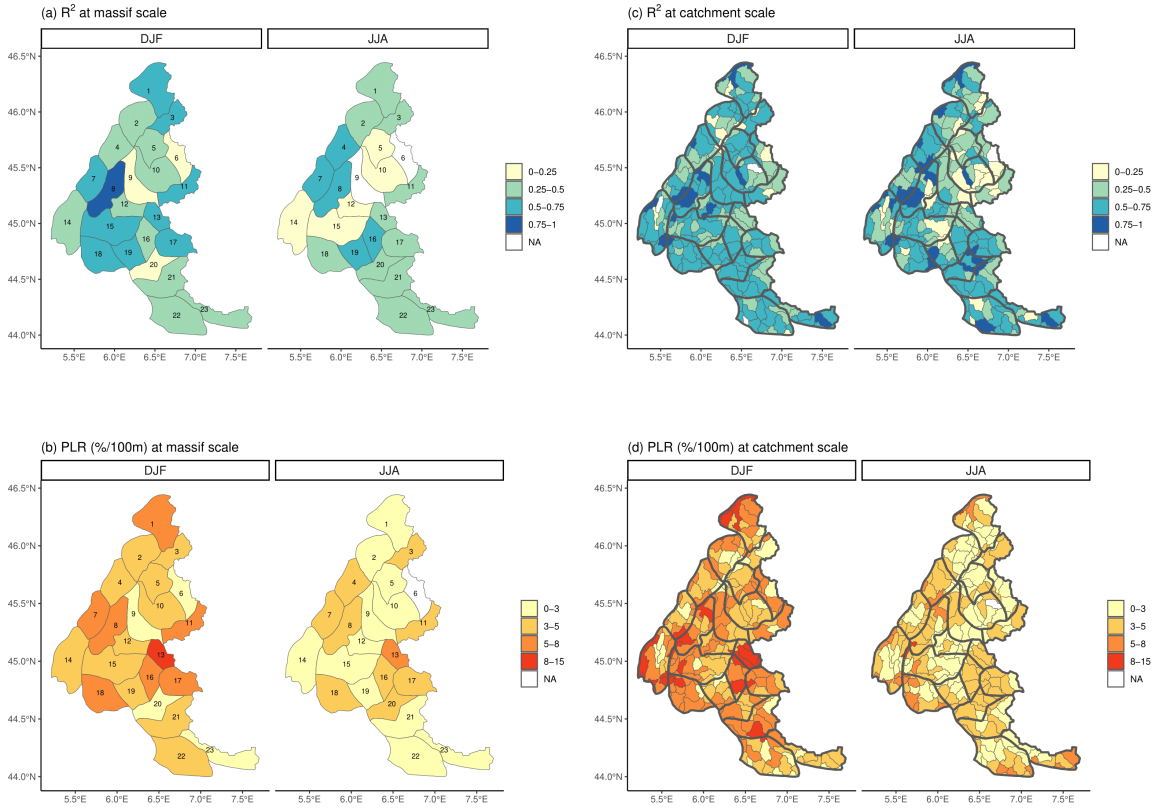

FIGURE 2.6 – Spatial distribution of R^2 **(a), (c)** and precipitation lapse rates (precipitation change per 100 m altitude difference divided by area-average precipitation) **(b), (d)** extracted from the precipitation-altitude regressions for all grids within each area. Categorical results are displayed in the French Alps at regional and catchment scales for both winter *DJF* and summer *JJA* precipitations. The area indicated as "NA" and filled in white represents regions with insufficient altitudinal variability to compute precipitation gradient. The indexes of the massifs are also printed and refer to Table 2.3.

the catchments close to the Mediterranean with enough altitude variation (standard deviation of the altitude higher than 50 m) have the strongest PLRs. These values are higher than those of the Alps, as they can reach 32 %/100 m. Values between 8 and 15 %/100 m are also considerably more frequent than in the Alps. In the study domain, 40 % of the catchments with $R^2 > 0.5$ have winter PLR greater than 8 %/100 m. This percentage drops to 15 % if we only consider the Alps. The slopes of the regression have higher variability in the Alps and the Pyrénées. PLRs are seasonally varying, with generally the highest values in winter. In winter, the Massif Central hosts the strongest PLRs. In summer, the Mediterranean area, ranging from the Eastern Pyrénées to the Mediterranean Alps, has the highest PLRs.

To summarise, PLRs are generally higher in winter than in summer. PLRs are sensitive to the spatial scale, with higher values at the catchment scale than the sub-regional (massif) scale. Spatial patterns of significant PLRs vary according to the season in France. In winter, the higher PLRs reach 32 %/100 m and are mainly located in the Massif Central. In summer, PLRs are lower and reach larger values on the Mediterranean coast. PLRs vary notably in space, even within a single mountain range such as the French Alps.

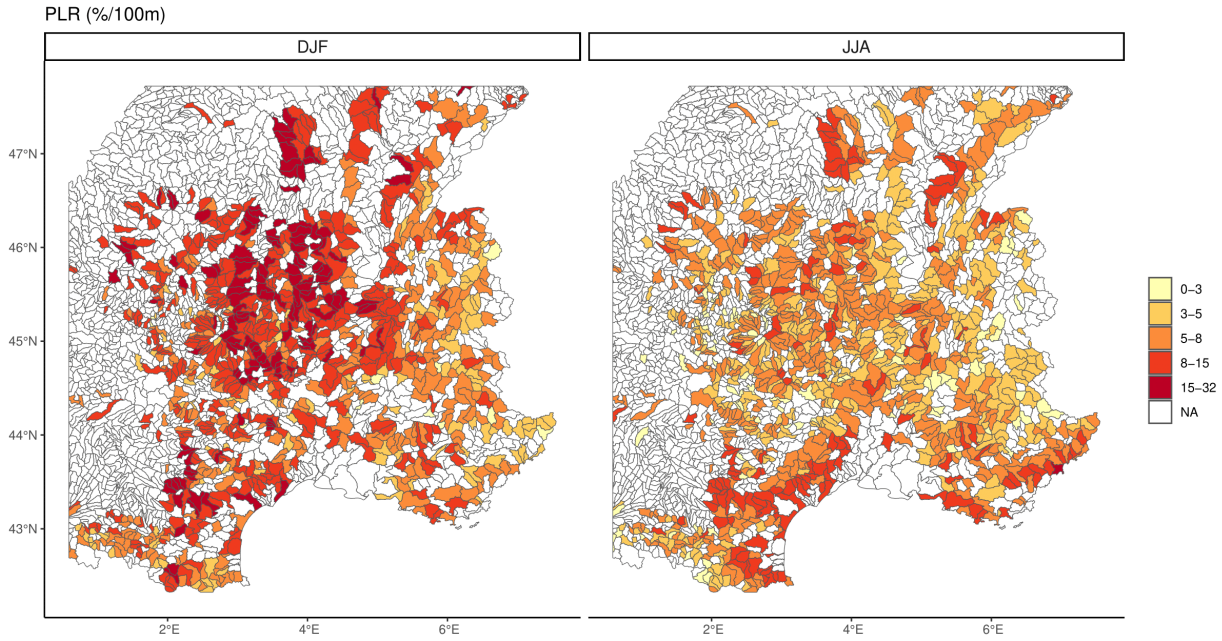

Figure 2.7 – Spatial distribution of winter *DJF* and summer *JJA* precipitation lapse rates (precipitation change per 100 m altitude difference divided by area-averaged precipitation) extracted from the precipitation-altitude regressions for all grids within each area. Categorical results are displayed in the study domain at the catchment scale. The area indicated as "NA" and filled in white represents catchments with insufficient altitudinal variability (standard deviation of the altitude lower than 50 m) or R^2 inferior to 0.5.

2.4.3 Linearity of the relationship between annual precipitation and altitude

To assess the linearity of the regressions performed in Fig. 2.7, piecewise linear regressions were compared to linear regressions through BIC ratio (see subsection 2.3.3). Figure 2.8**(a)** illustrates the BIC ratio categories (Table 2.2) with some examples of scatter plots and corresponding regressions. Colors refer to categories of the logarithm of B_r. Based on the scatter plots, we consider the relationship between annual precipitation and altitude not linear when there is strong or decisive evidence for M_1 (red color). Figure 2.8**(b)** shows the spatial distribution of the logarithm of the B_r values. 10 % of the catchments show decisive evidence for M_1. It appears mainly in the Massif Central, the Jura, and the Southern Alps. In the other regions (Northern Alps, Pyrénées), it is sufficient to use linear regression to derive PLR. Figure 2.8**(c)** shows the distribution in surface areas of the catchments among the five categories of B_r. Strong B_r are mainly found for large catchments, revealing the spatial scale dependence of PLR discussed in subsection 2.5.3. Too much spatial heterogeneity is still present in some catchments (last scatter plot in Fig. 2.8**(a)**), suggesting an even finer spatial division, taking into account the aspect and the slope of the terrain faces. Large catchments can have slopes with different orientations for instance. Figure S12 in the Supplements provides the same diagnostic of linearity for AROME seasonal precipitations.

In 90 % of the catchments, the regression between seasonal precipitation and altitude can be considered linear. The remaining 10 % often corresponds to larger catchments, which could motivate the estimation of the PLRs on smaller areas in these cases.

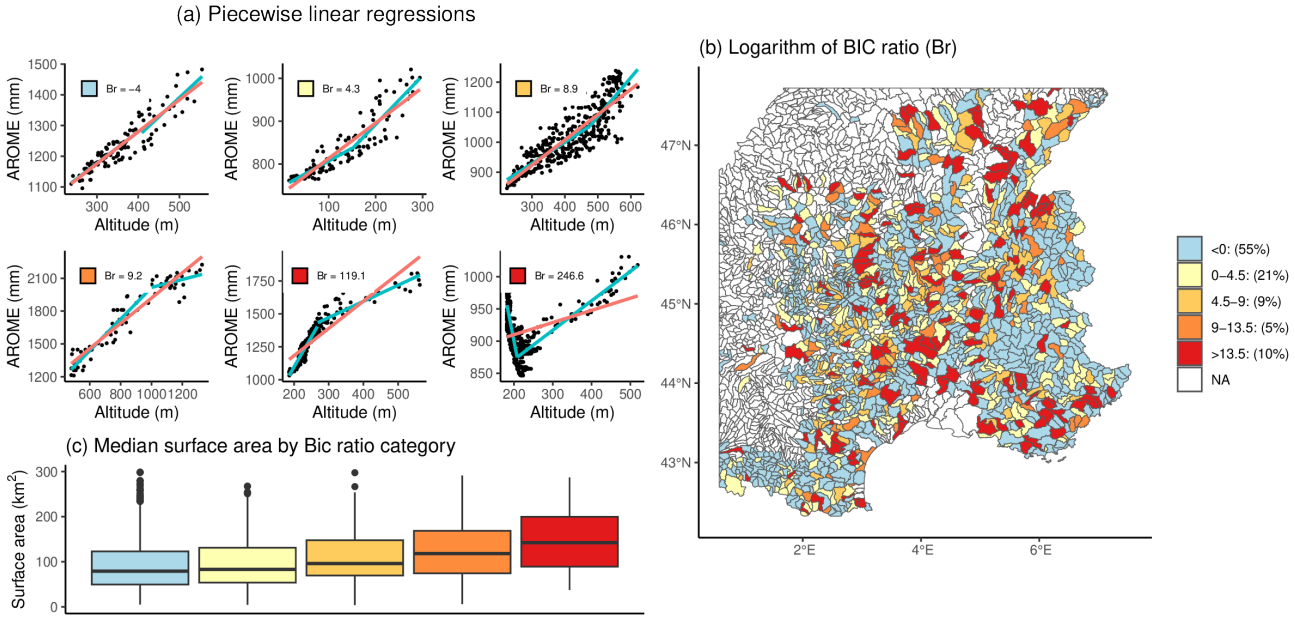

Figure 2.8 – **(a)** Scatter plots of AROME annual precipitation (mm) as a function of the altitude for some catchments taken as illustrative examples of the different categories of BIC ratio. Linear (red lines) and piecewise linear (blue curves) regressions are superimposed. **(b)** Spatial representation of the logarithm of the BIC ratios between linear and piecewise linear regression (annual precipitation ∼ altitude) models. The numbers expressed in % correspond to the percentage of catchments within the classes of the BIC ratio. **(c)** Distribution of the surface area of the catchments according to the categories of BIC ratio.

2.5 Discussion

2.5.1 Ability of gridded precipitation products to capture the relationship between annual/seasonal precipitations and altitude

This article reviews the potential of seven gridded precipitation products for precipitation gradient estimation in a complex topographic region. ERA5-Land, PDIR, and SERVAL underestimate annual precipitation gradients even for mid-range mountains. The limitations of these three gridded precipitation products are even more apparent in high-altitude regions such as the Northern Alps and the Southern Alps. The assimilation of satellite data and the non-use of rain gauge values in ERA5-Land and PDIR is an obstacle to their utilization in a complex topographic region such as France. These findings converge with those of Jiang et al. (2022), where they found that the satellite product IMREG cannot reproduce the precipitation gradient in Tibet. SERVAL does not use altitude as a co-variable to determine precipitation from individual radars. The uniform ratio applied for this product in the hourly correction only represents the station elevation range, not the entire radar coverage. The translation of reflectivity to precipitation amount using the vertical profile of reflectivity is another potential source of error that results in inaccurate negative precipitation gradients in Fig.2.3. In their study of the French Alps at the sub-regional level, Faure et al. (2019) found a significant underestimation of precipitation gradient using PANTHERE, SERVAL's predecessor.

CERRA-Land, COMEPHORE, and SPAZM assimilate ground precipitation measurements from weather stations and are thus correlated with the annual precipitation observed at the stations. COMEPHORE leads to an adequate relationship between annual/seasonal precipitations and altitude in mid-mountain ranges highly instrumented as the Southern Mas-

sif Central. However, in more complex topographical regions with sparse stations such as the Northern Alps, COMEPHORE relies heavily on radar data from high altitudes and is unable to accurately reproduce the increase of precipitation with altitude. COMEPHORE processes fewer high-altitude stations than SPAZM, making it unable to represent precipitation in high-altitude areas correctly. The sharp decrease of summer precipitation with altitude from COMEPHORE in the Northern Alps illustrated in Fig.2.5**(d)** is likely due to the shielding of the radar beams by mountain ranges (Germann et al., 2006). CERRA-Land can replicate the observed seasonal precipitation enhancement with the altitude. However, at the annual scale, CERRA-Land is slightly biased in some regions, and the bias may change of sign according to altitudinal bands such as in the Pyrénées (Fig.2.3**(a)**). SPAZM can reproduce the relationship between annual precipitation at station locations and altitude at the regional scale. This result is not surprising as SPAZM interpolates precipitation observations from the stations, incorporating the effect of the altitude through local linear regressions. However, SPAZM is affected by the density of stations. In regions where the stations are more sparse, as in the Pyrénées, annual precipitations from SPAZM do not match annual precipitations from the stations. This suggests a possible limitation of SPAZM in ungauged mountainous regions. AROME, without rain gauge assimilation, can reproduce the relationship between seasonal precipitations and altitude, despite a positive bias in winter in mountainous regions. We find that AROME produces higher annual/seasonal precipitations than the other gridded products. The difference in seasonal precipitations is limited at low altitudes and rises sharply at high altitudes. Higher precipitation accumulations with RCMs have been documented. In Western Montana, in high-altitude where observations are sparse, Silverman et al. (2013) remarked higher annual precipitation with the Weather Research and Forecasting (WRF) model than with the Parameter-elevation Regressions on Independent Slopes Model (PRISM) (Daly et al., 1994). In India, Li et al. (2017) found that annual precipitations obtained with WRF are twice or triple the amount of the satellite precipitation product Tropical Rainfall Measuring Mission (TRMM). The correlation between AROME and COMEPHORE on the Cévennes transect in summer (Fig.2.5**(c)**) is comforting as the radars operate well in summer in the Cévennes region (Delrieu et al., 2013). Moreover, the seasonality of precipitation is taken into account with AROME (see Fig.2.5**(c)**). AROME simulates precipitation without using rain gauge data and poorly matches the high-elevation gauges, which could be the combined effect of precipitation undercatch (Groisman and Legates, 1994; Sevruk, 1997; Pollock et al., 2018) and some deficiencies in AROME (Monteiro et al., 2022). In Fig. 2.3**(b)**, AROME shows a strong agreement with the rain gauges in summer, even the high-altitude ones. The differences are larger in winter, where precipitations mostly fall as snow. Precipitation undercatch is limited in summer and more important in winter with solid precipitation. This suggests that precipitation undercatch could partly explain the differences between AROME and rain gauges.

To summarize, this study shows that the simulations of the CP-RCM AROME, despite winter precipitation overestimation, offer the opportunity to derive PLRs at a fine spatial scale. The other grid precipitation products obtained from radar, satellite, or rain gauge data show important limitations in a complex topography region. Radar is among others subjected to beam blocking. Satellite resolution is too coarse to represent the altitude effect on precipitation. Rain gauge networks are too sparse and even high-density ones do not account for the spatial and altitudinal variability of seasonal precipitation.

2.5.2 Values and spatial variability of Precipitation Lapse Rates

Table 2.4 synthesizes the main research on PLRs. Like Ménégoz et al. (2020) in Switzerland, we find higher PLRs in winter, likely due to the large-scale circulation of air masses. In winter, the Western wind coming from the Atlantic loaded with moisture is dominant and hits

the primary mountainous regions on its way. The affected catchments correspond to the first orographical barrier and are located in the Massif Central, extending from the Languedoc to the Morvan regions. On those catchments, 50 % of the PLRs are in the range of 5–13 %/100 m. For the same reason, the PLRs are in the range of 5–15 %/100 for the first Western catchments of the Alps. Interestingly, a distinct pattern emerges in the Thabor where some PLRs are in the range of 8–15 %/100 m due to frequent Easterly weather fronts brought by Mediterranean circulation from Italy. In summer, the Mediterranean area is subjected to the dominant Southern flows and hosts the highest PLRs. The Southern air masses absorb the humidity from the Mediterranean Sea. For this reason, we found higher PLRs in the Eastern Pyrénées (8–15 %/100 m) compared to the Central Pyrénées (3–8 %/100 m). Convective processes are more frequent in summer than in winter. Daily precipitation amounts from convective processes are often negatively correlated to the altitude (Schäppi, 2013). That is likely to explain the lower PLRs in summer than in winter. To summarise, we notice high PLRs in areas subjected to the prevailing winds in France, which are Western, Southern, and Eastern winds depending on the season. Like Kotlarski et al. (2012), we find lower PLRs in the Alps than in the rest of France.

In the French Alps, a complex topographical region, we do not find a significant difference in PLR values between the Northern and the Southern Alps for the winter and summer seasons contrary to Sevruk (1997); Durand et al. (2009); Ménégoz et al. (2020). That is probably due to the finer spatial scale used in the study. At a larger spatial scale, large-scale circulation, rather than the local topography, drives seasonal precipitation amounts (Jiang et al., 2022). We find a large spatial variability of PLRs, which can vary inside the same massif from one catchment to another. For instance, winter PLRs range from 3–5 %/100 m to 8–15 %/100 m in Belledonne. Using rain gauges, Ogrin and Kozamernik (2018) highlighted the extreme spatial variability of PLRs in the range of 5–16 %/100 m for the summer season in three nearby alpine valleys of Slovenia. We find the same magnitude in PLR values and variability. PLRs are highly spatially varying in high-altitude and complex topographical regions such as the French Alps and Pyrénées. In the Massif Central, PLRs exhibit less spatial variability.

Study domain	Data	Spatial scale	Period	Findings	Reference
Switzerland	Rain gauges	massifs 4,000 km^2	1951–1980	Northern Alps : 5.4 %/100 m Southern Alps : 0.24 %/100 m	Sevruk (1997)
French Alps	SAFRAN	regions 1,000–10,000 km^2	1958–2002	Northern Alps : 29.4 mm/100 m Central Alps : 19.5 mm/100 m Southern Alps : 17.2 mm/100 m Mediterranean Alps : 17.8 mm/100 m	Durand et al. (2009)
Europe	RCM	country 200,000–1,000,000 km^2	1961–2000	Spain : -3.7 mm/100 m United-Kingdom : 131 mm/100 m France (without the Alps and the Pyrénées) : 32 mm/100 m Alps : 14.6 mm/100 m	Kotlarski et al. (2012)
Slovenia	Rain gauges		2012–2015 (MJJASON)	5–16 %/100 m	Ogrin and Kozamernik (2018)
Swiss and French Alps	RCM	regions 10,000–50,000 km^2	1971–2008	French Northern Alps : 2.6 %/100 m French Southern Alps : 1.6 %/100 m Swiss Alps : 4.3 %/100 m in winter (DJF) 2 %/100 m in summer (JJA)	Ménégoz et al. (2020)
Third pole	WRF	regions (1,000,000 km^2) catchments (10,000 km^2)	1980-2018	regions : 2.90–11.26 %/100 m Large catchments : -10–10 %/100 m Small catchments : -4–10 %/100 m	Jiang et al. (2022)

Table 2.4 – Summary of the studies on precipitation lapse rates (PLRs), namely study domain, data, spatial scale, period, findings, and reference.

In summary, PLRs are probably higher in winter because of the omnipresence of stratiform events that cause structured orographic precipitation in catchments exposed to oceanic weather patterns. In summer, the air masses are coming from the Mediterranean Sea, causing high PLRs in the coastal and hilly Mediterranean areas. In this season, precipitation is mainly caused by the combination of multiple convective events, resulting in unclear PLR spatial patterns.

2.5.3 Dependence of the Precipitation Lapse Rates to the spatial scale

The low R^2 found in Fig.2.6**(a)** is a reminder of the high intra-massif variability of the relationship between seasonal precipitations and altitude in large sub-regions. The sub-regions dissection into more homogeneous areas, such as small catchments with a surface area close to 100 km^2 allows a better description of PLRs. Regressions at the catchment scale have larger PLR and R^2 values than at the sub-regional scale. In winter in Maurienne, all catchments have R^2 greater than 0.5 with PLRs in the range 3–8 %/100 m. The R^2 is close to 0, and the slope is close to 2 %/100 m with a single regression covering all the Maurienne massif. Figure 2.9 shows the scatter plot between AROME annual precipitation and altitude for the pixels within three groups of catchments in the Vercors, a massif covering 1,350 km^2. The colors of pixels relate to distinct geographical locations. Figure S11 in the Supplements provides the scatter plots for seasonal precipitations. Figure 2.9 suggests that the Vercors encompasses several sub-regions with different relationships between annual precipitation and altitude. This relationship is linear for the Southern and Western Vercors catchments. However, the Western and Southern Vercors are not subject to the same meteorological influences. The PLRs are higher in the Western Vercors because of the dominant rainy westerly flow. The relationship is not linear for the catchments located in the Vercors plateaus. The attenuation of orographic precipitation after crossing the first hills of the West of the massif is a possible explanation. Figure 2.9 reveals the coexistence of PLR spatial patterns within a single massif.

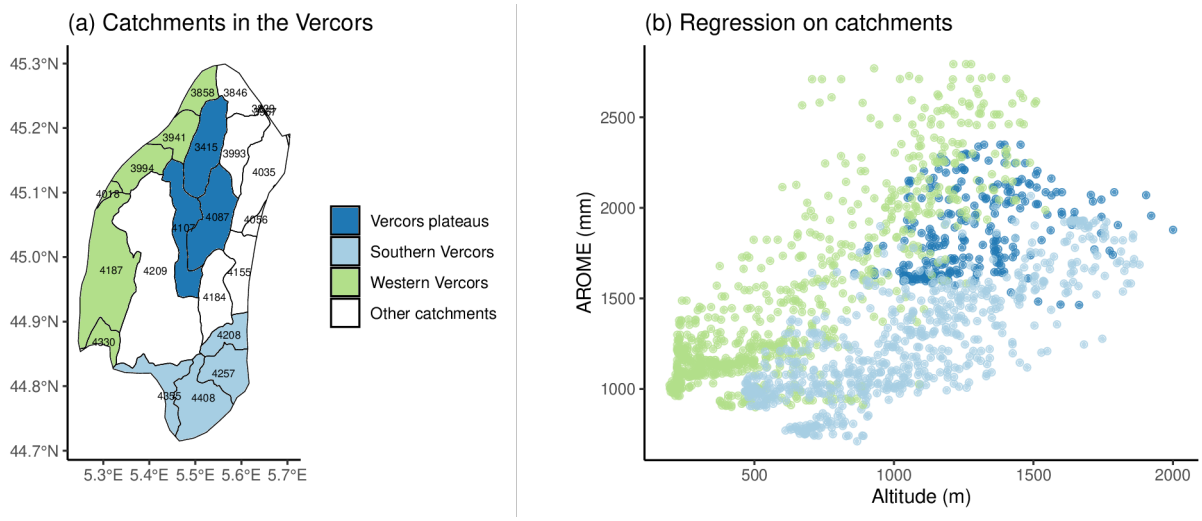

Figure 2.9 – **(a)** Catchments located in the Vercors massif and colored according to their geographic locations. Three groups of catchments are distinguished : the Vercors plateaus, the Western Vercors, and the Southern Vercors. ID numbers are printed for each catchment. **(b)** Scatter plot of AROME annual precipitation and altitude for the pixels in the Vercors (gray dots). The colors of dots correspond to the colors used in panel a).

In the French Alps, a complex topographical region, it is not appropriate to calculate PLRs on too vast sub-regions with surface areas of more than 1,000 km^2. In vast sub-regions, there is a risk of mixing areas with too much spatial heterogeneity and losing information about PLR spatial variability. Investigation of PLR with stations or stations-based precipitation products such as SPAZM should be conducted carefully in sparse station networks. For example, in the Aravis massif covering 1,070 km^2, linear regressions between precipitation and altitude in SPAZM are performed using all stations within the massif to ensure robustness. However, Fig. 2.6**(d)** indicates that the Aravis has high intra-massif variability of winter PLR with lower values in its western part. SPAZM can not capture this variability.

PLRs are thus scale-dependent. The linear regressions give better R^2 and larger PLRs at the catchment scale (100 km^2) than at the sub-regional scale (1,000 km^2). Too broad sub-regions often hide distinct altitude effects on precipitation.

2.5.4 Uncertainty in the study and outlooks

A limitation of our study is the potential undercatch of precipitation by the high-altitude stations. The underestimation can be as high as 50 % in winter during meteorological events with strong winds and a large proportion of snowfall. A 25 % underestimation of mountain annual precipitation is possible (Sevruk, 1997). In low altitudes, the underestimation is less severe. As a result, the comparison of PLRs in Fig.2.3**(a)** can lead to wrong conclusions on the bias of the gridded precipitation products. Despite the measuring uncertainty, we decided to include NPT in our study to account for high ungauged altitude regions. The available period from NPT differs from those of rain gauges and precipitation products. Additional data sources can enhance the spatial and altitudinal representation of PLR. High-altitude measurements of snow water equivalent (SWE) levels can constrain the regressions between winter precipitation and altitude and make PLRs more robust. However, the transition from daily SWE to seasonal precipitations is highly temperature and snowmelt-dependent. For high altitude measurements, it is possible to make the strong assumption that only solid precipitation has occurred and that snowmelt has been minimal, as stated in Avanzi et al. (2021). Due to the high level of uncertainty of the measure, we opt not to include those data.

At high altitudes, winter precipitation from AROME is significantly higher than that of the other precipitation products, including SPAZM. At 2700–3000 m in the Pyrénées, AROME simulates an extra 400 mm of precipitation compared to COMEPHORE, CERRA-Land, and SPAZM. SPAZM may underestimate high-altitude precipitations due to precipitation undercatch. It is also likely that AROME overestimates seasonal precipitations. Indeed, Monteiro et al. (2022) found excessive snow accumulation with AROME in the French Alps above 1800 m. The authors advanced assumptions about spurious snow accumulation, such as the AROME cold temperature bias and the weakness of the AROME snowpack schemes. The winter PLR values given in Fig.2.7**(b)** for high-altitude catchments should be considered with precaution. In addition to AROME, various CP-RCMs listed in (Ban et al., 2021, Table1) have been used to simulate precipitation at a fine resolution in France. PLRs derived as the slope of linear regressions are necessarily uncertain because of the regression uncertainty. A perspective of the study could be to include prediction intervals, *i.e.* a range of values containing the "true" value with a probability of 0.95, for example.

2.6 Conclusion

We address the question of the spatial variability of seasonal precipitation lapse rates in France, a country with varied and complex topography. A dense rain gauge network enriched with snow rain gauge totalizators characterizes the relationship between annual/seasonal precipitations and altitude in large regions. The ability to reproduce this link obtained from ground measurements is analyzed using seven different kinds of gridded precipitation products : ERA5-Land, the PDIR satellite product, the raw radar product SERVAL, a 37-year simulation from the CP-RCM AROME, two reanalysis named CERRA-Land and COMEPHORE, and the precipitation interpolator SPAZM. Precipitation products commonly used in hydrology are limited in high-altitude regions with complex topography, such as the French Alps. Radar products perform well in hilly terrain but underestimate annual precipitation in high altitudes, resulting in a negative association between annual precipitation and altitude. Satellite products are not subject to the same estimation errors as radar products. However,

the coarse resolutions do not accurately represent the annual precipitation altitude dependence in regions with topography heterogeneity. The performance of station-based products is dependent on the density of the weather station network. In ungauged mountainous areas, precipitation estimation from those kinds of products requires some degree of interpolation, whereas AROME uses physical laws. AROME does not incorporate rain gauge data and is therefore not subjected to bias caused by the under-sampling of particular high-altitude spatial areas. The simulations from the CP-RCM AROME, despite an overall overestimation of high-altitude precipitations, offer an opportunity to assess the altitude dependence of seasonal precipitations at the catchment scale. We employ the CP-RCM AROME to derive seasonal PLRs on 23 French Alps massifs and 2,748 catchments. The spatial-scale dependence of PLRs is investigated in the French Alps by comparing seasonal PLR values at the sub-regional (1,000 km^2) and the catchment (100 km^2) scales. PLRs are derived using linear regression between seasonal precipitations and altitude. PLRs are spatial scale-dependent as they tend to be higher and better represented when computed at the catchment scale. The local topography influence on seasonal precipitations is major at a small spatial scale but dominated by the large-scale atmospheric circulation influence at the larger sub-regional spatial scale. PLRs are higher in winter. Winter PLRs are in the majority positive. 95 % of them are in the range 0.55–13.10 %/100 m. The higher values are found in the Westerly and Mediterranean dominant flow-exposed regions, reaching up to 32 %/100 m. In high-altitude regions such as the French Alps and the Pyrénées, we notice sheltering effects with PLRs close to 0 %/100 m for some catchments enclosed by mountains. It is generally the first reliefs encountered by air masses that host the stronger PLRs. This article emphasizes the importance of considering the topography on a fine spatial scale to estimate PLRs in ungauged mountainous regions. CP-RCM models offer an opportunity to compute the enhancement of seasonal precipitations with the altitude.

3

Interpolation spatiale des précipitations saisonnières à l'aide de données pluviométriques et de simulations de modèles climatiques régionaux à convection résolue dans une région à la topographie complexe

Abstract In mountainous areas, accurately estimating the long-term climatology of seasonal precipitations is challenging due to the lack of high-altitude rain gauges and the complexity of the topography. This study addresses these challenges by interpolating seasonal precipitation data from 3,189 rain gauges across France over the 1982–2018 period, using geographical coordinates, and altitude. In this study, an additional predictor is provided from simulations of a Convection-Permitting Regional Climate Model (CP-RCM). The simulations are averaged to obtain seasonal precipitation climatology, which helps capture the relationship between topogrfaphy and long-term seasonal precipitation. Geostatistical and machine learning models are evaluated within a cross-validation framework to determine the most appropriate approach to generate seasonal precipitation reference fields. Results indicate that the best model uses a machine learning approach to interpolate the ratio between long-term seasonal precipitation from observations and CP-RCM simulations. This method successfully reproduces both the mean and variance of observed data, and slightly outperforms the best geostatistical model. Moreover, incorporating the CP-RCM outputs as an explanatory variable significantly improves interpolation accuracy and altitude extrapolation, especially when the rain gauge density is low. These results imply that the commonly used altitude-precipitation relationship may be insufficient to derive seasonal precipitation fields. The CP-RCM simulations, increasingly available worldwide, present an opportunity for improving precipitation interpolation, especially in sparse and complex topographical regions.

3.1 Introduction

Understanding seasonal precipitation patterns is crucial for various hydrological and environmental applications, such as modeling vegetation cover, studying glaciology, managing watersheds, assessing natural hazards, or evaluating the impact of climate change (e.g. Oerlemans and Reichert, 2000; Viviroli et al., 2007; Holzkämper et al., 2012; Wagnon et al., 2013). In hydro-meteorology, winter precipitation contributes to freshwater supply in high-altitude areas during summer. This information is essential for sectors like agriculture, energy production, industrial activities, and tourism (e.g. Pimentel et al., 1997; Gössling et al., 2012). Certain applications, such as hydrology modeling, climate model evaluation (Fantini et al., 2018), and interpolation of daily precipitation (Masson and Frei, 2014) can require seasonal precipitation at regular grid points, necessitating estimation at unobserved locations. Rain gauges provide spatially irregular point measurements and thus cannot capture the high spatial variability of precipitation (e.g. Hofstra et al., 2010). Going from irregular observed point measurements to a gridded dataset with many unobserved locations requires some degree of interpolation. Spatial interpolation aims at predicting values at unsampled locations, with the measurements observed from elsewhere, often with the help of explanatory variables.

Traditionally, spatial interpolation has been carried out using geostatistics models like kriging. Kriging relies on the spatial autocorrelation of the observations, meaning that neighborhood observations are more likely to be similar than distant observations. Kriging has various forms depending on the use or not of explanatory variables. Simple Kriging, Ordinary Kriging, Co-Kriging, and Kriging with External Drift are the most commonly used methods. Kriging with External Drift has produced satisfying results in numerous precipitation interpolation studies (Tobin et al., 2011; Masson and Frei, 2014; Pellicone et al., 2018). However, kriging makes strong assumptions about the normality and stationarity of observations, as well as the linear relationship between response and explanatory variables. In practice, environmental observations, including precipitation, are often found spatially non-stationary, having geographically varying relations with topographical factors. As an alternative to kriging, local interpolation methods, such as Geographically Weighted Regression (Bostan et al., 2012; Fan et al., 2021), relax the stationary assumption by considering only neighborhood

observations in the interpolation process through linear regressions. More recently, Machine Learning methods have emerged as effective tools in spatial interpolation. Random Forest has equivalent or better performances than traditional geostatistics methods in many statistical methods comparison studies (Møller et al., 2020; Sekulić et al., 2020; Nguyen et al., 2023). Machine Learning methods offer a way to handle the non-linearity between observed and explanatory variables.

In complex mountainous regions, spatial autocorrelation is often insufficient to predict precipitation at unobserved and high-altitude locations (e.g. Goovaerts, 2000; Lloyd, 2010; Di Piazza et al., 2011; Adhikary et al., 2017). Many covariates can be used to predict seasonal precipitation anywhere in a study area. Altitude is the most common predictor (Bárdossy and Pegram, 2013; Masson and Frei, 2014) as precipitation increases as a function of altitude at aggregated time scales (e.g. Barrows, 1933; Spreen, 1947; Schermerhorn, 1967; Smith, 1979; Dura et al., 2024a). However, high-altitude rain gauges are underrepresented. As a result, the orographic effect computed only with rain gauges is often not spatially variable enough. Instead of altitude, other authors try to learn from the spatial structure of radar precipitation (Haberlandt, 2007; Velasco-Forero et al., 2009; Sideris et al., 2014; Gyasi-Agyei, 2016). However, radar data have strong limitations in mountainous regions such as ground echoes and total beam blocking (Berne and Krajewski, 2013). Alternatively, Regional Climate Models (RCMs) and more recently Convection-Permitting Regional Climate Models (CP-RCMs, Rockel et al., 2008; Brousseau et al., 2016; Keuler et al., 2016; Belušić et al., 2020) can be used to provide fine-resolution (1–4 km^2) climate simulations. CP-RCMs are an extension of RCMs where deep convection is no longer parameterized. The parameterization is a dominant source of precipitation error. CP-RCMs resolve deep convective processes and incorporate a finer representation of the topography. As a result, CP-RCMs express more precisely some precipitation characteristics such as intensity, frequency, and duration (Lucas-Picher et al., 2021) than RCMs.

This paper compares several statistical models, including Ordinary Kriging (OK), Kriging with External Drift (KED), Geographically Weighted Regression (GWR), and Random Forest (RF) for interpolating seasonal precipitations. It discusses the ability of machine-learning approaches to compete with geostatistical or regression models in both spatial interpolation robustness and altitude extrapolation. The statistical models are compared in interpolation by considering a gradual decrease of measurement density, and in altitude extrapolation where few high-altitude rain gauges are available. The paper also intends to find the best predictors among geographical coordinates, altitude, and CP-RCM simulations to interpolate seasonal precipitation. France presents an ideal setting to compare spatial interpolation models because of topography complexity and the availability of a dense network of 3,189 rain gauges.

This paper is organized as follows. Section 2 describes the study domain and the available precipitation datasets. Section 3 presents the statistical methods used for interpolation. Section 4 shows the cross-validation results and the obtained seasonal precipitation maps. Section 5 compares the findings to the existing literature and discusses some perspectives. Finally Section 6 gives the conclusions.

3.2 Domain and data under study

The area under study, represented by Figure 3.1, encompasses a significant portion of France, with a surface area of 300,000 km^2 and elevations ranging from 0 to 4,808 m. The topography of the region is diverse and complex, featuring three distinct mountain ranges : the *French Alps*, the *Pyrénées*, and the *Massif Central*. The *French Alps* is a high-altitude region with a complex topography. The *Massif Central* is a large region with several (continental, oceanic, Mediterranean, mountain) climates, containing extensive low-altitude plateaus and

circular summits. The *Pyrénées* forms a natural boundary between France and Spain. The Atlantic Ocean and the Mediterranean Sea largely influence the climate of this region. Coastal areas are also present along the Mediterranean Sea and the Atlantic Ocean. The remaining part of the study domain contains plains or small hills.

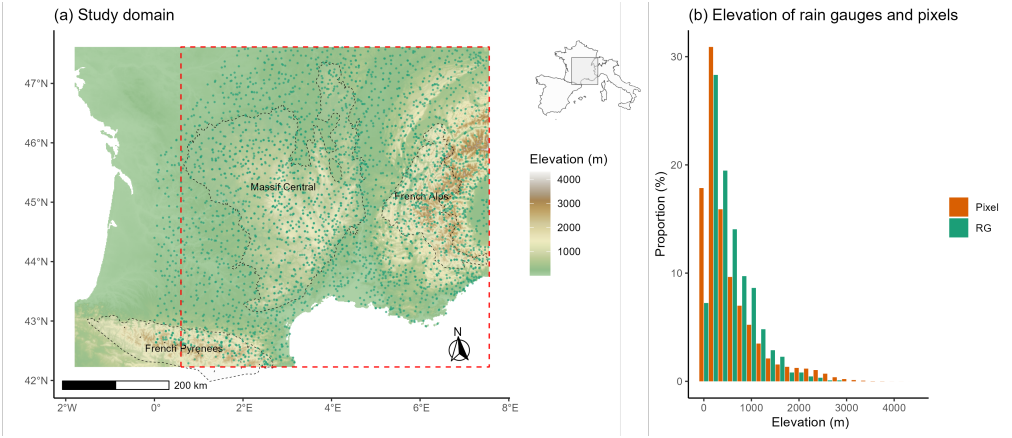

Figure 3.1 – **(a)** Topography of France. The study domain is located in France, bordered by Spain, Italy, and Switzerland, and is indicated by the dotted red rectangle. The names of the main mountainous regions are displayed in black. Green points refer to rain gauges. **(b)** Histogram of the rain gauges and pixels elevations.

Precipitation is a meteorological parameter highly variable in space and time (e.g. Türkeş et al., 2009). The climate of France is generally temperate but highly fluctuates depending on seasons and regions. Western France experiences an oceanic climate with frequent mild precipitation. Eastern France, on the other hand, has a continental climate with infrequent but intense precipitation. Southern France is characterized by a Mediterranean climate with a few rainy days, especially during the hot and dry summer months The mountainous regions, including the *Alps*, the *Pyrénées*, and the *Massif Central*, have their unique climate, and heavy storms can occur in these areas during summer or autumn. To capture the spatio-temporal variability of precipitation, a network of 3,189 daily rain gauges (as shown in Figure 3.1**(a)**) covers the study area. Daily precipitation data from these gauges, collected from 1982 to 2018, are aggregated to obtain mean seasonal precipitation. Table 3.1 reports statistics on seasonal observed precipitation. Summer precipitations are lower, with an average of 211 mm. Winter and autumn precipitation exhibits larger variability. In autumn, observed precipitation can reach 1,000 mm on average. The rain gauge network is denser in complex topographic regions such as the *French Alps* than in the plains, where precipitation varies less across space. However, most of the rain gauges are located below 2,000 m, as illustrated in Figure 3.1**(b)**. The lack of high-altitude instrumentation poses a limitation in predicting seasonal precipitation.

Table 3.1 – Mean, minimum, maximum, and standard deviation in mm of seasonal observed precipitations.

Season	Mean (mm)	Minimum (mm)	Maximum (mm)	Standard deviation (mm)
Winter (DJF)	233	35	695	89
Spring (MAM)	251	92	640	72
Summer (JJA)	211	39	578	76
Autumn (SON)	287	77	1025	96

The AROME hourly precipitation simulations from 1982 to 2018 (Caillaud et al., 2021), aggregated at the seasonal timescale, are used in seasonal precipitation interpolation. AROME simulations are available at a 2.5 km horizontal resolution and come from the CP-RCM *Applications de la Recherche à l'Opérationnel à Méso-Echelle* (AROME), with atmospheric conditions provided every hour by a CNRM-ALADIN RCM (Nabat et al., 2020) simulation, itself driven by the ERA-Interim reanalysis (Dee et al., 2011). AROME simulations are defined for the Alpine domain mentioned in the Flagship Pilot Study of the Coordinated Regional Climate Downscaling Experiment (CORDEX-FPS, Fantini et al., 2018). The Atlantic Pyrénées are not included in the domain under study. AROME simulations have been studied in several studies (Ban et al., 2021; Caillaud et al., 2021; Monteiro et al., 2022) that indicate a better representation of heavy precipitations than in the RCM CNRM-ALADIN model but doubtful snow accumulation in high-altitude regions. A pre-processing step that identifies significant inaccuracies in seasonal precipitation values has been applied. If seasonal precipitation in a pixel differs by more than 500 mm from an adjacent pixel, the pixel is considered problematic. To address the problematic pixels, an iterative approach is implemented in which the aberrant values are substituted with the weighted average of the precipitation amount in the surrounding pixels. Figure 3.2 shows the mean AROME seasonal precipitations in the study domain. Like the rain gauges, AROME simulations generate lower summer precipitation amounts. Seasonal precipitation is more variable in winter and autumn. More precipitation is simulated at high altitudes than in plains for all seasons.

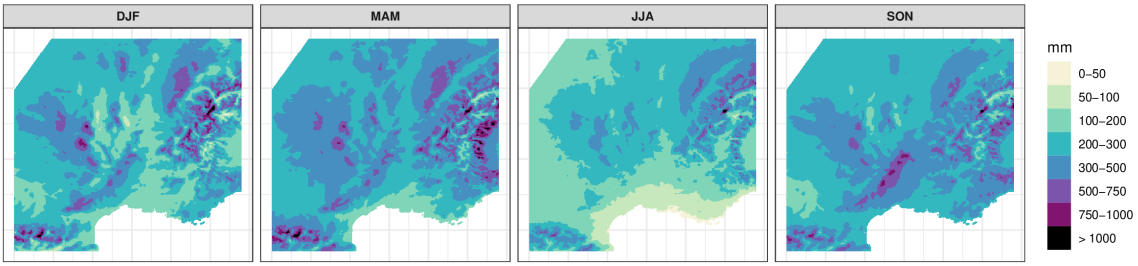

Figure 3.2 – Mean AROME seasonal precipitation over the 1982–2018 period. Winter (*DJF*), spring (*MAM*), summer (*JJA*), and autumn (*SON*) precipitations are displayed.

3.3 Methods

3.3.1 Kriging

Kriging considers the observations of the study variable Z as realizations of a second-order Gaussian process $Z(s) = \mu(s) + \epsilon(s)$ (Diggle et al., 2003). $\mu(s)$ is a deterministic mean and $\epsilon(s)$ is a stochastic residual that vary across space s. Kriging interpolates precipitation based on the spatial autocorrelation of observed precipitation at stations. Spatial autocorrelation means that nearby observations are likely more correlated than distant ones. The predicted value at an unsampled location is a weighted average of the sampled observations. Spatial autocorrelation helps identify the weights of each observation through the variogram. The variogram models the dissimilarity (semi-variance $\gamma(h)$) of the study variable as a function of the lag distance h. The underlying assumptions are second-order stationarity and isotropy, which state that the autocorrelation only depends on the distance and is space-directional invariant. A variogram model is fitted to the empirical variogram $gamma(h)$ estimated from the observations. $\gamma(h)$ is estimated using p bandwidths (class of distance) noted h_k, $k =$

$1, \ldots, p$ that contains N_k pairs of observations :

$$\hat{\gamma}(h_k) = \frac{1}{2N_k} \sum_{i=1}^{N_k} [Z(s_i + h) - Z(s_i)]^2.$$

$Z(s_i)$ denotes the precipitation observation at location s_i. The chosen variogram model is from the Matern family (Schabenberger and Gotway, 2005), an extension of the Exponential family with more flexibility. The choice of the Matern family is standard in geostatistical applications (Plouffe et al., 2015; Risser and Calder, 2015; Cantet, 2017). The Matern variogram model is of the form :

$$\gamma(h) = c_0 + c_1 \left[1 - \frac{1}{2^{\kappa-1}\Gamma(\kappa)} \left(\frac{h}{\alpha} \right)^{\kappa} \mathrm{K}_{\kappa} \left(\frac{h}{\alpha} \right) \right] \text{ , with } \mathrm{K}_{\kappa}(t) = \frac{\Gamma(\alpha)}{2} \left(\frac{t}{2} \right)^{-\kappa} \quad ,$$

where Γ denotes the gamma mathematical function, c_0 refers to the nugget effect, c_1 to the sill, α to the range, and κ controls the smoothness of the variogram. Variogram fitting is performed using the R package *gstat* by minimizing $\sum_{k=1}^{p} \omega_k \left[\gamma(\overline{h_k}) - \hat{\gamma}(h_k) \right]^2$, where $\overline{h_k}$ is the mean distance separation within the bandwidth h_k. The weights ω_k are given by $N_k / \overline{h_k}^2$. Kriging relies on the normality assumption of observed data, which is not met in practice for seasonal precipitations (Husak et al., 2007). For this reason, like other authors (e.g. Haberlandt, 2007; Bostan et al., 2012), kriging is performed on the logarithm of seasonal precipitations, followed by a back-transformation of the predictions (Erdin et al., 2012).

Ordinary Kriging (OK) is a commonly applied method for precipitation interpolation (Borges et al., 2016; Adhikary et al., 2017; Pellicone et al., 2018). In OK, the mean of the Gaussian process ($\mu(s) = \mu$) is assumed constant across space. This results in the following prediction at location s_0 :

$$\hat{Z}_{\mathrm{OK}}(s_0) = \sum_{i=1}^{N} \lambda_i Z(s_i),$$

where N denotes the number of observations, and λ_i are the kriging weights.

Kriging with External Drift (KED) (Schabenberger and Gotway, 2005) allows the mean of the Gaussian process to vary in space as a linear function of p explanatory variables noted x_k, leading to :

$$\hat{Z}_{\mathrm{KED}}(s_0) = \sum_{k=0}^{p} \hat{\beta}_k x_k(s_0) + \sum_{i=1}^{N} \lambda_i \left[Z(s_i) - \sum_{k=0}^{p} \hat{\beta}_k x_k(s_i) \right].$$

The weights λ_i and the coefficients of the linear regression $\hat{\beta}_k$ are estimated at the same time. Altitude or radar information is often introduced as a drift in kriging (Velasco-Forero et al., 2009; Schiemann et al., 2011; Aalto et al., 2013; Masson and Frei, 2014). Radar precipitation is available in France, but only since 1997. In this study, the altitude and the seasonal precipitation simulated by AROME are candidates as possible drifts. The respective models are denoted by $\mathrm{KED_z}$ and $\mathrm{KED_{arome}}$. To build $\mathrm{KED_z}$ and $\mathrm{KED_{arome}}$, local kriging (Carrera-Hernández and Gaskin, 2007; Sun et al., 2015) is considered by reducing the number of observations to reduce computational time and introduce non-stationarity in the co-variables effects. The neighborhood size is tuned.

3.3.2 Geographically Weighted Regressions

Geographically Weighted Regressions (GWR) do not use the spatial autocorrelation of the observed variable but rather perform local linear regression between observations and

explanatory variables as :

$$Z_{\text{GWR}}(s_0) = \beta_0(s_0) + \sum_{k=1}^{p} \beta_k(s_0) x_k(s_0) + \epsilon_{s_0}, \text{with } \epsilon_{s_0} \sim \mathcal{N}\big[0, \sigma^2(s_0)\big],$$

where $Z_{\text{GWR}}(s_0)$ is the seasonal precipitations in mm at location s_0, β_0 is the intercept at this location, β_k is the slope of the kth co-variable at location s_0, and $x_k(s_0)$ is the value of the kth co-variable at this location. The coefficients β_k vary in space and are estimated in a local neighborhood using the $n_{\max}$ closer observations. Each of the $n_{\max}$ neighborhood observations at location s_i is assigned a weight proportional to the distance to the location s_0 :

$$w_{s_i s_0} = \begin{cases} \left[1 - \left(\frac{d_{s_i s_0}}{b}\right)^2\right]^2 \text{ when } d_{s_i s_0} < b, \\ 0 \text{ when } d_{s_i s_0} > b. \end{cases}$$

$d_{s_i s_0}$ denotes the Euclidean distance between location s_i and location s_0. b is the kernel bandwidth. By construction, it introduces local effects of explanatory variables rather than global ones. The explanatory variable effects are indeed intended to vary across space. GWR has been commonly applied to consider the altitude effect on precipitation (Bostan et al., 2012; Gyasi-Agyei and Pegram, 2014; Sun et al., 2015; Fung et al., 2022). The regression fits are performed using the maximum likelihood method implemented in the R function *lm*. Geographical coordinates, altitude, and AROME simulations are considered as predictors in GWR.

3.3.3 Random Forest

Random Forest (RF) is an extension of Classification And Regression Trees (CART, Lewis, 2000) using bootstrap aggregation (bagging, Breiman, 1996). CART algorithms use a sequence of splitting rules to make predictions. The first tuning hyperparameter m_{try} corresponds to the number of co-variables to test to split a leaf into two sub-leafs. The selected co-variable minimizes the weighted (by observation numbers) sum of variances in the two created sub-leafs. The leaves continue to be split until a certain criterion is reached, such as maximum tree depth or minimum number of observations in terminal nodes. The second tuning hyperparameter is $\text{node}_{\text{size}}$, which sets the minimum number of observations in a leaf. The third tuning hyperparameter is n_{tree}, which is the number of weak learners (CART) used by RF to generate a prediction ensemble. A weak learner refers to a model that does only slightly better than random chance. The final prediction is the average of the ensemble predictions from the weak learners. RF has been successfully applied for spatial prediction of climatological variables such as precipitation and temperature (Sekulić et al., 2020; Fan et al., 2021; Zandi et al., 2022). The two hyperparameters n_{tree} and m_{try} are tuned in KFold cross-validation, as explained in the following subsection. The $\text{node}_{\text{size}}$ parameter is set to 1 to allow the maximum spatial variability of predictions, knowing the spatial variability behavior of precipitation.

Buffer distance maps (Hengl et al., 2018) from all observation locations are included in the explanatory variables to account for spatial autocorrelation. A buffer distance map is produced by determining the Euclidean distances between each prediction pixel and a speficic observation. The number of buffer distance maps equals the number of observations of the training dataset. RF is applied in two ways : to predict conventionally observed precipitations, and to predict AROME ratios. In both cases, the longitude, latitude, altitude, buffer distances, AROME, and the AROME logarithm are considered as covariates. AROME ratios refer to the ratio between observed precipitations and AROME precipitation extracted at rain gauge locations. The ratio map is multiplied by the AROME field to obtain seasonal precipitations

from RF_{ratio}. This approach is aimed at preserving the spatial structure of AROME and can be considered as a correction of AROME seasonal precipitations. The R package *ranger* is used to train the RF models and generate predictions.

For all statistical models except RF_{ratio}, the logarithm of seasonal precipitation is predicted to fulfill the normality assumption and then back-transformed. The explanatory variable AROME is used at the logarithm scale. In RF_{ratio}, the logarithms of the ratios are interpolated and then added to the logarithm of AROME.

3.3.4 Evaluation of spatial interpolation methods

Six models (OK, KED_{z} , $\text{KED}_{\text{arome}}$, GWR, RF, RF_{ratio}) are evaluated in cross-validation. The rain gauge dataset is separated into training and testing sets. To select p% of rain gauges in the training dataset, a KMeans clustering on spatial coordinates and altitude of the stations is performed, leading to 50 clusters. From these clusters, p% of rain gauges are selected in the training dataset. This method ensures both the spatial and altitudinal representativeness of the training and evaluation datasets. The hyper-parameters of the models are tuned in the training part using KFold (Fushiki, 2011) with $K = 10$. The names of the hyper-parameters and their corresponding tested values are available in the appendix. The statistical models are then calibrated on the entire training part using the selected best KFold hyper-parameters and evaluated on the test dataset with the computation of the Kling-Gupta efficiency (KGE, Gupta et al., 2009), defined below. The KGE metric is composed of three sub-metrics, including the correlation coefficient (R), the bias ratio (Beta), and the variability ratio (Gamma) between the observed and estimated precipitations. The closer the KGE and its three sub-metrics tend to 1, the better the performances of the statistical models.

$$
\begin{aligned}
KGE &= 1 - \sqrt{(1-R)^2 + \left(1-\text{Beta}^2\right) + \left(1-\text{Gamma}^2\right)^2}, \\
R &= \frac{\sum_{i=1}^{n}(Z(s_i)-\mu_Z)\left(\hat{Z}(s_i)-\mu_{\hat{Z}}\right)}{\sqrt{\sum_{i=1}^{n}(Z(s_i)-\mu_Z)^2}\sqrt{\sum_{i=1}^{n}\left(\hat{Z}(s_i)-\mu_{\hat{Z}}\right)^2}}, \\
\text{Beta} &= \frac{\mu_{\hat{Z}}}{\mu_Z}, \\
\text{Gamma} &= \frac{\sigma_{\hat{Z}}/\mu_{\hat{Z}}}{\sigma_Z/\mu_Z}.
\end{aligned}
$$

$Z(s_i)$ denotes the observed seasonal precipitation at location s_i. $\hat{Z}(s_i)$ is the estimation of seasonal precipitation at location s_i performed by the statistical models. n is the total number of observations. μ is the mean, and σ is the standard deviation. This analysis is repeated 10 times with multiple training/validation datasets for different proportions p (0.10, 0.25, 0.50, 0.75, 0.90) of training rain gauges to investigate the robustness of the statistical models. Table 3.2 summarizes the different number of stations in the training dataset related to the proportions and the sampling strategy. Moreover, the seasonal precipitations are provided on a regular grid at a resolution of 1 km using all rain gauges to train the models.

3.4 Results

3.4.1 Interpolation ability and robustness of the models

The robustness of the models is investigated by gradually reducing the number of rain gauges in the training dataset. Figure 3.3 shows the mean performances in terms of R, Beta,

Table 3.2 – Number of rain gauges in the training dataset for different proportions, sampling strategy and the mean surface area covered by one rain gauge. For 10% of rain gauges in the training dataset, there is 1 station per 476 km^2 on average.

Proportion (%)	**Train size**	**Mean surface covered by a rain gauge** (km^2)
10	641	476
25	1071	285
50	1775	172
75	2470	124
90	2887	106

Gamma, and KGE of the statistical models (OK, KED_z, KED_arome, GWR, RF, and RF_ratio) by seasons under different proportions p of rain gauges in the training dataset.

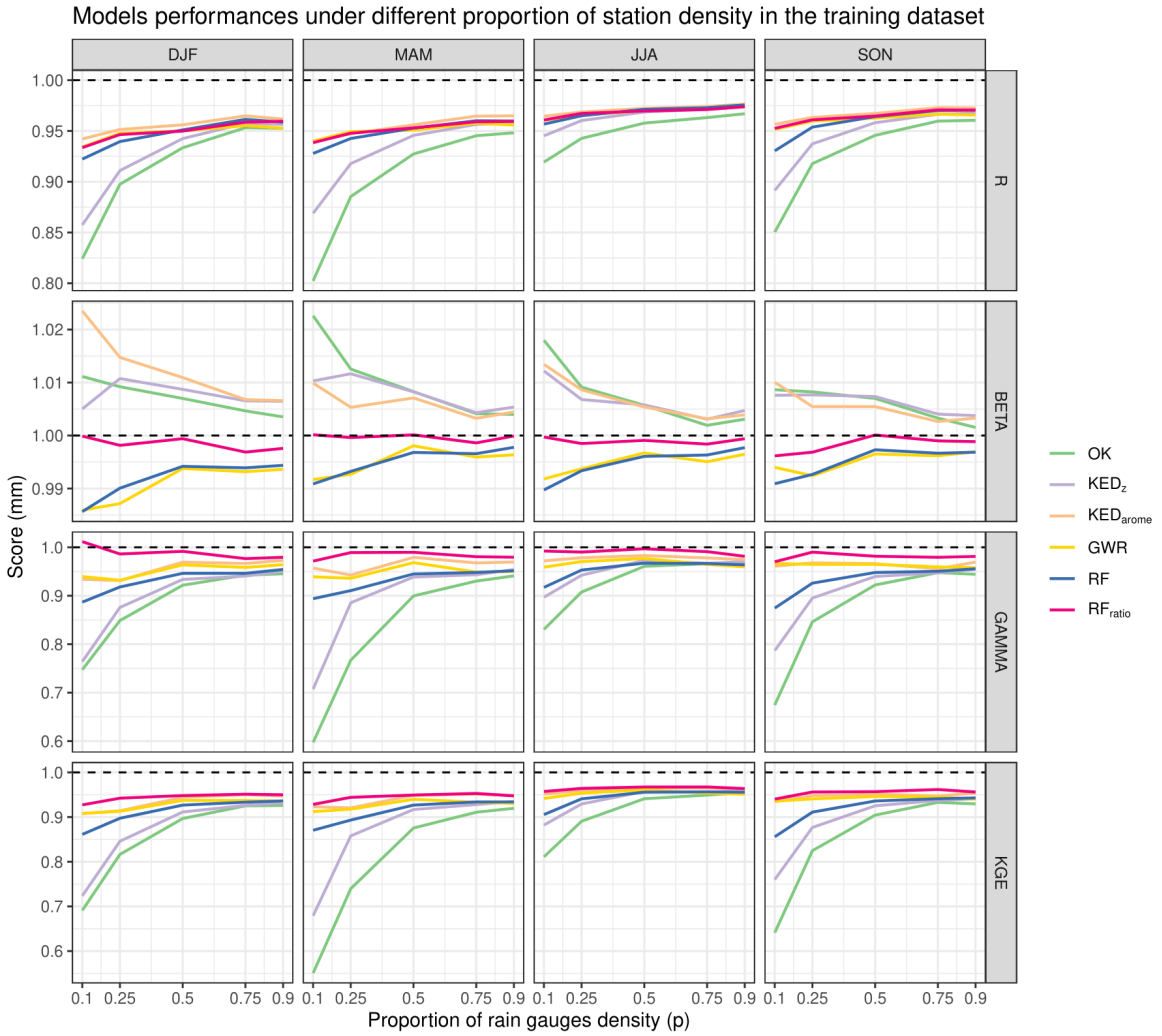

Figure 3.3 – Model performances under different station densities. Scores (KGE, R, β, and γ) are computed for each combination of the season (winter (DJF), spring (MAM), summer (JJA), and autumn (SON)), models (OK, KED_z, KED_arome, GWR, RF, and RF_ratio), and proportion of stations in the training dataset (0.10, 0.25, 0.50, 0.75, 0.90). The highest possible scores are equal to 1.

The OK and KED_z models are poorly correlated to the observations, as measured by the

R metric. On the other hand, the KED_{arome} model shows the strongest statistical correlations. Some statistical models consistently exhibit a mean bias (Beta higher than 1) across all seasons and station densities. Geostatistical models (OK, KED_z, KED_{arome}) tend to overestimate seasonal precipitation, while the non-geostatistical models (GWR, and RF) tend to underestimate it. RF_{ratio} is unbiased for all seasons and station densities. All statistical models, except RF_{ratio}, present a variance bias. The underestimation of the prediction variance is larger for the OK, KED_z, and RF models. The KGE summarises the R, Beta, and Gamma metrics, and the performance order of the models is consistent for all seasons and rain gauge densities. OK and KED_z are the poorest models with weak correlations to the observations and significant mean and variance biases. For example, in spring for $p = 0.10$, OK and KED_z have KGEs lower to 0.7, whereas the other models have KGEs higher to 0.85. RF is the third worst model, having a high variance bias. The top three models are GWR, KED_{arome}, and RF_{ratio}. RF_{ratio} has the best performances across all seasons and rain gauge densities.

For $p = 0.90$, the differences in KGE are low. Geostatistical models are unbiased, whereas the non-geostatistical models show slight bias. The decrease in rain gauge densities affects the performances of the statistical models to varying degrees. OK, and KED_z are less robust to a decrease in station density, resulting in poor correlation to the observations, significant overestimation (R higher to 1), and a large underestimation of the prediction variance (Gamma lower to 1). RF is robust up to a point. For p greater than 0.25, the metrics slowly decrease when degrading rain gauge density. However, the KGE of RF rises sharply at $p = 0.10$ in summer and autumn. GWR, KED_{arome}, and RF_{ratio} are the more robust models. GWR and KED_{arome} predictions tend to be too high and less correlated to the observations as the rain gauge density decreases, whereas only the correlation decreases for the RF_{ratio} model. As a result, RF_{ratio} is unbiased in mean and variance, even at $p = 0.10$, unlike the other models.

Figure 3.4 explores the differences shown in Figure 3.3 for $p = 10\%$. Predictions on evaluation stations with 10% of rain gauges for training are plotted against observed winter precipitation, for a single training/validation dataset. OK and KED_z predictions are poorly correlated to the observations (R lower to 0.85), and their variance is underestimated (Gamma lower to 0.75). AROME, without rain gauge assimilation, is better than those two models in this specific case, despite overestimating the prediction variance. RF performs well but struggles to predict high values with only 10% of rain gauges in the training dataset, causing a poor Gamma score. This issue is not observed for RF_{ratio}, which has the best scores. GWR and KED_{arome} have similar performances, despite slightly underestimating the prediction variance.

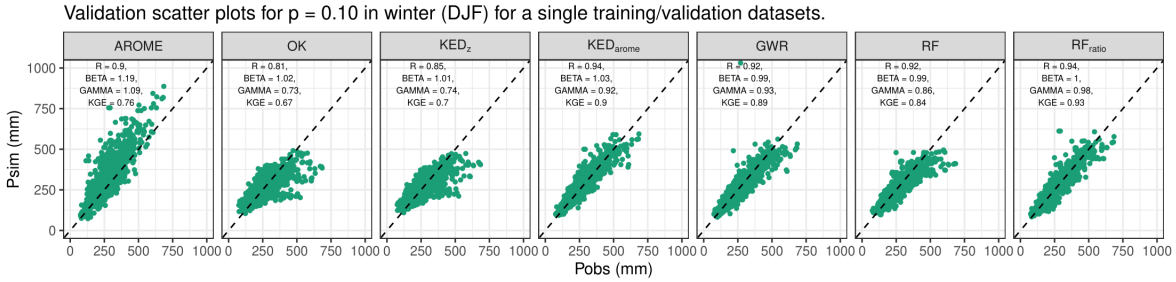

Figure 3.4 – Scatter plot between winter (*DJF*) observed and predicted precipitations at evaluation stations. 10% of the stations were used in the training process. The scatter plots are illustrated for each model (OK, KED_z, KED_{arome}, GWR, RF, RF_{ratio}) and for AROME. The dotted lines indicate the 1 :1 lines. R, Beta, Gamma, and KGE scores are printed.

3.4.2 Altitude extrapolation performances

To assess the robustness of interpolation, cross-validation was performed. Additionally, the extrapolation performances of the statistical models are evaluated through cross-validation with 50 % of rain gauges in the training dataset. Those rain gauges are not randomly selected. A clustering framework, similar to the one described earlier, was applied, considering only spatial coordinates (not the altitude of the stations) to divide the rain gauge dataset into 50 geographical groups based on KMeans. For each cluster, the 50% lower altitude rain gauges are selected in the training dataset. The statistical models are validated on a dataset representing higher areas than their neighboring areas. This assessment aimed to evaluate the altitude extrapolation performances of the statistical models. Figure 3.5 displays the scatter plot between observed and predicted seasonal precipitations. The differences among the statistical models are significant in winter and autumn. Therefore, only winter and autumn precipitations are considered. OK underestimates both winter and autumn precipitation with Beta scores close to 0.9. The bias appears for all observed seasonal precipitation amounts and increases for high precipitation accumulation (the points become further away from the 1 :1 dotted line). KED_z has the second-worst altitude extrapolation performance. Like OK, KED_z underestimates high seasonal observed precipitation. The underestimation is more evident in autumn. RF is nearly unbiased for low-medium observed seasonal precipitation (below 500 mm) but seems to be bounded by 500 mm in winter and 700 mm in autumn. Graphically, it is seen as a plateau effect, resulting in a notable underestimation of high observed seasonal precipitation. Those high errors impact the Gamma score (only equal to 0.8) and thus the KGE performances. GWR is almost unbiased on average but has considerable positive and negative errors for the highest observed seasonal precipitation, resulting in lower performances than KED_{arome} and RF_{ratio}, which are the only statistical models providing accurate predictions in the altitude extrapolation context. The points are not far from the 1 :1 dotted line. KED_{arome} and RF_{ratio} are the only models having KGE higer than 0.9 mm in winter, for example.

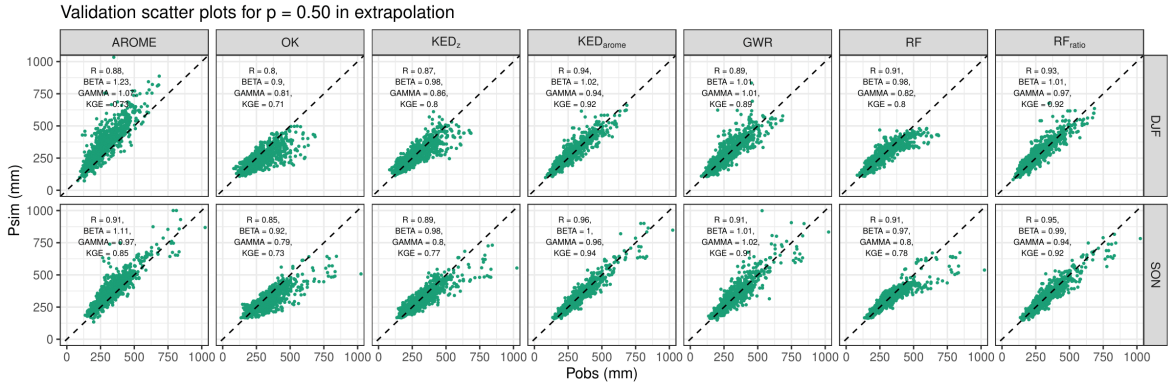

Figure 3.5 – Scatter plot between seasonal observed and predicted precipitations at rain gauges used to evaluate the extrapolation skills at higher altitudes. The scatter plots are illustrated for each model (OK, KED_z, KED_{arome}, GWR, RF, RF_{ratio}), and AROME, for two seasons (winter (*DJF*), autumn (*SON*)). The dotted lines indicate the 1 :1 lines. R, Beta, Gamma, and KGE scores are printed.

The annual precipitations from the models (trained with all the stations) are extracted on a transect, *i.e.*, an imaginary line crossing the topography, to investigate the effect of the altitude on the models. The transect is illustrated in Figure 3.6. The chosen transect is located in the *French Alps*, a complex topographic region. The altitude on the transect ranges from 2,000 to 4,000 m and is represented by the brown curve in Figure 3.6**(b)**. AROME is correlated to the altitude but does not follow it completely. AROME precipitation increases

from 3,500 mm to 5,500 mm in a gain of 1,000 m elevation. The differences among the models observed in Figures 3.3 to 3.5 are illustrated on the transect. OK and RF do not evolve with the topography contrary to KED_z, KED_{arome}, GWR, and RF_{ratio} , which are correlated to the altitude. At 4,000 m, the annual precipitation differences are large. GWR produces two times more precipitation than KED_{arome}. RF_{ratio} is closer to GWR, despite a different behavior. RF_{ratio} is, by construction, highly correlated to AROME, whereas GWR seems governed by the altitude profile. This transect illustrates the differences among the statistical models but can not be used for evaluating them as no rain gauges are available at 4,000 m elevation.

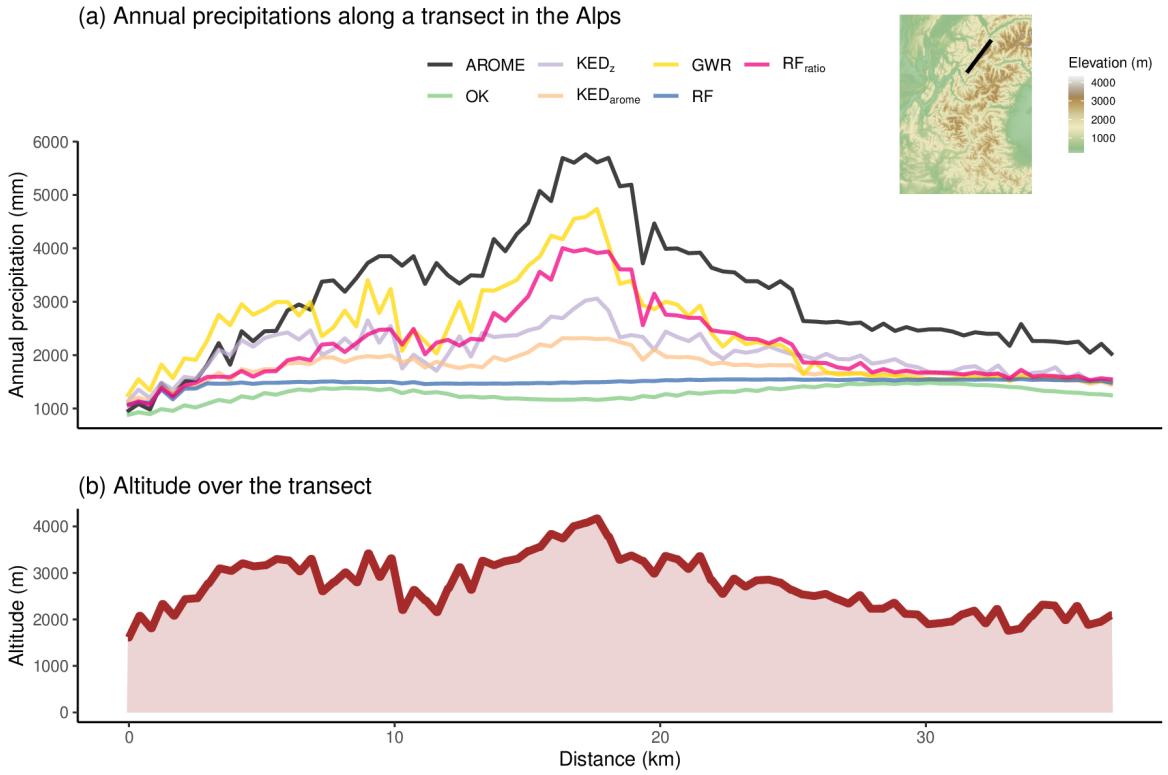

Figure 3.6 – **(a)** Annual precipitations extracted across the transect are colored according to the following models : OK, KED_z, KED_{arome}, GWR, RF, RF_{ratio}. AROME annual precipitation is added in black. The elevation is represented in brown as an altitude profile in **(b)**.

3.4.3 Seasonal precipitation maps

Seasonal precipitation maps are obtained using all rain gauges in the training process. Only maps obtained with the statistical models having the best performances in terms of KGE, for the different training datasets and the different range of altitudes are shown. Based on the previous results, only KED_{arome} and RF_{ratio} maps are illustrated in Figure 3.7**(a)**. Figure 3.7**(b)** reveals the difference between KED_{arome} and RF_{ratio} .

Both models generally agree on the seasonal and spatial variability of precipitation. For both approaches, winters are rainy in the mountainous regions (*Alps*, *Pyrénées*, *Southern Massif Central*), with winter precipitation ranging between 300 and 500 mm in these areas. High precipitation amounts (500–750 mm) can be observed in the *French Alps* and *Pyrénées*. Spring precipitation maps look like winter precipitation maps. Seasonal precipitation differences between reliefs and plains are less pronounced with generally 200–300 mm in the plains and 300–500 mm in the reliefs. Summers are dryer, and the spatial variability of sum-

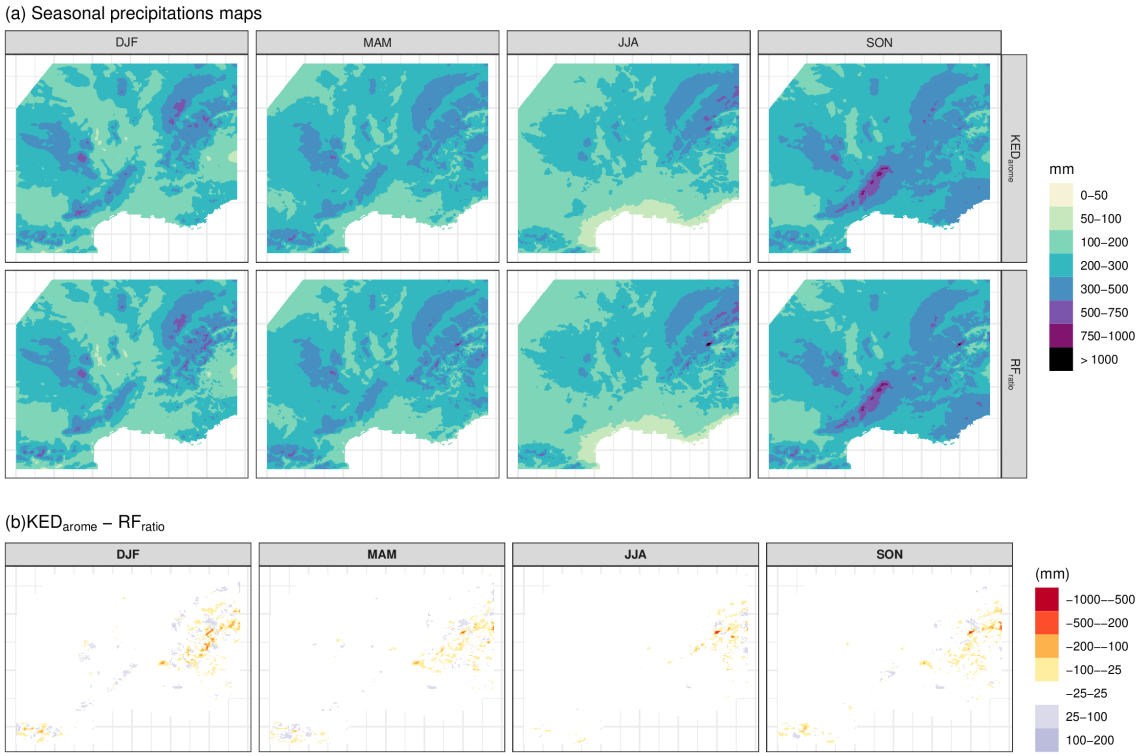

Figure 3.7 – **(a)** Precipitation maps obtained from $\text{KED}_{\text{arome}}$ and RF_{ratio} , using all the rain gauges, for all seasons (winter (*DJF*), spring (*MAM*), summer (*JJA*), and autumn (*SON*)). **(b)** Precipitation maps differences ($\text{KED}_{\text{arome}}$ - RF_{ratio}) for all seasons (winter (*DJF*), spring (*MAM*), summer (*JJA*), and autumn (*SON*)).

mer precipitation is important in high-altitude areas. The *Northern Alps* are rainier than the *Southern Alps*, with 300–500 mm estimated against 100–200 mm. Similarly, the *Central Pyrénées* experience higher precipitation than the *Eastern Pyrénées*. Autums are rainier than the other seasons. with the maximum precipitation (500–750 mm) falling in the *Southern Massif Central*. The Mediterranean area receives between 200–300 mm and even over 300 mm in its Eastern part. The Northwest of France, being farthest from the Mediterranean Sea, encounters only 100–200 mm. Remarkable seasonal precipitation differences between $\text{KED}_{\text{arome}}$ and RF_{ratio} are only observed in the *Alps*, the *Massif Central*, and the *Pyrénées*, which are high-altitude areas. In the *Massif Central*, only winter precipitations are different at the southern border of the region, with 25–100 mm more precipitation with $\text{KED}_{\text{arome}}$. In the *Pyrénées*, the differences do not follow a clear spatial pattern, mostly ranging from -100 to 100 mm. The larger differences are in the *French Alps*, where RF_{ratio} estimates more precipitation for all seasons. The differences can reach -1,000 mm on some pixels.

3.5 Discussion

3.5.1 Statistical model abilities

We first discuss the performances of the different statistical models in light of the results presented in the previous section. The statistical model abilities are summarised according to their interpolation, robustness, and extrapolation performances in Table 3.3. The remainder of this subsection synthesizes the strengths and limitations of each model.

■ **Performances in high rain gauge density** For $p = 0.90$ (high rain gauge density),

which corresponds to a network with one station per 156 km^2 on average, cross-validation performances of OK, KED$_z$, KED$_{arome}$, GWR, RF, and RF$_{ratio}$ differs marginally, see Figure 3.3. KED$_{arome}$ and RF$_{ratio}$ have slightly better results than the other statistical models across all seasons, while OK and KED$_z$ are generally less accurate.

- **Robustness performances** Differences among the models increase when the rain gauge network gets sparser, see Figure 3.3. OK and KED$_z$ show little robustness in terms of KGE. RF is not robust, as the variance bias increases sharply at $p = 0.10$. For low rain gauge densities, KED$_{arome}$ and GWR overestimate and underestimate seasonal precipitation respectively, but are rather robust regarding the variance bias. RF$_{ratio}$ is the most robust model. The degradation of the rain gauge density only affects its correlation to the observations.
- **Extrapolation performances** The statistical models do not show the same behavior when they are used to extrapolate seasonal precipitation in altitude, see Figure 3.5. OK and KED$_z$ constantly underestimates high seasonal precipitation. GWR is unbiased on average but has a high error variance. RF shows a plateau effect with severe underestimation of the highest seasonal precipitations. The two models that provide the best extrapolation performances are RF$_{ratio}$ and KED$_{arome}$.

3.5.1.1 Ordinary Kriging (OK)

OK has the worst prediction performances in the complex topographic study domain. OK lacks robustness with few stations available (see Figure 3.3), suggesting that spatial autocorrelation is insufficient in predicting seasonal precipitation with a sparse rain gauge network. This remark is particularly true in mountainous areas, where the predictions at high-altitude using low-altitude rain gauges are poor, see Figure 3.5. OK underestimation is due to the absence of altitude dependence and the lack of measurement in high-altitude areas. Disregarding the topographical effect leads to significant precipitation underestimations at high-altitude stations (see Figure 3.5). OK limitation in complex topography regions is also noted by Lloyd (2010), Di Piazza et al. (2011) and Adhikary et al. (2017).

3.5.1.2 Kriging with elevation drift (KED$_z$)

KED$_z$ has better interpolation and extrapolation performances than OK, in agreement with Tobin et al. (2011) and Pellicone et al. (2018). That is due to a more flexible model than OK as the mean of the Gaussian process varies according to the altitude. Masson and Frei (2014) explain that KED accounts for large-scale precipitation variations through autocorrelation and small-scale topography dependence through covariates. However, the gain of KGE observed in Figure 3.3 is very limited. The same issues as OK are present but with reduced magnitudes. KED$_z$ is thus outperformed by the other models in interpolation and altitude extrapolation. Indeed, the OK and KED$_z$ cloud points in Figure 3.5 are very similar, with serious underestimation of high observed seasonal precipitations, likely explained by the weak correlation between seasonal precipitation and altitude in the study domain. Frei and Schär (1998) indicate that a simple precipitation-altitude relationship does not exist in the European Alps because of slope and shielding effects.

3.5.1.3 Geographically Weighted Regression (GWR)

Compared to the other statistical models, GWR performs well when trained with few rain gauges (476 km^2 per rain gauge on average), but gives less accurate predictions with a medium-density rain gauge network (172 km^2 per rain gauge on average). GWR is robust, being the best statistical model with KED$_{arome}$ and RF$_{ratio}$ in low rain gauge density (see

Table 3.3 – Major weaknesses and strengths of the six statistical models : OK, KED_z, KED_{arome}, GWR, RF, RF_{ratio}.

Statistical models	**Weaknesses**	**Strengths**
OK	— Large mean and variance biases, especially for high-altitude rain gauges. — Predictions poorly correlated to the observations. — Lack of robustness relative to rain gauge density decrease.	— Model simplicity. — Computational speed.
KED_z	— Large mean and variance biases, especially for high-altitude rain gauges. — Lack of robustness relative to rain gauge density decrease. — Parametrization needed due to the bias–variance trade–off.	— No systematic bias in high altitudes. — Increase of the correlation to the observation compared to OK.
GWR	— Quickly reaches its performance limits when improving the rain gauge density. — Parameterization needed due to the bias–variance trade–off.	— No systematic bias at high altitudes. — The second best robust model.
RF	— Cannot predict above the maximum observed values, resulting in plateau effects.	— Small mean bias. — Highly correlated to the observations.
RF_{ratio}	— Highly subjected to AROME bias by construction.	— No systematic bias at high altitudes. — Small mean and variance biases. — Robustness.
KED_{arome}	— Parametrization needed due to the bias–variance trade–off. — Large mean bias when trained with few rain gauges.	— No systematic bias at high altitudes. — The more correlated models to the observations, whatever the rain gauge density. — Robustness.

Figure 3.3). According to Fan et al. (2021), GWR is robust and outperforms machine learning approaches for low rain gauge density. GWR can effectively represent the relationship of seasonal precipitation with altitude thanks to linear regressions. In Italy, Crespi et al. (2018) found that GWR has better altitude extrapolation scores than Regression Kriging (almost similar to KED) for monthly precipitation. However, the slopes of the linear regression are non-bounded, which may result in significant prediction errors (see Figure 3.5). On the other hand, GWR performs worse than $\text{KED}_{\text{arome}}$, and RF_{ratio} in medium and high rain gauge densities. Going from 50% to 75% of the rain gauges in the training dataset does not result in better GWR performances. That means that GWR fails to learn additional patterns despite denser observations. This result is unsurprising as Hengl (2007) stated that linear modeling is more affected by data sampling and correlation between observed and explanatory variables rather than rain gauge density. Masson and Frei (2014) also found better performances with KED than regression models in the European Alps.

3.5.1.4 Random Forest (RF)

RF has good correlation scores to the observations in low and high rain gauge densities but cannot predict values higher than the maximum seasonal observed precipitation, leading to a severe underestimation of the prediction variance. Moreover, this robustness in correlation strength has a cost for altitude extrapolation, an inherent issue of RF (Hengl et al., 2018). RF can indeed only predict precipitation values within the observational range. However, the measurement spatial sampling is not dense enough to conceive that the rain gauge network captures the seasonal precipitation maximums. In addition, RF reduces too much spatial variability of seasonal precipitation by predicting the median observed precipitation in a node. To fix this issue, the minimum number of observations in a node ($\text{node}_{\text{size}}$) was set to one in a node, but that was insufficient. As a result, RF precipitations show a plateau effect (Figure 3.6) in high-altitude areas, suggesting that RF is not suited to the study domain because of its complex topography.

3.5.1.5 Random Forest ratio (RF_{ratio})

Figure 3.8 displays the ratio obtained with the statistical model RF_{ratio}. Winter and spring ratio maps are similar, suggesting that AROME precipitation must be reduced almost over the entire area, with a larger proportion in high altitudes. On some pixels, AROME winter precipitation must be divided by three to match rain gauge values. The reduction is weaker in summer and autumn. In summer, AROME precipitation must be increased to be close to rain gauge values in the Mediterranean region. Note that this region's seasonal precipitation amount in summer is low, which likely explains those small ratios. The ratio values show spatial coherence. They are highly spatially autocorrelated in low-altitude regions. In high-altitude areas, the ratios are less spatially autocorrelated with values lower or higher than 1 from one mountain valley or mountainside to another.

RF_{ratio} has the lowest mean and variance biases and is highly correlated to the observations, see Figure 3.3. The plateau effects observed with RF can be overcome by interpolating the AROME ratio relative to observed precipitation and multiplying it by the AROME field. Even though the ratio still exhibits a plateau effect, seasonal precipitations do not suffer from insufficient spatial variability as the AROME spatial structure is preserved. More interestingly, the model is unbiased and represents well the prediction variance, although AROME simulations overestimate it (Gamma higher to 1 in Figure 3.4). The method can accurately represent the altitude effect on seasonal precipitations, as predictions can be outside the observational range. This result highlights the importance of interpolating ratio instead of precipitation in future spatial interpolation studies using RF. However, it is important to note that RF_{ratio}

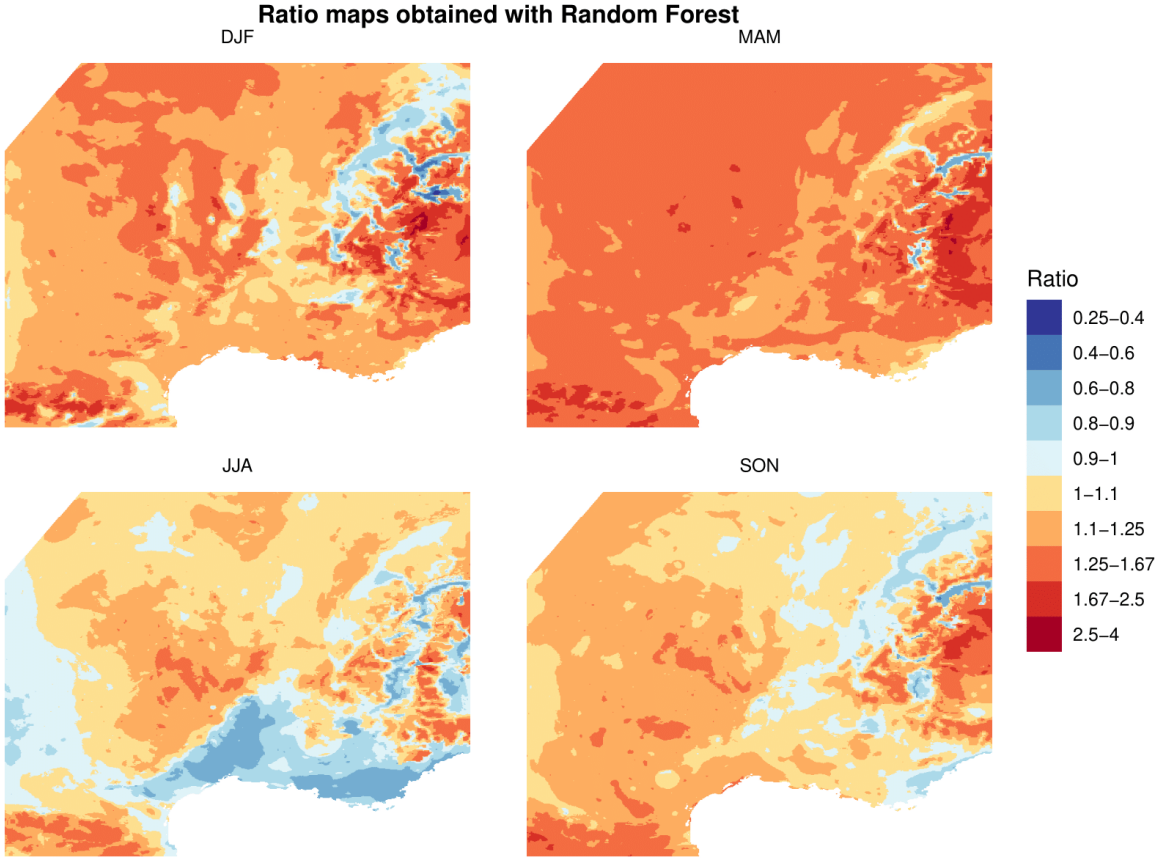

Figure 3.8 – Spatial distribution of the ratios obtained with the model RF_{ratio}. Winter (*DJF*), spring (*MAM*), summer (*JJA*), and autumn (*SON*) ratios are displayed.

is likely subjected to AROME bias, resulting in suspicious seasonal precipitation amounts exceeding 1,000 mm on some high-altitude pixels.

3.5.1.6 Kriging with AROME drift (KED_{arome})

The addition of AROME as a drift instead of the altitude in kriging leads to better performances. It indicates that AROME simulation carry more information than just the altitude. AROME is a physical-based model likely to include, for instance, shielding and slope effects. KED_{arome} demonstrates slightly lower cross-validation scores than RF_{ratio} at both low and high rain gauge densities (Figure 3.3). KED can produce high seasonal precipitation in high-altitude areas by modeling linear associations with the co-variables (Figure 3.5). The best performances are achieved by kriging the logarithm of observed precipitation with the help of the logarithm of AROME precipitation. However, in a complex topographic region, KED is very sensitive to the neighborhood size (Carrera-Hernández and Gaskin, 2007) defined for kriging. The choice of size represents a compromise between model robustness and altitude extrapolation performances. For a small neighborhood size, bias is low (good interpolation scores), and variance is high (altitude extrapolation issues). Conversely, with a larger neighborhood size, the conclusions reverse. In our application the neighborhood size in KED_{arome} was tuned based on RMSE metric, resulting in high bias and relatively low variance of prediction errors.

3.5.2 Physical interpretation of seasonal precipitation climatology

The seasonal patterns of precipitation are influenced by the topography (see e.g. Mock, 1996; Anders et al., 2006) and large-scale atmospheric circulations (Hewitson and Crane, 1992; Raziei et al., 2012; Bothe et al., 2012), which differ across seasons. During winter and spring, the western wet wind from the Atlantic dominates the atmospheric circulation. This results in stratiform cells being blocked on the western side of the mountains, creating a precipitation shadow effect (Foresti and Pozdnoukhov, 2012; Stockham et al., 2018). Winter precipitation ranges from 200 to 300 mm on the Atlantic coastline and 300 to 500 mm on windward slopes such as the *Western Massif Central* and the *Northern Alps*. Leeward slopes, corresponding to sheltered areas at the east of the reliefs (Eastern Alps, Coastal Mediterranean, Rhone Valley), receive less than 200 mm of precipitation. The same phenomenon persists in spring, with the plains experiencing more rainfall. In the summer, the *Northern Alps* experience violent storms due to clashes between air masses, with precipitation ranging from 300 to 500 mm. The Mediterranean area is dry during this season, with estimated rainfall of less than 100 mm. There is a noticeable precipitation gradient along the *Pyrénées*, with the Central Pyrénées receiving 200 to 300 mm, the Western Pyrénées receiving 100 to 200 mm, and the Mediterranean Pyrénées receiving less than 100 mm. During autumn, the entire domain under study is rainy, including the coastal Mediterranean region, which accumulates 200 to 300 mm from infrequent but intense events. The warm Mediterranean Sea significantly contributes to this precipitation. The Southern *Massif Central* also experiences intense precipitation, ranging from 500 to 750 mm. Our findings show similar seasonal and spatial precipitation variability as reported by Canellas et al. (2014), but higher precipitation at high altitudes due to using AROME simulations as a co-variable.

3.5.3 Uncertainty and outlooks

Precipitation undercatch by rain gauges is a major source of uncertainty. While measurement error is low for liquid precipitation, it is significant for solid precipitation (e.g. Sevruk, 1982). During windy winter events, precipitation underestimation can reach 80% (Goodison et al., 1998; MacDonald and Pomeroy, 2007), leading to up to 25% underestimation at high altitudes over a year (Sevruk, 1997). Rain gauge precipitation lapse rates are likely underestimated (Collados-Lara et al., 2018), as underestimation is more likely to happen in the mountains. Precipitation undercatch depends on various factors such as slope, aspect, wind direction, wind exposition, and temperature (Wolff et al., 2015; Pan et al., 2016). A precipitation correction phase ahead of this work would considerably enhance statistical model performances but is challenging and requires extensive data. An extension of this work is the consideration of precipitation undercatch and the comparison of these fields to glacier mass balance, runoff measurement, or Snow Water Equivalent (SWE) (Immerzeel et al., 2015; Avanzi et al., 2021). Seasonal precipitation could be estimated by assimilating the differences in SWE at the beginning and end of the season, assuming minimal melting. However, SWE measurements, and snow depth, can vary over small distances (Vögeli et al., 2016) because of wind redistribution and solar radiation, limiting their spatial representativeness.

AROME overestimation is documented in mountainous regions (Monteiro et al., 2022). The AROME model exhibits a negative temperature bias, leading to suspicious snow accumulation above 1,800 m, even during summer. Additionally, AROME data is derived from model simulations prone to numerical errors, such as excessively high values or unrealistic horizontal patterns (see Figure 3.7). AROME simulations have been used to derive climatologic seasonal precipitation maps despite being tainted with high and spatially variable bias. A natural follow-up of the work is the consideration of other CP-RCM simulations. In the context of the Coordinated Regional Climate Downscaling Experiment Flagship Pilot Study

(CORDEX-FPS) (Ban et al., 2021), 23 simulations with different model versions and physics schemes are available in the study domain. All of the simulations mostly present low bias in winter and spring. The simulations coming from the WRF (Weather Research and Forecasting, Skamarock et al., 2024) and RegCM4 (Regional Climate Modeling System, Giorgi et al., 2012) models are more biased than those from AROME, COSMO (Consortium for Small Scale Modeling, Rockel et al., 2008), REMO (Regional Climate Model, Pietikäinen et al., 2018), and UM (Unified Model, Chan et al., 2020) models, especially in summer and autumn. Simulations from the COSMO, REMO, and UM models could be directly used in precipitation interpolation. WRF simulations would be more challenging to deal with because of significant precipitation underestimation that can reach -80 % in summer.

The AROME simulations are obtained by forcing simulations from the RCM CNRM-ALADIN, which are driven by the ERA-Interim reanalysis. The Era-Interim reanalysis is no longer updated. To produce an operational reanalysis data set, an ongoing project, conducted at Meteo-France (the provider of the AROME simulations), aims at directly forcing the AROME model by ERA5.

The final source of uncertainty arises from the statistical models. The seasonal precipitation values obtained are predictions and therefore inherently uncertain. All of the statistical models provide an estimation of this uncertainty. In kriging (OK, KED) and GWR, prediction uncertainty can be quantified using the assumption of data normality (Hengl et al., 2018). The uncertainty of Random Forest predictions can be assessed in various ways : Quantile Regression Forest (Meinshausen, 2006), Jacknife-after-Bootstrap (Wager, 2016), U-statistics (Mentch and Hooker, 2016), Monte-Carlo simulations (Coulston et al., 2016). An extension of this work is the evaluation of interpolation uncertainty of the statistical models through the estimation of prediction standard deviations. These fields could be used to investigate the spatial variation of uncertainty, which is likely more important in mountain regions than in highly instrumented low-altitude areas. Interpolation uncertainty maps are needed to use or interpret seasonal precipitation maps carefully.

In addition, daily precipitation maps could be obtained via climatologically aided interpolation, which consists of the interpolation of daily anomalies relative to a climatological map (Hunter and Meentemeyer, 2005). The climatological map can also simply be considered as an explanatory variable for daily interpolation (Masson and Frei, 2014).

3.6 Conclusion

This study addresses the issue of seasonal precipitation interpolation in France, a complex topographic country. A dense rain gauge network of 3,189 stations and the simulation of a CP-RCM AROME are available over the 1982–2018 period. Various statistical models, including OK, KED, GWR, and RF, are evaluated for their robustness and altitude extrapolation performance. Robustness is investigated by gradually reducing the density of the rain gauge network, while altitude extrapolation is explored using low-altitude rain gauges for training and high-altitude ones for evaluation. OK and KED_z are not suited to the study domain. Despite adding altitude as a parameter, spatial autocorrelation of observations is insufficient to predict seasonal precipitation. GWR is highly robust to station density degradation and performs equally well in medium or high rain gauge density networks. RF shows a high correlation to the observations in a high rain gauge density network but delivers inaccurate altitude extrapolation predictions by reducing too much spatial variability of precipitation. KED_{arome} emerges among the best statistical models for altitude extrapolation and has low interpolation variance bias. However, it exhibits a negative bias in low rain gauge densities. To address the RF limitation, the study proposed interpolating the ratios between observed precipitations and AROME simulations rather than directly observed precipitation. The interpolated ratio

map is then multiplied by the AROME field. This approach is robust, has the best scores in high-rain gauge density, and can accurately represent the relationship between altitude and seasonal precipitation through the spatial structure of AROME.

The article implies that using RF for seasonal precipitation interpolation could be improved by considering CP-RCM ratio errors rather than direct measurements, potentially allowing predictions to surpass the maximum observed seasonal precipitation. This approach slightly outperforms traditional KED, maintaining the variance of observations without being limited by constraining assumptions and parametrization. Overall, the study emphasizes the potential of CP-RCM simulation for deriving seasonal precipitation maps. CP-RCMs are often more correlated to observed precipitation than altitude. The obtained precipitation maps show high spatial and seasonal variability depending on topography and large-scale circulation. Additionally, the study underlines the importance of selecting appropriate interpolated and explanatory variables, as well as fine-tuning hyperparameters of statistical models in seasonal precipitation studies.

3.A Hyper-parameters tested in the training process

In the following, the size of the training dataset is noted n_{obs}.

3.A.1 Ordinary Kriging (OK)

— No tuning of hyper-parameters.

3.A.2 Kriging with altitude drift ($\mathbf{KED_z}$)

— Size of neighboring $n_{\max} \in \{10; 20; 50; 100; 300; 1,000\}$.

3.A.3 Kriging with altitude drift ($\mathbf{KED_{arome}}$)

— Size of neighboring $n_{\max} \in \{10; 20; 50; 100; 300; 1,000\}$.

3.A.4 Geographically Weighted Regression (GWR)

— Size of neighboring $n_{\max} \in \{10; 20; 50; 100; 300\}$
— Kernel bandwidth b (km) $\in \{50; 60; 70; 80; 90; 100\}$

3.A.5 Random Forest (RF)

— Number of trees $n_{\text{tree}} \in \{50; 100; 500\}$
— Number of co-variables to test to split a leaf $m_{\text{try}} \in \left\{\frac{n_{obs}}{3}; \frac{n_{obs}}{2}; \frac{2 \times n_{obs}}{3}\right\}$

3.A.6 Random Forest ratio ($\mathbf{RF_{ratio}}$)

— Number of trees $n_{\text{tree}} \in \{50; 100; 500\}$
— Number of co-variables to test to split a leaf $m_{\text{try}} \in \left\{\frac{n_{obs}}{3}; \frac{n_{obs}}{2}; \frac{2 \times n_{obs}}{3}\right\}$

4

Amélioration de l'interpolation des précipitations à l'aide de variogrammes anisotropiques dérivés de simulations de modèles climatiques régionaux à convection résolue

Abstract The consideration of the spatial variability of daily precipitation, assessed through spatial covariance, is crucial for hydrological modeling. Estimating this covariance is particularly challenging in regions with sparse rain gauge networks or limited radar coverage. To address this issue, this study explores the potential of Convection-Permitting Regional Climate Model (CP-RCM) simulations to estimate anisotropic variograms. We compare five approaches : (1) SPAZM, an interpolator based on local precipitation-altitude regressions, Trans-Gaussian Random Fields, differing by their covariance structure and data source with (2) isotropic covariance from rain gauges, (3) anisotropic covariance from rain gauges, (4) isotropic covariance from CP-RCM simulations, and (5) anisotropic covariance from CP-RCM simulations. The models are evaluated with cross-validation and spatial metrics using radar-derived analyses. Results demonstrate that Trans-Gaussian Random Fields outperform SPAZM. Anisotropic covariance models derived from CP-RCM simulations capture orography-induced directional precipitation structures more effectively than the other models, leading to improved interpolation accuracy and better representation of spatial variability. The generated ensemble of conditional simulations successfully reproduces intense precipitation events at the catchment scale, providing valuable uncertainty quantification. For a 17 km^2 catchment, mean catchment precipitation can range from 175 mm to 450 mm for a convective event, despite high rain gauge density. These findings highlight the benefits of using CP-RCM simulations to generate anisotropic variograms for probabilistic precipitation interpolation. This approach improves the spatial variability of precipitation, making it highly relevant for hydrological applications such as flood forecasting. Future work will explore the integration of these ensembles into probabilistic hydrological modeling.

4.1 Introduction

Gridded daily precipitation data is essential for various environmental applications, such as assessing flood and drought risks or modeling glacier mass balance. However, rain gauge stations provide sparse and irregular observations in space, necessitating spatial interpolation models to estimate precipitation fields. Common interpolation procedures include local regression (Daly et al., 1994; Gottardi, 2009; Verdin et al., 2016), data assimilation (Alpuim and Barbosa, 1999; Devers et al., 2021; Vernay et al., 2025), geostatistics (Goovaerts, 2000; Sideris et al., 2014; Guédé et al., 2024), and more recently machine learning (Hengl et al., 2018; Sekulić et al., 2020; Zandi et al., 2022) models. Geostatistical models frequently outperform other statistical models for precipitation interpolation (Haberlandt, 2007; Bostan et al., 2012; Masson and Frei, 2014). They are considered Best Linear Unbiased Estimator (BLUE) methods (Rao et al., 1973), minimizing error variance but often producing excessive spatial smoothing that underestimates high precipitation intensities (Hofstra et al., 2010; Hiebl and Frei, 2018). To mitigate this issue, researchers use ensembles of equiprobable fields, known as conditional simulations (Frei and Isotta, 2019; Yan et al., 2021), all consistent with the measurements and the observational variance while displaying distinct spatial patterns.

Daily precipitation exhibits spatial autocorrelation as neighboring rain gauges often record similar values (Tobler, 1970). Spatial autocorrelation is mathematically modeled through the variogram (Cressie, 1993), which links spatial distance to observational variability. Traditionally, variograms are assumed to be isotropic, ignoring directional variations due to the limited number of rain gauge stations or for modeling simplicity (Adhikary et al., 2017). However, in complex topographic regions, anisotropy can arise from interactions between atmospheric conditions and mountain ranges (Tobin et al., 2011), degrading interpolation quality with isotropic variograms. To improve variogram estimation, researchers have explored alternative sources of spatial information, such as gridded precipitation products. Radar data has been used for deriving parametric or non-parametric variograms (Velasco-Forero et al.,

2009; Schiemann et al., 2011) but is often available for shorter timeframes than the multi-decadal period required for the daily precipitation analyses. Alternatively, simulations from Convection-Permitting Regional Climate Models (CP-RCMs) (Rockel et al., 2008; Brousseau et al., 2016; Keuler et al., 2016; Gerber et al., 2018) are supplied on extended periods and deliver new possibilities to infer variogram estimation. Although daily CP-RCM precipitation fields are frequently biased (Caillaud et al., 2021), they might still provide relevant information about anisotropy structure. This study evaluates the accuracy of daily precipitation interpolation by comparing isotropic and anisotropic variograms derived from rain gauges. It also investigates the potential of CP-RCM simulations for deriving anisotropic variograms, a novel approach that has not been previously explored. Additionally, the study aims to quantify the uncertainty in spatial interpolation at the catchment scale, a critical factor for hydrological modeling, which is rarely found in precipitation analyses or reanalysis (Frei and Isotta, 2019; Devers et al., 2021, 2024).

To address these objectives, we evaluate the ensemble means (kriging) and ensemble spreads (conditional simulations) from geostatistical models in a cross-validation framework across 786 intense precipitation events. We compare four types of variogram : (1) isotropic variogram estimated with rain gauge stations, (2) anisotropic variogram estimated with rain gauge stations, (3) isotropic variogram estimated with CP-RCM simulations, and (4) anisotropic variogram estimated with CP-RCM simulations. The geostatistical models are also compared to SPAZM (Gottardi, 2009), an interpolator based on local precipitation-altitude regressions stratified by weather patterns. Beyond point-scaled validation, we assess spatial structure using radar-derived analyses as a reference and evaluate the ability of the ensemble spread to capture mean catchment precipitation, an essential factor for hydrological modeling. The analysis is conducted over a mountainous region near the French Mediterranean Sea. This area encounters heavy rainfall due to the interaction of the air masses with elevation, offering an ideal setting for the study. The paper is structured as follows : Section 2 describes the domain under study and the available precipitation datasets. Section 3 introduces the four covariance modelings used for spatial interpolation. Section 4 displays the cross-validation and spatial evaluation results. Section 5 compares the findings to the existing literature and discusses future perspectives. Finally, Section 6 outlines the conclusions.

4.2 Domain and data under study

4.2.1 Study domain

The present study focuses on the Cevennes region in the southern Central Massif (see Fig.4.1). This mountainous study area is characterized by rugged terrain, including high plateaus and forested hills, with elevations reaching 1,700 m. Annual precipitation experiences significant spatial variability. The higher elevations can collect more than 2,000 mm while the lower foothills present a Mediterranean climate with annual precipitations ranging from 600 to 1,200 mm (Canellas et al., 2014). Winter precipitation can fall as snow at high elevations, even if snow cover is intermittent. Autumn is the wettest season. The moisture-laden air from the warm Mediterranean Sea faces colder air from the north, leading to frequent extreme rainfall events of 300-500 mm and generating heavy floods in the valleys (Delrieu et al., 2005).

To capture the spatial variability of precipitation induced by the complex topography, a dense network of 973 rain gauges is available, including 197 stations in the study domain and 776 additional stations near the borders of the study domain. Rain gauges are up to 1,500 m, encompassing the full elevation distribution. The number of available rain gauges on a daily timescale varies over the years, ranging from a minimum of 625 to a maximum of 836.

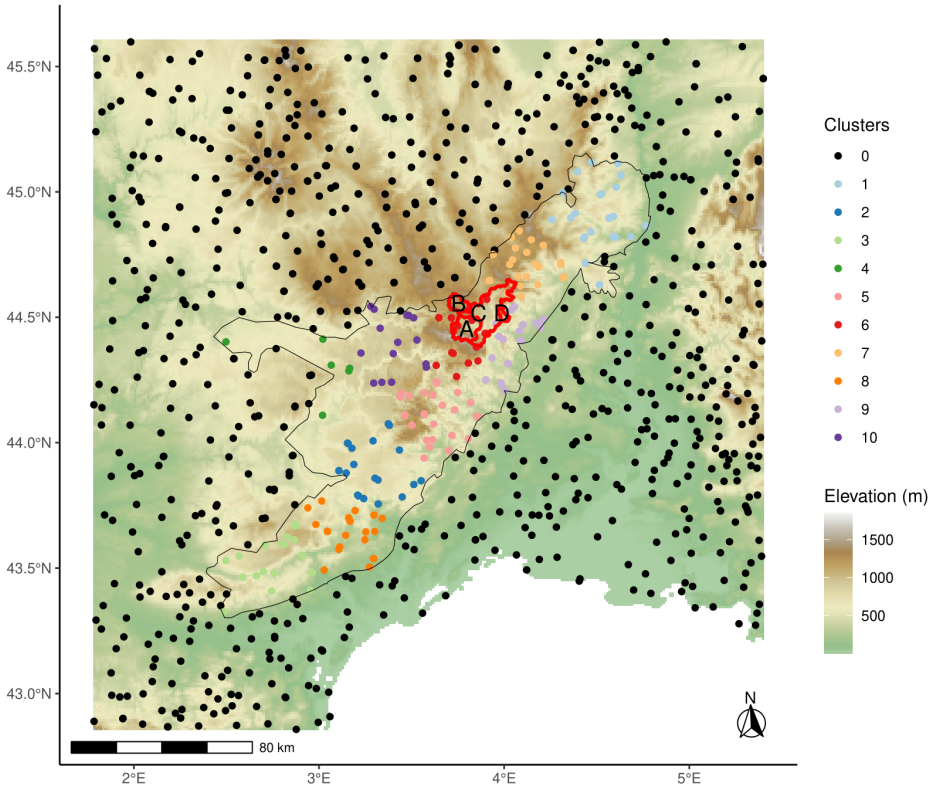

Figure 4.1 – Study domain (1.7—5.5°E, 42.8–45.6°N), colored by the elevation (height above sea level in meters), borders of the Cevennes region (black lines), borders and ID of four catchments (red lines, used in sections 3–5), and location of rain gauge stations (dots, around 800 stations available per day). The colors of the stations (dots) are explained in Section 3. Table 1 gathers information about the catchments.

ID	Name	Surface (km^2)	Mean altitude (m)	Maximum altitude (m)
A	Altier at la Goulette	106	1156	1629
B	Chassezac at Pont Du Mas	51	1246	1440
C	Chassezac at Sainte-Marguerite	413	1056	1629
D	Thines at Pont de Gournier	17	878	1065

Table 4.1 – ID, name, surface area in km^2, mean and maximum altitude in m of the four catchments. Figure 4.1 shows the locations of the catchments.

4.2.2 Meteorological data

4.2.2.1 COMEPHORE

The product called « COmbinaison en vue de la Meilleure Estimation de la Precipitation HOraiRE » (COMEPHORE) (Champeaux et al., 2009) is a high-resolution precipitation analysis product for France, developed at Meteo-France, and based on radar-gauge merging to generate spatial precipitation estimates at an hourly timescale with a spatial resolution of 1 km. COMEPHORE is assumed as a reference to assess the spatial variability of precipitation, taking advantage of the radar coverage. COMEPHORE covers the 1997 - 2025 period but presents a methodology change in 2007, which separates interpolation for convective and stratiform precipitation. It uses the radar corrected by rain gauges to estimate convective precipitation and performs ordinary kriging of the rain gauge amounts for stratiform precipitation using an isotropic variogram. Using radar data, COMEPHORE can accurately represent the size and direction of precipitation cells, and the very local storm cells that the rain gauge

network could miss. For this study, we aggregated the COMEPHORE hourly precipitation fields at the daily timescale over the 2008 - 2017 period. Some studies use COMEPHORE as a reference to evaluate climate models (Caillaud et al., 2021), and others use it for hydrological modeling (Evin et al., 2024).

4.2.2.2 AROME

AROME simulations (Caillaud et al., 2021) are generated through the CP-RCM AROME, using hourly atmospheric inputs provided by a CNRM-ALADIN RCM simulation (Nabat et al., 2020), which is driven by ERA-Interim reanalysis (Dee et al., 2011). The AROME simulations are available at the hourly timescale for the Alpine region, as described in the Flagship Pilot Study of the Coordinated Regional Climate Downscaling Experiment (CORDEX-FPS,Fantini et al. (2018)), at 2.5 km spatial resolution, and cover the 1982–2018 years. In the study, AROME simulations are aggregated to a daily timescale. Unlike RCM models, the AROME model fully resolves convection processes, removing parametrization. The 2.5 km resolution allows for capturing fine-scale atmospheric processes. Previous studies (Ban et al., 2021; Caillaud et al., 2021; Monteiro et al., 2022) have demonstrated that AROME provides an improved representation of intense precipitation events compared to the RCM-ALADIN model despite biases in the size and location of convective cells.

4.2.2.3 SPAZM

SPAZM (Gottardi, 2009) creates daily precipitation analyses at 1 km spatial resolution over a large part of France since 1948 and is continually updated by Electricité de France (EDF) for hydrological modeling. The daily precipitation fields constitute an adjustment of a climatological background field using the daily rain gauge amounts. A climatological background field represents the average daily structure of the precipitation field, where the influence of topography is easier to account for. The background fields incorporate local orographic effects conditioned by eight weather patterns. SPAZM leads to balanced water budgets at the annual scale, even in mountainous areas (Ruelland, 2020). However, the spatial variability of the daily fields is questionable, with an unrealistic correlation to the altitude. Moreover, SPAZM underestimates the spatial variance of intense precipitation, resulting in overly smoothed precipitation fields (Penot, 2014).

4.3 Methods

4.3.1 Spatial Interpolation

This study develops a probabilistic geostatistical framework for daily precipitation interpolation, using four variograms derived from rain gauges and CP-RCM simulations. Unlike traditional approaches that rely solely on rain gauge data, our method exploits CP-RCM fields to estimate daily isotropic and anisotropic covariance structures. In the following, we detail the stochastic modeling and evaluation procedures.

4.3.1.1 Data transformation

Geostatistics involving kriging methods are built in the Gaussian paradigm (Diggle et al., 2003). However, daily precipitation data often exhibits a positively skewed distribution due to left truncation at zero precipitation and the presence of high values. To address this issue, we assume the positive precipitation follows a Gamma distribution and apply quantile-quantile transformation (Gyasi-Agyei, 2018) to normalize the data each day. We perform Gamma fitting using the maximum-likelihood approach from the *fitdistr* package (Delignette-Muller

and Dutang, 2015). Spatial interpolation is then conducted in the Gaussian domain. Skewness and heteroscedasticity of the precipitation data are thus explicitly considered (Erdin et al., 2012), theoretically resulting in greater interpolation uncertainty in areas with high precipitation.

The modelization steps include :

1. Gamma to Normal transformation of positive precipitation :
   $Y^* = \Phi^{-1}[u_0+(1-u_0)F_\gamma(Y)]$, where Y represents daily positive observed precipitations, F_γ the distribution function of a Gamma distribution, Φ^{-1} is the quantile function of a Gaussian distribution with zero mean and unit variance, u_0 is the empirical probability of zero precipitation estimated by the number of rain gauges with less than 0.5 mm over the total number of rain gauges, and Y^* are the normalized precipitations.
2. Gamma to Normal transformation of zero precipitation :
   The zeros are transformed to $\Phi^{-1}[\mathcal{U}(0.01, u_0)]$, $\mathcal{U}$ is the uniform distribution.
3. Conditional simulations from geostatistical models (detailed in subsection 4.3.1.2).
4. Back-Transformation of precipitation predictions into Gamma distribution :
   $$\hat{Y} = \begin{cases} F_\gamma^{-1}\left\{\frac{\Phi(Y^*)-u_0}{1-u_0}\right\}, & \Phi(Y^*) > u_0, \\ 0, & \text{otherwise.} \end{cases}$$

Once the precipitation data is normalized, we model its spatial structure using geostatistical models, focusing on estimating covariance structures through variogram fitting.

4.3.1.2 Geostatistic models

Precipitation should be centered in the first instance to estimate its covariance structure accurately (Schabenberger and Gotway, 2005). The expectation of the Trans-Gaussian Random Field is modeled in the Gaussian domain as a function of geographical predictors (longitude, latitude, and altitude) and a seasonal climatological background field. The literature commonly employs geographical predictors such as altitude in kriging with external drift model (Bárdossy and Pegram, 2013). The seasonal climatological background fields have been built through Random Forest modelization using CP-RCM simulations in (Dura et al., 2024b). Their construction is based on the idea that the fine-resolution simulations of climate models should summarize the topographical influence on precipitation. Climatological background fields have been used broadly (see e.g. Hunter and Meentemeyer, 2005; Gottardi, 2009; Masson and Frei, 2014) to summarize long-term precipitation patterns influenced by orography, improving the robustness of daily precipitation interpolation. We successfully check the absence of multicollinearity by computing the correlation matrix among the predictors.

Spatial interpolation requires the estimation of a spatial covariance. We fit each day four different exponential variograms, all including a nugget effect :

- an isotropic variogram estimated with rain gauge observations (rgISO),
- an anisotropic variogram estimated with rain gauge observations (rgANISO),
- an isotropic variogram derived from daily AROME precipitation field (arISO),
- an anisotropic variogram derived from daily AROME precipitation field (arANISO).

The nugget parameter corresponds to micro-scale precipitation variability and measurement errors. The exponential choice is standard in numerous geostatistical studies (Masson and Frei, 2014; Frei and Isotta, 2019) because it effectively captures the gradual decline in autocorrelation as the separation distance increases. The weighted least-square estimation of the variograms is done in the Gaussian domain for both rain gauge and AROME precipitations. The weights are proportional to the number of pairs observations and inversely proportional

to the squared average distance between them. The estimation process only uses 25 % (randomly selected) of the AROME grid cells for computational reasons. We note η and θ as the estimated anisotropy ratio and angle. Schiemann et al. (2011) describes the methodology in more detail, with an ordinary least square estimation in contrast to a weighted least square estimation. The variograms are estimated with the *gstat* R packages (Pebesma, 2004).

4.3.1.3 Conditional simulations

Conditional simulation of Trans-Gaussian Random Field is conducted using sequential Gaussian simulations implemented in the *gstat* R package (Pebesma, 2004) to create each day an ensemble of 100 simulations. Gyasi-Agyei (2018) states that the conditional simulations obtained with *gstat* are too granular. They decided to apply a 3×3 window smoothing technique. We do not apply the same post-processing step because we will, in future developments, employ mean catchment precipitation, which is not sensitive to the granularity. While this ensemble size is sufficient for representing precipitation variability (Frei and Isotta, 2019), it does not account for all sources of uncertainty, such as covariance parameters inference or precipitation undercatch (see subsection 4.5.3).

4.3.2 Evaluation

In our analysis, the ensemble mean of the conditional simulations is equivalent to the result obtained using deterministic kriging with external drift (Schabenberger and Gotway, 2005) (KED). Later in the article, we will use the terms "kriging" and "ensemble mean" interchangeably. While kriging captures the most likely precipitation value, the conditional simulations capture the entire ensemble of possible realizations, providing spatial uncertainty. To assess the performance of the spatial interpolation models, we evaluate both deterministic and probabilistic interpolated precipitation fields. The evaluation focuses on three key aspects :

- point-scale accuracy using cross-validation on rain gauge stations ;
- spatial structure by comparing interpolated fields with radar-derived precipitation analyses ;
- uncertainty quantification by analyzing the ensemble spread of conditional simulations at the catchment scale.

The models are evaluated on 786 precipitation events (nearly 20 events per year), defined as the days with at least 50 mm recorded at a minimum of five rain gauges.

4.3.2.1 Cross-validation of ensemble means

The deterministic performance of the spatial interpolation models is evaluated through a leave-cluster-out cross-validation scheme. Unlike traditional leave-one-out cross-validation, this procedure removes entire clusters of neighboring stations to better mimic ungauged conditions and accentuate performance differences between the models. An accurate covariance estimation is crucial for sparse rain gauge station networks. Sequentially, a cluster of neighboring stations is removed from the training dataset and then predicted. Ten groups of stations are created by the K-means algorithm (MacQueen, 1967). The clustering variables are the longitude and the latitude of the stations. Figure 4.1 indicates the rain gauge station clusters.

The evaluated models include (1) SPAZM as the deterministic interpolation model, (2) rgISO : Kriging with an external drift with an isotropic variogram estimated from rain gauge data, (3) rgANISO : Kriging with an external drift with an anisotropic variogram estimated from rain gauge data, (4) arISO : Kriging with an external drift with an isotropic variogram derived from CP-RCM precipitation fields, (5) arANISO : Kriging with an external drift

Metric	Evaluates	Application
ME	Bias in predictions	Kriging (ensemble mean) + SPAZM
MAE	Overall accuracy	Kriging (ensemble mean) + SPAZM
TWS	Spatial variability	Kriging (ensemble mean) + SPAZM
CRPS	Probabilistic reliability	Full ensemble (conditional simulations)

Table 4.2 – Metrics computed for evaluation.

with an anisotropic variogram derived from CP-RCM precipitation fields. Mean error (ME) measures bias, indicating systematic over- or underestimation. Mean absolute error (MAE) quantifies overall prediction accuracy.

4.3.2.2 Spatial Structure Evaluation with Radar Analyses

Beyond point-scale accuracy, we assess whether interpolated precipitation fields reproduce the true observed spatial variability. The Teweles–Wobus Score (TWS,Teweles and Wobus (1954)) is used to compare the spatial gradients of interpolated precipitation fields with those from the radar-based COMEPHORE fields. Subsection 4.2.2.1 describes the COMEPHORE data. We consider COMEPHORE fields as a reference in the study domain because of the good radar coverage, allowing an accurate representation of the size and direction of the heavy precipitation cells. It should be noted that for stratiform events, COMEPHORE could favor geostatistic models with isotropic covariance by construction.

TWS is defined as :

$$\mathrm{TWS} = \frac{\sum_{(s,s')\in \mathrm{Adj}} |(p_s - p_{s'}) - (\hat{p}_s - \hat{p}_{s'})|}{2\sum_{(s,s')\in \mathrm{Adj}} \max(|p_s - p_{s'}|, |\hat{p}_s - \hat{p}_{s'}|)},$$

where Adj is the set of adjacent grid points (s, s') in the northern-southern and eastern-western direction within the study domain, p_s ($\hat{p}_s$) is the COMEPHORE (predicted) daily precipitation amount at the grid point s divided by the maximum grid amount. In this part, the interpolated fields are obtained using all rain gauges in the study domain. This metric is particularly relevant for evaluating the performance of variograms in capturing directional precipitation patterns. Lower values of TWS indicate better agreement with radar-based spatial structures.

4.3.2.3 Probabilistic Performances and Uncertainty Quantification

The ensemble spread of conditional simulations provides uncertainty estimates for interpolated precipitation fields. We evaluate whether these uncertainty estimates are both statistically reliable and hydrologically relevant.

We evaluate probabilistic performances from the geostatistical models (rgISO, rgANISO, arISO, arANISO) using Continuous Ranked Probability Score (Matheson and Winkler, 1976) (CRPS) metrics on the 786 precipitation events using the same leave-one-cluster out procedure. A lower CRPS indicates better probabilistic distribution. To assess whether interpolation uncertainty translates into hydrologically realistic precipitation estimates, we compare, for the 20 most intense events, the ensemble spread of mean catchment precipitation (from conditional simulations) to the radar-derived mean catchment precipitation (from COMEPHORE). A reliable spatial interpolation model should ensure that the observed catchment precipitation falls within the simulated uncertainty range.

Table 4.2 summarizes the considered metrics.

4.3.2.4 Case studies

We illustrate applications of the spatial interpolation models to provide concrete examples of how variograms affect precipitation interpolation. We show ensemble means, a sample of conditional simulations, and fitted anisotropic variograms for the 2008-05-26 and the 2014-09-18 days. The first event is an example of a South-North anisotropic event. The second is a Cevenol episode, with stationary storm cells, resulting in 300–400 mm precipitation amount in the first foothills of the Cevennes region.

4.4 Results

We conduct cross-validation at rain gauge stations and evaluate spatial structure using a radar-based metric to assess the performance of deterministic and stochastic models. The reliability of ensemble spreads is also examined. The ensemble of simulations provides uncertainty quantification, which is crucial for hydrological applications. Additionally, we illustrate the methodology with two case studies of daily precipitation fields, showing ensemble means and conditional simulations.

4.4.1 Evaluation of ensemble means

Leave-one-cluster-out cross-validation evaluates the accuracy of ensemble means for all rain gauge stations in the Cevennes region. We compute the mean error and mean absolute error on intense precipitation ($\geq$ 50 mm) for the 786 events.

SPAZM has lower spatial interpolation skills than rgISO, rgANISO, arISO, and arANISO (Fig.4.2). Notably, SPAZM systematically underestimates intense precipitation in the northernmost high-altitude areas, with mean errors ranging from -30 to -50 %, whereas other models (rgISO, rgANISO, arISO, arANISO) show less severe underestimation (-20 to -30 %). SPAZM simultaneously underestimates and overestimates precipitation at neighboring stations, raising concerns about its robustness. rgISO, rgANISO, arISO, and arANISO all underestimate intense precipitation on average. The anisotropy contribution is only visible in mean absolute error for the most northeasterly rain gauge stations.

4.4.2 Spatial evaluation using radar-analysis

To complement cross-validation, the TWS investigates the image gradient similarities, taking COMEPHORE fields as references. Lower TWS values indicate a better resemblance to COMEPHORE. Figure 4.3 illustrates the distribution of TWS values for three event classes : (1) Low anisotropy events ($0.75 \leq \eta \leq 1$), (2) Medium anisotropy events ($0.5 \leq \eta \leq 0.75$), (3) Strong anisotropy events ($0 \leq \eta \leq 0.5$). η results from the anisotropy ratio estimation with the daily AROME fields. TWS scores demonstrate a lower gradient image resemblance to COMEPHORE for SPAZM and a better resemblance for arANISO when strong anisotropy occurs. rgANISO does not outperform rgISO in image gradient similarities. The estimation of anisotropic variograms with rain gauges causes a loss of robustness, which is not attenuated even when strong anisotropy arises. COMEPHORE relies on kriging for stratiform precipitation and radar data for convective precipitation. For this reason, models (rgISO, rgANISO, arISO, arANISO) built on the Trans-Gaussian framework unsurprisingly outperform SPAZM. However, COMEPHORE uses isotropic covariance in the kriging step, meaning only radar carries anisotropy. This suggests that the anisotropic variogram allows the mimicking of radar fields.

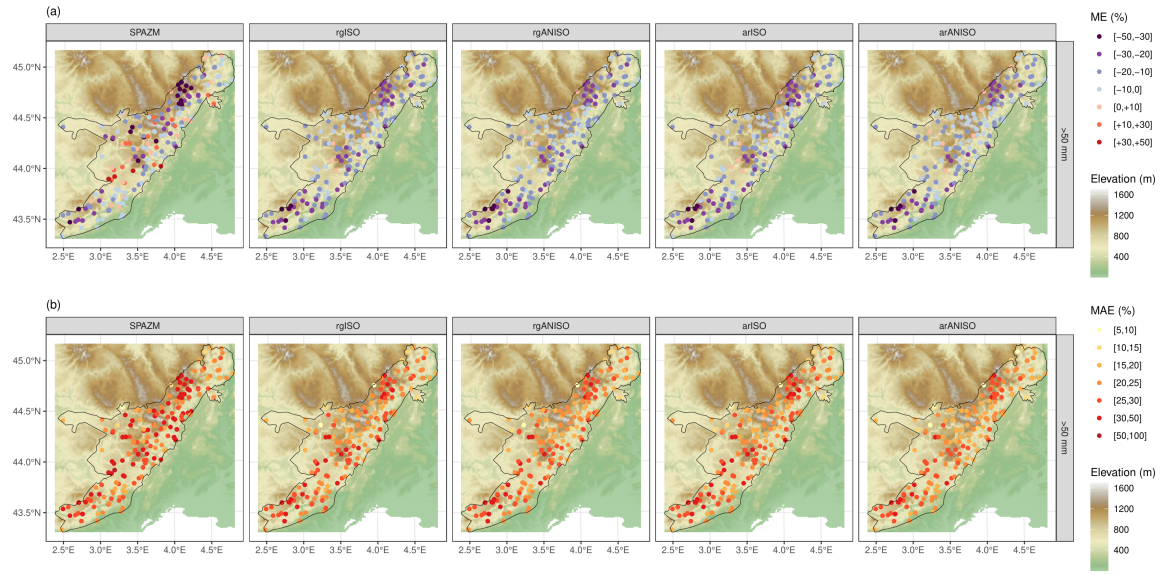

Figure 4.2 – Cross-validation mean error (ME, **(a)**) and mean absolute error (MAE, **(b)**) for rain gauge stations in the Cevennes region, considering days with more than 50 mm. Results are shown for deterministic models (SPAZM) and stochastic models (rgISO, rgANISO, arISO, arANISO). For stochastic models, the cross-validation is conducted on the mean of 100 ensemble members from conditional simulations. Black contours indicate the Cevennes region.

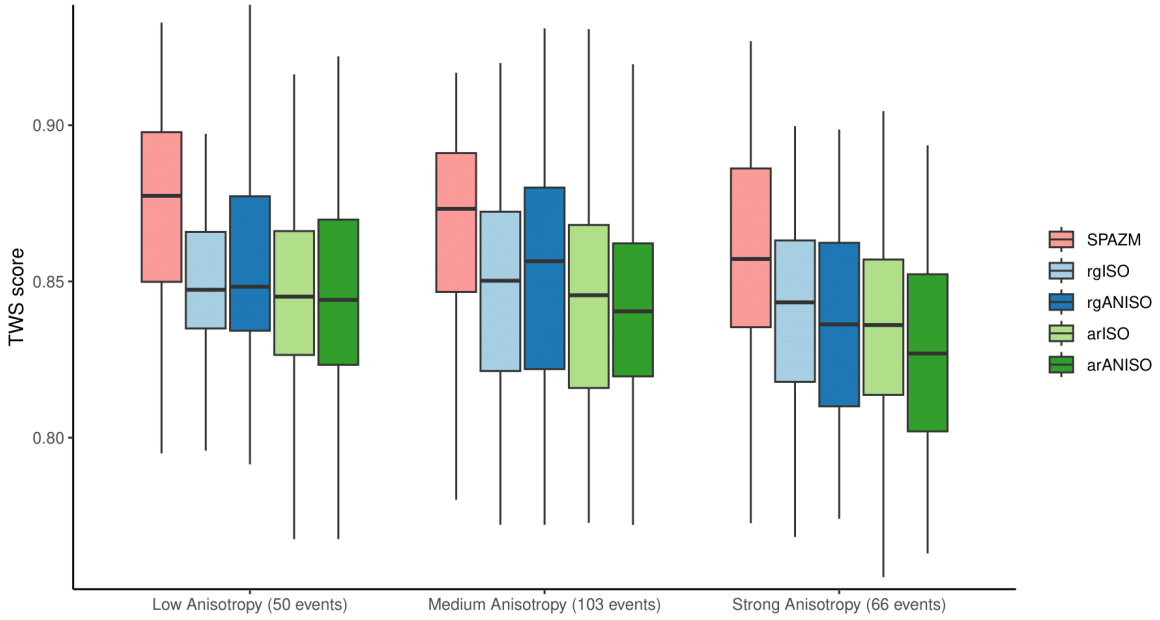

Figure 4.3 – Distribution of TWS scores for deterministic models (SPAZM) and stochastic models (rgISO, rgANISO, arISO, arANISO). Low values of TWS scores indicate better image gradients, using COMEPHORE fields as references. The distributions of TWS scores are plotted for low estimated anisotropy ratio ($0.75 \leq \eta \leq 1$, left), medium estimated anisotropy ratio ($0.5 \leq \eta \leq 0.75$, center), and strong estimated anisotropy ratio ($0 \leq \eta \leq 0.55$, right). The number of events is displayed per event class. For the stochastic models, the evaluation is conducted over the mean of 100 ensemble members of conditional simulations.

4.4.3 Probabilistic performances and Uncertainty Quantification

To assess the reliability of ensemble simulations, we apply the same cross-validation approach used for evaluating ensemble means (see Subsection 4.4.1). The Continuous Ranked Probability Score (CRPS) is computed to quantify probabilistic prediction accuracy, where lower values indicate better performance. Distribution of CRPS scores reveals similar performances for rgISO, rgANISO, and arISO but a notable improvement with arANISO (Fig.4.4). The error reduction is substantial for strong anisotropy events. This suggests that integrating anisotropy into the covariance structure using AROME enhances the ability of the ensemble to capture observed daily precipitation. For this reason, we later quantify precipitation uncertainty using conditional simulations from anisotropic covariance.

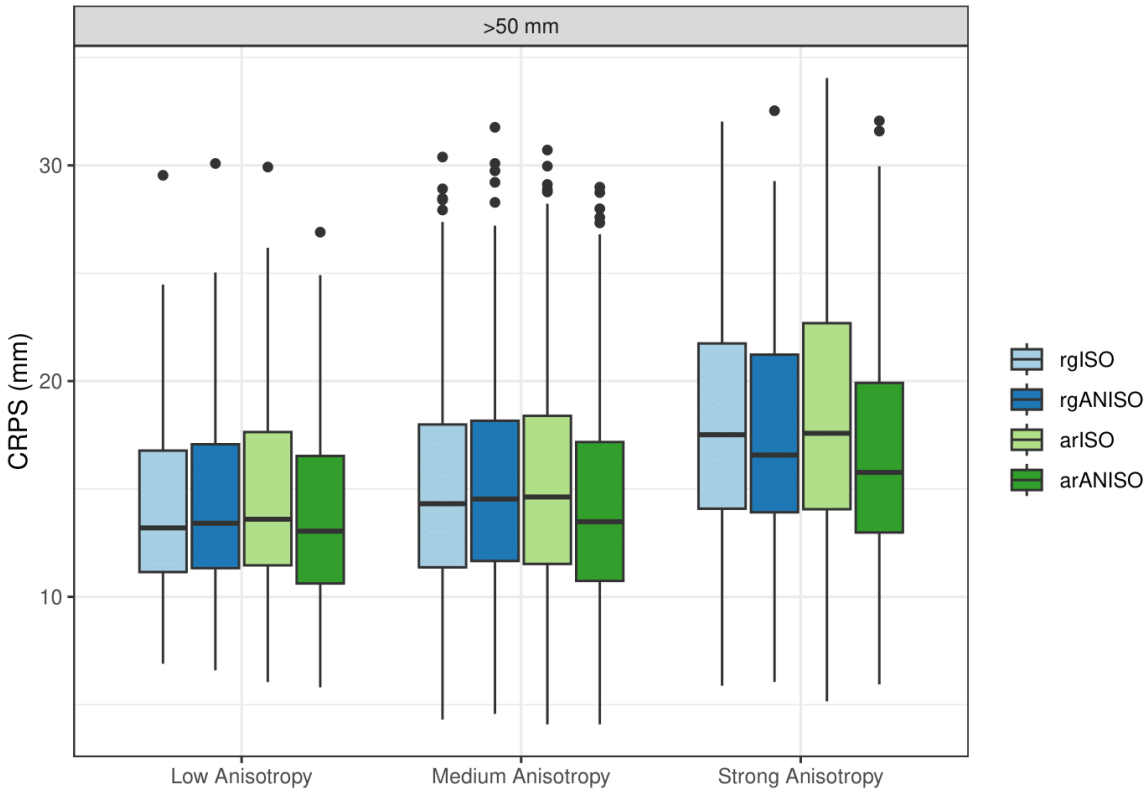

Figure 4.4 – Distribution of cross-validation CRPS scores for stochastic models (rgISO, rgANISO, arISO, arANISO). 1 mean value of CRPS is obtained for each station within the Cevennes region for the days with more than 50 mm. Lower CRPS values indicate better spatial interpolation. The distributions of CRPS scores are plotted for low estimated anisotropy ratio ($0.75 \leq \eta \leq 1$, left), medium estimated anisotropy ratio ($0.5 \leq \eta \leq 0.75$, center), and strong estimated anisotropy ratio ($0 \leq \eta \leq 0.5$, right).

For the 20 most intense events, the mean catchment precipitations derived from the ensembles of 100-member arANISO from conditional simulations closely agree with COMEPHORE estimates (Fig.4.5) with a high rain gauge density. The interquartile range of the simulations frequently contains the mean COMEPHORE precipitation for the Chassezac at Sainte-Marguerite and the Thines at Pont de Gournier catchments. For the Chassezac at Pont du Mas catchment, the interquartile range does not necessarily encompass COMEPHORE precipitation, but the full range of the ensemble does encompass it. This suggests the reliability of the uncertainty estimates provided by the ensemble. arANISO is robust, as conditional simulations nearly agree with COMEPHORE estimates in an ungauged scenario. The artificial

decrease of rain gauge density causes a slight negative bias in the conditional simulations. The latter frequently contain COMEPHORE precipitations through wider confidence intervals.

As expected, uncertainty increases with precipitation intensity, decreases with catchment size and rain gauge density, and provides asymmetrical distributions on mean precipitations. For instance, on 2014-09-18, the mean rainfall on the small Thines at Pont de Gournier catchment ranges from 175 mm to more than 450 mm with the complete set of rain gauges, representing a factor higher than 2.5. In contrast, the uncertainty is lower (factor of 1.33) for larger catchments such as the Chassezac at Sainte-Marguerite.

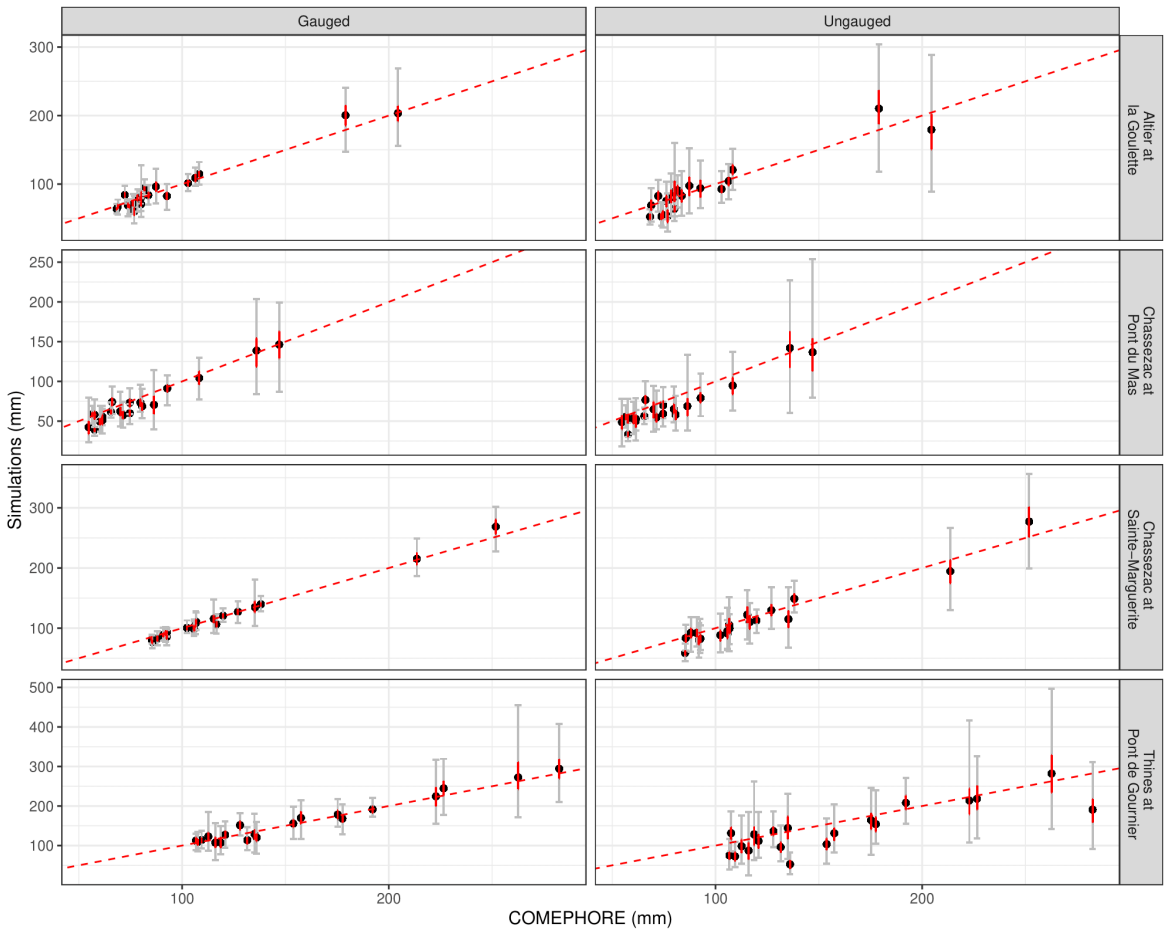

Figure 4.5 – Scatter plot between mean catchment COMEPHORE (x-axis) and simulated (y-axis) precipitations in two rain gauge density scenario : using all rain gauge available (*Gauged*, left panels), removing the rain gauge of the main catchment (*Ungauged*, right panels). The 20 days with the highest COMEPHORE precipitation are considered for each catchment represented in the vertical panels. The simulations are derived from conditional simulations with anisotropic covariance (arANISO). The vertical lines in red (grey) illustrate the 25-75 (0-100) % range of simulations. Black points indicate the ensemble means. The dashed line represents the diagonal.

4.4.4 Case studies

To further illustrate model performance, we analyze precipitation fields for two selected events, using COMEPHORE as the reference. Subsection 4.2.2.1 describes the COMEPHORE data. Figure 4.6 presents daily precipitation maps for four catchments. While all models broadly reproduce the spatial structure of COMEPHORE fields, important differences

emerge. SPAZM exhibits both local overestimation and underestimation, producing overly broad precipitation cells. rgISO also yields overly smooth fields, leading to high-intensity underestimation. arISO slightly mitigates this issue, as seen in the 2014-09-18 case, where it captures more intense precipitation than rgISO. rgANISO captures the radar anisotropy for the 2008-05-26 events but produces an inaccurate spatial structure for the 2014-09-18 event. arANISO provides the most realistic interpolation, reducing both excessive smoothing and underestimation of high intensities. It is the only stochastic model able to capture the highest precipitation values (388–444 mm) in the 2014-09-18 event, demonstrating the advantage of incorporating directional effects.

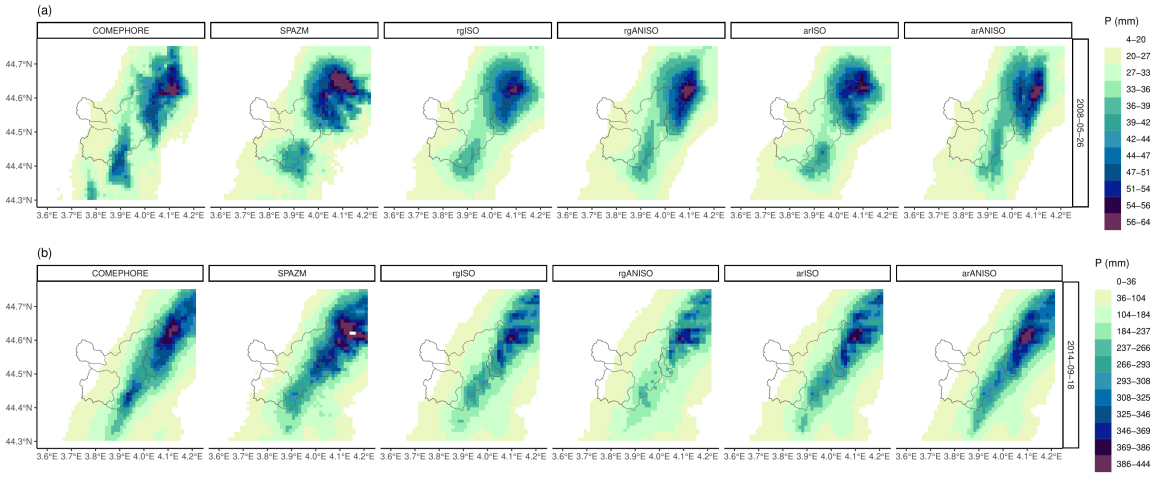

Figure 4.6 – Daily precipitation field illustrations, with a focus on the four catchments for the 2008-05-26 **(a)** and 2014-09-18 **(b)** days. Daily precipitation fields are obtained with deterministic models (COMEPHORE, SPAZM) and stochastic models (rgISO, rgANISO, arISO, arANISO). For the stochastic models, the fields correspond to the mean of 100 ensemble members derived from conditional simulations. Precipitation is expressed in mm. Figure 4.1 shows the locations of the catchments.

A single precipitation field does not reflect the interpolation uncertainty, leading to unwanted smoothing spatial patterns. Conditional simulations provide an attractive alternative to derive a set of equiprobably plausible fields. Figure 4.7 illustrates five conditional simulations with anisotropic covariance (arANISO) for the 2008-05-26 and 2014-09-18 days, revealing different spatial patterns and precipitation intensities. The Thines at Pont de Gournier catchment, located near the center of the strong cell intensities, has a substantial mean precipitation uncertainty on 2014-09-18. Simulation 49 gives rise to nearly 250 mm mean catchment precipitation, compared to more than 350 mm for simulation 15.

Figure 4.8 displays the AROME fields and the corresponding anisotropic fitted variograms for the two case studies. Although the AROME fields do not show the same spatial variability and precipitation intensity as COMEPHORE (Fig.4.6), they include nearly the same anisotropy. The 2008-05-26 event shows a higher spatial correlation in the north-south direction. The 2014-09-18 one is characteristic of a Cevenol episode with a higher spatial correlation in the southwest-to-northeast direction. Table 4.3 collects information about η and θ estimated in the 786 events. 50 % of events have $\eta < 0.5$. The directional effects mainly occur in the north-south direction to the southwest-to-northeast direction.

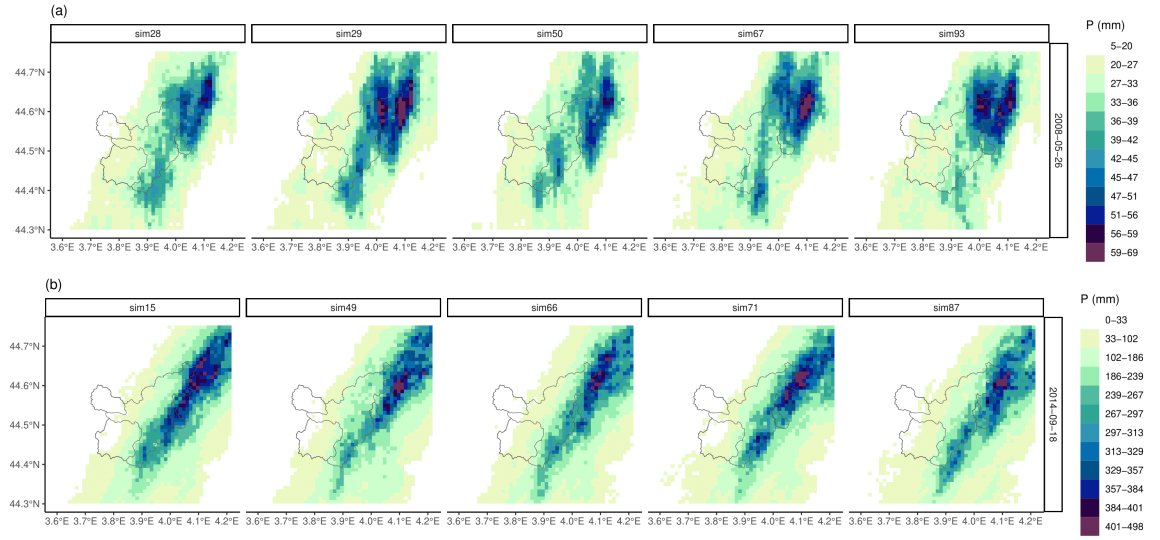

Figure 4.7 – Anisotropic (arANISO) illustration of conditional simulations of daily precipitation fields, with a focus on the four catchments for the 2008-05-26 **(a)** and 2014-09-18 **(b)** days. Five members are randomly sampled from a 100 ensemble. Precipitation is expressed in mm. Figure 4.1 shows the locations of the catchments.

Parameter/Quantile	q0	q10	q20	q30	q40	q50	q60	q70	q80	q90	q100
θ	0	6	11	18	23	29	39	68	158	171	180
η	1	0.80	0.67	0.62	0.56	0.50	0.48	0.43	0.38	0.31	0.18

Table 4.3 – Anisotropy parameters estimated with daily AROME precipitation fields, namely the angle (θ) of dominant spatial autocorrelation and the anisotropy ratio (η) with the corresponding orthogonal direction. Deciles summarize the parameter values.

4.5 Discussion

In this study, we derive anisotropic variograms from CP-RCM simulations for spatial interpolation of precipitation, an approach that, to our knowledge, has not been previously explored. Estimating anisotropy parameters based solely on rain gauge stations is challenging due to the sparse and irregular station networks. However, CP-RCM simulations provide a way of characterizing anisotropy. We demonstrate that anisotropic variograms improve probabilistic precipitation analysis compared to isotropic ones through both point-based and spatial evaluations. In the following, we discuss the advantages and limitations of our approach and outline the further developments that are needed.

4.5.1 Ensemble from conditional simulations versus local regression approach

This study highlights that Trans-Gaussian Random Fields (kriging with external drift) outperform local regression models in robustness and spatial variability. SPAZM, a local regression interpolator, excessively spreads precipitation cells and overcorrelates precipitation with altitude. This overcorrelation results in poor performance for convective events, leading to regional inconsistencies where SPAZM significantly underestimates or overestimates intense precipitation in localized areas. In contrast, the ensemble mean from Trans-Gaussian Random Fields shows better regional coherence, despite the global underestimation of intense precipitation. This bias is well-known in kriging studies (Hiebl and Frei, 2018). Conditional simulations from Trans-Gaussian Random Fields provide an alternative to generate more realistic preci-

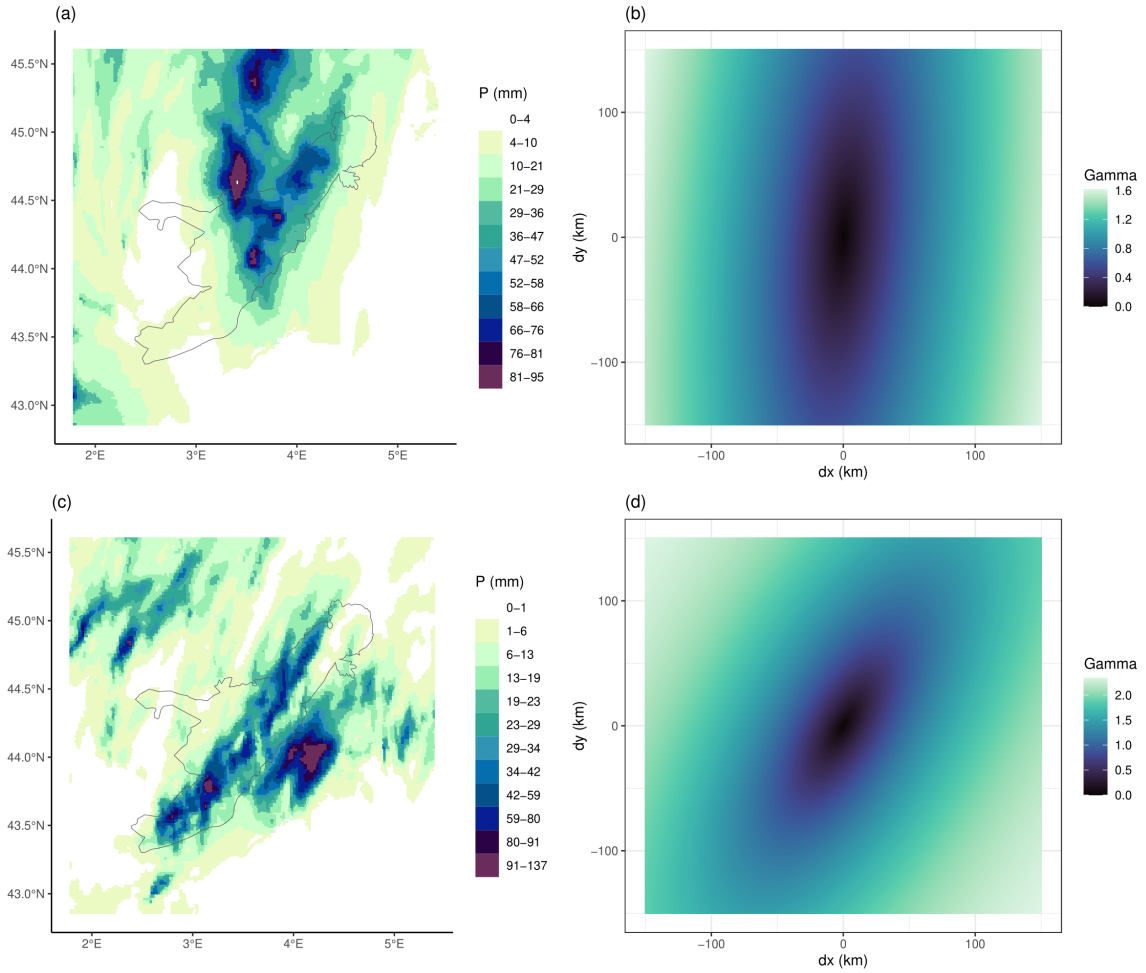

Figure 4.8 – Examples of two AROME daily precipitation fields used to derive anisotropic variograms for the 2008-05-26 **(a)** and 2014-09-18 **(c)** days. Precipitation is expressed in mm. Black contours represent the Cevennes region. In the 2D variograms **(b), (d)**, low (high) gamma values indicate strong (weak) spatial autocorrelation between observations, spaced from dx (dy) in horizontal (vertical) km scale.

pitation. This approach accurately captures large-scale convective events. Further evaluation is needed in ungauged areas with localized convection cells and complex topography, where orographic effects drive uncertainty.

4.5.2 Covariance estimation

Estimating anisotropic parameters typically requires a high density of rain gauge stations, a condition rarely met in practice. Our results show that CP-RCM simulations, despite their imperfections, effectively capture anisotropic precipitation structures, making them valuable for informing variogram parameters in regions with limited observational data.

In this study, we estimate four covariance models using weighted least squares : (1) isotropic covariance from rain gauge stations (rgISO), (2) anisotropic covariance from rain gauge stations (rgANISO), (3) isotropic covariance from CP-RCM simulations (arISO), and (4) anisotropic covariance from CP-RCM simulations (arANISO). Considering anisotropy into the covariance structure using rain gauges (rgANISO) does not necessarily improve interpolation performances compared to isotropic covariance (rgISO). This result agrees with the few studies on covariance comparisons (Haberlandt, 2007; Shi et al., 2007; Haylock et al., 2008).

Using a limited number of rain gauges generates a loss of robustness in estimating the covariance parameters despite actual anisotropy presented in the daily precipitation fields. arISO shows similar performances to rgISO. This suggests that the rain gauge density is high enough to capture spatial autocorrelation in the study region. This also implies that CP-RCM simulations could serve as a viable alternative for estimating spatial autocorrelation in areas with sparse rain gauge station coverage. Estimating anisotropic parameters usually requires a large number of rain gauge stations, which is rarely met in practice. arANISO outperforms the other stochastic models. This approach aligns with previous studies that have used radar data to infer anisotropy through nonparametric estimation (Velasco-Forero et al., 2009; Schiemann et al., 2011; Gyasi-Agyei, 2016). High-quality CP-RCM simulations, increasingly available worldwide, might correctly carry anisotropic information.

The covariance modeling in this study has two main limitations. Firstly, CP-RCM simulations may miss or inaccurately generate precipitation cells, leading to biases in the estimation of covariance parameters such as the range, the anisotropy ratio, and the anisotropy angle. Secondly, the assumption of second-order stationarity may not hold on large spatial domains. Topographical effects might induce spatial non-stationarity in the covariance structure. The windward mountainsides might encounter more spatial variability than the leeward ones. The study region has daily oceanic or Mediterranean influences, but not both simultaneously, limiting spatial non-stationarity. Several authors implement spatial non-stationarity of the covariance (Paciorek and Schervish, 2006; Risser and Calder, 2017; Risser et al., 2019). For computational reasons, we decided not to include non-stationarity.

Despite those limitations, we are confident in the study's transposability to other regions of similar size with high-quality CP-RCM simulations. Furthermore, the scientific community should explore whether the same methodology can be applied using RCM simulations in regions where CP-RCM simulations are unavailable. The methodology might also be applied to real-time interpolation using numerical weather forecasts.

4.5.3 Quantification of interpolation uncertainty

We assess precipitation interpolation uncertainty at the catchment scale, which is relevant for hydrological applications. For very small catchments (17 km^2), the simulated mean catchment precipitation can vary widely by a factor of 2.5, highlighting substantial uncertainty despite high rain gauge density. Using a gamma distribution to normalize daily observations creates an asymmetrical distribution of mean catchment precipitation, which appears to be physically reasonable. Other authors (Erdin et al., 2012; Frei and Isotta, 2019) frequently used the Box-Cox transformation to normalize data, causing uncertainties in the back-transformation step. Box-Cox transformations can lead to over- or under-normalization, artificially inflating or deflating the uncertainty in spatial interpolation. Standard square root transformation, a special case of Box-Cox (parameter equal to 0.5), often leads to flattening high precipitation values (Erdin et al., 2012), causing underestimation of spatial interpolation uncertainty.

Uncertainty in precipitation analysis mainly arises from precipitation undercatch and spatial interpolation methods.

In this study, rainfall prevails over snowfall, and precipitation undercatch might be considered negligible. However, in snow-dominated regions, precipitation undercatch is significant (Sevruk et al., 2009; Pollock et al., 2018) under windy conditions. We propose fitting an asymmetrical gamma distribution to the catch ratio to handle this issue. The parameters of this distribution would depend on several factors, including the precipitation phase (rain or snow), precipitation intensity, rain gauge type, its exposure, and wind speed.

While we modeled the primary sources of uncertainty related to spatial interpolation, additional uncertainty remains unaddressed :

- We assume fixed parameters for the gamma distribution used to normalize the data. A natural extension would be to generate multiple sets of gamma parameters and run conditional simulations for each.
- The seasonal climatological background fields used in this study are treated as deterministic despite inherent uncertainties. Further developments should explore probabilistic background fields to propagate uncertainty better.
- In addition, we did not consider the uncertainty related to the estimation of the covariance parameters. Bayesian inference to estimate covariance parameters (Frei and Isotta, 2019), using informative priors derived from CP-RCM simulations, is a logical extension.

Bayesian hierarchical models present an ideal framework to deal with this combination of interdependent uncertainties that can be propagated into hydrological models.

4.6 Conclusion

This study compares different covariance estimations for conditional simulations of daily precipitation using rain gauge stations. The evaluated models include (1) local regression interpolator called SPAZM ; Trans-Gaussian Random Fields with (2) isotropic covariance estimated with rain gauges, (3) anisotropic covariance estimated with rain gauges, (4) isotropic and (5) anisotropic covariances estimated from daily CP-RCM simulations. The expectation of the Random Fields is a function of topographical variables and a seasonal climatological background field. We assess interpolation performance through cross-validation and a spatial metric, using radar-derived analysis as a reference.

Results indicate that Trans-Gaussian Random Fields modeling, whatever the covariance used, consistently outperforms the local regression interpolator SPAZM in cross-validation and spatial metrics. The geostatistical models are more robust to low rain gauge density and resemble more radar fields. Among the covariance models tested, anisotropic covariance derived from CP-RCM simulations better captures directional precipitation structures observed in radar data and shows superior cross-validation scores for both ensemble mean and spread. By bypassing the lack of robustness of anisotropy estimation using sparse rain gauge networks, this approach reveals the clear value of incorporating anisotropy into the spatial interpolation of daily precipitation. The obtained ensemble of 100 mean catchment precipitation simulations successfully encompasses radar-based estimates for intense precipitation events, highlighting its potential for uncertainty quantification, a key consideration for hydrological modeling.

These findings suggest that deriving anisotropic variograms from high-quality CP-RCM simulations is a promising approach for probabilistic precipitation interpolation. A natural extension of this work is to integrate the generated precipitation ensembles into probabilistic hydrological modeling, further improving flood risk assessment and water resource management.

5

Un cadre géostatistique reproductible pour les ensembles de précipitations quotidiennes en terrain montagneux : évaluation multi-échelle et applications hydrologiques

Abstract Gridded precipitation datasets are essential for hydrological and climate applications. However, commonly used products suffer from systematic biases such as seasonal total underestimations in mountainous regions and excessive smoothing of the spatial variability of extremes. Here, we present a reproducible workflow to generate daily precipitation ensembles, conditioned on rain gauges, at 1 km resolution for mountain regions. The approach leverages climatological information and spatial variability from convection-permitting regional climate model (CP-RCM) simulations. The workflow corrects rain-gauge undercatch, incorporates CP-RCM-based climatology to improve seasonal totals, and estimates anisotropic variograms from CP-RCM daily fields to capture directional precipitation structures. Finally, Sequential Trans-Gaussian Simulations generate the daily ensembles of 100 members. We evaluate commonly used gridded precipitation products and the proposed approach using independent evaluation data, including in-situ measurements in mountainous areas (snow water equivalent, glacier mass balances, streamflow), regional catchment-scale water balance models, and hydrological models. Results demonstrate that it outperforms deterministic gridded products. First, it more accurately captures seasonal totals in high-altitude SWE and glacier observations, and reproduces both seasonal precipitation amounts and their interannual variability. Second, the daily ensembles capture fine-scale spatial variability and quantify interpolation uncertainty, improving flood hydrological modelling. The workflow is fully reproducible via open-source code, transferable to regions with sparse rain-gauge networks or limited radar coverage. Beyond precipitation, it is generalisable to other climate variables simulated by weather models.

5.1 Introduction

Daily gridded precipitation datasets are essential for a wide range of applications, including snowpack modeling (Quéno et al., 2016), glacier mass balance assessments (Vionnet et al., 2019), hydrological modeling (Evin et al., 2024), or climate model evaluation (Fantini et al., 2018). While rain gauges primarily measure precipitation, their sparse and uneven distribution, especially in mountainous regions, limits their ability to capture spatial variability (Hofstra et al., 2010). Interpolating these point measurements onto regular grids is therefore necessary, but particularly challenging in complex terrain due to strong orographically induced gradients (Dura et al., 2024a) and localized extremes.

Several categories of gridded precipitation datasets exist, each with its specific strengths and limitations, particularly when applied to mountainous hydrology. Atmospheric reanalyses, including The Copernicus European Regional ReAnalysis Land (CERRA-Land, Le Moigne, 2021), the *Système d'Analyse Fournissant des Renseignements Adaptés à la Nivologie* (SAFRAN, Vidal et al., 2010), offer physically consistent long-term records but remain limited by their coarse resolution, smoothing of orographic effects (Dura et al., 2024a), and underestimation of extremes. Radar-based datasets such as *COmbinaison en vue de la Meilleure Estimation de la Précipitation HOraiRE* (COMEPHORE , Champeaux et al., 2009) or CombiPrecip (Sideris et al., 2014) capture the small-scale variability of extremes. However, ground echoes, beam blockage, and bright-band contamination (e.g. Berne and Krajewski, 2013) cause large seasonal total underestimations (Faure et al., 2019; Gugerli et al., 2020), limiting their application in mountain environments. Gauge-based interpolation products such as SPAZM (Gottardi, 2009), and SPARTACUS (Hiebl and Frei, 2018) offer an improved mountain climatology representation using climatological background fields (Masson and Frei, 2014; Jiang et al., 2023), but remain affected by sparse gauge coverage, undercatch bias (Sevruk et al., 2009; Grossi et al., 2017), and oversmoothing of daily spatial variability (Hofstra et al., 2010; Hiebl and Frei, 2018). More recently, ensemble datasets such as E-OBS (Cornes et al., 2018), RhydchprobD (Frei and Isotta, 2019), and FYRE Climate (Devers et al., 2021) have emerged,

improving representation of extremes while quantifying uncertainty. But they still fall short in capturing high-elevation precipitation patterns required for mountainous hydrology.

Despite these advances, no existing product simultaneously meets the combined requirements of mountainous hydrology, namely high spatial resolution, long-term coverage, realistic orographic representation, and uncertainty quantification for extreme events. This gap limits our ability to robustly model both seasonal water balances and extreme hydrological events in mountain catchments. This study addresses these shortcomings by introducing a reproducible workflow that combines climatological background fields from the Convection-Permitting Regional Climate Model (CP-RCM) (Caillaud et al., 2021) and conditional geostatistical simulation of daily anomalies to generate ensemble daily precipitation fields. The framework is distributed as a modular open-source code, allowing users to apply it in other regions or update it with new inputs. We ensure reproducibility by delivering ensemble precipitation fields for two years over the Southern Alps, relying solely on open-access gauge stations. We conduct a multi-perspective evaluation of this product using a diverse set of independent datasets. The novelty of this work does not lie in the individual methods, which are well established, but in their integration into a coherent framework tailored to mountainous regions, the open-source implementation, and the richness of the multi-evaluation. This evaluation encompasses streamflow balances in high-altitude basins, *in-situ* snow water equivalent sensors, glacier mass balance observations, and daily streamflow time series. The remainder of the paper is structured as follows : Section 2 describes the study domain, the data used for interpolation, and the evaluation datasets. Section 3 presents the interpolation framework and evaluation design. Section 4 reports the evaluation results for hydrological, nivologic, and glaciological applications. Section 5 discusses limitations, perspectives, and reproducibility. Section 6 gives the conclusions.

5.2 Study domain and hydrometeorological data

5.2.1 Study domain

The study focuses on the major mountainous regions of France, including the Alps, the Pyrénées, the Massif Central, and the Cévennes. These areas exhibit strong altitudinal gradients (Dura et al., 2024a), which significantly influence precipitation patterns and hydrological processes. The Alps and Pyrénées experience a mix of oceanic and continental influences, with substantial snow accumulation in winter and convective rainfall in summer. The Massif Central and Cévennes are more exposed to Mediterranean influences, leading to intense autumnal precipitation events, particularly in the Cévennes. The observational network used in this study comprises approximately 5,305 rain gauges, from Météo-France and Electricité de France (EDF, the main electricity provider in France), providing daily precipitation from 1982 to 2018. The rain gauge distribution is irregular in space : denser in the Massif Central and the Cévennes, and sparser in the Alps and the Pyrénées. In addition, 14 Cosmic Ray Snow Sensors (in French *Nivomètre à Rayonnement Cosmique*, NRC) (Gottardi, 2009) are distributed in alpine catchments to monitor seasonal SWE, and three glaciers from the GLACIOCLIM observatory network [1] (namely Saint-Sorlin, Sarennes, Argentière) assess winter accumulation reproduction at high elevations. A subset of 15 catchments, located in the Southern French Alps, where intense convective storms occur primarily during summer and autumn, will be used in hydrological modeling. These catchments are particularly well-suited to assess the ability of precipitation products to reproduce high-intensity events.

1. https://GLACIOCLIM.osug.fr/

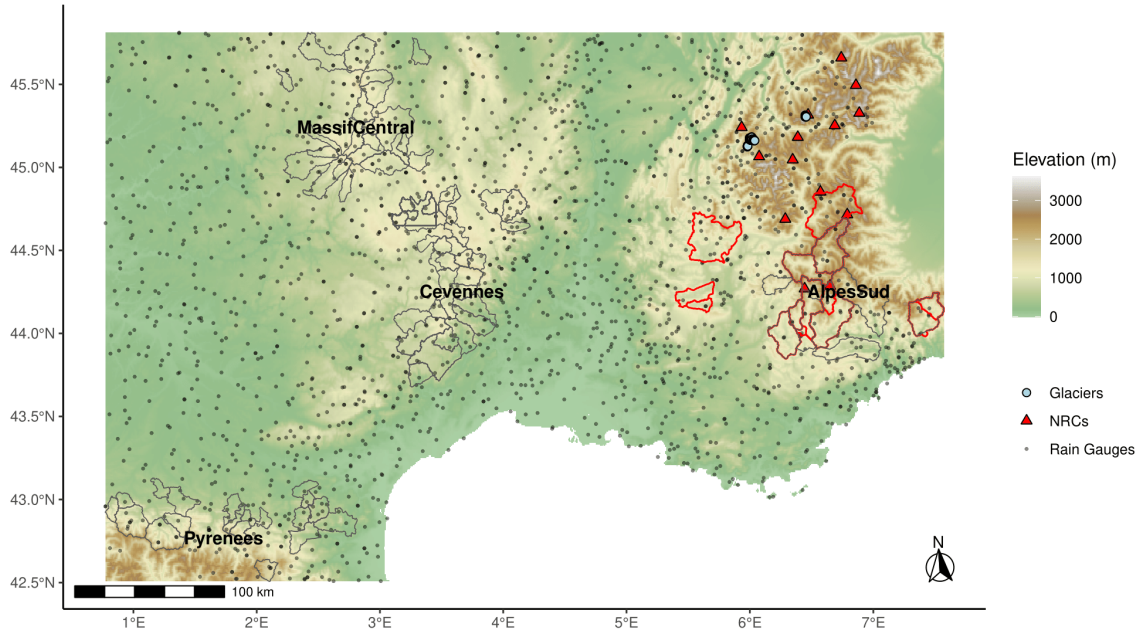

Figure 5.1 – Study domain with elevation (meters). Grey dots indicate rain gauges, light blue dots mark glacier sites, and red triangles show Cosmic Ray Snow Sensors (NRC). Names of major mountain regions and associated catchments are labeled in bold and black, while catchments used for hydrological modeling are highlighted in red. To assess the hydrological mass balance constraints (see sub-section 5.3.2), 11 (AlpesSud), 46 (Cévennes), 42 (MassifCentral), and 20 (Pyrénées) catchments are colored in grey.

5.2.2 Gridded precipitation products

5.2.2.1 ERA5-Land

The fifth generation of European ReAnalysis (ERA5-Land, Muñoz-Sabater et al., 2021) is a global reanalysis dataset that simulates atmospheric and surface variables, including precipitation on an hourly basis. It builds upon the atmospheric fields of ERA5 (Hersbach et al., 2020), downscaled to a finer spatial resolution of 9 km. ERA5-Land solely assimilates satellite and radar data and does not include rain gauge measurements. The density and coverage of satellite and radar networks involved in the assimilation, therefore, influence the accuracy of its precipitation estimates (Hassler and Lauer, 2021). Regions such as Central Europe and the United States exhibit higher data quality, compared to more poorly observed areas like tropical oceans. A key advantage of ERA5-Land is its enhanced spatial resolution, 9 km versus the 31 km resolution of ERA5 or the 80 km of ERA-Interim (Muñoz-Sabater et al., 2021), which contributes to a more accurate representation of precipitation spatial patterns (Gomis-Cebolla et al., 2023).

5.2.2.2 CERRA-Land

The Copernicus European Regional ReAnalysis Land (CERRA-Land, Ridal et al., 2024) represents the latest regional reanalysis product for Europe, available from 1984 onward at a horizontal resolution of 5.5 km. It employs the HIRLAM ALADIN Regional/Mesoscale

Operational NWP In Europe (HARMONIE) atmospheric model, driven by ERA5 boundary conditions, and is executed every 3 hours at its native resolution. The MESCAN system (Soci et al., 2016) refines the outputs through optimal interpolation with approximately 8,000 daily rain gauge records. According to Le Moigne (2021), CERRA-Land offers improved representation of snow depth seasonality in the Alps when compared to ERA5-Land.

5.2.2.3 SPAZM

The *SPAtialisation en Zones de Montagne* (SPAZM) (Gottardi, 2009) is a high-resolution precipitation interpolation tool tailored for mountainous regions. It combines rain gauge measurements with a meteorological background field adjusted based on topographic features and the prevailing weather type of the day. Using geopotential fields, eight distinct weather patterns are identified (Garavaglia et al., 2010), each associated with a corresponding daily mean precipitation field. Local linear regressions incorporating altitude generate these 1 km spatial resolution fields. For any specific day, the daily observed precipitations are used to derive anomalies, which are interpolated and then applied to the mean precipitation field to obtain the daily precipitation field. Historically, SPAZM integrates data from 2,101 stations operated by EDF (including rain gauges (603) and snow totalizers (216)), Météo-France (555), MeteoSwiss (213), Arpa Piemonte (383), and Instituto Nacional de Météorologia (131). Although it incorporates fewer stations than COMEPHORE, those used are at higher altitudes. Several hydrological studies (Gottardi, 2009; Ménégoz et al., 2020; Ruelland, 2020) used SPAZM due to its capacity to yield accurate annual precipitation estimates.

subsectionSnow datasets

5.2.2.4 NRC

The *Nivomètres à Rayonnement Cosmique* (NRCs, Gottardi, 2009) are innovative instruments developed by EDF to monitor SWE using cosmic ray neutron sensing at the daily timescale. These sensors estimate the amount of water stored in the snowpack without the need for snow pits. NRC improves snowpack evolution tracking in the 2,030-2,730 m altitude range for operational hydrological forecasting, especially in the framework of EDF's water resource and hydropower management.

5.2.2.5 Glacier winter mass balance measurements

Winter Surface Mass Balance (WSMB) data is available for five glaciers, namely Saint-Sorlin, Sarennes, Gebroulaz, Argentière, and Mer de Glace, located throughout the French Alps. These glaciers are part of the GLACIOCLIM observatory (Six and Vincent, 2014). WSMB is measured (in $kg \times m^{-2}$) at the end of the snow accumulation season (typically between late April and early May), using snow cores combined with density measurements in both accumulation and ablation zones, with approximately 200 [$kg \times m^{-2}$] (200 mm of SWE) uncertainty (Thibert et al., 2008). We exclude the Argentière and Mer de Glace glaciers from the evaluation as the CP-RCM simulations, used in this study, contain artefacts that cause excessive precipitation in the Mont-Blanc area (Monteiro et al., 2022). Measurement points on the three remaining glaciers are located at relatively high elevations, typically between 2,690 and 3,390 m, thus providing valuable information at altitudes not covered by NRCs. For each glacier and accumulation period, we average WSMB measurements because of the small size of the glaciers (≤ 3 km^2).

5.2.3 Hydrological models

5.2.3.1 GR6J

The *Génie Rural à 6 paramètres Journalier* (GR6J, Pushpalatha et al., 2011) is a lumped daily rainfall–runoff model developed in the context of the airGR hydrological modelling package (Coron et al., 2017). It simulates streamflow based on daily precipitation and potential evapotranspiration, using six parameters that control storage, routing, and exchange processes. Its simplicity and parsimony make it well-suited for large-sample hydrological studies (Tyralis et al., 2023; Devers et al., 2024). GR6J performs well across diverse catchments and climatic conditions (Flores et al., 2021; Kuana et al., 2024; Hrour et al., 2025). We calibrate the model using Kling–Gupta efficiency (Gupta et al., 2009, KGE,) on the daily streamflow.

5.2.3.2 MORDOR-SD

The *MOdèle de RUissellement et de Débit d'ORdre Supérieur – Semi-Distribué* (MORDOR-SD) is a semi-distributed conceptual hydrological model, structured by elevation bands, and developed by EDF (Garavaglia et al., 2017) for simulating river discharges at hourly to daily scales. It incorporates snow accumulation and melt, evapotranspiration, soil moisture dynamics, and flow routing. The catchments are discretized based on elevation bands to better simulate snow and rainfall processes. It is particularly suited for mountainous catchments (Evin et al., 2024) and operational use (Paquet, 2004). Calibration uses multi-objective criteria (Garavaglia et al., 2017).

5.3 Methods

5.3.1 Interpolation framework

Interpolating daily precipitation fields over mountainous terrain requires addressing both measurement errors and spatial variability. The proposed methodology involves three main steps :

(1) correction of gauge undercatch,
(2) construction of climatological background fields stratified by weather regimes, and
(3) conditional geostatistical simulation of daily precipitation anomalies.

Figure 5.2 illustrates the spatial interpolation workflow.

5.3.1.1 Step 1 : Gauge correction

We corrected rain gauge observations for wind-induced undercatch by multiplying all snowfall measurements by 1.6, although undercatch depends on local wind (Sevruk et al., 2009), precipitation intensity (Cauteruccio et al., 2024), gauge type, and also affects rainfall (Pollock et al., 2018). The order of magnitude of 1.6 as a snow correction factor is commonly applied for hydrological and snow applications (e.g. Gottardi, 2009; Jonas and Schirmer, 2022). Daily precipitation at station x_s and day t, denoted $P^{\text{corr}}(x_s, t)$, is corrected for gauge undercatch before interpolation as follows :

$$P^{\text{corr}}(x_s,t) = \alpha_{\text{snow}} \cdot f_{\text{snow}}[T(x_s,t)] \cdot P(x_s,t) + \alpha_{\text{liquid}} \cdot \{1 - f_{\text{snow}}[T(x_s,t)]\} \cdot P(x_s,t) \quad (5.1)$$

where $\alpha_{\text{snow}} = 1.6$ is the correction factor for solid precipitation and $\alpha_{\text{liquid}} = 1.0$ for the liquid precipitation. The solid fraction f_{snow} depends on the mean daily temperature $T(x_s, t)$. Appendix 5.A gives more details on the expression of the solid fraction given the temperature. Determining appropriate temperature thresholds for rain–snow partitioning remains an active area of research, and the sensitivity to this choice was not evaluated in this study.

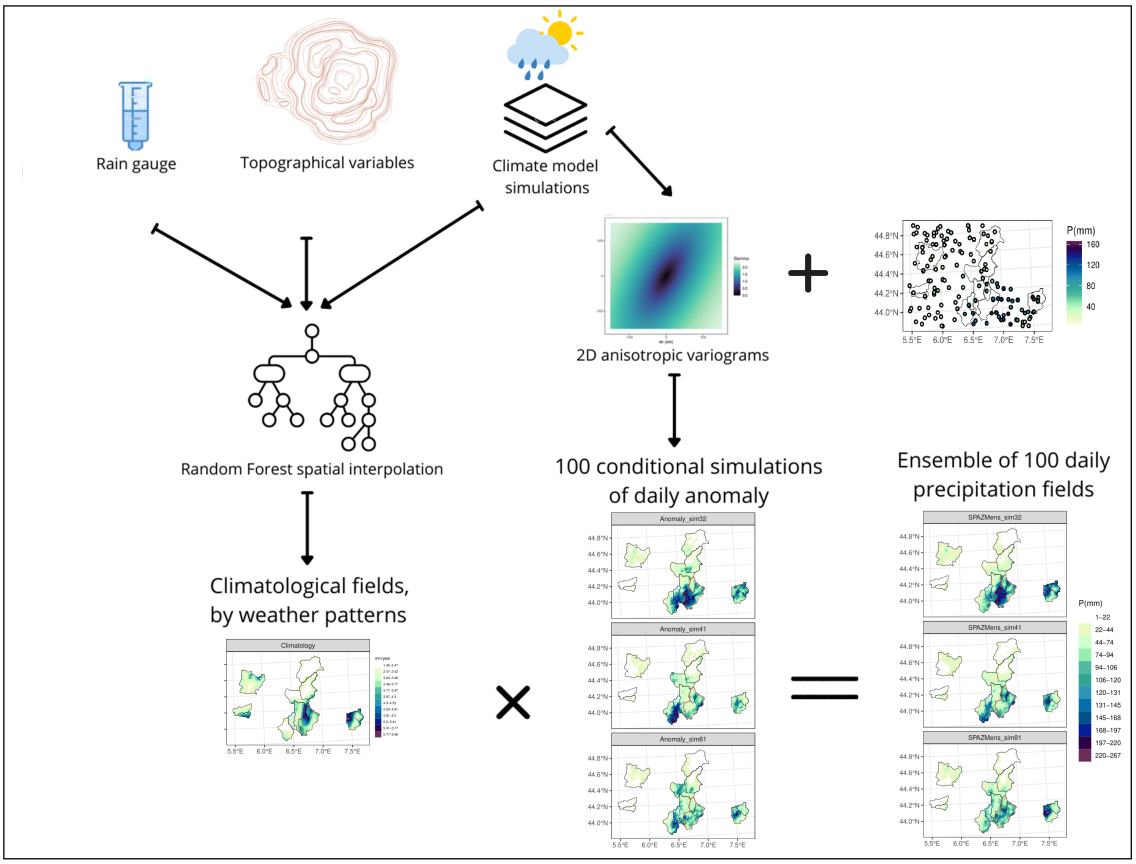

Figure 5.2 – Workflow for generating an ensemble of 100 daily precipitation fields. The process integrates rain gauge undercatch correction, topographical variables, and convection-permitting climate model simulations. These inputs are used in a random forest spatial interpolation to produce climatological fields by weather patterns. Simultaneously, climate model outputs inform 2D daily anisotropic variograms, which are used to generate 100 conditional simulations of daily anomalies. The final ensemble is obtained by multiplying climatological fields with daily anomalies.

5.3.1.2 Step 2 : Climatological construction

A key component of the interpolation framework is the use of climatological background fields stratified by class that represent the mean spatial distribution of precipitation and account for orographic effects. These fields are built from CP-RCM simulations AROME (Caillaud et al., 2021), and refined using long-term rain gauge observations. A machine learning model is used to adjust the model climatology to match observed seasonal totals (Dura et al., 2024b). For each station s and climatological class c (e.g., month, season, or weather regime), the ratio between corrected observations and CP-RCM climatology is $R(x_s, c) = \frac{\overline{P^{\text{corr}}}(x_s,c)}{\overline{M}(x_s,c)}$ where overlines denote climatological averages, and $\overline{M}(x_s, c)$ is the CP-RCM climatology at station x_s. The log-ratios $\log R(x_s, c)$ are interpolated spatially with a Random Forest regression using the following predictors :

$$\log R(x, c) = f[M(x, c), \log M(x, c), \text{alt}(x), \text{lon}(x), \text{lat}(x), d(x, \mathcal{S})], \tag{5.2}$$

where $\text{alt}(x)$ is the altitude at pixel x, $\text{lon}(x)$ is the longitude at pixel x, $\text{lat}(x)$ is the latitude at pixel x, $d(x, \mathcal{S})$ are buffer distances to the station network $\mathcal{S}$. We tune the Random Forest algorithm to choose the hyperparameters. Appendix 5.B indicates the hyperparameters

tested. We use the *ranger* (Wright and Ziegler, 2017) package for Random Forest spatial interpolation.

The background field is reconstructed as :

$$B(x,c) = \exp\big[\log R(x,c) + \log M(x,c)\big]. \tag{5.3}$$

5.3.1.3 Step 3 : Daily anomaly interpolation

Each day t is considered independently. These background fields are then adjusted to match daily rain gauge observations. Anomalies relative to the climatological background are computed as $A(x_s,t) = \frac{P^{\text{corr}}(x_s,t)}{B(x_s,c_t)}$ where c_t is the climatological class of day t. Positive anomalies are transformed into the Gaussian domain through a quantile transformation, which accounts for the skewed nature of precipitation data. Appendix 5.C shows the applied formula for the transformation and back-transformation steps.

The transformed anomalies are modeled as a Gaussian random field as :

$$Z(x,t) = m(x) + \varepsilon(x,t), \tag{5.4}$$

$$m(x) = \beta_0 + \beta_1\,\text{alt}(x) + \beta_2\,\text{lon}(x) + \beta_3\,\text{lat}(x) + \beta_4\,B(x,c_t), \tag{5.5}$$

where all covariates are standardized. The trend $m(x)$ helps capture large-scale spatial gradients in precipitation while allowing the residual component to model finer-scale variability. Spatial variability of the residuals $\varepsilon(x,t)$ is modeled using a daily anisotropic exponential variogram, estimated from CP-RCM precipitation fields. This allows the interpolation to incorporate directional dependence and reproduce elongated structures typical of convective or orographic precipitation. The exponential variogram is widely adopted in geostatistics (Masson and Frei, 2014; Frei and Isotta, 2019), as it captures the smooth decrease of autocorrelation with distance.

$$\gamma(h) = c_0 + c\left[1 - \exp\left(-\frac{d_{\text{aniso}}(h)}{a}\right)\right], \tag{5.6}$$

where c_0 denotes the nugget, c the partial sill, a the range parameter, and d_{aniso} the anisotropic distance. Appendix 5.D defines the anisotropic distance. The variogram parameters are optimized by weighted least squares on CP-RCM anomalies, using weights $w(h) = \frac{N_h}{h^2}$, where N_h is the number of pixel pairs separated by distance h..

For each day t, $N = 100$ conditional simulations $\{Z^{(n)}(x,t)\}_{n=1}^{N}$ are generated with Sequential Gaussian Simulation, conditioned on gauge anomalies, using the *gstat* package (Pebesma, 2018). These simulations reproduce both the observed anomaly values and the spatial structure inferred from the variogram and trend, while providing spatial uncertainty. Back-transformation yields $N = 100$ conditional simulations $\{A^{(n)}(x,t)\}_{n=1}^{N}$ of anomaly fields, and final daily precipitation fields are $\hat{P}^{(n)}(x,t) = A^{(n)}(x,t)\,B(x,c_t)$. This precipitation product is named *Interpolated Station precipitation for Alpine Regions at Daily resolution* (ISARD).

We use the *raster* (Hijmans, 2025) package to manipulate spatial matrix, *sf* (Pebesma, 2018) and *sp* (Pebesma and Bivand, 2005) packages to deal with spatial point data.

5.3.2 Evaluation

5.3.2.1 Accumulated precipitation amounts in mountain catchments

To assess the performance of precipitation products in mountainous environments, a two-scale evaluation strategy is applied : one at the catchment scale, utilizing hydrological mass balance constraints, and another at high-altitude point locations using independent snow-related observations.

At the catchment scale, the evaluation is based on the long-term hydrological mass balance. The Turc-Pike models (also known as the Turc or Budyko-type function) (Turc, 1955; Pike, 1964) are widely used to relate runoff (Q) to precipitation (P) and potential evapotranspiration (ETP) via a simple empirical relationship. It expresses the runoff coefficient $\frac{Q}{P}$ as a function of the humidity index $\frac{P}{ETP}$ as follows :

$$\frac{Q}{P} = \left[1 + \left(\frac{\mathrm{P}}{ETP}\right)^{n}\right]^{-\frac{1}{n}}. \tag{5.7}$$

Q, P, and ETP are in mm.yr^{-1}, and n is a shape parameter fitted using least squares, and describing the climate of the catchments. Low n values (≈ 1) are associated with humid climates and energy-limited regimes. High n values (≈ 3) reveal arid or semi-arid regions, where water is limited and potential evapotranspiration exceeds precipitation. For each precipitation product and mountainous region, we compute the deviation of individual catchments from the fitted regional Turc-Pike model, summarized by the sum of squared errors.

5.3.2.2 Accumulated precipitation amounts at high-elevation sites

At high-elevation sites equipped with NRC, seasonal snow accumulation assesses the interannual variability of gridded precipitation products. For each year, we compute the seasonal SWE accumulation as the difference between the maximum and minimum daily SWE values over the winter season (December 1 to February 28). We select the NRC above 2,000 m, where we assume negligible melt during winter. Considering the sum of daily SWE variations over a season would relax this assumption, but such comparisons are sensitive to snow redistribution and measurement noise. For each year and precipitation product, the correlation coefficient between accumulated SWE and total precipitation assesses interannual agreement. In the case of the ISARD ensemble, the correlation is computed between the SWE accumulation and the ensemble-mean precipitation. We conduct a similar analysis using winter glacier mass balance data from GLACIOCLIM observatories. Since the measurement dates change each year, precipitation accumulation is computed based on the observed start and end dates of the winter mass balance survey. The correlation between observed glacier winter mass balance and accumulated precipitation provides a complementary evaluation of precipitation products in glacierized environments.

5.3.2.3 Hydrological modeling of floods

The hydrological models allow the assessment of precipitation intensity and variability at the catchment scale, using measured streamflow as a reference. 15 catchments in the Southern French Alps are selected due to the high occurrence of intense precipitation in summer and autumn. A split-sample approach is applied independently for each catchment and hydrological model. The available simulation period is split into two equal-length sub-periods. For each configuration, the model is calibrated on the first half and evaluated on the second half, then the procedure is reversed. In both cases, one additional year is used as a warm-up period before each calibration or evaluation phase to minimize the influence of initial conditions. We calibrate independently the models for each precipitation forcing. In the case of the 100-member ensemble precipitation forcing, a first calibration is conducted using the ensemble mean precipitation. The resulting parameter set constitutes initial conditions for calibrating each of the 100 individual ensemble members.

Flood events are selected based on the observed discharge time series. We pick an average of three events per year, ensuring a minimum 5-day separation : if multiple events occur within a 5-day window, we retain only the maximum. Additional criteria are applied to ensure the events are rainfall-driven. Specifically, at least one of the two days preceding the flood must

exhibit precipitation above the 90th percentile, and the basin-averaged daily air temperature on the flood day must be greater than 0°C.

To evaluate the quality of ensemble streamflow forecasts during flood events, we use the Continuous Ranked Probability Score (CRPS), which measures the distance between a predicted cumulative distribution function (CDF) and an observed scalar value. Let $y_t \in \mathbb{R}$ be the observed streamflow on day t, and $F_t(x)$ the forecasted CDF for that day. The CRPS is defined as :

$$\text{CRPS}_t = \int_{-\infty}^{+\infty} \left(F_t(x) - \mathbb{1}_{\{x \geq y_t\}}\right)^2 dx, \tag{5.8}$$

where $\mathbb{1}_{\{x \geq y_t\}}$ is the step function equal to 1 when $x \geq y_t$ and 0 otherwise. We compute CRPS values using the *scoringRules* package (Jordan et al., 2019).

The mean CRPS over the set of flood days in month m, denoted $\mathcal{T}_m$, is equal to :

$$\overline{\text{CRPS}_m} = \frac{1}{|\mathcal{T}_m|} \sum_{t \in \mathcal{T}_m} \text{CRPS}_t. \tag{5.9}$$

To compare gridded precipitation products, we compute the Continuous Ranked Probability Skill Score (CRPSS) relative to SPAZM as :

$$\text{CRPSS}_m(P \mid \text{SPAZM}) = 1 - \frac{\overline{\text{CRPS}_m(P)}}{\overline{\text{CRPS}_m(\text{SPAZM})}}, \tag{5.10}$$

where P denotes any gridded precipitation product under evaluation (ERA5-Land, CERRA-Land, ISARD). CRPSS equals 0 indicates similar skill in hydrological modeling of floods to SPAZM. Positive (negative) values indicate improvements (degradation) over SPAZM.

Furthermore, we evaluate how well the model reproduces the distribution of observed streamflows using the Quantile Relative Error (QRE) metric (Evin et al., 2024). This indicator compares the simulated and observed streamflow quantiles and is defined as follows :

$$QRE_p = 1 - \frac{\hat{F}_o^{-1}(p) - \hat{F}_s^{-1}(p)}{\hat{F}_o^{-1}(p)}, \tag{5.11}$$

where $\hat{F}_o^{-1}(p)$ is the empirical distribution of observed streamflows associated with probability p, $\hat{F}_s^{-1}(p)$ is the empirical distribution of simulated streamflows associated with the same probability. QRE below (above) 1 indicates quantile underestimation (overestimation).

5.4 Results

5.4.1 Accumulated precipitation amounts in mountain catchments

Figure 5.3 displays the fitted Turc-Pike models, stratified by mountainous regions, for the four precipitation products under consideration. Points located in the red zones correspond to catchments exhibiting non-physical hydrological behavior. Specifically, the annual runoff Q must not exceed the yearly precipitation P, and the difference $P - Q$ (*i.e.*, the water available for evapotranspiration) must not exceed the potential evapotranspiration ETP. For each region and precipitation product, the sum of squared errors (SSE) between individual catchments and the fitted curve can be computed. A lower SSE indicates a better agreement between the precipitation estimates and the expected hydrological behavior of the catchments, assuming that catchments within a given region share similar physical characteristics. The ERA5-Land product underestimates average annual precipitation, resulting in inconsistencies

in the hydrological balance. Specifically, the scaled runoff coefficient (Q/P) is too high, and the humidity index (P/ETP) is too low in the Cévennes and Massif Central regions. For instance, the catchment ID 187 situated in the Massif Central is close to 1. In contrast, CERRA-Land shows notable improvements over ERA5-Land, with point clouds aligning more closely with the Turc-Pike model curves. For example, in the Cévennes, CERRA-Land reduces the sum of squared errors (SSE) from 0.58 to 0.22. SPAZM ranks second among the precipitation products, but its interpolation lacks robustness in the Massif Central, where the SSE reaches 0.16, compared to 0.11 with CERRA-Land. This discrepancy is due to several catchments falling into the red zone, indicating a possible overestimation of annual precipitation. The ISARD product helps reduce the spread of deviations from the Turc-Pike models in all studied regions. In the Pyrénées, ISARD produces more annual precipitation amounts than SPAZM for some high-altitude catchments (ID 118 and 120), reducing SSE from 0.17 to 0.1.

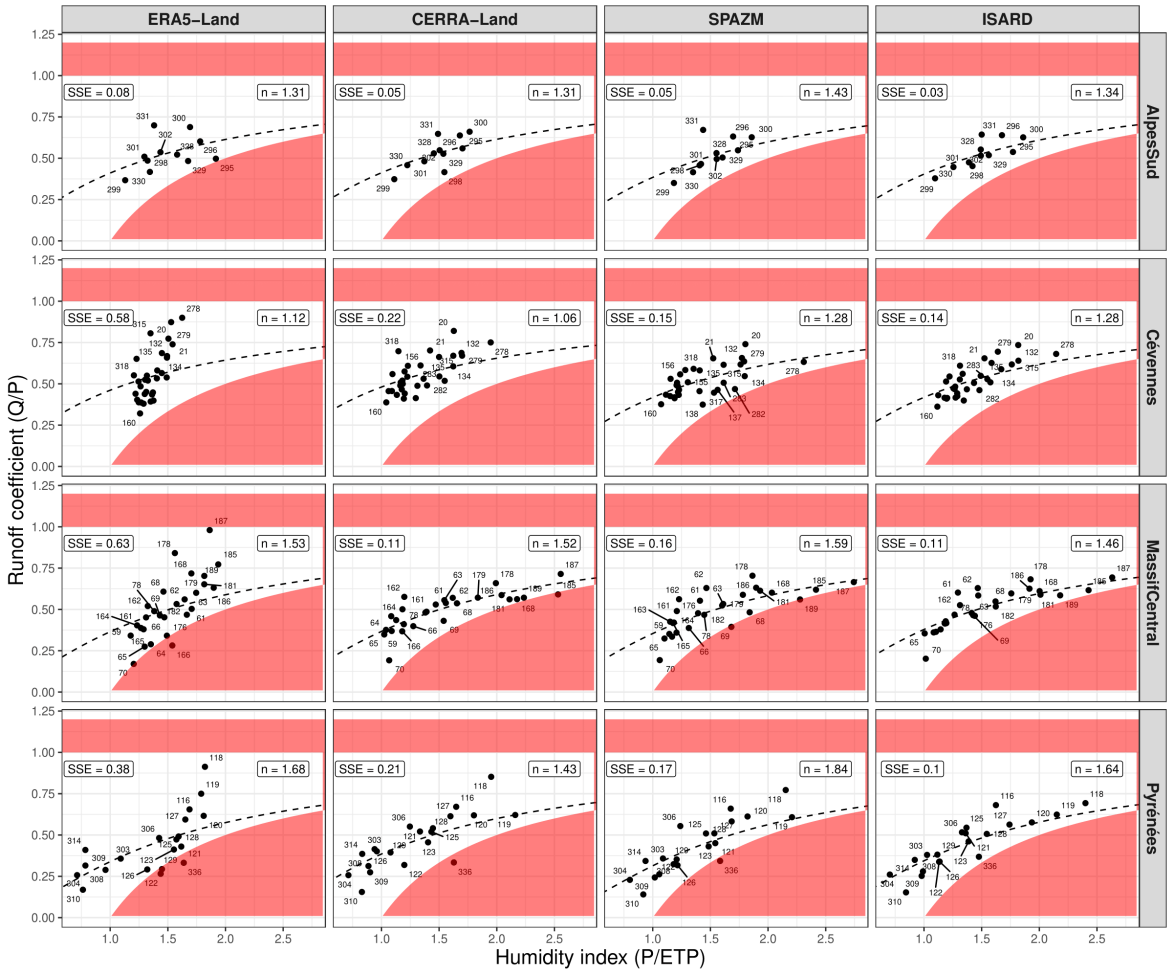

Figure 5.3 – Turc–Pike model results showing the runoff coefficient (y-axis) as a function of the humidity index (x-axis). Black points represent individual catchments. Vertical facets correspond to different regions, and horizontal facets to different gridded precipitation products. Within each facet, the dotted line indicates the fitted Turc–Pike curve, with the fitted parameter n and the sum of squared errors (SSE) reported.

5.4.2 Accumulated precipitation amounts at high-elevation sites

The Turk-Pike model provides an indirect assessment of the mean precipitation amounts at the catchment scale and over a climatological period, by comparison with long-term means of

streamflow measurements and empirical formulations of the evapotranspiration. *In-situ* snow measurements can provide a complementary reference at the point scale and for different years, highlighting interannual variability and systematic biases. Figure 5.4 displays the reproduction of the inter-annual variability of SWE measurements at **(a)** NRC and **(b)** glacier sites.

At NRC sites, the ISARD spread derived from the ensemble often contains the SWE measurements, whereas the other gridded precipitation largely underestimates SWE observations. We find the same ranking of performance as in Fig. 5.3. ERA5-Land severely underestimates winter precipitation and the inter-annual variability. CERRA-Land shows a notable but insufficient improvement. SPAZM outperforms CERRA-Land only in terms of inter-annual variability, but not in terms of bias. ISARD is the least biased gridded precipitation product, but it overestimates SWE for some NRCs (N1669, N1716). Additionally, it can represent, as does SPAZM, the inter-annual variability of SWE measurements.

Figure 5.4 **(b)** provides the same information as Fig. 5.4 **(a)** using winter mass balance measured at glaciers as references instead of SWE measurements. The glaciers are slightly at a higher altitude than SWE-measured sites, but the same conclusions remain. ISARD is the most accurate precipitation product, remaining unbiased at Gebroulaz and Saint-Sorlin glaciers, slightly underestimating precipitation at the Sarennes glacier, while effectively capturing the inter-annual variability of the observations.

ISARD is the least biased precipitation product in mountainous regions according to three different data sources : water balance at catchment scale, SWE, and winter mass balance observations. The confidence intervals derived from interpolation uncertainty contain the observations, while not being excessively widespread. We will also evaluate the proposed approach as precipitation input for hydrological modeling to simulate floods.

5.4.3 Hydrological modeling of floods

5.4.3.1 Case study

Figure 5.2 illustrates the spatial interpolation workflow of ISARD for 1996-01-11. The climatological background field is adjusted using 100 conditional simulations of anomaly fields. These anomaly fields show distinct spatial patterns, reflecting interpolation uncertainty, and give precipitation members with associated spatial patterns. The 32nd and 81st members yield 200 mm precipitation cells in the Var at Entrevaux catchment (colored in red), whereas the 41st member exhibits much lower precipitation totals. The members appear less smooth than the deterministic gridded products ERA5-Land, CERRA-Land, and SPAZM, and contain high-intensity cells. The color of the catchments is reflected in the sub-titles of Fig. 5.6.

Figure 5.6 illustrates the estimated average precipitation time series for two catchments, along with the associated streamflows derived from hydrological modeling using MORDOR-SD. We focus on the 1991-01-12 flood peak, related to Fig. 5.5. The precipitation uncertainty is significant, even averaged at the catchment scale, and propagates up to hydrological modeling. At the Issole at Mourefrey catchment, the deterministic gridded precipitation products smooth out the spatial variability of the precipitation field, resulting in an underestimation of intense cells, followed by an understimation of the flood peak. On the contrary, ISARD precipitation ranges from 60 to 130 mm. This corresponds to an estimated flood between 25 and 100 m^3s^{-1}, which enables the reproduction of the flood peak, measured at 65 m^3s^{-1}. At the Var at Entrevaux catchment, deterministic products can reproduce the flood peak this time, and some ISARD members show excessive precipitation.

5.4.3.2 Systematic evaluation

Figure 5.7 exhaustively evaluates the precipitation products as inputs for hydrological modeling of floods. In Fig. 5.7 **(a)**, for each catchment, month, and hydrological model, the

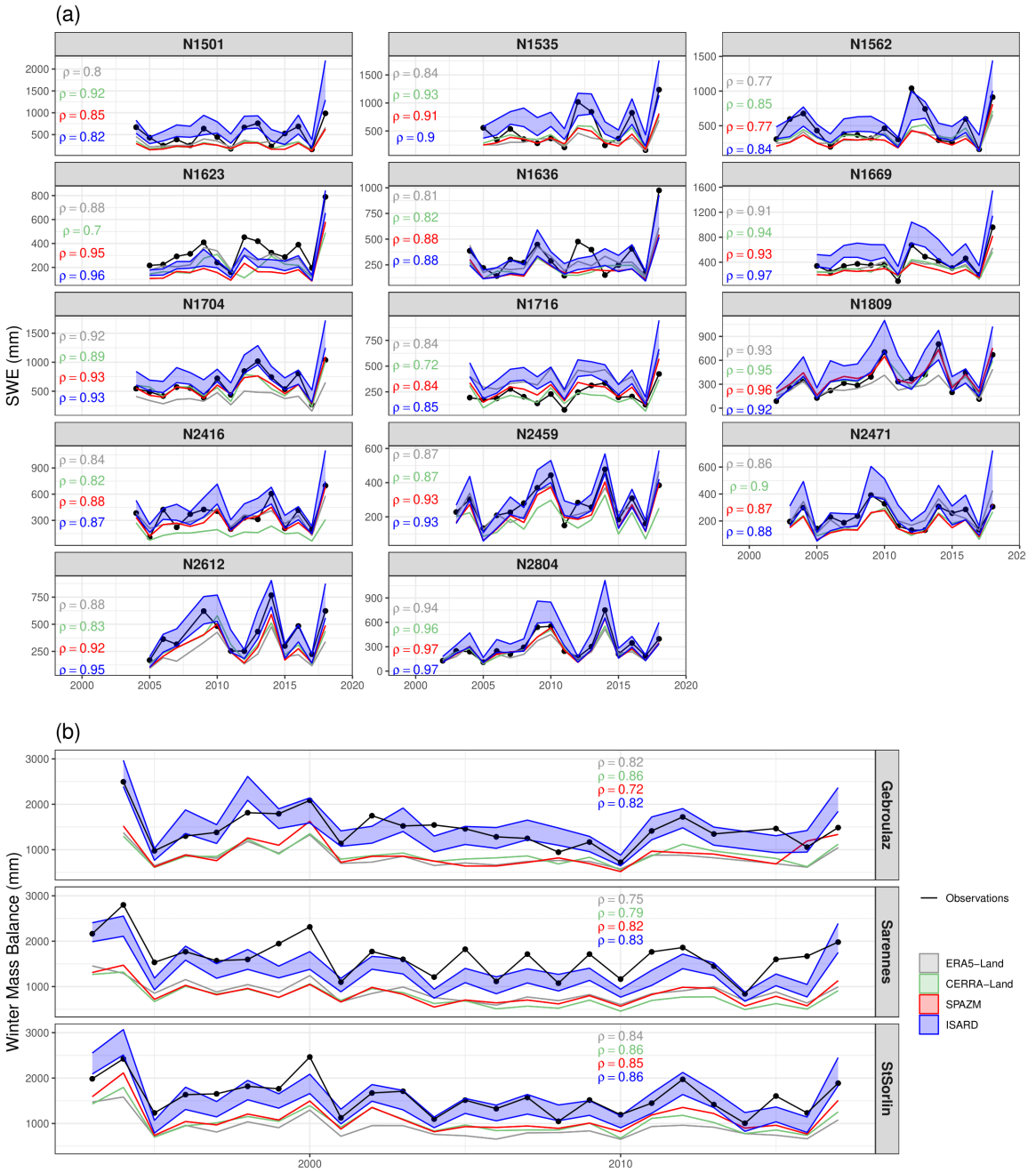

Figure 5.4 – (a) Interannual variability of winter snow water equivalent (SWE) accumulation and accumulated precipitation from 1 December to 28 February, for CERRA-Land, ERA5-Land, SPAZM, and ISARD. Black points denote *in-situ* measurements. (b) Same as (a), but for glacier winter mass balance measurements.

mean CRPS for floods is computed for both SPAZM and the other precipitation products, with their relative differences shown. Regardless of the catchments, months, and hydrological models considered, SPAZM consistently outperforms ERA5-Land and CERRA-Land in flood modeling. Additionally, the ISARD ensemble outperforms the deterministic SPAZM. We observe substantial improvements in autumn, which is the season most susceptible to flooding due to heavy rainfall. Figure 5.7 **(b)** compares the precipitation products in terms of flood distribution. ERA5-Land underestimates the high flood quantiles, across all hydrological mo-

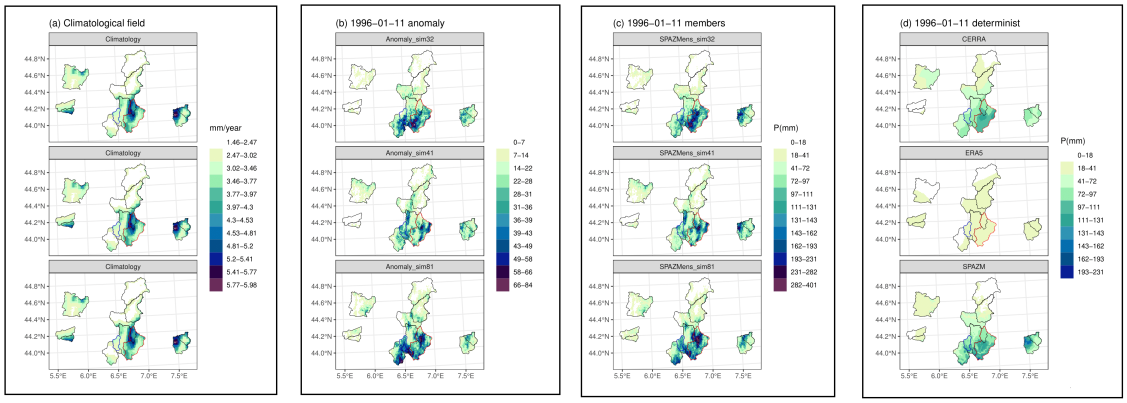

Figure 5.5 – Interpolation workflow illustrated for 11 January 1996. **(a)** Climatological background field (shown three times for visualization), **(b)** three randomly selected daily anomaly fields from conditional simulations, and **(c)** daily precipitation estimates from ERA5-Land, CERRA-Land, SPAZM, and three ensemble members of ISARD corresponding to the simulated anomalies. Catchment outlines are indicated ; simulated runoff for the blue and red catchments is presented in Fig. 5.6.

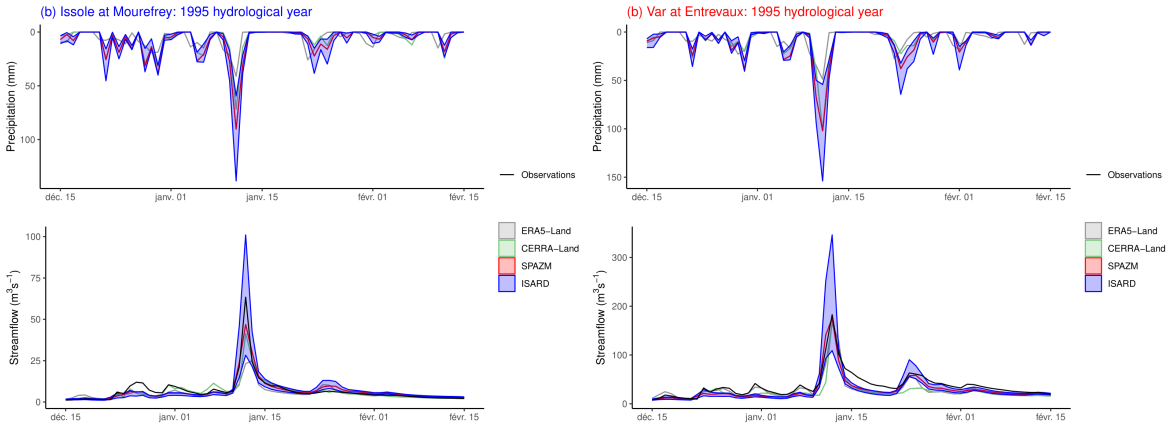

Figure 5.6 – Simulated catchment precipitation and runoff for the 1995 hydrological year (1 September to 31 August), colored by gridded precipitation product, for **(a)** the Issole at Mourefrey catchment and **(b)** the Var at Entrevaux catchment. Black curves indicate observed runoff.

dels, which is expected and explains the results in Fig. 5.7 **(a)**. CERRA-Land, in contrast, yields unbiased distribution scores. The poorer CRPS performance relative to SPAZM is therefore not due to a systematic bias in flood quantiles. Despite an improvement in CRPS, ISARD shows similar performance to SPAZM in terms of distribution, with both products being unbiased for large quantiles.

5.5 Discussion

5.5.1 Seasonal accumulation in mountains

The interpolation framework reproduces accumulated precipitation amounts in mountainous regions with good consistency across multiple independent datasets. At the catchment scale, annual precipitation balances well with evapotranspiration and runoff (see Fig. 5.3). At the point scale, the ensemble reproduces seasonal snow water equivalent (SWE) from nivolo-

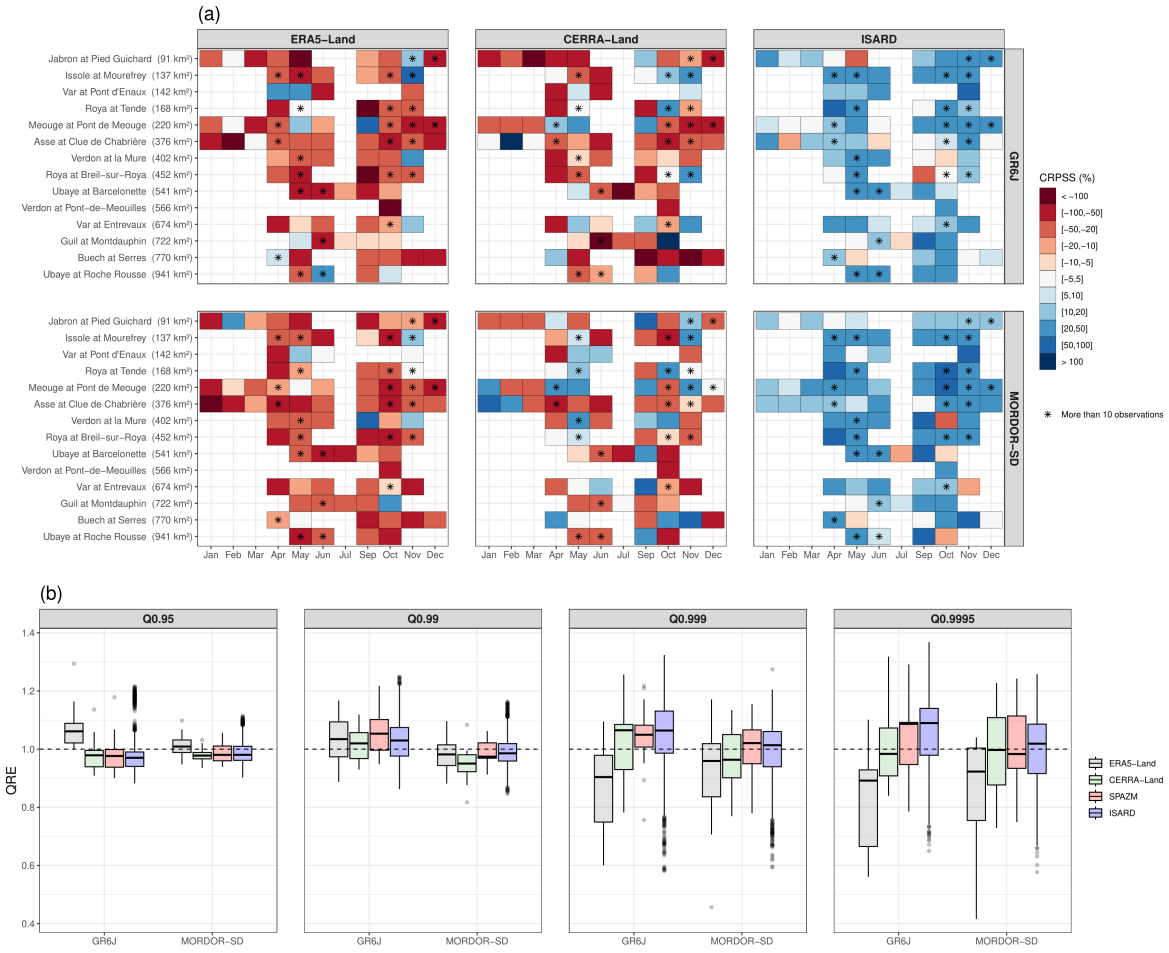

Figure 5.7 – **(a)** Continuous Ranked Probability Skill Score (CRPSS, % relative to SPAZM) for flood modeling across catchments (y-axis) and months (x-axis), stratified by gridded precipitation products (horizontal facets) and hydrological models (vertical facets). Catchments are ordered by increasing surface area. Box colors correspond to CRPSS values, with red (blue) indicating performance degradation (improvement) relative to SPAZM. Boxes marked with a star indicate more than 10 flood events for the given catchment and month, while empty boxes correspond to fewer than 2 events. **(b)** Distribution of quantile relative errors (y-axis) for the two hydrological models (x-axis), filled by gridded precipitation products and stratified by quantiles (horizontal facets).

gical reference catchments (NRCs) and winter mass balances of glaciers, providing confidence in the representation of high-elevation precipitation. Despite this overall agreement, some limitations remain :

- **Methodological limitations** : The applied methodology presents two main limitations.
  - **Uniform snowfall undercatch correction** : To account for the systematic undercatch of snowfall by rain gauges, we applied a uniform correction factor of 1.6 to all snowfall measurements. This choice is consistent with values reported in Alpine studies (Gottardi, 2009; Jonas and Schirmer, 2022), but we emphasize that it represents a coarse approximation. To our knowledge, no operational gridded precipitation product currently includes an explicit undercatch correction. At the seasonal scale, this adjustment largely removes the bias in total snowfall accumu-

lation (see Fig. 5.4). However, it inevitably compensates both overestimations and underestimations at shorter timescales. In particular, the correction likely misrepresents daily precipitation amounts, since undercatch is not constant but depends on wind speed (Sevruk et al., 2009), precipitation intensity (Cauteruccio et al., 2024), and gauge exposure. Spatial variability is also an issue : in some regions, especially the southernmost NRCs, the correction appears to produce unrealistically high accumulations. We therefore caution that our corrected dataset should not be interpreted as a physically consistent representation of snowfall at the daily scale. Instead, it should be seen as a first-order seasonal adjustment. Further improvements could rely on more refined transfer functions that explicitly account for wind speed and station metadata (Buisán et al., 2017; Kochendorfer et al., 2020), for example, by exploiting hourly AROME reanalysis winds. The main challenge is the availability and quality of rain gauge metadata, which are often incomplete or subject to change over time.

— **Dependence on CP-RCM quality** : The reliability of high-altitude precipitation estimates in ungauged regions strongly depends on the capacity of the CP-RCM to reproduce spatial variability in complex mountainous terrain. In particular, the quality of the precipitation–altitude relationship (lapse rates) provided by the CP-RCM is critical. We therefore caution potential users that these lapse rates should always be evaluated before the interpolation step, as illustrated in Dura et al. (2024a). This dependence becomes more pronounced when the rain gauge network is sparse : the sparser the rain gauge network, the more critical the CP-RCM performance becomes.

- **Evaluation biases** : Some limitations could alter the evaluation of high-altitude precipitation.

  — **No-melt assumption** : Our evaluation against SWE and glacier mass balances assumes negligible melt during winter. This assumption, historically valid above 2,000 m, is increasingly questionable under present warming. The SWE chronicles of NRC N1669 and N1716 show (not shown here) snow melting in winter, which could explain the supposedly overestimation of ISARD (see Fig. 5.4). Considering daily SWE variations would relax this assumption, but such comparisons are sensitive to snow redistribution.

  — **Scale mismatch** : Furthermore, the native resolution of the precipitation ensemble is 1 km, but the resolved resolution is coarser, which is insufficient to explain the spatial variability of snowfall. NRCs are point data, and the Sarennes only covers 0.09 km^2. This scale mismatch could also explain the differences between precipitation accumulated at the km scale and point SWE measurements, especially in this complex topography area.

5.5.2 Reproduction of floods using hydrological models

The proposed spatial interpolation framework allows hydrological modeling of floods by providing an ensemble to represent the spatial variability of daily precipitation. The cross-reading of Fig. 5.5 and Fig. 5.7 illustrates this point. The ensemble outperforms the best deterministic gridded precipitation products in terms of flood peak representation, but not in long-term runoff frequency distributions. Here are a few points that need to be discussed.

— **Model calibration** : Hydrological models are recalibrated for each precipitation forcing, which may attenuate differences between the gridded products. We try to mitigate this issue by performing a split-sample evaluation. One possible improvement would

be to generate a synthetic reference precipitation field each day, and use it for model calibration. From this field, we could extract several points to act as virtual rain gauges, then apply different spatial interpolation methods to reconstruct the full field. Streamflow simulations could then be performed using the parameters obtained from the full-field calibration, allowing us to assess how interpolation methods affect hydrological performance.

— **Hydrological model structure** : The models used here are lumped or stratified by elevation bands, which do not fully exploit the ensemble's spatial variability. While mean precipitation inputs appear similar across products, spatial patterns differ notably. Fully distributed hydrological models such as MORDOR-TS (Rouhier et al., 2017) would better value the ensemble information and represent the link between spatial rainfall variability and flood response (Bárdossy and Anwar, 2023).

— **Evaluation uncertainties** : Imperfect hydrological modeling could also contaminate the evaluation of precipitation forcings. Several factors could affect the modeling, such as poor temperature inputs, imperfect evapotranspiration formulation, undercatch of snowfall and rainfall, groundwater exchanges, and hourly hydrological signatures modeled at the daily timescale.

5.5.3 Scope and reproducibility of the framework

A considerable strength of the framework lies in its reproducibility and applicability across contexts. It requires only rain gauge observations and CP-RCM simulations, making it transferable to regions with varying data availability.

— **Station density** : We speculate that the interpolation framework is designed for whatever the available rain gauge density, and could also be successful in a low rain gauge density scenario. The construction of the climatological background fields is robust to low station density. The use of Random Forest to interpolate climatological anomalies of rain gauge amounts on CP-RCMs simulations produces unbiased fields even for low rain gauge density, while reproducing the spatial variance of the observations (Dura et al., 2024b). This approach considerably values CP-RCMs simulations, keeping in mind that our ability in precipitation modeling is now outperforming our ability to measure precipitation in mountainous regions (Lundquist et al., 2019). The final step of the interpolation framework, the interpolation of anomalies, is performed through conditional simulations using CP-RCM variograms. As a result, the variogram estimation is not affected by an insufficient rain gauge density, and the interpolation does not produce overly smooth fields (Hofstra et al., 2010). With fewer gauges, the ensemble members diverge more strongly, reflecting actual interpolation uncertainty. In sparser rain gauge networks, generating more members should be considered.

— **Flexibility of inputs** : While we use CP-RCMs at 2.5 km resolution, the framework might ingest any high-quality RCM depending on the target application scale.

— **Extension to other variables** : Although developed for daily precipitation, the framework is likely applicable for temperature, wind, or radiation. Temperature is less spatially variable and better represented by CP-RCM, while anisotropic variograms support wind interpolation.

Overall, the framework successfully merges point observations and CP-RCM information, providing ensemble precipitation fields that improve hydrological modeling while remaining transparent and reproducible. Its main current limits lie in snowfall undercatch correction, CP-RCM dependence, and evaluation uncertainty, defining clear pathways for future research.

5.6 Conclusion

This study presents a spatial interpolation reproducible workflow applied to daily precipitation in alpine regions. The workflow consists of : (i) correcting rain-gauge measurements for undercatch, (ii) constructing climatological background fields stratified by weather regimes by merging rain gauges with CP-RCM climatologies to account for orographic effects, and (iii) generating conditional simulations of daily anomalies that exploit CP-RCM-derived spatial variability. The approach is benchmarked against widely used products (ERA5-Land, CERRA-Land, and SPAZM, a regression-based interpolator) and evaluated with multiple independent datasets, including catchment-scale water balance, *in-situ* SWE, glacier winter mass balance, and flood hydrological modelling.

Results show that the proposed workflow outperforms existing gridded precipitation products in reproducing seasonal totals in mountainous regions and hydrological modelling of floods. By correcting undercatch and integrating CP-RCM climatology, it provides higher and more realistic precipitation totals at high-elevation sites, while preserving observed interannual variability. The ensemble simulations explicitly represent interpolation uncertainty and capture fine-scale spatial variability, leading to improved flood simulations across all studied catchments and with both hydrological models. Even higher benefits might arise with fully distributed hydrological models.

Overall, these findings highlight the potential of the proposed workflow as a robust approach for precipitation interpolation in regions with complex topography. It is particularly promising in data-scarce areas where high-quality CP-RCM or RCM simulations are available. By providing modular, open-source code and a test case, we ensure the workflow's adaptability to other regions and its extension to diverse climate variables.

5.A Solid fraction of precipitation

$$f_s(T(x_s,t)) = \begin{cases} 1, & T(x_s,t) < -2°\text{C}, \\ 0.5 + \dfrac{T(x_s,t)}{4}, & -2°\text{C} \leq T(x_s,t) \leq 2°\text{C}, \\ 0, & T(x_s,t) > 2°\text{C}. \end{cases} \quad T(x_s,t) = \frac{T_{min}(x_s,t) + T_{max}(x_s,t)}{2} \tag{5.12}$$

5.B Random Forest hyperparameters

The Random Forest algorithm hyperparameters are chosen by cross-validation. We perform cross-validation separately for each weather pattern. n_{obs} refers to the number of observations in the training dataset.

— Number of trees $n_{\text{tree}} \in \{50; 100; 500\}$
— Number of co-variables to test to split a leaf $m_{\text{try}} \in \left\{\frac{n_{obs}}{3}; \frac{n_{obs}}{2}; \frac{2\times n_{obs}}{3}\right\}$
— Number of minimum observations to split a leaf $nodesize = 1$

5.C Transformation into Gaussian distribution and back-transformation

$$Z_{s,t} = \begin{cases} \Phi^{-1}[u_0 + (1-u_0)F_\gamma(A_{s,t})], & A_{s,t} > 0, \\ \Phi^{-1}[\mathcal{U}(0.01, u_0)], & A_{s,t} = 0, \end{cases} \tag{5.13}$$

where F_γ is the Gamma CDF fitted to nonzero values,Φ^{-1} the Gaussian quantile function, u_0 the empirical probability of zero precipitation, and $\mathcal{U}$ is the uniform distribution.

Back-transformation yields simulated anomalies

$$A^{(n)}(x,t) = \begin{cases} F_\gamma^{-1}\left\{\frac{\Phi[Z^{(n)}(x,t)]-u_0}{1-u_0}\right\}, & \Phi[Z^{(n)}(x,t)] > u_0, \\ 0, & \text{otherwise}, \end{cases} \tag{5.14}$$

5.D Anisotropic distance

The anisotropic distance $d_{\text{aniso}}(h)$ between two locations separated by a lag vector $h = (h_x, h_y)$ is defined as :

$$d_{\text{aniso}}(h) = \sqrt{\left(\frac{h_x\cos\theta + h_y\sin\theta}{a_x}\right)^2 + \left(\frac{-h_x\sin\theta + h_y\cos\theta}{a_y}\right)^2}, \tag{5.15}$$

with $a_x = a$, $a_y = a/\eta$, η the anisotropy ratio, and θ the anisotropy direction (measured counterclockwise from the x axis).

6 Conclusions and perspectives

6.1 Contributions

6.1.1 Contributions à l'estimation des cumuls saisonniers de précipitations en montagne

Cette thèse contribue à l'amélioration de l'estimation des cumuls de précipitations en contexte montagneux en mobilisant les simulations à haute résolution spatiale issues des modèles climatiques régionaux à convection résolue (CP-RCM). Malgré des biais persistants aux altitudes les plus élevées ($>$ 2200 m), ces données permettent d'analyser de manière robuste la variabilité spatiale des gradients altitudinaux de précipitations dans des zones insuffisamment instrumentées, et d'obtenir des champs climatologiques de référence. Ces résultats sont cohérents avec ceux de Jing et al. (2017) dans l'ouest des États-Unis, qui montrent que les simulations du modèle Weather Research and Forecasting (WRF) (Skamarock et al., 2019) reproduisent fidèlement les gradients hivernaux observés, tandis que les cumuls saisonniers issus de ces simulations diffèrent fortement des produits grillés dérivés de pluviomètres. Ces différences s'accentuent dans les régions d'altitude peu instrumentées.

Les travaux effectués dans le chapitre 2 montrent qu'en France, les gradients saisonniers sont généralement plus élevés en hiver, avec 95 % des valeurs comprises entre 0,55 et 13,10 %/100 m, et des maxima atteignant 32 %/100 m dans les zones exposées aux flux dominants comme le Massif Central. Les gradients sont plus faibles dans les Alpes, possiblement en raison d'une proportion moindre d'épisodes stratiformes produisant des précipitations orographiques organisées. Ce constat rejoint celui de Kotlarski et al. (2012), qui identifie des gradients plus faibles dans les Alpes européennes que dans le reste de la France à une échelle régionale. L'analyse réalisée sur les Alpes françaises met en évidence la forte dépendance des gradients à l'échelle spatiale. À l'échelle du massif ($\sim$ 1 000 km^2), l'effet de l'altitude sur les précipitations saisonnières est trop hétérogène pour être généralisé. En revanche, une analyse à l'échelle du bassin versant ($\sim$ 100 km^2) révèle l'influence déterminante de la topographie locale : les premiers reliefs rencontrés par les masses d'air présentent de forts gradients altitudinaux, tandis que certains bassins enclavés sont soumis à des effets d'abri qui tendent à réduire les gradients proches de 0 %/100 m. Ce résultat confirme tout d'abord les conclusions de Jiang et al. (2022), qui recommande d'analyser les gradients à l'échelle spatiale la plus fine possible dans la région du troisième pôle tibétain. Notre travail étend ces recommandations en France, où de telles analyses restaient jusqu'ici limitées. Nos résultats corroborent ceux de Ogrin and Kozamernik (2018), qui a mis en évidence une variabilité spatiale extrême des gradients en Slovénie dans trois vallées alpines voisines. Nous confirmons cette hétérogénéité sur un plus grand territoire. Par ailleurs, contrairement aux résultats de Sevruk (1997), Durand et al.

(2009) et Ménégoz et al. (2020), qui concluaient à des gradients plus marqués dans les Alpes du Nord que dans les Alpes du Sud, notre étude ne retrouve pas ce contraste. Cette divergence peut s'expliquer par notre analyse menée à une résolution spatiale plus fine, qui révèle une variabilité locale forte au sein même des massifs.

Combinées à plus de 3 000 pluviomètres, les simulations issues des CP-RCM permettent de construire des champs climatologiques de référence. La méthode repose sur l'interpolation, à l'aide d'un modèle de Machine Learning, à savoir l'algorithme Random Forest, des ratios entre les précipitations observées et celles simulées par les CP-RCM. Le champ interpolé des ratios est ensuite multiplié par le champ climatologique du CP-RCM. La limitation bien connue du Random Forest, qui ne permet pas d'extrapoler en dehors de la gamme des observations (Hengl et al., 2018), n'apparaît pas problématique dans ce contexte : la climatologie CP-RCM fournit une variabilité spatiale suffisante ainsi que des valeurs plus élevées en zones de montagne. Cette approche présente plusieurs avantages par rapport à la méthode de krigeage avec dérive externe (KED), couramment utilisée. Elle maintient la variance spatiale des observations sans être contrainte par des hypothèses fortes, telles que la normalité et la stationnarité du second ordre. Elle permet notamment de représenter de façon plus précise la relation entre l'altitude et les précipitations saisonnières grâce à la structure spatiale fournie par les simulations CP-RCM. Les travaux existants, tels que Daly et al. (1994) ou Hiebl and Frei (2018), reposent principalement sur l'utilisation de variables topographiques (altitude, orientation des massifs) comme prédicteurs. Or ces facteurs sont déjà représentés physiquement dans les CP-RCM, ce qui rend pertinent l'usage direct des simulations CP-RCM, moyennant une correction par les observations pluviométriques afin de réduire les biais. Les cartes de précipitations obtenues mettent ainsi en évidence une forte variabilité spatiale et saisonnière, liée à la fois à la topographie locale et à la circulation atmosphérique de grande échelle. Ces résultats illustrent le potentiel des CP-RCM, combinés aux observations, pour améliorer la représentation climatologique des précipitations en montagne.

Dans le cadre du processus d'interpolation journalière, les champs climatologiques de référence servent de support spatial et sont ajustés quotidiennement à l'aide des observations pluviométriques, elles-mêmes corrigées de la sous-captation liée au vent. Cette méthodologie permet d'obtenir des cumuls hivernaux en montagne cohérents avec plusieurs sources indépendantes, telles que les bilans hydriques de bassin versant, les mesures ponctuelles de *Snow Water Equivalent* (SWE) et les bilans de masse glaciaire. La convergence de ces résultats renforce la confiance dans la qualité du produit obtenu en contexte alpin. Contrairement à la plupart des approches classiques d'interpolation spatiale, qui tendent à sous-estimer systématiquement les précipitations en altitude (*e.g Gottardi, 2009; MeteoSwiss, 2022; Pulka et al., 2024)*, l'intégration explicite de champs climatologiques issus des CP-RCM améliore significativement la représentation des cumuls en montagne. En tenant compte de la variabilité spatiale et des effets orographiques déjà présents dans les CP-RCM, cette approche contribue à une meilleure estimation des apports solides en altitude, un enjeu majeur pour l'hydrologie de montagne et la gestion des ressources en eau.

Plusieurs recommandations sur l'estimation des précipitations en montagne peuvent être tirées de ces travaux :

- **Privilégier les simulations CP-RCM** (modèles régionaux à convection explicite) aux seules observations pluviométriques pour estimer les gradients altitudinaux. En effet, les simulations permettent de représenter plus finement la variabilité spatiale des précipitations en fonction de l'altitude, contrairement aux réseaux de pluviomètres souvent trop clairsemés en montagne.
- **Analyser les gradients altitudinaux à une échelle spatiale fine**, compte

tenu de leur forte variabilité locale. À l'échelle d'un massif, on observe des différences marquées de gradients, les plus fortes valeurs se situant généralement sur les premiers reliefs exposés aux flux atmosphériques dominants.

— **Combiner les simulations CP-RCM et les observations pluviométriques** à l'aide de modèles de *machine learning* (Random Forest), afin de produire des champs climatologiques de référence. Ces champs intègrent à la fois la représentation réaliste des gradients altitudinaux issue des simulations et la cohérence avec les valeurs pluviométriques observées.

6.1.2 Contributions à la représentation des précipitations journalières intenses

Dans cette thèse, l'interpolation journalière repose sur la simulation conditionnelle de champs trans-gaussiens, où l'estimation de la covariance joue un rôle déterminant pour représenter la variabilité spatiale des précipitations intenses.

Parmi les modèles testés, la covariance anisotrope dérivée des simulations journalières CP-RCM s'avère la plus performante. Elle restitue plus fidèlement les structures directionnelles observées dans les données radar et présente de meilleurs scores de validation croisée, aussi bien pour les valeurs moyennes que pour la dispersion. Cependant, les cellules de précipitations journalières issues des simulations CP-RCM peuvent présenter des décalages spatiaux, ce qui pourrait altérer l'estimation de la covariance. La prise en compte de l'anisotropie à partir des seuls réseaux pluviométriques n'apporte en revanche pas d'amélioration notable par rapport à une covariance isotrope. Ce résultat est cohérent avec les travaux antérieurs (Haberlandt, 2007; Shi et al., 2007; Haylock et al., 2008), qui soulignent la difficulté d'estimer de manière robuste les paramètres anisotropes à partir d'un nombre limité de stations. En pratique, l'estimation de l'anisotropie exige un réseau pluviométrique dense, rarement disponible. L'utilisation des simulations CP-RCM permet de contourner cette limitation : elles offrent une estimation réaliste de l'anisotropie et renforcent ainsi la robustesse de l'interpolation spatiale. Cette approche s'inscrit dans la continuité des travaux ayant exploité les données radar pour estimer l'anisotropie (Velasco-Forero et al., 2009; Schiemann et al., 2011; Gyasi-Agyei, 2016). À l'avenir, la disponibilité croissante de simulations CP-RCM de haute résolution pourrait fournir, au même titre que les champs radar, une source fiable pour caractériser la structure de covariance des précipitations quotidiennes.

L'ensemble de 100 simulations conditionnelles de précipitations moyennes spatiales de bassin versant, généré au cours de cette thèse, recouvre les estimations issues des lames d'eau radar lors des événements intenses. Cela souligne son potentiel pour la quantification de l'incertitude, un aspect essentiel en modélisation hydrologique. Le processus d'interpolation proposé dépasse en outre les performances des produits de précipitations grillés existants. Les ensembles obtenus représentent explicitement l'incertitude d'interpolation et restituent la variabilité spatiale à fine échelle, ce qui conduit à une amélioration systématique des simulations de crues dans les bassins versants étudiés, indépendamment du modèle hydrologique appliqué. Ce travail s'inscrit dans un contexte où la prise en compte de l'incertitude d'interpolation est particulièrement critique pour la modélisation hydrologique des crues, alors même que les réanalyses et produits ensemblistes de précipitations demeurent rares, bien qu'en développement croissant ces dernières années (Cornes et al., 2018; Frei and Isotta, 2019; Devers et al., 2021; Vernay et al., 2025).

Trois recommandations principales peuvent être tirées des travaux pour l'estimation des précipitations intenses :

- **S'appuyer sur des champs trans-gaussiens**, qui décrivent fidèlement la variabilité spatiale des précipitations intenses. Ces champs se révèlent plus robustes en présence d'un réseau clairsemé de pluviomètres et plus informatifs dans les zones à forte densité d'observations qu'un modèle de régression linéaire locale.
- **Utiliser une covariance anisotropique**, estimée à partir des simulations CP-RCM, afin de générer des champs de précipitations intenses plus réalistes, similaires aux lames d'eau radar. Cette approche est prometteuse dans les régions montagneuses, où les réseaux pluviométriques sont souvent peu denses et les données radar de qualité limitée ou disponibles sur une période trop courte.
- **Mettre en œuvre des simulations conditionnelles** pour quantifier l'incertitude d'interpolation. Cette information est essentielle pour une meilleure simulation des crues dans les modèles hydrologiques.

6.2 Perspectives

De multiples perspectives sont à envisager, de la donnée à son utilisation. La qualité et la quantité des observations pourraient être renforcées (voir sous-section 6.2.1), la méthodologie affinée (sous-section 6.2.2), le champ d'application étendu (sous-section 6.2.3), et le produit de précipitations mobilisé dans diverses applications opérationnelles (sous-section 6.2.4).

6.2.1 Renforcer la qualité et la quantité de données

Pour mieux représenter les précipitations intenses en montagne, il ne suffit pas d'affiner les méthodes d'interpolation : il faut également renforcer la qualité et la densité des observations disponibles.

- **Corriger les biais instrumentaux**

  Un premier axe d'amélioration concerne la **correction de la sous-captation liée au vent**, qui reste une limite majeure dans l'estimation des précipitations en montagne. Notre correction globale de 60 % corrige, au premier ordre, les sous-estimations à l'échelle saisonnière, mais elle ne prend pas en compte l'effet du vent. Une piste pour remédier à cela consiste à tester différentes fonctions de transfert (Buisán et al., 2017; Kochendorfer et al., 2020) afin d'améliorer la représentativité des cumuls observés. Ces fonctions sont souvent appliquées à l'échelle horaire et prennent la forme :

  $$P_{\text{cor}} = \frac{P}{a \exp(-bw)},$$

  où P_{cor} désigne la précipitation corrigée, P la précipitation observée, w le vent mesuré au pluviomètre, et a et b des paramètres à ajuster selon le type de précipitation (neige, pluie/neige). Ces paramètres pourraient être calibrés en comparant les précipitations corrigées aux chroniques journalières de SWE selon le protocole suivant :

  1. Interpolation spatiale des observations pluviométriques pour les jours d'intérêt, avec différents couples de paramètres a et b,
  2. Extraction des précipitations journalières aux emplacements des NRCs,
  3. Comparaison avec les précipitations estimées aux NRCs, calculées comme la différence de SWE entre le jour et la veille.

Une correction dépendante du vent devrait améliorer la variabilité interannuelle des cumuls en montagne, et donc la connaissance de la ressource en eau (Masuda et al., 2019; Huidobro et al., 2023). Les hivers où le cumul résulte d'un faible nombre d'événements sont particulièrement sensibles à ce type de correction.

Mieux représenter les précipitations intenses implique aussi de mieux les mesurer. Les pluviomètres à augets basculants, largement utilisés dans ces travaux, présentent une **sous-captation des précipitations intenses** en raison de la saturation mécanique des augets (Duchon et al., 2014). Cette sous-estimation peut atteindre jusqu'à 9 % pour de très fortes intensités (> 175 mm.h^{-1}). Ces très fortes intensités étant rares, leur correction reste secondaire par rapport aux problématiques de sous-captation dus au vent.

— **Renforcer la résolution effective**

Un second axe d'amélioration concerne le raffinement de la résolution effective du produit de précipitation, qui reste plus grossière que la résolution spatiale du produit de 1 km^2 en raison de l'échantillonnage spatial limité des pluviomètres (Isotta et al., 2014; Bandhauer et al., 2022), surtout en montagne. L'analyse des champs d'incertitude liés à l'interpolation spatiale peut permettre d'identifier les zones critiques où le maintien, voire l'ajout, de pluviomètres serait particulièrement bénéfique (Henriksen et al., 2024). La forte croissance du nombre de pluviomètres amateurs constitue une opportunité pour compléter le réseau professionnel, mais pose des défis de contrôle de qualité des données (Bárdossy et al., 2021). En France, environ 800 stations semi-professionnelles, regroupées dans le réseau STATions InfoClimat (StatIC, https://www.infoclimat.fr/climato/), transmettent des cumuls de précipitations à l'échelle infra-horaire depuis 2007. Ces stations respectent les normes d'installation de Météo-France, avec certaines tolérances acceptées. Elles pourraient être intégrées au réseau opérationnel dans les régions les moins densément fournies. Par ailleurs, l'utilisation de simulations CP-RCM à plus haute résolution (1.3 km au lieu de 2.5 km actuellement) constitue une perspective prometteuse pour mieux représenter l'influence de la topographie sur les précipitations et affiner l'estimation des cumuls en montagne.

6.2.2 Affiner la méthodologie

Les prochaines étapes consistent à repousser les limites actuelles de la méthodologie, en explorant des approches statistiques plus sophistiquées.

— **Utiliser une covariance spatiale non-stationnaire**

Dans cette thèse, nous avons considéré les observations comme stationnaires au second ordre, et ainsi appliqué l'interpolation spatiale par régions climatiquement peu hétérogènes pour respecter cette hypothèse. Dans le souhait d'obtenir des champs de précipitations sur toute la France, il convient de supprimer cette hypothèse et d'utiliser une covariance non-stationnaire. Cette extension, fondée sur une combinaison de covariance stationnaire locale (Risser and Calder, 2017) ou sur une déformation du système de coordonnées (Sampson and Guttorp, 1992), est coûteuse en temps de calcul.

— **Interroger la dépendance de la covariance à l'intensité des précipitations**

Par ailleurs, l'interpolation journalière des anomalies repose actuellement sur l'hypothèse que la dépendance spatiale est similaire pour les faibles et les fortes valeurs, via l'utilisation d'un variogramme unique. Or, les faibles valeurs sont susceptibles de présenter une autocorrélation spatiale plus forte que les fortes valeurs (Maier et al., 2020). Cette simplification peut conduire à une surestimation de l'incertitude d'interpolation dans

les zones à faible cumul, et inversement, à une sous-estimation dans les zones de forts cumuls. L'intégration de **copules**, dans un cadre de simulation conditionnelle (Hörning and Bárdossy, 2025), constituerait une approche prometteuse pour mieux représenter cette asymétrie.

— **Intégrer d'autres sources d'incertitudes**
L'incertitude d'interpolation ne constitue qu'une composante, certes majeure, de l'incertitude totale des champs de précipitations journaliers, mais d'autres sources d'incertitude pourraient être intégrées. Les champs climatologiques eux-mêmes pourraient être considérés comme incertains, par exemple en étendant le Random Forest utilisé vers une approche de **Quantile Random Forest** (Meinshausen, 2006). De même, la génération de plusieurs ensembles de simulations journalières de CP-RCM, obtenus en perturbant la réanalyse utilisée comme forçage à grande échelle, permettrait de quantifier l'incertitude associée à l'estimation du variogramme. De plus, les observations pourraient elles-mêmes être considérées comme incertaines en raison de la sous-captation liée au vent. Une approche simpliste consisterait à tester plusieurs combinaisons de paramètres (correction, transformation, variogramme) sans les pondérer selon leur adéquation aux observations : toutes étant considérées comme également plausibles. Une **modélisation hiérarchique bayésienne**, au contraire, pondère chaque combinaison par sa vraisemblance, donnant plus de poids aux paramètres qui reproduisent le mieux les données observées, et offre ainsi un cadre méthodologique particulièrement adapté pour combiner ces différentes sources d'incertitude. Nous pourrions associer au modèle de champs trans-gaussien, un modèle d'erreurs de mesure. Les lois *a priori* devront être suffisamment informatives pour assurer l'identifiabilité des paramètres (Simpson et al., 2017). Les simulations CP-RCM pourront être utilisées pour déterminer ces lois *a priori*.

6.2.3 Étendre le champs d'action d'ISARD

Pour accroître son utilisation, ISARD doit dépasser son périmètre actuel et s'adapter à de nouveaux contextes, du pas de temps horaire aux régions peu instrumentées.

— **Changer d'échelle temporelle**
En hydrologie comme en nivologie, certaines applications requièrent des chroniques de forçages atmosphériques **horaires**. C'est notamment le cas pour les petits bassins versants dynamiques (au régime nival ou sujets à des crues éclair), dont la modélisation hydrologique est plus pertinente à cette échelle temporelle. L'extension du produit ISARD à l'échelle horaire constitue cependant un défi méthodologique. À l'échelle journalière, les jours ont été considérés comme indépendants, ce qui est déjà discutable dans le cas d'épisodes avec une mémoire temporelle tels que les événements cévenols stationnaires ou certains orages généralisés qui traversent la France. À l'échelle horaire, cette hypothèse n'est plus respectée, et la dépendance temporelle devrait être intégrée, à l'image de ce qui est réalisé dans le produit Combi-Precip (Sideris et al., 2014) ou dans les travaux de Frey and Frei (2025). La disponibilité limitée de pluviomètres horaires complique l'exercice : deux stratégies sont envisageables, soit accepter de restreindre la base de données aux seules stations horaires, soit désagréger les observations journalières à l'aide des simulations CP-RCM, à condition de vérifier la cohérence temporelle de ces dernières afin d'éviter tout biais. La restriction aux stations horaires semble trop limitante au vu du grand nombre de stations supprimées.

— **Evoluer vers une approche temps réel**
Une seconde perspective concerne le développement d'un produit ISARD en **temps réel**. L'accessibilité du produit de précipitation en temps réel est essentielle pour l'hy-

drologie opérationnelle comme la prévision à court terme des débits, ou dans la gestion de situations de crises comme les crues extrêmes. Dans ce contexte, il nous paraît intéressant d'inclure des mesures radar au processus d'interpolation, tout en respectant les cumuls pluviométriques et une climatologie de précipitations orographiques, à l'image de ce qui a été réalisé dans Zhang et al. (2014). Si l'accès incrémental en temps réel aux observations pluviométriques et radars ne pose pas de difficulté majeure, l'utilisation possible de prévisions météorologiques en substitution aux simulations météorologiques doit être vérifiée. La disponibilité de prévisions ensemblistes donne l'opportunité d'une estimation de l'incertitude sur les paramètres du variogramme. L'approche d'estimation non-paramétrique proposée par Velasco-Forero et al. (2009) constitue une piste prometteuse dans le contexte temps-réel. Cette extension prendrait tout son sens en combinaison avec une modélisation hydrologique horaire.

— **Explorer de nouveaux territoires**

Le processus d'interpolation développé durant cette thèse est généralisable à d'autres régions à topographie complexe, où les réseaux de pluviomètres sont trop peu denses pour capter la variabilité spatiale et où le radar est soumis à des problèmes de mesure (Berne and Krajewski, 2013). L'utilisation des simulations CP-RCM pour estimer les précipitations climatologiques en montagne ainsi que la variabilité spatiale des précipitations journalières permet d'étendre cette méthode à des régions disposant de très peu de pluviomètres. La seule condition est de disposer de simulations CP-RCM de bonne qualité. Des simulations CP-RCM sont disponibles en Europe centrale (Ban et al., 2021), au Royaume-Uni (Kendon et al., 2012), en Afrique (Stratton et al., 2018), en Australie (Argüeso et al., 2013), en Asie (Prasanna et al., 2024), aux États-Unis (Liu et al., 2017), et en Amérique du Sud (Halladay et al., 2023). Selon la résolution spatiale souhaitée, il pourrait être intéressant de tester si des simulations RCM peuvent se substituer aux simulations CP-RCM, ce qui permettrait d'élargir considérablement le périmètre d'utilisation de ce produit.

— **Aller au-delà des précipitations**

Enfin, le cadre méthodologique proposé pourrait être élargi à d'autres variables atmosphériques (Cornes et al., 2018; Hiebl and Frei, 2018) telles que le vent ou la température, dont la spatialisation en zone de montagne reste particulièrement difficile. Ces variables sont mesurées par des réseaux instrumentaux et simulées par les modèles météorologiques, et se prêtent donc à une approche d'interpolation spatiale similaire à celle développée ici. On peut anticiper que l'anisotropie des variogrammes sera particulièrement adaptée pour interpoler la vitesse du vent, tandis que la construction de champs climatologiques jouera un rôle plus déterminant pour la température.

6.2.4 Valoriser l'utilisation opérationnelle à EDF-DTG

Le produit ISARD, destiné à remplacer SPAZM, ouvre de nouvelles perspectives d'utilisation au sein d'EDF-DTG, aussi bien pour la prévision hydrologique que pour l'évaluation des aléas extrêmes. Il est prévu que ISARD couvre la période 1950–2025 sur l'ensemble du territoire français, avec une mise à jour annuelle. L'interpolation spatiale pourra être réalisée par régions hydrographiques (Ariège, Aude, Dordogne, Drac, Durance, Isère amont, Isère aval, Loire, Lot, ...), où la covariance spatiale est supposée stationnaire.

Dans le cadre du projet ARRA mené par Météo-France, des réanalyses atmosphériques seront produites à partir de 1960, incluant notamment les précipitations. À cette occasion, des simulations AROME, similaires à celles exploitées dans le cadre de cette thèse, ont été géné-

rées avec une résolution spatiale affinée de 1.3 km (contre 2.5 km actuellement). L'extension des séries de données jusqu'aux années 1950 nécessite une estimation de la covariance, sans simulations CP-RCM disponibles. La manière la plus simple se baserait sur l'utilisation d'une covariance climatologique. Une approche par analogues pourrait également être utilisée. Elle consisterait à comparer les précipitations journalières observées avec les champs simulés par AROME, en mesurant leur proximité.

— **Mieux modéliser les extrêmes**

À EDF-DTG, l'évaluation des crues extrêmes repose sur la méthode SCHADEX (Paquet, 2004), qui combine un modèle hydrologique déterministe avec une représentation statistique des précipitations extrêmes. Les pluies sont simulées stochastiquement à partir d'une loi ajustée (MEWP, Garavaglia et al. 2010), puis injectées dans le modèle pluie-débit. La qualité de la pluie de bassin, c'est-à-dire des cumuls spatialisés utilisés en entrée, conditionne directement la validité des crues simulées.

Or, il a été montré que le produit SPAZM tend à lisser la variabilité spatiale des précipitations, ce qui conduit à une sous-estimation des fortes intensités. Penot (2014) a ainsi mis en évidence un biais d'environ 10 % sur les quantiles de précipitation supérieurs à 10 ans de période de retour. Ce biais se répercute directement dans SCHADEX, aboutissant à des crues extrêmes sous-estimées, ce qui empêche l'utilisation de SPAZM dans les études de sûreté des ouvrages hydroélectriques.

Le produit ISARD permet de représenter des intensités localement plus fortes que SPAZM grâce à l'intégration des CP-RCM et à une interpolation anisotrope. Toutefois, les analyses du chapitre 5 ne permettent pas encore de conclure à une amélioration systématique des quantiles extrêmes. L'apport majeur d'ISARD réside surtout dans sa capacité à fournir un ensemble de champs de précipitations, offrant ainsi la possibilité de développer un SCHADEX probabiliste (un SCHADEX par membre de l'ensemble). Cette extension permettrait de mieux caractériser l'incertitude sur les précipitations extrêmes et, par conséquent, sur les crues rares.

— **Renforcer la modélisation hydrologique**

Une seconde perspective concerne l'amélioration de la modélisation hydrologique spatialisée. Les simulations menées avec MORDOR-TS sur l'Isère à EDF-DTG (Rouhier et al., 2017) ont mis en évidence des sous-estimations marquées des cumuls issus de SPAZM dans des massifs tels que la Vanoise et le Beaufortain. Sur plusieurs bassins versants en Vanoise, il faudrait multiplier par 1.4 l'ensemble des précipitations journalières SPAZM pour respecter les bilans hydrologiques. Au vu des résultats présentés dans cette thèse, ISARD offre l'espoir d'atténuer significativement ces biais. Contrairement aux modèles conceptuels traditionnels, qui utilisent des forçages pluviométriques moyennés spatialement, les modèles spatialisés tirent parti de la variabilité spatiale des précipitations. Grâce à son approche ensembliste, ISARD restitue mieux la structure spatiale des événements intenses tout en fournissant une estimation explicite de l'incertitude d'interpolation. Cette capacité ouvre la voie à l'intégration de méthodes plus avancées, telles que la modélisation bayésienne (Renard et al., 2011), pour mieux représenter et propager l'incertitude liée aux forçages atmosphériques.

— **Servir la prévision**

ISARD présente un fort potentiel pour l'appui à la prévision opérationnelle, tant à court terme qu'à moyen terme. Intégré dans une chaîne de prévision en temps réel et étendu au pas de temps horaire, ISARD permettrait de corriger les forçages hydrologiques en remplaçant les précipitations prévisionnelles, souvent incertaines, par des observations

plus récentes et spatialement cohérentes. Ces champs de pluie actualisés pourraient également servir à mettre à jour les états internes des modèles hydrologiques, tels que l'humidité des sols, les stocks nivaux ou le ruissellement de surface, afin que le modèle entre en phase de prévision dans un état plus réaliste. Une telle mise à jour dynamique renforcerait la capacité des systèmes de prévision à anticiper les crues soudaines sur les petits bassins de montagne, souvent les plus vulnérables à ces événements. Enfin, la disponibilité d'ISARD sous forme d'ensemble ouvre la voie à des prévisions hydrologiques probabilistes, désormais devenues une référence dans la science de la prévision.

Par ailleurs, ISARD peut contribuer à la prévision des apports liés à la fonte nivale à l'image de ce qui est réalisé en Suisse (Mott et al., 2023). En fournissant une estimation robuste des stocks de neige disponibles en sortie d'hiver, il aide à anticiper les volumes d'eau mobilisables durant le printemps et l'été. De telles informations sont essentielles pour anticiper les périodes d'étiage de plus en plus fréquentes, et pour ainsi optimiser à la fois la gestion des ressources hydriques et la planification énergétique.

Pour conclure, cette thèse propose un processus d'interpolation spatiale des précipitations journalières fondé sur la fusion entre les simulations issues d'un modèle météorologique à convection profonde résolue (CP-RCM) et les observations pluviométriques. Dans un premier temps, des champs climatologiques de référence sont construits à l'aide d'un algorithme de Random Forest, en intégrant les observations pluviométriques et la structure spatiale de la climatologie simulée par le CP-RCM. Dans un second temps, les anomalies journalières sont interpolées par simulation conditionnelle de champs trans-gaussiens, en utilisant une covariance anisotropique estimée à partir des simulations CP-RCM. Le produit obtenu a été évalué pour des applications hydrologiques, nivologiques et glaciologiques. Il permet de reproduire simultanément : i) les cumuls saisonniers en montagne, grâce à la prise en compte de la variabilité spatiale de la climatologie du CP-RCM ; ii) les crues en modélisation hydrologique, grâce à une approche ensembliste restituant la variabilité spatiale des champs journaliers tout en fournissant une quantification de l'incertitude. Les perspectives d'utilisation de ce produit sont nombreuses : modélisation hydrologique et glaciologique, estimation des précipitations extrêmes, et pourraient être étendues en passant à un interpolateur au pas de temps horaire avec une dimension temps réel.

Bibliographie

Aalto, J., Pirinen, P., Heikkinen, J., and Venäläinen, A. : Spatial interpolation of monthly climate data for Finland : comparing the performance of kriging and generalized additive models, Theoretical and Applied Climatology, 112, 99–111, doi: 10.1007/s00704-012-0716-9, URL https://doi.org/10.1007/s00704-012-0716-9, 2013. (Cited on page 50.)

Adhikary, S. K., Muttil, N., and Yilmaz, A. G. : Cokriging for enhanced spatial interpolation of rainfall in two Australian catchments, Hydrological Processes, 31, 2143–2161, doi: 10.1002/hyp.11163, URL https://onlinelibrary.wiley.com/doi/abs/10.1002/hyp.11163, 2017. (Cited on pages 47, 50, 58, and 68.)

Alpuim, T. and Barbosa, S. : The Kalman filter in the estimation of area precipitation, Environmetrics, 10, 377–394, doi: 10.1002/(SICI)1099-095X(199907/08)10:4<377::AID-ENV363>3.0.CO;2-L, 1999. (Cited on page 68.)

Anders, A. M., Roe, G. H., Hallet, B., Montgomery, D. R., Finnegan, N. J., and Putkonen, J. : Spatial patterns of precipitation and topography in the Himalaya, in : Tectonics, Climate, and Landscape Evolution, edited by Willett, S. D., Hovius, N., Brandon, M. T., and Fisher, D. M., vol. 398, p. 0, Geological Society of America, doi: 10.1130/2006.2398(03), URL https://doi.org/10.1130/2006.2398(03), 2006. (Cited on page 62.)

Argüeso, D., Evans, J. P., and Fita, L. : Precipitation bias correction of very high resolution regional climate models, Hydrology and Earth System Sciences, 17, 4379–4388, doi: 10.5194/hess-17-4379-2013, URL https://hess.copernicus.org/articles/17/4379/2013/, 2013. (Cited on page 111.)

Avanzi, F., Ercolani, G., Gabellani, S., Cremonese, E., Pogliotti, P., Filippa, G., Morra Di Cella, U., Ratto, S., Stevenin, H., Cauduro, M., and Juglair, S. : Learning about precipitation lapse rates from snow course data improves water balance modeling, Hydrology and Earth System Sciences, 25, 2109–2131, doi: 10.5194/hess-25-2109-2021, URL https://hess.copernicus.org/articles/25/2109/2021/, 2021. (Cited on pages 21, 29, 42, and 62.)

Bales, R. C., Molotch, N. P., Painter, T. H., Dettinger, M. D., Rice, R., and Dozier, J. : Mountain hydrology of the western United States, Water Resources Research, 42, doi: 10.1029/2005WR004387, URL https://onlinelibrary.wiley.com/doi/abs/10.1029/2005WR004387, 2006. (Cited on page 20.)

Ban, N., Caillaud, C., Coppola, E., Pichelli, E., Sobolowski, S., Adinolfi, M., Ahrens, B., Alias, A., Anders, I., Bastin, S., Belušić, D., Berthou, S., Brisson, E., Cardoso, R. M., Chan, S. C., Christensen, O. B., Fernández, J., Fita, L., Frisius, T., Gašparac, G., Giorgi, F., Goergen, K., Haugen, J. E., Hodnebrog, , Kartsios, S., Katragkou, E., Kendon, E. J., Keuler, K., Lavin-Gullon, A., Lenderink, G., Leutwyler, D., Lorenz, T., Maraun, D., Mercogliano, P., Milovac, J., Panitz, H.-J., Raffa, M., Remedio, A. R., Schär, C., Soares, P. M. M., Srnec, L., Steensen, B. M., Stocchi, P., Tölle, M. H., Truhetz, H., Vergara-Temprado, J., de Vries, H., Warrach-Sagi, K., Wulfmeyer, V., and Zander, M. J. : The first multi-model ensemble of regional climate simulations at kilometer-scale resolution, part I : evaluation of precipitation, Climate Dynamics, 57, 275–302, doi: 10.1007/s00382-021-05708-w, URL https://doi.org/10.1007/s00382-021-05708-w, 2021. (Cited on pages 8, 21, 26, 42, 49, 63, 71, and 111.)

Bandhauer, M., Isotta, F., Lakatos, M., Lussana, C., Båserud, L., Izsák, B., Szentes, O., Tveito, O. E., and Frei, C. : Evaluation of daily precipitation analyses in E-OBS (v19.0e) and ERA5 by comparison to regional high-resolution datasets in European regions, International Journal of Climatology, 42, 727–747, doi: 10.1002/joc.7269, URL https://onlinelibrary.wiley.com/doi/abs/10.1002/joc.7269, 2022. (Cited on page 109.)

Barrows : Precipitation and runoff and altitude relations for connecticut River, Eos, Transactions American Geophysical Union, URL https://agupubs.onlinelibrary.wiley.com/doi/abs/10.1029/TR014i001p00396, 1933. (Cited on pages 20 and 47.)

Beck, J. and Bousquet, O. : Using Gap-Filling Radars in Mountainous Regions to Complement a National Radar Network : Improvements in Multiple-Doppler Wind Syntheses, Journal of Applied Meteorology and Climatology, 52, 1836–1850, doi: 10.1175/JAMC-D-12-0187.1, URL https://journals.ametsoc.org/view/journals/apme/52/8/jamc-d-12-0187.1.xml, 2013. (Cited on page 26.)

Beguería, S., Vicente-Serrano, S. M., Tomás-Burguera, M., and Maneta, M. : Bias in the variance of gridded data sets leads to misleading conclusions about changes in climate variability, International Journal of Climatology, 36, 3413–3422, doi: 10.1002/joc.4561, URL https://onlinelibrary.wiley.com/doi/abs/10.1002/joc.4561, 2016. (Cited on page 5.)

Bell, B. A., Hughes, P. D., Fletcher, W. J., Cornelissen, H. L., Rhoujjati, A., Hanich, L., and Braithwaite, R. J. : Climate of the Marrakech High Atlas, Morocco : Temperature lapse rates and precipitation gradient from piedmont to summits, Arctic, Antarctic, and Alpine Research, 54, 78–95, doi: 10.1080/15230430.2022.2046897, URL https://doi.org/10.1080/15230430.2022.2046897, 2022. (Cited on page 21.)

Belušić, D., de Vries, H., Dobler, A., Landgren, O., Lind, P., Lindstedt, D., Pedersen, R. A., Sánchez-Perrino, J. C., Toivonen, E., van Ulft, B., Wang, F., Andrae, U., Batrak, Y., Kjellström, E., Lenderink, G., Nikulin, G., Pietikäinen, J.-P., Rodríguez-Camino, E., Samuelsson, P., van Meijgaard, E., and Wu, M. : HCLIM38 : a flexible regional climate model applicable for different climate zones from coarse to convection-permitting scales, Geoscientific Model Development, 13, 1311–1333, doi: 10.5194/gmd-13-1311-2020, URL https://gmd.copernicus.org/articles/13/1311/2020/, 2020. (Cited on pages 21 and 47.)

Bergström, S. : The HBV model–its structure and applications, SMHI, 1992. (Cited on page 20.)

Berne, A. and Krajewski, W. F. : Radar for hydrology : Unfulfilled promise or unrecognized potential ?, Advances in Water Resources, 51, 357–366, doi: 10.1016/j.advwatres.2012.05.005, URL https://www.sciencedirect.com/science/article/pii/S0309170812001157, 2013. (Cited on pages 21, 47, 86, and 111.)

Bonsoms, J. and Ninyerola, M. : Comparison of linear, generalized additive models and machine learning algorithms for spatial climate interpolation, Theoretical and Applied Climatology, 155, 1777–1792, doi: 10.1007/s00704-023-04725-5, URL https://doi.org/10.1007/s00704-023-04725-5, 2024. (Cited on page 11.)

Borges, P. d. A., Franke, J., da Anunciação, Y. M. T., Weiss, H., and Bernhofer, C. : Comparison of spatial interpolation methods for the estimation of precipitation distribution in Distrito Federal, Brazil, Theoretical and Applied Climatology, 123, 335–348, doi: 10.1007/s00704-014-1359-9, URL https://doi.org/10.1007/s00704-014-1359-9, 2016. (Cited on page 50.)

Bostan, P. A., Heuvelink, G. B. M., and Akyurek, S. Z. : Comparison of regression and kriging techniques for mapping the average annual precipitation of Turkey, International Journal of Applied Earth Observation and Geoinformation, 19, 115–126, doi: 10.1016/j.jag.2012.04.010, URL https://www.sciencedirect.com/science/article/pii/S030324341200089X, 2012. (Cited on pages 46, 50, 51, and 68.)

Bothe, O., Fraedrich, K., and Zhu, X. : Precipitation climate of Central Asia and the large-scale atmospheric circulation, Theoretical and Applied Climatology, 108, 345–354, doi: 10.1007/s00704-011-0537-2, URL https://doi.org/10.1007/s00704-011-0537-2, 2012. (Cited on page 62.)

Boudevillain, B. : Caractérisation et estimation quantitative des précipitations atmosphériques par la télédétection, thesis, Université Grenoble Alpes, URL https://hal.science/tel-04945052, 2018. (Cited on page 15.)

Breiman, L. : Bagging predictors, Machine Learning, 24, 123–140, doi: 10.1007/BF00058655, URL https://doi.org/10.1007/BF00058655, 1996. (Cited on page 51.)

Brousseau, P., Seity, Y., Ricard, D., and Léger, J. : Improvement of the forecast of convective activity from the AROME-France system, Royal Meteorological Society, URL https://rmets.onlinelibrary.wiley.com/doi/abs/10.1002/qj.2822, 2016. (Cited on pages 21, 26, 47, and 69.)

Buisán, S. T., Earle, M. E., Collado, J. L., Kochendorfer, J., Alastrué, J., Wolff, M., Smith, C. D., and López-Moreno, J. I. : Assessment of snowfall accumulation underestimation by tipping bucket gauges in the Spanish operational network, Atmospheric Measurement Techniques, 10, 1079–1091, doi: 10.5194/amt-10-1079-2017, URL https://amt.copernicus.org/articles/10/1079/2017/, 2017. (Cited on pages 100 and 108.)

Buzzi, A., Tartaglione, N., and Malguzzi, P. : Numerical Simulations of the 1994 Piedmont Flood : Role of Orography and Moist Processes, Monthly Weather Review, 126, 2369–2383, doi: 10.1175/1520-0493(1998)126<2369:NSOTPF>2.0.CO;2, URL https://journals.ametsoc.org/view/journals/mwre/126/9/1520-0493_1998_126_2369_nsotpf_2.0.co_2.xml, 1998. (Cited on page 20.)

Bárdossy, A. and Anwar, F. : Why do our rainfall–runoff models keep underestimating the peak flows ?, Hydrology and Earth System Sciences, 27, 1987–2000, doi: 10.5194/hess-27-1987-2023, URL https://hess.copernicus.org/articles/27/1987/2023/, 2023. (Cited on page 101.)

Bárdossy, A. and Pegram, G. : Interpolation of precipitation under topographic influence at different time scales, Water Resources Research, 49, 4545–4565, doi: 10.1002/wrcr.20307, 2013. (Cited on pages 47 and 72.)

Bárdossy, A., Seidel, J., and El Hachem, A. : The use of personal weather station observations to improve precipitation estimation and interpolation, Hydrology and Earth System Sciences, 25, 583–601, doi: 10.5194/hess-25-583-2021, URL https://hess.copernicus.org/articles/25/583/2021/, publisher : Copernicus GmbH, 2021. (Cited on page 109.)

Caillaud, C., Somot, S., Alias, A., Bernard-Bouissières, I., Fumière, Q., Laurantin, O., Seity, Y., and Ducrocq, V. : Modelling Mediterranean heavy precipitation events at climate scale : an object-oriented evaluation of the CNRM-AROME convection-permitting regional climate model, Climate Dynamics, 56, 1717–1752, doi: 10.1007/s00382-020-05558-y, URL https://link.springer.com/article/10.1007/s00382-020-05558-y, 2021. (Cited on pages 8, 21, 26, 27, 49, 69, 71, 87, and 91.)

Caine, N. : The rainfall intensity-duration control of shallow landslides and debris flows, Geografiska annaler : series A, physical geography, 62, 23–27, publisher : Taylor & Francis, 1980. (Cited on page 20.)

Canellas, C., Gibelin, A.-L., Lassègues, P., Kerdoncuff, M., Dandin, P., and Simon, P. : Les normales climatiques spatialisées Aurelhy 1981-2010 : températures et précipitations, La Météorologie, pp. 47–55, doi: 10.4267/2042/53750, URL https://lameteorologie.fr/issues/2014/85/meteo_2014_85_47, 2014. (Cited on pages 62 and 69.)

Cantet, P. : Mapping the mean monthly precipitation of a small island using kriging with external drifts, Theoretical and Applied Climatology, 127, 31–44, doi: 10.1007/s00704-015-1610-z, URL https://doi.org/10.1007/s00704-015-1610-z, 2017. (Cited on page 50.)

Caracena, F., Maddox, R. A., Hoxit, L. R., and Chappell, C. F. : Mesoanalysis of the Big Thompson storm, Monthly Weather Review, 107, 1–17, 1979. (Cited on page 20.)

Carrera-Hernández, J. J. and Gaskin, S. J. : Spatio temporal analysis of daily precipitation and temperature in the Basin of Mexico, Journal of Hydrology, 336, 231–249, doi: 10.1016/j.jhydrol.2006.12.021, URL https://www.sciencedirect.com/science/article/pii/S0022169406006718, 2007. (Cited on pages 50 and 61.)

Cauteruccio, A., Chinchella, E., and Lanza, L. G. : The Overall Collection Efficiency of Catching-Type Precipitation Gauges in Windy Conditions, Water Resources Research, 60, e2023WR035 098, doi: 10.1029/2023WR035098, URL https://onlinelibrary.wiley.com/doi/abs/10.1029/2023WR035098, 2024. (Cited on pages 90 and 100.)

Champeaux, J.-L., Dupuy, P., Laurantin, O., Soulan, I., Tabary, P., and Soubeyroux, J.-M. : Les mesures de précipitations et l'estimation des lames d'eau à Météo-France : état de l'art et perspectives, La Houille Blanche, Numero 5, 28–34, doi: 10.1051/lhb/2009052, 2009. (Cited on pages 14, 15, 21, 25, 27, 70, and 86.)

Chan, S. C., Kendon, E. J., Berthou, S., Fosser, G., Lewis, E., and Fowler, H. J. : Europe-wide precipitation projections at convection permitting scale with the Unified Model, Climate Dynamics, 55, 409–428, doi: 10.1007/s00382-020-05192-8, URL https://doi.org/10.1007/s00382-020-05192-8, 2020. (Cited on page 63.)

Collados-Lara, A.-J., Pardo-Igúzquiza, E., Pulido-Velazquez, D., and Jiménez-Sánchez, J. : Precipitation fields in an alpine Mediterranean catchment : Inversion of precipitation gradient with elevation or undercatch of snowfall ?, International Journal of Climatology, 38, 3565–3578, doi: 10.1002/joc.5517, URL https://onlinelibrary.wiley.com/doi/abs/10.1002/joc.5517, 2018. (Cited on page 62.)

Conway, H. and Raymond, C. : Snow stability during rain, Journal of Glaciology, 39, 635–642, publisher : Cambridge University Press, 1993. (Cited on page 20.)

Coppola, E., Sobolowski, S., Pichelli, E., Raffaele, F., Ahrens, B., Anders, I., Ban, N., Bastin, S., Belda, M., Belusic, D., Caldas-Alvarez, A., Cardoso, R. M., Davolio, S., Dobler, A., Fernandez, J., Fita, L., Fumiere, Q., Giorgi, F., Goergen, K., Güttler, I., Halenka, T., Heinzeller, D., Hodnebrog, O., Jacob, D., Kartsios, S., Katragkou, E., Kendon, E., Khodayar, S., Kunstmann, H., Knist, S., Lavín-Gullón, A., Lind, P., Lorenz, T., Maraun, D., Marelle, L., van Meijgaard, E., Milovac, J., Myhre, G., Panitz, H.-J., Piazza, M., Raffa, M., Raub, T., Rockel, B., Schär, C., Sieck, K., Soares, P. M. M., Somot, S., Srnec, L., Stocchi, P., Tölle, M. H., Truhetz, H., Vautard, R., de Vries, H., and Warrach-Sagi, K. : A first-of-its-kind multi-model convection permitting ensemble for investigating convective phenomena over Europe and the Mediterranean, Climate Dynamics, 55, 3–34, doi: 10.1007/s00382-018-4521-8, URL https://doi.org/10.1007/s00382-018-4521-8, 2020. (Cited on page 26.)

Cornes, R. C., Van Der Schrier, G., Van Den Besselaar, E. J. M., and Jones, P. D. : An Ensemble Version of the E-OBS Temperature and Precipitation Data Sets, Journal of Geophysical Research : Atmospheres, 123, doi: 10.1029/2017JD028200, URL https://agupubs.onlinelibrary.wiley.com/doi/10.1029/2017JD028200, 2018. (Cited on pages 12, 17, 86, 107, and 111.)

Coron, L., Thirel, G., Delaigue, O., Perrin, C., and Andréassian, V. : The suite of lumped GR hydrological models in an R package, Environmental Modelling & Software, 94, 166–171, doi: 10.1016/j.envsoft.2017.05.002, URL https://www.sciencedirect.com/science/article/pii/S1364815217300208, 2017. (Cited on page 90.)

Coulston, J. W., Blinn, C. E., Thomas, V. A., and Wynne, R. H. : Approximating Prediction Uncertainty for Random Forest Regression Models, Photogrammetric Engineering & Remote Sensing, 82, 189–197, doi: 10.14358/PERS.82.3.189, 2016. (Cited on page 63.)

Crespi, A., Brunetti, M., Lentini, G., and Maugeri, M. : 1961–1990 high-resolution monthly precipitation climatologies for Italy, International Journal of Climatology, 38, 878–895, doi: 10.1002/joc.5217, URL https://onlinelibrary.wiley.com/doi/abs/10.1002/joc.5217, 2018. (Cited on pages 14 and 60.)

Cressie, N. : Statistics for spatial data, John Wiley & Sons, 1993. (Cited on pages 10 and 68.)

Cuo, L. and Zhang, Y. : Spatial patterns of wet season precipitation vertical gradients on the Tibetan Plateau and the surroundings, Scientific Reports, 7, 5057, doi: 10.1038/s41598-017-05345-6, URL https://www.nature.com/articles/s41598-017-05345-6, 2017. (Cited on page 21.)

Dallan, E., Marra, F., Fosser, G., Marani, M., Formetta, G., Schär, C., and Borga, M. : How well does a convection-permitting regional climate model represent the reverse orographic effect of extreme hourly precipitation ?, Hydrology and Earth System Sciences, 27, 1133–1149, doi: 10.5194/hess-27-1133-2023, URL https://hess.copernicus.org/articles/27/1133/2023/, 2023. (Cited on page 21.)

Daly, C. : Guidelines for assessing the suitability of spatial climate data sets, International Journal of Climatology, 26, 707–721, doi: 10.1002/joc.1322, URL https://onlinelibrary.wiley.com/doi/abs/10.1002/joc.1322, 2006. (Cited on page 17.)

Daly, C., Neilson, R. P., and Phillips, D. L. : A Statistical-Topographic Model for Mapping Climatological Precipitation over Mountainous Terrain, Journal of Applied Meteorology and Climatology, 33, 140–158, doi: 10.1175/1520-0450(1994)033<0140:ASTMFM>2.0.CO;2, URL https://journals.ametsoc.org/view/journals/apme/33/2/1520-0450_1994_033_0140_astmfm_2_0_co_2.xml, 1994. (Cited on pages 10, 14, 20, 39, 68, and 106.)

Dee, D., P, d., Uppala, Simmons, Berrisford, Poli, P., Kobayashi, S., Andrae, U., Balmaseda, M., Balsamo, G., Bauer, Bechtold, Beljaars, Berg, v., Bidlot, J., Bormann, N., Delsol, Dragani, R., Fuentes, M., and Vitart, F. : The ERA-Interim reanalysis : Configuration and performance of the data assimilation system, Quarterly Journal of the Royal Meteorological Society, 137, 553–597, doi: 10.1002/qj.828, 2011. (Cited on pages 49 and 71.)

Delignette-Muller, M. L. and Dutang, C. : fitdistrplus : An R Package for Fitting Distributions, Journal of Statistical Software, 64, 1–34, doi: 10.18637/jss.v064.i04, URL https://doi.org/10.18637/jss.v064.i04, 2015. (Cited on page 71.)

Delrieu, G., Nicol, J., Yates, E., Kirstetter, P.-E., Creutin, J.-D., Anquetin, S., Obled, C., Saulnier, G.-M., Ducrocq, V., Gaume, E., and others : The catastrophic flash-flood event of 8–9 September 2002 in the Gard Region, France : a first case study for the Cévennes–Vivarais Mediterranean Hydrometeorological Observatory, Journal of hydrometeorology, 6, 34–52, 2005. (Cited on page 69.)

Delrieu, G., Boudevillain, B., Wijbrans, A., Faure, D., Bonnifait, L., Kirstetter, P.-E., and Confoland, A. : Prototype de ré-analyses pluviométriques pour la région Cévennes-Vivarais, La Météorologie, 2013, 35–41, doi: 10.4267/2042/52052, URL https://lameteorologie.fr/issues/2013/83/meteo_2013_83_35, 2013. (Cited on page 39.)

Devers, A., Vidal, J.-P., Lauvernet, C., and Vannier, O. : FYRE Climate : a high-resolution reanalysis of daily precipitation and temperature in France from 1871 to 2012, Climate of the Past, 17, 1857–1879, doi: 10.5194/cp-17-1857-2021, URL https://cp.copernicus.org/articles/17/1857/2021/, 2021. (Cited on pages 68, 69, 86, and 107.)

Devers, A., Vidal, J.-P., Lauvernet, C., Vannier, O., and Caillouet, L. : 140-year daily ensemble streamflow reconstructions over 661 catchments in France, Hydrology and Earth System Sciences, 28, 3457–3474, doi: 10.5194/hess-28-3457-2024, URL https://hess.copernicus.org/articles/28/3457/2024/, 2024. (Cited on pages 69 and 90.)

Di Piazza, A., Conti, F. L., Noto, L. V., Viola, F., and La Loggia, G. : Comparative analysis of different techniques for spatial interpolation of rainfall data to create a serially complete monthly time series of precipitation for Sicily, Italy, International Journal of Applied Earth Observation and Geoinformation, 13, 396–408, doi: 10.1016/j.jag.2011.01.005, URL https://www.sciencedirect.com/science/article/pii/S0303243411000225, 2011. (Cited on pages 47 and 58.)

Diggle, P. J., Ribeiro, P. J., and Christensen, O. F. : An introduction to model-based geostatistics, Spatial statistics and computational methods, pp. 43–86, 2003. (Cited on pages 49 and 71.)

Dozier, J., Bair, E. H., and Davis, R. E. : Estimating the spatial distribution of snow water equivalent in the world's mountains, WIREs Water, 3, 461–474, doi: 10.1002/wat2.1140,

URL https://onlinelibrary.wiley.com/doi/abs/10.1002/wat2.1140, 2016. (Cited on page 20.)

Duchon, C., Fiebrich, C., and Grimsley, D. : Using High-Speed Photography to Study Undercatch in Tipping-Bucket Rain Gauges, American Meteorological Society, doi: 10.1175/JTECH-D-13-00169.1, URL https://journals.ametsoc.org/view/journals/atot/31/6/jtech-d-13-00169_1.xml, 2014. (Cited on page 109.)

Dura, V., Evin, G., Favre, A.-C., and Penot, D. : Spatial variability in the seasonal precipitation lapse rates in complex topographical regions – application in France, Hydrology and Earth System Sciences, 28, 2579–2601, doi: 10.5194/hess-28-2579-2024, URL https://hess.copernicus.org/articles/28/2579hb/2024/, 2024a. (Cited on pages 47, 86, 87, and 100.)

Dura, V., Evin, G., Favre, A.-C., and Penot, D. : Spatial Interpolation of Seasonal Precipitations Using Rain Gauge Data and Convection-Permitting Regional Climate Model Simulations in a Complex Topographical Region, International Journal of Climatology, 44, 5745–5760, doi: 10.1002/joc.8662, URL https://onlinelibrary.wiley.com/doi/abs/10.1002/joc.8662, 2024b. (Cited on pages 72, 91, and 101.)

Durand, Y., Laternser, M., Giraud, G., Etchevers, P., Lesaffre, B., and Mérindol, L. : Reanalysis of 44 Yr of Climate in the French Alps (1958–2002) : Methodology, Model Validation, Climatology, and Trends for Air Temperature and Precipitation, Journal of Applied Meteorology and Climatology, 48, 429–449, doi: 10.1175/2008JAMC1808.1, URL https://journals.ametsoc.org/view/journals/apme/48/3/2008jamc1808.1.xml, 2009. (Cited on pages 40 and 105.)

Erdin, R., Frei, C., and Künsch, H. R. : Data Transformation and Uncertainty in Geostatistical Combination of Radar and Rain Gauges, Journal of Hydrometeorology, 13, 1332–1346, doi: 10.1175/JHM-D-11-096.1, URL https://journals.ametsoc.org/view/journals/hydr/13/4/jhm-d-11-096_1.xml, 2012. (Cited on pages 50, 72, and 82.)

Evin, G., Le Lay, M., Fouchier, C., Penot, D., Colleoni, F., Mas, A., Garambois, P.-A., and Laurantin, O. : Evaluation of hydrological models on small mountainous catchments : impact of the meteorological forcings, Hydrology and Earth System Sciences, 28, 261–281, doi: 10.5194/hess-28-261-2024, URL https://hess.copernicus.org/articles/28/261/2024/, 2024. (Cited on pages 15, 17, 71, 86, 90, and 94.)

Fan, Z., Li, W., Jiang, Q., Sun, W., Wen, J., and Gao, J. : A Comparative Study of Four Merging Approaches for Regional Precipitation Estimation, IEEE Access, 9, 33 625–33 637, doi: 10.1109/ACCESS.2021.3057057, URL https://ieeexplore.ieee.org/abstract/document/9358010, 2021. (Cited on pages 11, 46, 51, and 60.)

Fantini, A., Raffaele, F., Torma, C., Bacer, S., Coppola, E., Giorgi, F., Ahrens, B., Dubois, C., Sanchez, E., and Verdecchia, M. : Assessment of multiple daily precipitation statistics in ERA-Interim driven Med-CORDEX and EURO-CORDEX experiments against high resolution observations, Climate Dynamics, 51, 877–900, doi: 10.1007/s00382-016-3453-4, URL https://doi.org/10.1007/s00382-016-3453-4, 2018. (Cited on pages 46, 49, 71, and 86.)

Faure, D., Delrieu, G., and Gaussiat, N. : Impact of the Altitudinal Gradients of Precipitation on the Radar QPE Bias in the French Alps, Atmosphere, 10, 306, doi: 10.3390/atmos10060306, URL https://www.mdpi.com/2073-4433/10/6/306, 2019. (Cited on pages 21, 38, and 86.)

Flores, N., Rodríguez, R., Yépez, S., Osores, V., Rau, P., Rivera, D., and Balocchi, F. : Comparison of Three Daily Rainfall-Runoff Hydrological Models Using Four Evapotranspiration Models in Four Small Forested Watersheds with Different Land Cover in South-Central Chile, Water, 13, 3191, doi: 10.3390/w13223191, URL https://www.mdpi.com/2073-4441/13/22/3191, 2021. (Cited on page 90.)

Foley, A. : Uncertainty in regional climate modelling : A review, Progress in Physical Geography : Earth and Environment, 34, 647–670, doi: 10.1177/0309133310375654, URL https://doi.org/10.1177/0309133310375654, 2010. (Cited on page 21.)

Foresti, L. and Pozdnoukhov, A. : Exploration of alpine orographic precipitation patterns with radar image processing and clustering techniques, Meteorological Applications, 19, 407–419, doi: 10.1002/met.272, URL https://onlinelibrary.wiley.com/doi/abs/10.1002/met.272, 2012. (Cited on page 62.)

Formetta : Differential orographic impact on sub-hourly, hourly, and daily extreme precipitation, Advances in Water Resources, doi: 10.1016/j.advwatres.2021.104085, URL https://doi.org/10.1016/j.advwatres.2021.104085, 2021. (Cited on page 20.)

Frei and Isotta : Ensemble Spatial Precipitation Analysis From Rain Gauge Data : Methodology and Application in the European Alps, JGR Atmospheres, URL https://doi.org/10.1029/2018JD030004, 2019. (Cited on pages 12, 17, 20, 21, 68, 69, 72, 73, 82, 83, 86, 92, and 107.)

Frei, C. and Schär, C. : A precipitation climatology of the Alps from high-resolution rain-gauge observations, International Journal of Climatology, 18, 873–900, doi: 10.1002/(SICI)1097-0088(19980630)18:8<873::AID-JOC255>3.0.CO;2-9, URL https://onlinelibrary.wiley.com/doi/10.1002/(SICI)1097-0088(19980630)18:8<873::AID-JOC255>3.0.CO;2-9, 1998. (Cited on page 58.)

Frey, L. and Frei, C. : Interpolation of Hourly Surface Air Temperature—Application of a Spatio-Temporal Statistical Model in Complex Terrain, International Journal of Climatology, n/a, e8796, doi: 10.1002/joc.8796, URL https://rmets.onlinelibrary.wiley.com/doi/abs/10.1002/joc.8796, 2025. (Cited on page 110.)

Fung, K. F., Chew, K. S., Huang, Y. F., Ahmed, A. N., Teo, F. Y., Ng, J. L., and Elshafie, A. : Evaluation of spatial interpolation methods and spatiotemporal modeling of rainfall distribution in Peninsular Malaysia, Ain Shams Engineering Journal, 13, 101 571, doi: 10.1016/j.asej.2021.09.001, URL https://www.sciencedirect.com/science/article/pii/S209044792100335X, 2022. (Cited on page 51.)

Fushiki, T. : Estimation of prediction error by using K-fold cross-validation, Statistics and Computing, 21, 137–146, doi: 10.1007/s11222-009-9153-8, URL https://doi.org/10.1007/s11222-009-9153-8, 2011. (Cited on page 52.)

Garavaglia, F., Gailhard, J., Paquet, E., Lang, M., Garçon, R., and Bernardara, P. : Introducing a rainfall compound distribution model based on weather patterns sub-sampling, Hydrology and Earth System Sciences, 14, 951–964, doi: 10.5194/hess-14-951-2010, URL https://hess.copernicus.org/articles/14/951/2010/, 2010. (Cited on pages 22, 26, 89, and 112.)

Garavaglia, F., Le Lay, M., Gottardi, F., Garçon, R., Gailhard, J., Paquet, E., and Mathevet, T. : Impact of model structure on flow simulation and hydrological realism : from a

lumped to a semi-distributed approach, Hydrology and Earth System Sciences, 21, 3937–3952, doi: 10.5194/hess-21-3937-2017, URL https://hess.copernicus.org/articles/21/3937/2017/, 2017. (Cited on pages 20 and 90.)

Gerber, F., Besic, N., Sharma, V., Mott, R., Daniels, M., Gabella, M., Berne, A., Germann, U., and Lehning, M. : Spatial variability in snow precipitation and accumulation in COSMO–WRF simulations and radar estimations over complex terrain, The Cryosphere, 12, 3137–3160, doi: 10.5194/tc-12-3137-2018, URL https://tc.copernicus.org/articles/12/3137/2018/, 2018. (Cited on pages 21 and 69.)

Germann, U., Galli, G., Boscacci, M., and Bolliger, M. : Radar precipitation measurement in a mountainous region, Quarterly Journal of the Royal Meteorological Society, 132, 1669–1692, doi: 10.1256/qj.05.190, URL https://onlinelibrary.wiley.com/doi/abs/10.1256/qj.05.190, 2006. (Cited on page 39.)

Gervais, M., Tremblay, L. B., Gyakum, J. R., and Atallah, E. : Representing extremes in a daily gridded precipitation analysis over the United States : Impacts of station density, resolution, and gridding methods, Journal of Climate, 27, 5201–5218, doi: 10.1175/JCLI-D-13-00319.1, URL http://www.scopus.com/inward/record.url?scp=84904488714&partnerID=8YFLogxK, 2014. (Cited on page 5.)

Giorgi, F., Coppola, E., Solmon, F., Mariotti, L., Sylla, M. B., Bi, X., Elguindi, N., Diro, G. T., Nair, V., Giuliani, G., Turuncoglu, U. U., Cozzini, S., Güttler, I., O.Brien, T. A., Tawfik, A. B., Shalaby, A., Zakey, A. S., Steiner, A. L., Stordal, F., Sloan, L. C., and Brankovic, C. : RegCM4 : model description and preliminary tests over multiple CORDEX domains, Climate Research, 52, 7–29, doi: 10.3354/cr01018, URL https://www.int-res.com/abstracts/cr/v52/p7-29/, 2012. (Cited on page 63.)

Gomis-Cebolla, J., Rattayova, V., Salazar-Galán, S., and Francés, F. : Evaluation of ERA5 and ERA5-Land reanalysis precipitation datasets over Spain (1951–2020), Atmospheric Research, 284, 106 606, doi: 10.1016/j.atmosres.2023.106606, URL https://www.sciencedirect.com/science/article/pii/S0169809523000030, 2023. (Cited on pages 25 and 88.)

Goodison, B., Louie, P., and Yang, D. : WMO solid precipitation measurement intercomparison, WMO/TD 872, World Meteorol, Org., Geneva, 1998. (Cited on page 62.)

Goovaerts, P. : Geostatistical approaches for incorporating elevation into the spatial interpolation of rainfall, Journal of Hydrology, 228, 113–129, doi: 10.1016/S0022-1694(00)00144-X, URL https://www.sciencedirect.com/science/article/pii/S002216940000144X, 2000. (Cited on pages 10, 47, and 68.)

Gottardi, F. : Estimation statistique et réanalyse des précipitations en montagne\textlessbr /\textgreaterUtilisation d'ébauches par types de temps et assimilation de données d'enneigement\textlessbr /\textgreaterApplication aux grands massifs montagneux français, phdthesis, Institut National Polytechnique de Grenoble - INPG, URL https://tel.archives-ouvertes.fr/tel-00419170, 2009. (Cited on pages 8, 10, 13, 15, 16, 20, 21, 23, 26, 27, 68, 69, 71, 72, 86, 87, 89, 90, 99, and 106.)

Groisman, P. Y. and Legates, D. R. : The Accuracy of United States Precipitation Data, Bulletin of the American Meteorological Society, 75, 215–228, doi: 10.1175/1520-0477(1994)075<0215:TAOUSP>2.0.CO;2, URL https://journals.ametsoc.org/view/journals/bams/75/2/1520-0477_1994_075_0215_taousp_2_0_co_2.xml, 1994. (Cited on pages 21 and 39.)

Grossi, G., Lendvai, A., Peretti, G., and Ranzi, R. : Snow Precipitation Measured by Gauges : Systematic Error Estimation and Data Series Correction in the Central Italian Alps, Water, 9, 461, doi: 10.3390/w9070461, URL https://www.mdpi.com/2073-4441/9/7/461, 2017. (Cited on page 86.)

Grundmann, J., Hörning, S., and Bárdossy, A. : Stochastic reconstruction of spatio-temporal rainfall patterns by inverse hydrologic modelling, Hydrology and Earth System Sciences, 23, 225–237, doi: 10.5194/hess-23-225-2019, URL https://hess.copernicus.org/articles/23/225/2019/, publisher : Copernicus GmbH, 2019. (Cited on page 9.)

Gugerli, R., Gabella, M., Huss, M., and Salzmann, N. : Can Weather Radars Be Used to Estimate Snow Accumulation on Alpine Glaciers ? An Evaluation Based on Glaciological Surveys, Journal of Hydrometeorology, doi: 10.1175/JHM-D-20-0112.1, URL https://journals.ametsoc.org/view/journals/hydr/21/12/jhm-d-20-0112.1.xml, 2020. (Cited on page 86.)

Gupta, H. V., Kling, H., Yilmaz, K. K., and Martinez, G. F. : Decomposition of the mean squared error and NSE performance criteria : Implications for improving hydrological modelling, Journal of Hydrology, 377, 80–91, doi: 10.1016/j.jhydrol.2009.08.003, URL https://www.sciencedirect.com/science/article/pii/S0022169409004843, 2009. (Cited on pages 52 and 90.)

Guédé, K. G., Yu, Z., Hofmeister, F., Gu, H., Mohammadi, B., Chen, X., Lin, H., Shen, T., and Gouertoumbo, W. F. : Geostatistical Interpolation Approach for Improving Flood Simulation Within a Data-Scarce Region in the Tibetan Plateau, Hydrological Processes, 38, e15 336, doi: 10.1002/hyp.15336, URL https://onlinelibrary.wiley.com/doi/abs/10.1002/hyp.15336, 2024. (Cited on page 68.)

Gyasi-Agyei, Y. : Assessment of radar-based locally varying anisotropy on daily rainfall interpolation, Hydrological Sciences Journal, 61, 1890–1902, doi: 10.1080/02626667.2015.1083652, URL https://doi.org/10.1080/02626667.2015.1083652, 2016. (Cited on pages 10, 47, 82, and 107.)

Gyasi-Agyei, Y. : Realistic sampling of anisotropic correlogram parameters for conditional simulation of daily rainfields, Journal of Hydrology, 556, 1064–1077, doi: 10.1016/j.jhydrol.2016.10.014, URL https://www.sciencedirect.com/science/article/pii/S0022169416306606, 2018. (Cited on pages 71 and 73.)

Gyasi-Agyei, Y. and Pegram, G. : Interpolation of daily rainfall networks using simulated radar fields for realistic hydrological modelling of spatial rain field ensembles, Journal of Hydrology, 519, 777–791, doi: 10.1016/j.jhydrol.2014.08.006, URL https://www.sciencedirect.com/science/article/pii/S0022169414006040, 2014. (Cited on pages 17 and 51.)

Gössling, S., Peeters, P., Hall, C. M., Ceron, J.-P., Dubois, G., Lehmann, L. V., and Scott, D. : Tourism and water use : Supply, demand, and security. An international review, Tourism Management, 33, 1–15, doi: 10.1016/j.tourman.2011.03.015, URL https://www.sciencedirect.com/science/article/pii/S0261517711000793, 2012. (Cited on pages 20 and 46.)

Haberlandt, U. : Geostatistical interpolation of hourly precipitation from rain gauges and radar for a large-scale extreme rainfall event, Journal of Hydrology, 332, 144–157, doi: 10.1016/j.jhydrol.2006.06.028, URL https://www.sciencedirect.com/science/article/pii/S0022169406003416, 2007. (Cited on pages 47, 50, 68, 81, and 107.)

Halladay, K., Kahana, R., Johnson, B., Still, C., Fosser, G., and Alves, L. : Convection-permitting climate simulations for South America with the Met Office Unified Model, Climate Dynamics, 61, 5247–5269, doi: 10.1007/s00382-023-06853-0, URL https://doi.org/10.1007/s00382-023-06853-0, 2023. (Cited on page 111.)

Hassler, B. and Lauer, A. : Comparison of Reanalysis and Observational Precipitation Datasets Including ERA5 and WFDE5, Atmosphere, 12, 1462, doi: 10.3390/atmos12111462, URL https://www.mdpi.com/2073-4433/12/11/1462, 2021. (Cited on pages 24 and 88.)

Haylock, M. R., Hofstra, N., Klein Tank, A. M. G., Klok, E. J., Jones, P. D., and New, M. : A European daily high-resolution gridded data set of surface temperature and precipitation for 1950–2006, Journal of Geophysical Research : Atmospheres, 113, doi: 10.1029/2008JD010201, URL https://onlinelibrary.wiley.com/doi/abs/10.1029/2008JD010201, 2008. (Cited on pages 11, 13, 81, and 107.)

Hengl, T. : A Practical Guide to Geostatistical Mapping of Environmental Variables, Tech. rep., Office for Official Publications of the European Communities, URL https://publications.jrc.ec.europa.eu/repository/handle/JRC38153, 2007. (Cited on page 60.)

Hengl, T., Nussbaum, M., Wright, M., Heuvelink, G., and Graeler, B. : Random forest as a generic framework for predictive modeling of spatial and spatio-temporal variables, PeerJ, 6, e5518, doi: 10.7717/peerj.5518, 2018. (Cited on pages 11, 51, 60, 63, 68, and 106.)

Henriksen, R. L. T., Hubrechts, J. B., Møller, J. K., Knudsen, P., and Pedersen, J. W. : Large-scale rain gauge network optimization using a kriging emulator, Journal of Hydrology, 637, 131 360, doi: 10.1016/j.jhydrol.2024.131360, URL https://www.sciencedirect.com/science/article/pii/S0022169424007558, 2024. (Cited on page 109.)

Hersbach, H., Bell, B., Berrisford, P., Hirahara, S., Horányi, A., Muñoz-Sabater, J., Nicolas, J., Peubey, C., Radu, R., Schepers, D., Simmons, A., Soci, C., Abdalla, S., Abellan, X., Balsamo, G., Bechtold, P., Biavati, G., Bidlot, J., Bonavita, M., De Chiara, G., Dahlgren, P., Dee, D., Diamantakis, M., Dragani, R., Flemming, J., Forbes, R., Fuentes, M., Geer, A., Haimberger, L., Healy, S., Hogan, R. J., Hólm, E., Janisková, M., Keeley, S., Laloyaux, P., Lopez, P., Lupu, C., Radnoti, G., de Rosnay, P., Rozum, I., Vamborg, F., Villaume, S., and Thépaut, J.-N. : The ERA5 global reanalysis, Quarterly Journal of the Royal Meteorological Society, 146, 1999–2049, doi: 10.1002/qj.3803, URL https://onlinelibrary.wiley.com/doi/abs/10.1002/qj.3803, 2020. (Cited on page 88.)

Hewitson, B. C. and Crane, R. G. : Large-scale atmospheric controls on local precipitation in tropical Mexico, Geophysical Research Letters, 19, 1835–1838, doi: 10.1029/92GL01423, URL https://onlinelibrary.wiley.com/doi/abs/10.1029/92GL01423, 1992. (Cited on page 62.)

Hiebl, J. and Frei, C. : Daily precipitation grids for Austria since 1961—development and evaluation of a spatial dataset for hydroclimatic monitoring and modelling, Theoretical and Applied Climatology, 132, 327–345, doi: 10.1007/s00704-017-2093-x, URL https://doi.org/10.1007/s00704-017-2093-x, 2018. (Cited on pages 14, 68, 80, 86, 106, and 111.)

Hijmans, R. J. : raster : Geographic Data Analysis and Modeling, URL https://rspatial.org/raster, 2025. (Cited on page 92.)

Hofstra, N., New, M., and McSweeney, C. : The influence of interpolation and station network density on the distributions and trends of climate variables in gridded daily data, Climate

Dynamics, 35, 841–858, doi: 10.1007/s00382-009-0698-1, URL https://doi.org/10.1007/s00382-009-0698-1, 2010. (Cited on pages 21, 46, 68, 86, and 101.)

Hohenegger, C., Brockhaus, P., and Schär, C. : Towards climate simulations at cloud-resolving scales, Meteorologische Zeitschrift, pp. 383–394, doi: 10.1127/0941-2948/2008/0303, URL https://www.schweizerbart.de/papers/metz/detail/17/56729/Towards_climate_simulations_at_cloud_resolving_sca, 2008. (Cited on page 21.)

Holzkämper, A., Calanca, P., and Fuhrer, J. : Statistical crop models : Predicting the effects of temperature and precipitation changes, Climate Research, 51, 11–21, doi: 10.3354/cr01057, 2012. (Cited on page 46.)

Hrour, Y., Thomas, Z., Rousseau-Gueutin, P., Ait-Brahim, Y., and Fovet, O. : Enhancing hydrological modeling with bias-corrected satellite weather data in data-scarce catchments : a comparative analysis of SWAT and GR4J models, Frontiers in Water, 7, doi: 10.3389/frwa.2025.1582589, URL https://www.frontiersin.org/journals/water/articles/10.3389/frwa.2025.1582589/full, 2025. (Cited on page 90.)

Huang, W.-R., Liu, P.-Y., and Hsu, J. : Multiple timescale assessment of wet season precipitation estimation over Taiwan using the PERSIANN family products, International Journal of Applied Earth Observation and Geoinformation, 103, 102 521, doi: 10.1016/j.jag.2021.102521, URL https://www.sciencedirect.com/science/article/pii/S0303243421002282, 2021. (Cited on page 25.)

Huidobro, G., Chiu, C.-M., Byun, K., and Hamlet, A. F. : Meteorological Driving Datasets for the U.S. Midwest and Great Lakes Region Incorporating Precipitation Gauge Undercatch Corrections, Journal of Hydrometeorology, doi: 10.1175/JHM-D-22-0148.1, URL https://journals.ametsoc.org/view/journals/hydr/24/5/JHM-D-22-0148.1.xml, 2023. (Cited on page 109.)

Hunter, R. D. and Meentemeyer, R. K. : Climatologically Aided Mapping of Daily Precipitation and Temperature, Journal of Applied Meteorology and Climatology, 44, 1501–1510, doi: 10.1175/JAM2295.1, URL https://journals.ametsoc.org/view/journals/apme/44/10/jam2295.1.xml, 2005. (Cited on pages 63 and 72.)

Husak, G. J., Michaelsen, J., and Funk, C. : Use of the gamma distribution to represent monthly rainfall in Africa for drought monitoring applications, International Journal of Climatology, 27, 935–944, doi: 10.1002/joc.1441, URL https://onlinelibrary.wiley.com/doi/abs/10.1002/joc.1441, 2007. (Cited on page 50.)

Hörning, S. and Bárdossy, A. : Simulation of conditional non-Gaussian random fields with directional asymmetry, Spatial Statistics, 65, 100 872, doi: 10.1016/j.spasta.2024.100872, URL https://www.sciencedirect.com/science/article/pii/S2211675324000630, 2025. (Cited on page 110.)

Immerzeel, W. W., Wanders, N., Lutz, A. F., Shea, J. M., and Bierkens, M. F. P. : Reconciling high-altitude precipitation in the upper Indus basin with glacier mass balances and runoff, Hydrology and Earth System Sciences, 19, 4673–4687, doi: 10.5194/hess-19-4673-2015, URL https://hess.copernicus.org/articles/19/4673/2015/, 2015. (Cited on pages 17 and 62.)

Ingebrigtsen, R., Lindgren, F., and Steinsland, I. : Spatial models with explanatory variables in the dependence structure, Spatial Statistics, 8, 20–38, doi: 10.1016/j.spasta.2013.06.002, URL https://www.sciencedirect.com/science/article/pii/S2211675313000377, 2014. (Cited on page 10.)

Isotta, F. A., Frei, C., Weilguni, V., Perčec Tadić, M., Lassègues, P., Rudolf, B., Pavan, V., Cacciamani, C., Antolini, G., Ratto, S. M., Munari, M., Micheletti, S., Bonati, V., Lussana, C., Ronchi, C., Panettieri, E., Marigo, G., and Vertačnik, G. : The climate of daily precipitation in the Alps : development and analysis of a high-resolution grid dataset from pan-Alpine rain-gauge data, International Journal of Climatology, 34, 1657–1675, doi: 10.1002/joc.3794, URL https://rmets.onlinelibrary.wiley.com/doi/10.1002/joc.3794, 2014. (Cited on pages 13 and 109.)

Jiang, Q. : Moist dynamics and orographic precipitation, Tellus A : Dynamic Meteorology and Oceanography, 55, 301, doi: 10.3402/tellusa.v55i4.14577, URL https://a.tellusjournals.se/articles/10.3402/tellusa.v55i4.14577, publisher : Taylor & Francis, 2003. (Cited on page 20.)

Jiang, Y., Yang, K., Shao, C., Zhou, X., Zhao, L., Chen, Y., and Wu, H. : A downscaling approach for constructing high-resolution precipitation dataset over the Tibetan Plateau from ERA5 reanalysis, Atmospheric Research, 256, 105 574, doi: 10.1016/j.atmosres.2021.105574, URL https://www.sciencedirect.com/science/article/pii/S0169809521001265, 2021. (Cited on page 22.)

Jiang, Y., Yang, K., Yang, H., Lu, H., Chen, Y., Zhou, X., Sun, J., Yang, Y., and Wang, Y. : Characterizing basin-scale precipitation gradients in the Third Pole region using a high-resolution atmospheric simulation-based dataset, Hydrology and Earth System Sciences, 26, 4587–4601, doi: 10.5194/hess-26-4587-2022, URL https://hess.copernicus.org/articles/26/4587/2022/, 2022. (Cited on pages 22, 38, 40, and 105.)

Jiang, Y., Yang, K., Qi, Y., Zhou, X., He, J., Lu, H., Li, X., Chen, Y., Li, X., Zhou, B., Mamtimin, A., Shao, C., Ma, X., Tian, J., and Zhou, J. : TPHiPr : a long-term (1979–2020) high-accuracy precipitation dataset (1\/30 $^{\circ}$, daily) for the Third Pole region based on high-resolution atmospheric modeling and dense observations, Earth System Science Data, 15, 621–638, doi: 10.5194/essd-15-621-2023, URL https://essd.copernicus.org/articles/15/621/2023/, 2023. (Cited on pages 14 and 86.)

Jing, X., Geerts, B., Wang, Y., and Liu, C. : Evaluating Seasonal Orographic Precipitation in the Interior Western United States Using Gauge Data, Gridded Precipitation Estimates, and a Regional Climate Simulation, Journal of Hydrometeorology, doi: 10.1175/JHM-D-17-0056.1, URL https://journals.ametsoc.org/view/journals/hydr/18/9/jhm-d-17-0056_1.xml, 2017. (Cited on page 105.)

Jonas, T. and Schirmer, M. : Enhance existing Swiss precipitation products with particular regards to snowfall, Final report, Federal Office of Meteorology and Climatology (MeteoSwiss) and Swiss Federal Institute for Forest, Snow and Landscape Research (WSL), 2022. (Cited on pages 90 and 99.)

Jordan, A., Krüger, F., and Lerch, S. : Evaluating Probabilistic Forecasts with scoringRules, Journal of Statistical Software, 90, 1–37, doi: 10.18637/jss.v090.i12, 2019. (Cited on page 94.)

Kass, R. E. and Raftery, A. E. : Bayes Factors, Journal of the American Statistical Association, 90, 773–795, doi: 10.1080/01621459.1995.10476572, URL https://www.tandfonline.com/doi/abs/10.1080/01621459.1995.10476572, 1995. (Cited on page 29.)

Kendon, E. J., Roberts, N. M., Senior, C. A., and Roberts, M. J. : Realism of Rainfall in a Very High-Resolution Regional Climate Model, Journal of Climate, doi: 10.1175/

JCLI-D-11-00562.1, URL https://journals.ametsoc.org/view/journals/clim/25/17/jcli-d-11-00562.1.xml, 2012. (Cited on pages 21 and 111.)

Keuler, K., Radtke, K., Kotlarski, S., and Lüthi, D. : Regional climate change over Europe in COSMO-CLM : Influence of emission scenario and driving global model, Meteorologische Zeitschrift, pp. 121–136, doi: 10.1127/metz/2016/0662, URL https://www.schweizerbart.de/papers/metz/detail/25/85532/Regional_climate_change_over_Europe_in_COSMO_CLM_I?af=crossref, 2016. (Cited on pages 21, 47, and 69.)

Kochendorfer, J., Earle, M. E., Hodyss, D., Reverdin, A., Roulet, Y.-A., Nitu, R., Rasmussen, R., Landolt, S., Buisán, S., and Laine, T. : Undercatch Adjustments for Tipping-Bucket Gauge Measurements of Solid Precipitation, Journal of Hydrometeorology, 21, 1193–1205, doi: 10.1175/JHM-D-19-0256.1, URL https://journals.ametsoc.org/view/journals/hydr/21/6/jhm-d-19-0256.1.xml, 2020. (Cited on pages 3, 100, and 108.)

Kotlarski, S., Bosshard, T., Lüthi, D., Pall, P., and Schär, C. : Elevation gradients of European climate change in the regional climate model COSMO-CLM, Climatic Change, 112, 189–215, doi: 10.1007/s10584-011-0195-5, URL https://doi.org/10.1007/s10584-011-0195-5, 2012. (Cited on pages 21, 40, and 105.)

Kuana, L. A., Almeida, A. S., Mercuri, E. G. F., and Noe, S. M. : Regionalization of GR4J model parameters for river flow prediction in Paraná, Brazil, Hydrology and Earth System Sciences, 28, 3367–3390, doi: 10.5194/hess-28-3367-2024, URL https://hess.copernicus.org/articles/28/3367/2024/, 2024. (Cited on page 90.)

Kumar, B., Roy, D., and Lakshmi, V. : Impact of temperature and precipitation lapse rate on hydrological modelling over Himalayan Gandak River Basin, Journal of Mountain Science, 19, 3487–3502, doi: 10.1007/s11629-020-6602-5, URL https://doi.org/10.1007/s11629-020-6602-5, 2022. (Cited on page 20.)

Le Moigne, P. : Documentation of the CERRA-Land system, Tech. rep., Météo-France, 2021. (Cited on pages 25, 27, 86, and 89.)

Lewis, R. J. : An introduction to classification and regression tree (CART) analysis, in : Annual meeting of the society for academic emergency medicine in San Francisco, California, vol. 14, Citeseer, 2000. (Cited on page 51.)

Li, L., Gochis, D. J., Sobolowski, S., and Mesquita, M. D. S. : Evaluating the present annual water budget of a Himalayan headwater river basin using a high-resolution atmosphere-hydrology model, Journal of Geophysical Research : Atmospheres, 122, 4786–4807, doi: 10.1002/2016JD026279, URL https://onlinelibrary.wiley.com/doi/abs/10.1002/2016JD026279, 2017. (Cited on pages 21 and 39.)

Lindgren, F., Rue, H., and Lindström, J. : An Explicit Link between Gaussian Fields and Gaussian Markov Random Fields : The Stochastic Partial Differential Equation Approach, Journal of the Royal Statistical Society Series B : Statistical Methodology, 73, 423–498, doi: 10.1111/j.1467-9868.2011.00777.x, URL https://doi.org/10.1111/j.1467-9868.2011.00777.x, 2011. (Cited on page 12.)

Liu, C., Ikeda, K., Rasmussen, R., Barlage, M., Newman, A. J., Prein, A. F., Chen, F., Chen, L., Clark, M., Dai, A., Dudhia, J., Eidhammer, T., Gochis, D., Gutmann, E., Kurkute, S., Li, Y., Thompson, G., and Yates, D. : Continental-scale convection-permitting modeling of the current and future climate of North America, Climate Dynamics, 49, 71–95, doi:

10.1007/s00382-016-3327-9, URL https://doi.org/10.1007/s00382-016-3327-9, 2017. (Cited on page 111.)

Lloyd, C. D. : Nonstationary models for exploring and mapping monthly precipitation in the United Kingdom, International Journal of Climatology, 30, 390–405, doi: 10.1002/joc.1892, URL https://onlinelibrary.wiley.com/doi/abs/10.1002/joc.1892, 2010. (Cited on pages 47 and 58.)

Lucas-Picher, P., Argüeso, D., Brisson, E., Tramblay, Y., Berg, P., Lemonsu, A., Kotlarski, S., and Caillaud, C. : Convection-permitting modeling with regional climate models : Latest developments and next steps, WIREs Climate Change, 12, e731, doi: 10.1002/wcc.731, URL https://onlinelibrary.wiley.com/doi/abs/10.1002/wcc.731, 2021. (Cited on pages 21 and 47.)

Lundquist, J., Hughes, M., Gutmann, E., and Kapnick, S. : Our skill in modeling mountain rain and snow is bypassing the skill of our observational networks, Bulletin of the American Meteorological Society, pp. 2473–2490, doi: 10.1175/BAMS-D-19-0001.1, URL https://journals.ametsoc.org/view/journals/bams/100/12/bams-d-19-0001.1.xml, 2019. (Cited on pages 8, 21, and 101.)

Lussana, C., Saloranta, T., Skaugen, T., Magnusson, J., Tveito, O. E., and ndersen, J. : seNorge2 daily precipitation, an observational gridded dataset over Norway from 1957 to the present day, Earth System Science Data, 10, 235–249, doi: 10.5194/essd-10-235-2018, URL https://essd.copernicus.org/articles/10/235/2018/, 2018. (Cited on page 13.)

MacDonald, J. and Pomeroy, J. W. : Gauge undercatch of two common snowfall gauges in a prairie environment, in : Proceedings of the 64th Eastern Snow Conference, vol. 29, pp. 119–126, 2007. (Cited on page 62.)

MacQueen, J. : Some methods for classification and analysis of multivariate observations, in : Proceedings of the Fifth Berkeley Symposium on Mathematical Statistics and Probability, Volume 1 : Statistics, vol. 5, pp. 281–298, University of California press, 1967. (Cited on page 73.)

Mahmood, T. H., Putkonen, J., and Sobbe, A. : Spatially Variable Precipitation and Its Influence on Water Balance in a Headwater Alpine Basin, Nepal, Water, 13, 254, doi: 10.3390/w13030254, URL https://www.mdpi.com/2073-4441/13/3/254, 2021. (Cited on page 21.)

Maier, R., Krebs, G., Pichler, M., Muschalla, D., and Gruber, G. : Spatial Rainfall Variability in Urban Environments—High-Density Precipitation Measurements on a City-Scale, Water, 12, 1157, doi: 10.3390/w12041157, URL https://www.mdpi.com/2073-4441/12/4/1157, 2020. (Cited on page 109.)

Markstrom, S. L., Regan, R. S., Hay, L. E., Viger, R. J., Webb, R. M., Payn, R. A., and LaFontaine, J. H. : PRMS-IV, the precipitation-runoff modeling system, version 4, Tech. rep., US Geological Survey, 2015. (Cited on page 20.)

Masson, D. and Frei, C. : Spatial analysis of precipitation in a high-mountain region : exploring methods with multi-scale topographic predictors and circulation types, Hydrology and Earth System Sciences, 18, 4543–4563, doi: 10.5194/hess-18-4543-2014, URL https://hess.copernicus.org/articles/18/4543/2014/, 2014. (Cited on pages 13, 46, 47, 50, 58, 60, 63, 68, 72, 86, and 92.)

Masuda, M., Yatagai, A., Kamiguchi, K., and Tanaka, K. : Daily Adjustment for Wind-Induced Precipitation Undercatch of Daily Gridded Precipitation in Japan, Earth and Space Science, 6, 1469–1479, doi: 10.1029/2019EA000659, URL https://onlinelibrary.wiley.com/doi/abs/10.1029/2019EA000659, _eprint : https ://agupubs.onlinelibrary.wiley.com/doi/pdf/10.1029/2019EA000659, 2019. (Cited on page 109.)

Matheson, J. E. and Winkler, R. L. : Scoring Rules for Continuous Probability Distributions, Management Science, doi: 10.1287/mnsc.22.10.1087, URL https://pubsonline.informs.org/doi/abs/10.1287/mnsc.22.10.1087, 1976. (Cited on page 74.)

Meinshausen, N. : Quantile Regression Forests, Journal of Machine Learning Research, 2006. (Cited on pages 63 and 110.)

Mentch, L. and Hooker, G. : Quantifying Uncertainty in Random Forests via Confidence Intervals and Hypothesis Tests, Journal of Machine Learning Research, 2016. (Cited on page 63.)

Mestre, O., Domonkos, P., Picard, F., Auer, I., Robin, S., Lebarbier, E., Böhm, R., Aguilar, E., Guijarro Pastor, J. A., Vertacnik, G., Klancar, M., Dubuisson, B., and Stepanek, P. : HOMER : a homogenization software – methods and applications, Idojaras, URL https://repositorio.aemet.es/handle/20.500.11765/1494, 2013. (Cited on page 26.)

MeteoSwiss : RhiresD : Gridded daily precipitation data for Switzerland, 1 km grid (1961–present), URL https://www.meteoswiss.admin.ch/climate/the-climate-of-switzerland/spatial-climate-analyses.html, published : Open dataset via MeteoSwiss Open Data portal, 2022. (Cited on page 106.)

Mock, C. J. : Climatic Controls and Spatial Variations of Precipitation in the Western United States, Journal of Climate, 9, 1111–1125, doi: 10.1175/1520-0442(1996)009<1111:CCASVO>2.0.CO;2, URL https://journals.ametsoc.org/view/journals/clim/9/5/1520-0442_1996_009_1111_ccasvo_2_0_co_2.xml, 1996. (Cited on page 62.)

Monteiro, D., Caillaud, C., Samacoïts, R., Lafaysse, M., and Morin, S. : Potential and limitations of convection-permitting \textlessspan style="font-variant :small-caps;"\textgreaterCNRM-AROME\textless/span\textgreater climate modelling in the French Alps, International Journal of Climatology, 42, 7162–7185, doi: 10.1002/joc.7637, URL https://onlinelibrary.wiley.com/doi/10.1002/joc.7637, 2022. (Cited on pages 26, 39, 42, 49, 62, 71, and 89.)

Mott, R., Scipión, D., Schneebeli, M., Dawes, N., Berne, A., and Lehning, M. : Orographic effects on snow deposition patterns in mountainous terrain, Journal of Geophysical Research : Atmospheres, 119, 1419–1439, doi: 10.1002/2013JD019880, URL https://onlinelibrary.wiley.com/doi/abs/10.1002/2013JD019880, 2014. (Cited on page 20.)

Mott, R., Winstral, A., Cluzet, B., Helbig, N., Magnusson, J., Mazzotti, G., Quéno, L., Schirmer, M., Webster, C., and Jonas, T. : Operational snow-hydrological modeling for Switzerland, Frontiers in Earth Science, 11, doi: 10.3389/feart.2023.1228158, URL https://www.frontiersin.org/journals/earth-science/articles/10.3389/feart.2023.1228158/full, publisher : Frontiers, 2023. (Cited on page 113.)

Muggeo, V. M. R. : segmented : an R Package to Fit Regression Models with Broken-Line Relationships., R News, 8, 20–25, URL https://cran.r-project.org/doc/Rnews/, 2008. (Cited on page 29.)

Muñoz-Sabater, J., Dutra, E., Agustí-Panareda, A., Albergel, C., Arduini, G., Balsamo, G., Boussetta, S., Choulga, M., Harrigan, S., Hersbach, H., Martens, B., Miralles, D. G., Piles, M., Rodríguez-Fernández, N. J., Zsoter, E., Buontempo, C., and Thépaut, J.-N. : ERA5-Land : a state-of-the-art global reanalysis dataset for land applications, Earth System Science Data, 13, 4349–4383, doi: 10.5194/essd-13-4349-2021, URL https://essd.copernicus.org/articles/13/4349/2021/, 2021. (Cited on pages 24, 27, and 88.)

Ménégoz, M., Valla, E., Jourdain, N. C., Blanchet, J., Beaumet, J., Wilhelm, B., Gallée, H., Fettweis, X., Morin, S., and Anquetin, S. : Contrasting seasonal changes in total and intense precipitation in the European Alps from 1903 to 2010, Hydrology and Earth System Sciences, 24, 5355–5377, doi: 10.5194/hess-24-5355-2020, URL https://hess.copernicus.org/articles/24/5355/2020/, 2020. (Cited on pages 20, 21, 26, 39, 40, 89, and 106.)

Møller, A. B., Beucher, A. M., Pouladi, N., and Greve, M. H. : Oblique geographic coordinates as covariates for digital soil mapping, SOIL, 6, 269–289, doi: 10.5194/soil-6-269-2020, URL https://soil.copernicus.org/articles/6/269/2020/, 2020. (Cited on page 47.)

Nabat, P., Somot, S., Cassou, C., Mallet, M., Michou, M., Bouniol, D., Decharme, B., Drugé, T., Roehrig, R., and Saint-Martin, D. : Modulation of radiative aerosols effects by atmospheric circulation over the Euro-Mediterranean region, Atmospheric Chemistry and Physics, 20, 8315–8349, doi: 10.5194/acp-20-8315-2020, URL https://acp.copernicus.org/articles/20/8315/2020/, 2020. (Cited on pages 49 and 71.)

Napoli, A., Crespi, A., Ragone, F., Maugeri, M., and Pasquero, C. : Variability of orographic enhancement of precipitation in the Alpine region, Scientific Reports, 9, 13 352, doi: 10.1038/s41598-019-49974-5, URL https://www.nature.com/articles/s41598-019-49974-5, 2019. (Cited on pages 20 and 21.)

Nguyen, G. V., Le, X.-H., Nguyen Van, L., May, D. T. T., Jung, S., and Lee, G. : Machine learning approaches for reconstructing gridded precipitation based on multiple source products, Journal of Hydrology : Regional Studies, 48, 101 475, doi: 10.1016/j.ejrh.2023.101475, URL https://www.sciencedirect.com/science/article/pii/S2214581823001623, 2023. (Cited on page 47.)

Nguyen, P., Ombadi, M., Gorooh, V. A., Shearer, E. J., Sadeghi, M., Sorooshian, S., Hsu, K., Bolvin, D., and Ralph, M. F. : PERSIANN Dynamic Infrared–Rain Rate (PDIR-Now) : A Near-Real-Time, Quasi-Global Satellite Precipitation Dataset, Journal of Hydrometeorology, 21, 2893–2906, doi: 10.1175/JHM-D-20-0177.1, URL https://journals.ametsoc.org/view/journals/hydr/21/12/jhm-d-20-0177.1.xml, 2020. (Cited on pages 21, 25, and 27.)

Nie, S., Luo, Y., Wu, T., Shi, X., and Wang, Z. : A merging scheme for constructing daily precipitation analyses based on objective bias-correction and error estimation techniques, Journal of Geophysical Research : Atmospheres, 120, 8671–8692, doi: 10.1002/2015JD023347, URL https://onlinelibrary.wiley.com/doi/abs/10.1002/2015JD023347, 2015. (Cited on page 21.)

Ochoa-Rodriguez, S., Wang, L.-P., Willems, P., and Onof, C. : A Review of Radar-Rain Gauge Data Merging Methods and Their Potential for Urban Hydrological Applications, Water Resources Research, 55, 6356–6391, doi: 10.1029/2018WR023332, URL https://onlinelibrary.wiley.com/doi/abs/10.1029/2018WR023332, 2019. (Cited on page 21.)

Oerlemans, J. and Reichert, B. K. : Relating glacier mass balance to meteorological data by using a seasonal sensitivity characteristic, Journal of Glaciology, 46, 1–6, doi: 10.3189/172756500781833269, URL https:

//www.cambridge.org/core/journals/journal-of-glaciology/article/relating-glacier-mass-balance-to-meteorological-data-by-using-a-seasonal-sensitivity-chara BADC55CE8CD235345DF5554B5C2F5024, 2000. (Cited on page 46.)

Ogrin, M. and Kozamernik, E. : Horizontal Precipitation Gradients in Alpine Valleys of Northwestern Slovenia, Dela, pp. 5–36, doi: 10.4312/dela.49.5-36, URL https://journals-test.uni-lj.si/Dela/article/view/8097, 2018. (Cited on pages 40 and 105.)

Ogrin, M. and Kozamernik, E. : Vertical precipitation gradients : a case study of Alpine valleys of northwestern Slovenia, Theoretical and Applied Climatology, 140, 401–409, doi: 10.1007/s00704-019-03051-z, URL https://doi.org/10.1007/s00704-019-03051-z, 2020. (Cited on page 21.)

Olea, R. A. and Pawlowsky, V. : Compensating for estimation smoothing in kriging, Mathematical Geology, 28, 407–417, doi: 10.1007/BF02083653, URL https://doi.org/10.1007/BF02083653, 1996. (Cited on page 5.)

Oudin, L., Perrin, C., Mathevet, T., Andréassian, V., and Michel, C. : Impact of biased and randomly corrupted inputs on the efficiency and the parameters of watershed models, Journal of Hydrology, 320, 62–83, doi: 10.1016/j.jhydrol.2005.07.016, URL https://www.sciencedirect.com/science/article/pii/S0022169405003409, 2006. (Cited on pages 9 and 20.)

Paciorek, C. J. and Schervish, M. J. : Spatial modelling using a new class of nonstationary covariance functions, Environmetrics, 17, 483–506, doi: 10.1002/env.785, URL https://onlinelibrary.wiley.com/doi/abs/10.1002/env.785, 2006. (Cited on pages 10 and 82.)

Pahaut, E. : L'organisation de la prevision du risque d'avalanches en France, Tech. rep., Météo-France, Toulouse, 1991. (Cited on page 23.)

Pan, X., Yang, D., Li, Y., Barr, A., Helgason, W., Hayashi, M., Marsh, P., Pomeroy, J., and Janowicz, R. J. : Bias corrections of precipitation measurements across experimental sites in different ecoclimatic regions of western Canada, The Cryosphere, 10, 2347–2360, doi: 10.5194/tc-10-2347-2016, URL https://tc.copernicus.org/articles/10/2347/2016/, 2016. (Cited on page 62.)

Panziera, L., James, C. N., and Germann, U. : Mesoscale organization and structure of orographic precipitation producing flash floods in the Lago Maggiore region, Quarterly Journal of the Royal Meteorological Society, 141, 224–248, doi: 10.1002/qj.2351, URL https://onlinelibrary.wiley.com/doi/abs/10.1002/qj.2351, 2015. (Cited on page 20.)

Paquet, E. : Evolution du modèle hydrologique MORDOR : modélisation du stock nival à différentes altitudes, La Houille Blanche, pp. 75–82, doi: 10.1051/lhb:200402008, URL https://www.shf-lhb.org/articles/lhb/abs/2004/02/2004_2_75/2004_2_75.html, 2004. (Cited on pages 90 and 112.)

Pebesma, E. : Simple Features for R : Standardized Support for Spatial Vector Data, The R Journal, 10, 439–446, doi: 10.32614/RJ-2018-009, URL https://doi.org/10.32614/RJ-2018-009, 2018. (Cited on page 92.)

Pebesma, E. J. : Multivariable geostatistics in S : the gstat package, Computers & Geosciences, 30, 683–691, doi: 10.1016/j.cageo.2004.03.012, URL https://www.sciencedirect.com/science/article/pii/S0098300404000676, 2004. (Cited on page 73.)

Pebesma, E. J. and Bivand, R. : Classes and methods for spatial data in R, R News, 5, 9–13, URL https://CRAN.R-project.org/doc/Rnews/, 2005. (Cited on page 92.)

Pellicone, G., Caloiero, T., Modica, G., and Guagliardi, I. : Application of several spatial interpolation techniques to monthly rainfall data in the Calabria region (southern Italy), International Journal of Climatology, 38, 3651–3666, doi: 10.1002/joc.5525, URL https://onlinelibrary.wiley.com/doi/abs/10.1002/joc.5525, 2018. (Cited on pages 46, 50, and 58.)

Penot, D. : Cartographie des événements hydrologiques extrêmes et estimation SCHADEX en sites non jaugés, phdthesis, Université de Grenoble, URL https://theses.hal.science/tel-01233267, 2014. (Cited on pages 16, 71, and 112.)

Pietikäinen, J.-P., Markkanen, T., Sieck, K., Jacob, D., Korhonen, J., Räisänen, P., Gao, Y., Ahola, J., Korhonen, H., Laaksonen, A., and Kaurola, J. : The regional climate model REMO (v2015) coupled with the 1-D freshwater lake model FLake (v1) : Fenno-Scandinavian climate and lakes, Geoscientific Model Development, 11, 1321–1342, doi: 10.5194/gmd-11-1321-2018, URL https://gmd.copernicus.org/articles/11/1321/2018/, 2018. (Cited on page 63.)

Pike, J. G. : The estimation of annual run-off from meteorological data in a tropical climate, Journal of Hydrology, 2, 116–123, doi: 10.1016/0022-1694(64)90022-8, URL https://www.sciencedirect.com/science/article/pii/0022169464900228, 1964. (Cited on pages 9 and 93.)

Pimentel, D., Houser, J., Preiss, E., White, O., Fang, H., Mesnick, L., Barsky, T., Tariche, S., Schreck, J., and Alpert, S. : Water Resources : Agriculture, the Environment, and Society, BioScience, 47, 97–106, doi: 10.2307/1313020, URL https://www.jstor.org/stable/1313020, 1997. (Cited on pages 20 and 46.)

Plouffe, C. C. F., Robertson, C., and Chandrapala, L. : Comparing interpolation techniques for monthly rainfall mapping using multiple evaluation criteria and auxiliary data sources : A case study of Sri Lanka, Environmental Modelling & Software, 67, 57–71, doi: 10.1016/j.envsoft.2015.01.011, URL https://www.sciencedirect.com/science/article/pii/S1364815215000328, 2015. (Cited on page 50.)

Pollock, M. D., O'Donnell, G., Quinn, P., Dutton, M., Black, A., Wilkinson, M. E., Colli, M., Stagnaro, M., Lanza, L. G., Lewis, E., Kilsby, C. G., and O'Connell, P. E. : Quantifying and Mitigating Wind-Induced Undercatch in Rainfall Measurements, Water Resources Research, 54, 3863–3875, doi: 10.1029/2017WR022421, URL https://onlinelibrary.wiley.com/doi/abs/10.1029/2017WR022421, 2018. (Cited on pages 3, 21, 39, 82, and 90.)

Prasanna, V., Dipankar, A., Liu, J., Lim, G., Moise, A., Chua, X. R., Sanchez, C., Chen, C., Yu, J., Raavi, H. P., Luo, F., Hassim, M. E., Sahany, S., and Webster, S. : SINGV-RCM : the convection-permitting regional climate model for Singapore, Climate Dynamics, 62, 5129–5141, doi: 10.1007/s00382-024-07154-w, URL https://doi.org/10.1007/s00382-024-07154-w, 2024. (Cited on page 111.)

Pulka, T., Herrnegger, M., Ehrendorfer, C., Lücking, S., Avanzi, F., Formayer, H., Schulz, K., and Koch, F. : Evaluating precipitation corrections to enhance high-alpine hydrological modeling, Journal of Hydrology, 645, 132 202, doi: 10.1016/j.jhydrol.2024.132202, URL https://www.sciencedirect.com/science/article/pii/S0022169424015981, 2024. (Cited on pages 17 and 106.)

Pushpalatha, R., Perrin, C., Le Moine, N., Mathevet, T., and Andréassian, V. : A downward structural sensitivity analysis of hydrological models to improve low-flow simulation, Journal of Hydrology, 411, 66–76, doi: 10.1016/j.jhydrol.2011.09.034, URL https://www.sciencedirect.com/science/article/pii/S0022169411006846, 2011. (Cited on page 90.)

Quintana-Seguí, P., Le Moigne, P., Durand, Y., Martin, E., Habets, F., Baillon, M., Canellas, C., Franchisteguy, L., and Morel, S. : Analysis of Near-Surface Atmospheric Variables : Validation of the SAFRAN Analysis over France, Journal of Applied Meteorology and Climatology, 47, 92–107, doi: 10.1175/2007JAMC1636.1, URL https://journals.ametsoc.org/doi/10.1175/2007JAMC1636.1, 2008. (Cited on page 15.)

Quéno, L., Vionnet, V., Dombrowski-Etchevers, I., Lafaysse, M., Dumont, M., and Karbou, F. : Snowpack modelling in the Pyrenees driven by kilometric-resolution meteorological forecasts, The Cryosphere, 10, 1571–1589, doi: 10.5194/tc-10-1571-2016, URL https://tc.copernicus.org/articles/10/1571/2016/, 2016. (Cited on page 86.)

Ragettli, S. and Pellicciotti, F. : Calibration of a physically based, spatially distributed hydrological model in a glacierized basin : On the use of knowledge from glaciometeorological processes to constrain model parameters, Water Resources Research, 48, doi: 10.1029/2011WR010559, URL https://onlinelibrary.wiley.com/doi/abs/10.1029/2011WR010559, 2012. (Cited on page 20.)

Rao, C. R., Rao, C. R., Statistiker, M., Rao, C. R., and Rao, C. R. : Linear statistical inference and its applications, vol. 2, Wiley New York, URL https://academic.oup.com/jlms/article-pdf/doi/10.1112/jlms/s1-42.1.382b/2509705/s1-42-1-382b.pdf, 1973. (Cited on page 68.)

Raziei, T., Mofidi, A., Santos, J. A., and Bordi, I. : Spatial patterns and regimes of daily precipitation in Iran in relation to large-scale atmospheric circulation, International Journal of Climatology, 32, 1226–1237, doi: 10.1002/joc.2347, URL https://onlinelibrary.wiley.com/doi/abs/10.1002/joc.2347, 2012. (Cited on page 62.)

Renard, B., Kavetski, D., Leblois, E., Thyer, M., Kuczera, G., and Franks, S. W. : Toward a reliable decomposition of predictive uncertainty in hydrological modeling : Characterizing rainfall errors using conditional simulation, Water Resources Research, 47, W11 516, doi: 10.1029/2011WR010643, URL https://ui.adsabs.harvard.edu/abs/2011WRR....4711516R, 2011. (Cited on pages 17 and 112.)

Ridal, M., Bazile, E., Le Moigne, P., Randriamampianina, R., Schimanke, S., Andrae, U., Berggren, L., Brousseau, P., Dahlgren, P., Edvinsson, L., El-Said, A., Glinton, M., Hagelin, S., Hopsch, S., Isaksson, L., Medeiros, P., Olsson, E., Unden, P., and Wang, Z. Q. : CERRA, the Copernicus European Regional Reanalysis system, Quarterly Journal of the Royal Meteorological Society, 150, 3385–3411, doi: 10.1002/qj.4764, URL https://onlinelibrary.wiley.com/doi/abs/10.1002/qj.4764, 2024. (Cited on page 88.)

Risser, M. D. and Calder, C. A. : Regression-based covariance functions for nonstationary spatial modeling, Environmetrics, 26, 284–297, doi: 10.1002/env.2336, URL https://onlinelibrary.wiley.com/doi/10.1002/env.2336, 2015. (Cited on page 50.)

Risser, M. D. and Calder, C. A. : Local likelihood estimation for covariance functions with spatially-varying parameters : the convoSPAT package for R, arXiv, doi: 10.48550/arXiv.1507.08613, URL http://arxiv.org/abs/1507.08613, publisher : arXiv, 2017. (Cited on pages 10, 82, and 109.)

Risser, M. D., Paciorek, C. J., Wehner, M. F., O'Brien, T. A., and Collins, W. D. : A probabilistic gridded product for daily precipitation extremes over the United States, Climate Dynamics, 53, 2517–2538, doi: 10.1007/s00382-019-04636-0, URL http://link.springer.com/10.1007/s00382-019-04636-0, 2019. (Cited on page 82.)

Rockel, B., Will, A., and Hense, A. : The Regional Climate Model COSMO-CLM (CCLM), Meteorologische Zeitschrift, pp. 347–348, doi: 10.1127/0941-2948/2008/0309, URL https://www.schweizerbart.de/papers/metz/detail/17/56726/The_Regional_Climate_Model_COSMO_CLM_CCLM?af=crossref, 2008. (Cited on pages 21, 47, 63, and 69.)

Roger, L. : Validation et utilisation climatologiques de la ré-analyse de lame d'eau radar Comephore étendue, Stage de fin d'étude, Météo-France, Toulouse, 2017. (Cited on page 25.)

Rouhier, L., Le Lay, M., Garavaglia, F., Le Moine, N., Hendrickx, F., Monteil, C., and Ribstein, P. : Impact of mesoscale spatial variability of climatic inputs and parameters on the hydrological response, Journal of Hydrology, 553, 13–25, doi: 10.1016/j.jhydrol.2017.07.037, URL https://www.sciencedirect.com/science/article/pii/S0022169417305012, 2017. (Cited on pages 101 and 112.)

Rouzeau, S. : Validation climatologique de la réanalyse lame d'eau Comephore 1997-2006, Stage de fin d'étude, Météo-France, Toulouse, 2013. (Cited on page 25.)

Rudy, S. H. and Sapsis, T. P. : Output-weighted and relative entropy loss functions for deep learning precursors of extreme events, Physica D : Nonlinear Phenomena, 443, 133 570, doi: 10.1016/j.physd.2022.133570, URL https://www.sciencedirect.com/science/article/pii/S0167278922002743, 2023. (Cited on page 11.)

Rue, H., Martino, S., and Chopin, N. : Approximate Bayesian Inference for Latent Gaussian models by using Integrated Nested Laplace Approximations, Journal of the Royal Statistical Society Series B : Statistical Methodology, 71, 319–392, doi: 10.1111/j.1467-9868.2008.00700.x, URL https://doi.org/10.1111/j.1467-9868.2008.00700.x, 2009. (Cited on page 12.)

Ruelland, D. : Should altitudinal gradients of temperature and precipitation inputs be inferred from key parameters in snow-hydrological models ?, Hydrology and Earth System Sciences, 24, 2609–2632, doi: 10.5194/hess-24-2609-2020, URL https://hess.copernicus.org/articles/24/2609/2020/, 2020. (Cited on pages 20, 26, 71, and 89.)

Salamon, P. and Feyen, L. : Disentangling uncertainties in distributed hydrological modeling using multiplicative error models and sequential data assimilation, Water Resources Research, 46, doi: 10.1029/2009WR009022, URL https://onlinelibrary.wiley.com/doi/abs/10.1029/2009WR009022, 2010. (Cited on page 9.)

Sampson, P. D. and Guttorp, P. : Nonparametric Estimation of Nonstationary Spatial Covariance Structure, Journal of the American Statistical Association, 87, 108–119, doi: 10.1080/01621459.1992.10475181, URL https://www.tandfonline.com/doi/abs/10.1080/01621459.1992.10475181, 1992. (Cited on page 109.)

Sandre : Bassins versant topographiques - Métropole 2019 - BD Topage®, URL https://geo.data.gouv.fr/fr/datasets/06431249ccb898a370cdacba02347d2f5f0e2d77, publication Title : geo.data.gouv.fr, 2020. (Cited on page 23.)

Schabenberger, O. and Gotway, C. A. : Statistical Methods for Spatial Data Analysis, CRC Press, 2005. (Cited on pages 50, 72, and 73.)

Schermerhorn : Relations between topography and annual precipitation in western Oregon and Washington, Water Resources Research, URL https://agupubs.onlinelibrary.wiley.com/doi/abs/10.1029/WR003i003p00707, 1967. (Cited on pages 20 and 47.)

Scheuerer, M. : Probabilistic quantitative precipitation forecasting using Ensemble Model Output Statistics, Quarterly Journal of the Royal Meteorological Society, 140, 1086–1096, doi: 10.1002/qj.2183, URL https://onlinelibrary.wiley.com/doi/abs/10.1002/qj.2183, 2014. (Cited on page 12.)

Schiemann, R., Erdin, R., Willi, M., Frei, C., Berenguer, M., and Sempere-Torres, D. : Geostatistical radar-raingauge combination with nonparametric correlograms : methodological considerations and application in Switzerland, Hydrology and Earth System Sciences, 15, 1515–1536, doi: 10.5194/hess-15-1515-2011, URL https://hess.copernicus.org/articles/15/1515/2011/, 2011. (Cited on pages 10, 14, 50, 69, 73, 82, and 107.)

Schlosser, L., Hothorn, T., Stauffer, R., and Zeileis, A. : Distributional regression forests for probabilistic precipitation forecasting in complex terrain, The Annals of Applied Statistics, 13, 1564–1589, doi: 10.1214/19-AOAS1247, URL https://projecteuclid.org/journals/annals-of-applied-statistics/volume-13/issue-3/Distributional-regression-forests-for-probabilistic-precipitation-forecasting-in-complex-te
10.1214/19-AOAS1247.full, 2019. (Cited on page 12.)

Schäppi, B. : Measurement and analysis of rainfall gradients along a hillslope transect in the Swiss Alps, PhD Thesis, ETH Zurich, doi: 10.3929/ETHZ-A-009913260, URL http://hdl.handle.net/20.500.11850/69019, 2013. (Cited on pages 20, 21, and 40.)

Seity, Y., Brousseau, P., Malardel, S., Hello, G., Bénard, P., Bouttier, F., Lac, C., and Masson, V. : The AROME-France Convective-Scale Operational Model, Monthly Weather Review, 139, 976–991, doi: 10.1175/2010MWR3425.1, URL https://journals.ametsoc.org/view/journals/mwre/139/3/2010mwr3425.1.xml, 2011. (Cited on page 26.)

Sekulić, A., Kilibarda, M., Heuvelink, G. B. M., Nikolić, M., and Bajat, B. : Random Forest Spatial Interpolation, Remote Sensing, 12, 1687, doi: 10.3390/rs12101687, URL https://www.mdpi.com/2072-4292/12/10/1687, 2020. (Cited on pages 11, 47, 51, and 68.)

Sevruk, B. : Methods of correction for systematic error in point precipitation measurement for operational use, Secretariat of the World Meteorological Organization Geneva, Switzerland, 1982. (Cited on page 62.)

Sevruk, B. : Regional dependency of precipitation-altitude relationship in the Swiss Alps, Climatic Change, 36, 355–369, doi: 10.1023/A:1005302626066, URL https://doi.org/10.1023/A:1005302626066, 1997. (Cited on pages 21, 39, 40, 42, 62, and 105.)

Sevruk, B. and Mieglitz, K. : The effect of topography, season and weather situation on daily precipitation gradients in 60 Swiss valleys, Water Science and Technology, 45, 41–48, doi: 10.2166/wst.2002.0025, URL https://iwaponline.com/wst/article/45/2/41/9079/The-effect-of-topography-season-and-weather, 2002. (Cited on page 20.)

Sevruk, B., Ondrás, M., and Chvíla, B. : The WMO precipitation measurement intercomparisons, Atmospheric Research, 92, 376–380, doi: 10.1016/j.atmosres.2009.01.016, URL https://www.sciencedirect.com/science/article/pii/S0169809509000337, 2009. (Cited on pages 82, 86, 90, and 100.)

Shen, Y., Hong, Z., Pan, Y., Yu, J., and Maguire, L. : China's 1 km Merged Gauge, Radar and Satellite Experimental Precipitation Dataset, Remote Sensing, 10, 264, doi: 10.3390/rs10020264, URL https://www.mdpi.com/2072-4292/10/2/264, 2018. (Cited on page 21.)

Shi, Y., Li, L., and Zhang, L. : Application and comparing of IDW and Kriging interpolation in spatial rainfall information, in : Geoinformatics 2007 : Geospatial Information Science, vol. 6753, pp. 539–550, SPIE, doi: 10.1117/12.761859, URL https://www.spiedigitallibrary.org/conference-proceedings-of-spie/6753/67531I/Application-and-comparing-of-IDW-and-Kriging-interpolation-in-spatial/10.1117/12.761859.full, 2007. (Cited on pages 81 and 107.)

Sideris, I. V., Gabella, M., Erdin, R., and Germann, U. : Real-time radar–rain-gauge merging using spatio-temporal co-kriging with external drift in the alpine terrain of Switzerland, Quarterly Journal of the Royal Meteorological Society, 140, 1097–1111, doi: 10.1002/qj.2188, URL https://onlinelibrary.wiley.com/doi/abs/10.1002/qj.2188, 2014. (Cited on pages 47, 68, 86, and 110.)

Silverman, N. L., Maneta, M. P., Chen, S.-H., and Harper, J. T. : Dynamically downscaled winter precipitation over complex terrain of the Central Rockies of Western Montana, USA, Water Resources Research, 49, 458–470, doi: 10.1029/2012WR012874, URL https://onlinelibrary.wiley.com/doi/abs/10.1029/2012WR012874, 2013. (Cited on pages 21 and 39.)

Simpson, D., Rue, H., Riebler, A., Martins, T. G., and Sørbye, S. H. : Penalising Model Component Complexity : A Principled, Practical Approach to Constructing Priors, Statistical Science, 32, 1–28, doi: 10.1214/16-STS576, URL https://projecteuclid.org/journals/statistical-science/volume-32/issue-1/Penalising-Model-Component-Complexity--A-Principled-Practical-Approach-to/10.1214/16-STS576.full, 2017. (Cited on page 110.)

Six, D. and Vincent, C. : Sensitivity of mass balance and equilibrium-line altitude to climate change in the French Alps, Journal of Glaciology, 60, 867–878, doi: 10.3189/2014JoG14J014, URL https://www.cambridge.org/core/journals/journal-of-glaciology/article/sensitivity-of-mass-balance-and-equilibriumline-altitude-to-climate-change-in-the-french-5C8093FF717BFC29B6D105CB8BF746BB, 2014. (Cited on page 89.)

Skamarock, C., Klemp, B., Dudhia, J., Gill, O., Barker, D., Duda, G., Huang, X.-y., Wang, W., and Powers, G. : A Description of the Advanced Research WRF Version 3, Tech. rep., University Corporation for Atmospheric Research, doi: 10.5065/D68S4MVH, 2024. (Cited on page 63.)

Skamarock, W. C., Klemp, J. B., Dudhia, J., Gill, D. O., Liu, Z., Berner, J., Wang, W., Powers, J. G., Duda, M. G., Barker, D. M., et al. : A description of the advanced research WRF version 4, NCAR tech. note ncar/tn-556+ str, 145, 2019. (Cited on page 105.)

Smith, R. B. : The Influence of Mountains on the Atmosphere, in : Advances in Geophysics, edited by Saltzman, B., vol. 21, pp. 87–230, Elsevier, doi: 10.1016/S0065-2687(08)60262-9, URL https://www.sciencedirect.com/science/article/pii/S0065268708602629, 1979. (Cited on pages 20 and 47.)

Soci, C., Bazile, E., Besson, F., and Landelius, T. : High-resolution precipitation re-analysis system for climatological purposes, Tellus A : Dynamic Meteorology and Oceanography,

68, 29 879, doi: 10.3402/tellusa.v68.29879, URL https://doi.org/10.3402/tellusa.v68.29879, 2016. (Cited on pages 25 and 89.)

Spreen : A determination of the effect of topography upon precipitation, Eos, Transactions American Geophysical Union, 28, 285–290, doi: 10.1029/TR028i002p00285, URL https://onlinelibrary.wiley.com/doi/abs/10.1029/TR028i002p00285, 1947. (Cited on pages 20 and 47.)

Stockham, A. J., Schultz, D. M., Fairman, J. G., and Draude, A. P. : Quantifying the Rain-Shadow Effect : Results from the Peak District, British Isles, Bulletin of the American Meteorological Society, 99, 777–790, doi: 10.1175/BAMS-D-17-0256.1, URL https://journals.ametsoc.org/view/journals/bams/99/4/bams-d-17-0256.1.xml, 2018. (Cited on page 62.)

Stratton, R. A., Senior, C. A., Vosper, S. B., Folwell, S. S., Boutle, I. A., Earnshaw, P. D., Kendon, E., Lock, A. P., Malcolm, A., Manners, J., Morcrette, C. J., Short, C., Stirling, A. J., Taylor, C. M., Tucker, S., Webster, S., and Wilkinson, J. M. : A pan-African convection-permitting regional climate simulation with the Met Office Unified Model : CP4-Africa, Journal of Climate, 31, doi: 10.1175/JCLI-D-17-0503.1, URL https://doi.org/10.1175/JCLI-D-17-0503.1, publisher : American Meteorological Society, 2018. (Cited on page 111.)

Sun, W., Zhu, Y., Huang, S., and Guo, C. : Mapping the mean annual precipitation of China using local interpolation techniques, Theoretical and Applied Climatology, 119, 171–180, doi: 10.1007/s00704-014-1105-3, URL https://doi.org/10.1007/s00704-014-1105-3, 2015. (Cited on pages 50 and 51.)

Suri, A. and Azad, S. : Optimal placement of rain gauge networks in complex terrains for monitoring extreme rainfall events : a review, Theoretical and Applied Climatology, 155, 2511–2521, doi: 10.1007/s00704-024-04856-3, URL https://doi.org/10.1007/s00704-024-04856-3, 2024. (Cited on page 1.)

Termonia, P., Fischer, C., Bazile, E., Bouyssel, F., Brožková, R., Bénard, P., Bochenek, B., Degrauwe, D., Derková, M., El Khatib, R., Hamdi, R., Mašek, J., Pottier, P., Pristov, N., Seity, Y., Smolíková, P., Španiel, O., Tudor, M., Wang, Y., Wittmann, C., and Joly, A. : The ALADIN System and its canonical model configurations AROME CY41T1 and ALARO CY40T1, Geoscientific Model Development, 11, 257–281, doi: 10.5194/gmd-11-257-2018, URL https://gmd.copernicus.org/articles/11/257/2018/gmd-11-257-2018.html, 2018. (Cited on page 26.)

Teweles, S. and Wobus, H. B. : Verification of Prognostic Charts, Bulletin of the American Meteorological Society, doi: 10.1175/1520-0477-35.10.455, URL https://journals.ametsoc.org/view/journals/bams/35/10/1520-0477-35_10_455.xml, 1954. (Cited on page 74.)

Thibert, E., Blanc, R., Vincent, C., and Eckert, N. : Glaciological and volumetric mass-balance measurements : error analysis over 51 years for Glacier de Sarennes, French Alps, Journal of Glaciology, 54, 522–532, doi: 10.3189/002214308785837093, URL https://www.cambridge.org/core/journals/journal-of-glaciology/article/glaciological-and-volumetric-massbalance-measurements-error-analysis-over-51-years-for-gla
D86F595E9FB73290DBBF6B072FE62A1F, 2008. (Cited on page 89.)

Thiessen, A. H. : Precipitation averages for large areas, Monthly weather review, URL https://journals.ametsoc.org/view/journals/mwre/39/7/1520-0493_1911_39_1082b_pafla_2_0_co_2.xml, 1911. (Cited on page 10.)

Thornton, P. E., Shrestha, R., Thornton, M., Kao, S.-C., Wei, Y., and Wilson, B. E. : Gridded daily weather data for North America with comprehensive uncertainty quantification, Scientific Data, 8, 190, doi: 10.1038/s41597-021-00973-0, URL https://www.nature.com/articles/s41597-021-00973-0, 2021. (Cited on page 11.)

Tobin, C., Nicotina, L., Parlange, M. B., Berne, A., and Rinaldo, A. : Improved interpolation of meteorological forcings for hydrologic applications in a Swiss Alpine region, Journal of Hydrology, 401, 77–89, doi: 10.1016/j.jhydrol.2011.02.010, URL https://www.sciencedirect.com/science/article/pii/S0022169411001156, 2011. (Cited on pages 8, 46, 58, and 68.)

Tobler, W. R. : A computer movie simulating urban growth in the Detroit region, Economic geography, 46, 234–240, publisher : Taylor & Francis, 1970. (Cited on page 68.)

Turc, L. : Le bilan d'eau des sols : relations entre les précipitations, l'évaporation et l'écoulement, Persée - Portail des revues scientifiques en SHS, URL https://www.persee.fr/doc/jhydr_0000-0001_1955_act_3_1_3278, 1955. (Cited on pages 9 and 93.)

Tyralis, H., Papacharalampous, G., and Khatami, S. : Expectile-based hydrological modelling for uncertainty estimation : Life after mean, Journal of Hydrology, 617, 128 986, doi: 10.1016/j.jhydrol.2022.128986, URL http://arxiv.org/abs/2201.05712, arXiv : 2201.05712 [stat], 2023. (Cited on page 90.)

Türkeş, M., Koç, T., and Sariş, F. : Spatiotemporal variability of precipitation total series over Turkey, International Journal of Climatology, 29, 1056–1074, doi: 10.1002/joc.1768, URL https://onlinelibrary.wiley.com/doi/abs/10.1002/joc.1768, 2009. (Cited on page 48.)

Uysal, G. : Product- and Hydro-Validation of Satellite-Based Precipitation Data Sets for a Poorly Gauged Snow-Fed Basin in Turkey, Water, 14, 2758, doi: 10.3390/w14172758, URL https://www.mdpi.com/2073-4441/14/17/2758, 2022. (Cited on page 25.)

Velasco-Forero, C. A., Sempere-Torres, D., Cassiraga, E. F., and Jaime Gómez-Hernández, J. : A non-parametric automatic blending methodology to estimate rainfall fields from rain gauge and radar data, Advances in Water Resources, 32, 986–1002, doi: 10.1016/j.advwatres.2008.10.004, URL https://www.sciencedirect.com/science/article/pii/S0309170808001760, 2009. (Cited on pages 10, 14, 47, 50, 68, 82, 107, and 111.)

Verdin, A., Funk, C., Rajagopalan, B., and Kleiber, W. : Kriging and Local Polynomial Methods for Blending Satellite-Derived and Gauge Precipitation Estimates to Support Hydrologic Early Warning Systems, IEEE Transactions on Geoscience and Remote Sensing, 54, 2552–2562, doi: 10.1109/TGRS.2015.2502956, 2016. (Cited on page 68.)

Vernay, M., Lafaysse, M., and Augros, C. : Radar-based high-resolution ensemble precipitation analyses over the French Alps, Atmospheric Measurement Techniques, 18, 1731–1755, doi: 10.5194/amt-18-1731-2025, URL https://amt.copernicus.org/articles/18/1731/2025/, 2025. (Cited on pages 14, 17, 68, and 107.)

Vidal, J.-P., Martin, E., Franchistéguy, L., Baillon, M., and Soubeyroux, J.-M. : A 50-year high-resolution atmospheric reanalysis over France with the Safran system, International Journal of Climatology, 30, P. 1627, doi: 10.1002/joc.2003, URL https://meteofrance.hal.science/meteo-00420845, 2010. (Cited on pages 15 and 86.)

Vionnet, V., Six, D., Auger, L., Dumont, M., Lafaysse, M., Quéno, L., Réveillet, M., Dombrowski-Etchevers, I., Thibert, E., and Vincent, C. : Sub-kilometer Precipitation Datasets for Snowpack and Glacier Modeling in Alpine Terrain, Frontiers in Earth Science, 7, doi: 10.3389/feart.2019.00182, URL https://www.frontiersin.org/journals/earth-science/articles/10.3389/feart.2019.00182/full, 2019. (Cited on page 86.)

Vischel, T., Lebel, T., Massuel, S., and Cappelaere, B. : Conditional simulation schemes of rain fields and their application to rainfall–runoff modeling studies in the Sahel, Journal of Hydrology, 375, 273–286, doi: 10.1016/j.jhydrol.2009.02.028, URL https://www.sciencedirect.com/science/article/pii/S0022169409000900, 2009. (Cited on pages 5 and 17.)

Viviroli, D., Dürr, H. H., Messerli, B., Meybeck, M., and Weingartner, R. : Mountains of the world, water towers for humanity : Typology, mapping, and global significance, Water Resources Research, 43, doi: 10.1029/2006WR005653, URL https://onlinelibrary.wiley.com/doi/abs/10.1029/2006WR005653, 2007. (Cited on pages 20 and 46.)

Vogl, S., Laux, P., Qiu, W., Mao, G., and Kunstmann, H. : Copula-based assimilation of radar and gauge information to derive bias-corrected precipitation fields, Hydrology and Earth System Sciences, 16, 2311–2328, doi: 10.5194/hess-16-2311-2012, URL https://hess.copernicus.org/articles/16/2311/2012/, 2012. (Cited on page 14.)

Vögeli, C., Lehning, M., Wever, N., and Bavay, M. : Scaling Precipitation Input to Spatially Distributed Hydrological Models by Measured Snow Distribution, Frontiers in Earth Science, 4, URL https://www.frontiersin.org/articles/10.3389/feart.2016.00108, 2016. (Cited on page 62.)

Wager, S. : Asymptotic Theory for Random Forests, doi: 10.48550/arXiv.1405.0352, URL http://arxiv.org/abs/1405.0352, 2016. (Cited on page 63.)

Wagnon, P., Vincent, C., Arnaud, Y., Berthier, E., Vuillermoz, E., Gruber, S., Ménégoz, M., Gilbert, A., Dumont, M., Shea, J. M., Stumm, D., and Pokhrel, B. K. : Seasonal and annual mass balances of Mera and Pokalde glaciers (Nepal Himalaya) since 2007, The Cryosphere, 7, 1769–1786, doi: 10.5194/tc-7-1769-2013, URL https://tc.copernicus.org/articles/7/1769/2013/, 2013. (Cited on page 46.)

Wasko, C., Sharma, A., and Rasmussen, P. : Improved spatial prediction : A combinatorial approach, Water Resources Research, 49, 3927–3935, doi: 10.1002/wrcr.20290, URL https://onlinelibrary.wiley.com/doi/abs/10.1002/wrcr.20290, 2013. (Cited on page 14.)

Willmott, C. J., Rowe, C. M., and Philpot, W. D. : Small-Scale Climate Maps : A Sensitivity Analysis of Some Common Assumptions Associated with Grid-Point Interpolation and Contouring, The American Cartographer, 12, 5–16, doi: 10.1559/152304085783914686, URL https://doi.org/10.1559/152304085783914686, 1985. (Cited on page 10.)

Wolff, M. A., Isaksen, K., Petersen-Øverleir, A., Ødemark, K., Reitan, T., and Brækkan, R. : Derivation of a new continuous adjustment function for correcting wind-induced loss of solid precipitation : results of a Norwegian field study, Hydrology and Earth System Sciences, 19, 951–967, doi: 10.5194/hess-19-951-2015, URL https://hess.copernicus.org/articles/19/951/2015/, 2015. (Cited on page 62.)

Wright, M. N. and Ziegler, A. : ranger : A Fast Implementation of Random Forests for High Dimensional Data in C++ and R, Journal of Statistical Software, 77, 1–17, doi: 10.18637/jss.v077.i01, 2017. (Cited on page 92.)

Wrzesien, M. L., Pavelsky, T. M., Durand, M. T., Dozier, J., and Lundquist, J. D. : Characterizing Biases in Mountain Snow Accumulation From Global Data Sets, Water Resources Research, 55, 9873–9891, doi: 10.1029/2019WR025350, URL https://onlinelibrary.wiley.com/doi/abs/10.1029/2019WR025350, 2019. (Cited on page 20.)

Xu, L., Chen, N., Yang, C., Yu, H., and Chen, Z. : Quantifying the uncertainty of precipitation forecasting using probabilistic deep learning, Hydrology and Earth System Sciences, 26, 2923–2938, doi: 10.5194/hess-26-2923-2022, URL https://hess.copernicus.org/articles/26/2923/2022/, 2022. (Cited on page 12.)

Yan, J., Li, F., Bárdossy, A., and Tao, T. : Conditional simulation of spatial rainfall fields using random mixing : a study that implements full control over the stochastic process, Hydrology and Earth System Sciences, 25, 3819–3835, doi: 10.5194/hess-25-3819-2021, URL https://hess.copernicus.org/articles/25/3819/2021/, 2021. (Cited on page 68.)

Zandi, O., Zahraie, B., Nasseri, M., and Behrangi, A. : Stacking machine learning models versus a locally weighted linear model to generate high-resolution monthly precipitation over a topographically complex area, Atmospheric Research, 272, 106 159, doi: 10.1016/j.atmosres.2022.106159, URL https://www.sciencedirect.com/science/article/pii/S0169809522001454, 2022. (Cited on pages 11, 51, and 68.)

Zhang, J., Qi, Y., Langston, C., Kaney, B., and Howard, K. : A Real-Time Algorithm for Merging Radar QPEs with Rain Gauge Observations and Orographic Precipitation Climatology, Journal of Hydrometeorology, doi: 10.1175/JHM-D-13-0163.1, URL https://journals.ametsoc.org/view/journals/hydr/15/5/jhm-d-13-0163_1.xml, 2014. (Cited on page 111.)